MAGNETOTELLURIC MONITORING

by

Jared Peacock

Dissertation submitted in partial fulfilment of
course work requirements for the degree of
Doctor in Philosophy in Geophysics
School of Earth and Environmental Sciences
University of Adelaide
November 2012

Contents

List of Figures

Abstract

Enhanced geothermal systems (EGS) are emerging as an alternative energy supply, though progress has been slowed due to multiple uncertainties in subsurface processes. The most important unknown that needs to be overcome is how to spatially characterize injected fluids. Micro-seismic tomography can locate fractures opening caused by hydraulic pressure, but cannot directly discriminate whether that fracture is fluid filled or connected to other fractures. Magnetotellurics (MT) is sensitive to volumetric electrical conductivity contrasts with depth, specifically thermally enhanced saline fluids in a resistive host rock. Presented in this dissertation are 2 experiments designed for employing MT as a monitoring tool to characterize a fluid injection for the first stage of an EGS at Paralana, South Australia. The first experiment utilizes 11 MT stations set around the injection well continuously measuring 2 days before, 5 days during and 2 days after the fluid injection. Comparing the MT response estimated before the injection with subsequent responses estimated in 24 hour blocks demonstrates a temporal variation associated with injection of an electrically conductive fluid. Residual phase tensor analysis suggests that injected fluids migrated NE of the injection well in a preferred NNE direction, which correlates well with a concurrent micro-seismic array. The second experiment is a time-lapse MT survey that measures the MT response before and after the fluid injection by repeating the same 56 station array. The array contains 2 orthogonal lines of 22 stations each and 2 off diagonal lines of 6 stations each. Multiple pre-injection surveys were collected to ensure data precision and accuracy with a repeatability between surveys being on the order of 0.4 percent for periods above 1 second. However, in the MT dead band (1-20 s) repeatability is on the order of 3-4 percent. This is because of poor source signal and noise from a near by pipeline. The post-injection survey was collected a week after the injection finished and repeatability between pre and post-injection at high frequencies is on the order of 1 percent. Residual phase tensor analysis again suggest fluids propagated NE of the injection well but mostly into an existing fracture network trending NNE. These experiments suggest that MT can be used as a monitoring tool for a fluid injection, but care must be taken in collecting precise and accurate data as well as a detailed analysis of what can cause an anomalous MT response. Residual phase tensor analysis proves to be the most useful representation of the MT response because it provides directionality and is insensitive to near surface distortions. Finally, it is suggested that a dense grid of MT and micro-seismic measurements be collected as complimentary pairs to fully characterize a fluid injection.

Acknowledgements

There have been a plethora of people who helped me get to where I am today especially my family. No doubt my parents Karl and Debby are the first to thank, for supporting me through everything I've done, even when I'm on the other side of the world. Thanks to my brother Ryan who has always been there pushing me every step of the way, instilling my ferocious competitive spirit. Thanks to all my friends back in Colorado who have been supporting me since I stepped on the plane. I've been in school a long time and there have been so many teachers, coaches and pupils that have taught me that life is one big research experiment and I thank all of them, especially Mr. John Martin for entrenching the scientific method into personal habit. Thanks to my advisors Dr. Stephan Thiel, Dr. Martin Hand, and Dr. Graham Heinson for first a useful project and then cultivating my research into a successful experiment. Especially, to Stephan for engaging conversations and great travel experiences, also Dr. Mike Hatch for useful banter and Grant Caldwell for insightful discussions. Thanks to Paul Pedrosian and Graham Hill for insightful reviews and insuring this work is of a high standard worthy of a PhD. Gratitude to all the PhD candidates and honors students for extending the expertise in magnetotellurics and making geophysics fun. Thanks to the South Australian Center for Geothermal Energy Research (SACGER) for support and all the enjoyable meetings with edibles. Also, to Department for Manufacturing, Innovation, Trade, Resources and Energy, Petratherm and SACGER for financial support of this project. Without the financial support from the University of Adelaide I would have never completed a post-graduate program in Australia. I am extremely grateful to Tammie Hamilton for being my Australian ambassador and family away from home, without her this research would not have been done. Finally, I would like to thank everyone on Team Tempo for letting me run with them and keep some sanity in my life, training was usually the best part of my day. Again, there are so many people to thank so I'll end with one big 'Cheers mate!'

I certify that this work contains no material which has been accepted for the award of any other degree or diploma in any university or other tertiary institution and, to the best of my knowledge and belief, contains no material previously published or written by another person, except where due reference has been made in the text. In addition, I certify that no part of this work will, in the future, be used in a submission for any other degree or diploma in any university or other tertiary institution without the prior approval of the University of Adelaide and where applicable, any partner institution responsible for the joint-award of this degree. I give consent to this copy of my thesis when deposited in the University Library, being made available for loan and photocopying, subject to the provisions of the Copyright Act 1968. The author acknowledges that copyright of published works contained within this thesis resides with the copyright holder(s) of those works. I also give permission for the digital version of my thesis to be made available on the web, via the Universitys digital research repository, the Library catalogue and also through web search engines, unless permission has been granted by the University to restrict access for a period of time.

Date _____ Signed: _____
Jared Peacock

Chapter 1

Introduction

Thomas Kuhn defined a paradigm shift as a change in thought due to scientific evidence, classically exemplified by Copernicus' heliocentric universe (Kuhn, 1962). Unfortunately, people are innately resistant to change as observed from the present situation of global climate change due to man's excessive pecuniary lust. Scientists have presented measurements undeniably correlating mass fossil fuel combustion with rise in atmospheric greenhouse gas composition and global climate change (Parry *et al.*, 2007). The need for a paradigm shift has never been more important, not only for humans but the survival of planet Earth. The simple solution is to stop the cause, fossil fuel consumption, but logistically proves to be difficult as money continues to manipulate political and economic flow. Thus, alternative solutions must be made post haste. Alternative energy from renewables provided by nature, such as solar, wind, water and geothermal provide a logical solution to the climactic conundrum.

Geothermal energy has a significant advantage over other renewable energies in that it produces base load power. Traditionally, geothermal energy has been generated in regions of volcanic activity such as Iceland, New Zealand and Japan. However, in the 1970's a group from Los Alamos National Laboratory designed and tested an enhanced or engineered geothermal system (EGS) at Fenton Hill, New Mexico (Purtymun *et al.*, 1974). The principle simply exploits the Earth's natural increasing heat gradient with depth by pumping fluids down to a certain depth where they can absorb heat and be extracted to produce energy efficiently. Most drilling, fracturing and fluid injection techniques have been transferred from the petroleum industry, however EGS is not the same process as oil and gas extraction. Again, thinking needs to be shifted to the problem at hand. Many different aspects of the system need to be addressed namely corrosion of well casing and pipes, heat exchangers, and most importantly monitoring fluid properties and location within the proposed reservoir.

The main geophysical technique to characterize fractures opening during hydraulic stimulation for an EGS is micro-seismic monitoring (Wohlenberg & Keppler, 1987; House, 1987), where size and orientation of the fractures can be estimated from shear wave splitting (Rial *et al.*, 2005). However, micro-seismic is not directly sensitive to fluids being included in fractures nor how well fractures are connected. Electromagnetic (EM) techniques are directly sensitive to electrical conductivity contrasts, specifically connected paths of conductive material, such as a brine solution in a resistive host rock.

Electric and EM methods have been successfully employed to monitor subsurface processes. Typically used for shallow targets (above $\sim$ 2 km), the self-potential (SP) method maps electrical potential differences as a function of position on the surface. SP is directly sensitive to subsurface fluid movement and can be used as a monitoring tool for near for fluid movement (ex. Aizawa *et al.* (2005); Yasukawa *et al.* (2005)).

Time domain electromagnetics have also been applied to map and monitor near surface fluids (ex. (Buselli & Lu, 2001)). However, deeper targets need different methods. Magnetotellurics (MT) is a passive EM method that measures the Earth's response to natural time varying magnetic fields, which gives it a versatile depth of investigation (Kaufman & Keller, 1981). In one of the first detailed long term monitoring MT studies, Kappler *et al.* (2010) collected continuous MT measurement along the San Andreas Fault. No precursor electromagnetic signal to seismic activity was detected, however Kappler *et al.* (2010) described vigourous and thorough analysis methods valuable to monitoring MT surveys. Bedrosian *et al.* (2004) conducted one of the first MT surveys aimed at monitoring a fluid injection. They conducted hypothesis testing to estimate the viability of using MT as a monitoring tool. They found that a conductive sphere with a 1 km diameter would be detectable. They test this hypothesis by continuously measuring during the fluid injection with 11 MT stations setup in an L centered on the borehole. Then, 2D inversions were employed to compare the MT response before and after, unfortunately they found noise masked any MT response originating from a fluid injection at depth. Aizawa *et al.* (2011) deployed two continuous MT stations aimed at monitoring volcanic processes on Sakurajima volcano, Japan. They estimated the MT response each day and estimated a 20% change in the apparent resistivity coincident with subsurface uplift and degassing. These monitoring surveys support the extension of MT to a monitoring tool, while exhibiting the necessity for precise, accurate, and spatially dense measurements.

1.1 Problem Statement

Can magnetotellurics measure changes in subsurface resistivity structure caused by the injection of conductive fluids at depth?

The goal of this dissertation is to prove the viability of MT as a tool to temporally and spatially monitor a fluid injection designed to create an EGS. Paralana, South Australia is the test site. Here the first stage of hydraulic stimulation for a planned EGS is the fluid injection being monitored in this project. The fluid injection was successfully completed in July, 2011 where 3.1 million liters of saline fluids were injected at 3.6 km depth.

To test the viability of MT as a monitoring tool two separate experiments are preformed to test different methods. The first experiment is nominated 'continuous monitoring,' here MT instruments are set out a few days before the fluid injection and continuously record until a few days after the injection. Then, the MT response is estimated in time blocks and compared to the MT response estimate pre-injection to characterize coherent changes above measurement error. The second experiment is nominated 'time-lapse,' here the same survey setup is repeated pre and post injection. The MT response are then compared to characterize coherent changes above measurement error. In both experiments, residual phase tensors are estimated to characterize directional changes associated with variations in subsurface resistivity structure. These results are compared to micro-seismic data collected during the fluid injection.

1.2 Outline

This dissertation is split into two parts. Part I describes methods used to process and analyze data, beginning with a brief overview of the MT method in Chapter 2.

Methods for time series analysis and filtering are discussed in Chapter 3, and Chapter 4 describes method to analyze MT data. Part II discusses in detail the two experiments, beginning with a brief description of EGS, survey layout and the resistivity structure at Paralana estimated from 2D and 3D modeling in Chapter 5. Chapters 6 and 7 are in the form of scientific papers following the scientific method and have been either accepted or submitted as papers. Chapter 6 describes the continuous monitoring experiment. Parts of Chapter 6 have been accepted as a short paper in *Geophysical Research Letters*, which is Appendix C, but because it is a short paper more detail is provided. Chapter 7 describes the time-lapse experiment and has been submitted to *Geophysics*. Finally, Chapter 8 wraps up this dissertation with some concluding remarks and suggestions on how to improve these experiments.

Part I

MT Methods

Chapter 2

Magnetotellurics

2.1 Introduction

Magnetotellurics (MT) is a wonderful example of natural physics and dynamic interstellar processes. A passive geophysical measurement, MT exploits Faradays's Law of induction via the Earth's natural time dependent magnetic field. Early formalism by Tikhonov (1950) (reprint in Tikhonov (1986)) and Cagniard (1953) built the formal foundations of MT as a geophysical tool and exemplified the MT method with analytical solutions to simple layered models. A very basic assumption of MT is that the frequency dependent electric and magnetic fields are related by a linear transfer function representing the Earth's response to electrical and magnetic structure. This transfer function is known as the impedance tensor $\hat{\mathbf{Z}}$, which contains all the information about the electrical response of the system. By nature, MT is a diffusive electromagnetic process and needs at least 2-dimensions to describe it physically. However, the Earth is heterogeneous and anisotropic prescribing the need for three dimensions to fully characterize the system, (Niblett & Sayn-Wittgenstein, 1960; Dmitriev & Berdichevsky, 1979; Wannamaker, 2005; Berdichevsky & Dmitriev, 2008). Herein lies a problem: how to get out the information in such a way that it makes physical sense? This chapter gives a brief overview and formally defines MT.

2.2 MT Summary

The Earth has a natural magnetic field due to an internal dynamo that can be approximated as a magnetic dipole. Serendipity strikes twice. Firstly, this magnetic field is the first line of defense against solar radiation providing an environment for life to evolve and nurture creatures of cognitive thought. Secondly, interaction with the solar wind generates time varying electric currents that provide the main magnetic source field for MT. Complex interaction of solar wind and the Earth's magnetic field is of great interest to many fields of geophysics and proves to be difficult to characterize formally (Lui, 2002; Omura *et al.*, 2010). Generally, solar wind impinges on the magnetosphere at normal incidence near the equator. This intense pressure field displaces energized particles, some propagate vertically and others horizontally. The Earth's magnetic field pulls on these particles along the magnetic field lines, generating massive currents that are the main source for MT at periods greater than 1 s. At mid latitudes , the magnetic field can be approximated as a plane wave at normal incidence, but near the equator and near the poles fields can go non-planar. Moreover, diurnal cycles, solar cycles, seasonal tilt, and more affects particle flux flowing along the field lines changing source field strength and polarization. Therefore, care must be taken when conducting

an MT survey, being sure to know the nature of the source field at that location and time (Mareschal, 1986; Viljanen *et al.*, 2001).

MT is diffusive, energy is only lost through absorbtion. Formally, the electromagnetic propagation vector is complex, which makes the amplitude and phase of the EM fields time and frequency dependent. Measurements of the electric and magnetic fields are usually collected in the time domain, whereas formalism is in the frequency domain. Assuming the system is linear, which is necessary for Maxwell's equations to hold, a Fourier Transform can be applied to the data (Hermance, 1973; Kunetz, 1972). To estimate the MT transfer function, the time series are split into different window sizes, where Fourier coefficients are calculated to represent the time series as a weighted sum of orthonormal harmonic basis functions. It is these coefficients that are used to estimate the MT transfer function and over the years several methods have been utilized to improve signal extraction and reduce the influence of noise. Gamble *et al.* (1979) suggests remote referencing, the technique of comparing magnetic field measured at a station with reference magnetic field measurements simultaneously recorded at a distant location ($\sim$ 10 times the largest target skin depth). Chave *et al.* (1987), Larsen *et al.* (1996), Smirnov (2003) and Chave & Thomson (2004) suggest statistically robust processing techniques to remove outliers from the cross powers to get the best estimate of $\hat{\mathbf{Z}}$. Egbert (1997) suggests multivariate robust methods for multi-station processing. Jones *et al.* (1989) compare the methods of transfer function estimation, finding that robust processing methods in conjunction with remote referencing methods are the most effective at accurate estimating the MT transfer function.

It is important to note that the impedance tensor contains all the information about the Earth; this proves to be ambiguously helpful. All the information is there but this includes effects that cannot currently be uniquely determined, consequently information is lost. For instance static shift (Pellerin & Hohmann, 1990), galvanic distortion (Jiracek, 1990), induced polarization (Stoyer, 1976), dispersion (Yee & Paulson, 1988), frequency dependent dispersion (Patella, 1987), and dimensionality effects (Kunetz, 1972; Ledo, 2005; Eisel & Egbert, 2001; Bibby *et al.*, 2005) are all included in the impedance tensor. Multiple methods have been developed to extract or remove the influence of such information but unfortunately no method is universal. Groom & Bailey (1989),Bahr (1988) and McNeice & Jones (2001) propose to use matrix decomposition to analyze the contents of the impedance tensor, specifically trying to extract the regional response. Szarka & Menvielle (1997) examine the seven invariants of the impedance tensor demonstrating their usefulness with a synthetic example. Lilley (1993), Lilley (1998a), Lilley (1998b), Weaver *et al.* (2000), and Weaver & Lilley (2004) relate invariants of the impedance tensor to physical parameters, using Mohr's circle as a graphical representation. Romo *et al.* (2005) suggest a series and parallel basis transformation for estimating geoelectric structure. Reilly (1979) defines a real resistivity tensor and real permittivity tensor, while Weckmann *et al.* (2003) demonstrate the usefulness of the resistivity tensor for synthetic and real examples. Similarly, Caldwell *et al.* (2004) compute the MT phase tensor from the impedance tensor which is free of galvanic distortions, making it a powerful tool for estimating the regional MT response. All these methods aim at deciphering dimensionality and estimating the regional MT response.

As with all geophysical methods, the measured observables are usually not the information desired, the physical parameters that can be derived from the measured observables are. Similarly, with MT, resistivity is computed from the impedance tensor where geolectric structure can be inverted for and modeled. Various methods have been developed depending on the dimensionality (eg. Ledo (2005); Gatzemeier & Moorkamp

(2005)). One dimensional inversions are useful for simple structure and depth estimation (Oldenburg, 1979). Two dimensional (depth and the lateral dimension perpendicular to geoelectric strike) inversions prove to be useful in most environments and has been the weapon of choice due to computation speed. Constable *et al.* (1987) formulate an inversion technique that finds the smoothest model possible subject to regularization constraints on model simplicity based on an Occam algorithm. The inversion utilizes the forward operator of Wannamaker *et al.* (1987). Rodi & Mackie (2001) employ a conjugate gradient method to find the optimum model. Recently, three dimensional inversion has become more efficient due to technological advances. Multiple codes have been written (Mackie *et al.*, 1993; Mackie & Madden, 1993a,b; Sasaki, 2004; Sasaki & Meju, 2006; Siripunvaraporn *et al.*, 2005; Siripunvaraporn & Egbert, 2009; Han *et al.*, 2009a; Avdeev, 2005; Farquharson & Craven, 2009). Four codes of (Mackie *et al.*, 1993; Sasaki, 2004; Siripunvaraporn *et al.*, 2005; Han *et al.*, 2009a) are briefly compared by (Han *et al.*, 2009b), which reveals little difference in results, where as computation time is on the same order of time except for the method of Han *et al.* (2009a) which takes 2 orders of magnitude longer. It is important to note that these are deterministic methods that depend on the starting model and can get caught in local minima of the model space. Therefore, it is important to test the robustness and sensitivity of the model.

Once the resistivity structure is modeled (Wannamaker, 2005), many other material properties can be calculated. Spichak (2006) and Spichak *et al.* (2007) estimate temperature. Using Archie's law one can derive porosity (Griffiths, 1976; Garg *et al.*, 2007; Spichak & Manzella, 2009). Patella (1987) and Patella (1993) suggest complex resistivity can be measured implying something about the frequency dependance of the resistivity. Interpretation can also be initiated and here is where non-uniqueness tests knowledge and experience. Strike relations suggested by Zhang *et al.* (1987) can be used as guidelines. Using impedance tensor information aids in deciphering dimensionality and areas of high conductivity. The only way to make sense of the model is to use any geological and geophysical data available.

2.3 Derivation

Derivation of MT formalism can be straight forward with some clever simplifying assumptions. These will be presented at the beginning as a reference for the derivations and to introduce reasoning behind physical theory. Following Simpson & Bahr (2005), eight assumptions are made to simplify the problem.

1. **Linearity:** The measured electromagnetic fields obey Maxwell's equations.
2. **Far Field:** The fields are conservative and analytic away from their source.
3. **Passive Earth:** The Earth is a dielectric and only absorbs or dissipates EM energy and does not create its own fields.
4. **Plane Wave:** The time varying magnetic source fields generated from ionospheric currents produce polarized EM plane waves at near normal incidence to the Earth's surface.
5. **No Free Charges:** Free charges cannot be supported by the Earth, however charges can accumulate at subsurface discontinuities that produce non-inductive response (galvanic distortion).

6. **Conservative:** Charge is conserved and the Earth acts as an ohmic conductor obeying the dispersion equation known as Ohm's Law.

7. **Quasi-Static:** Displacement currents arising from polarization of free charges are negligible, allowing the process to be only diffusive.

8. **Volumetric:** Subsurface variations in permittivity and magnetic permeability are negligible compared to the conductivity.

The MT derivation will start from Maxwell's equations, but first a brief understanding of vector calculus is presented for clarity of physical processes.

2.3.1 Basic Calculus Operators

Some basic calculus operators are defined for a clear understanding to the physical processes underlying MT. The main operator is ∇ (partial derivative operator 'del'), which is a differential operator defined in Cartesian coordinates as $(\partial/\partial x, \partial/\partial y, \partial/\partial z)$, where the derivative $\partial/\partial x$ defines the rate at which a function changes in a particular direction (x). For instance the time derivative of a time-dependent function gives velocity, the second time derivative gives acceleration and the third time derivative gives jerk. Basically, three ways to use ∇ are the gradient, divergence and curl. First, the gradient eq. (2.1) is a vector quantity describing the spatial rate of change of a vector function $\mathbf{A}$, where the resultant vector points in the direction of the greatest rate of change.

$$\nabla \mathbf{A} = \frac{\partial \mathbf{A}}{\partial x}\hat{\mathbf{x}} + \frac{\partial \mathbf{A}}{\partial y}\hat{\mathbf{y}} + \frac{\partial \mathbf{A}}{\partial z}\hat{\mathbf{z}} \tag{2.1}$$

Next, the divergence eq. (2.2) is a scalar quantity that measures the magnitude of sources and sinks in a given volume. A source radiates information, conversely a sink is where information converges. The resulting quantity is a scalar quantity of how sources and sinks are distributed within the given volume.

$$\nabla \cdot \mathbf{A} = \frac{\partial \mathbf{A}}{\partial x} + \frac{\partial \mathbf{A}}{\partial y} + \frac{\partial \mathbf{A}}{\partial z} \tag{2.2}$$

A third way to use ∇ is the curl eq. (2.3), which is a vector quantity that describes the rate of rotation of a function. The resultant vector is normal to the plane of rotation as prescribed by the right hand rule.

$$\nabla \times \mathbf{A} = \left(\frac{\partial \mathbf{A}_z}{\partial y} - \frac{\partial \mathbf{A}_y}{\partial z}\right)\hat{\mathbf{x}} - \left(\frac{\partial \mathbf{A}_x}{\partial z} - \frac{\partial \mathbf{A}_z}{\partial x}\right)\hat{\mathbf{y}} + \left(\frac{\partial \mathbf{A}_x}{\partial y} - \frac{\partial \mathbf{A}_y}{\partial x}\right)\hat{\mathbf{z}} \tag{2.3}$$

Along with these three field operators, two important theorems arise. That is the Divergence Theorem, or Gauss' Theorem, and Stoke's Theorem. Gauss' Theorem relates the volume integral of the divergence to the flux emitted from a closed surface eq. (2.4). More precisely, the volumetric sum of sources and sinks of a system is equal to the flux on a closed surface of the same volume.

$$\int_V \nabla \cdot \mathbf{A}\, dV = \oint_S \mathbf{A} \cdot d\mathbf{S} \tag{2.4}$$

Similarly, Stoke's Theorem relates the integral of the curl along a closed surface to the integral along a closed loop eq. (2.5). Stoke's Theorem suggests that the curl does not need to be calculated only the integral along a closed loop.

$$\oint_S \nabla \times \mathbf{A}\, d\mathbf{S} = \oint_l \mathbf{A} \cdot d\mathbf{l} \tag{2.5}$$

2.3.2 Maxwell's Equations

Beginning with Maxwell's equations describing electromagnetic fields in free space (on the left is the derivative form and on the right is the equivalent integral form):

$$\nabla \cdot \mathbf{E} = \frac{\rho_t}{\epsilon_o} \quad \Leftrightarrow \quad \oint_S \mathbf{E} \cdot d\mathbf{S} = \frac{1}{\epsilon_o} \int_V \rho_{free} \cdot dV \tag{2.6}$$

$$\nabla \times \mathbf{E} = -\frac{\partial \mathbf{B}}{\partial t} \quad \Leftrightarrow \quad \oint_l \mathbf{E} \cdot d\mathbf{l} = -\frac{\partial}{\partial t} \int_S \mathbf{B} \cdot d\mathbf{S} \tag{2.7}$$

$$\nabla \cdot \mathbf{B} = 0 \quad \Leftrightarrow \quad \oint_S \mathbf{B} \cdot d\mathbf{S} = 0 \tag{2.8}$$

$$\nabla \times \mathbf{B} = \mu_o \mathbf{J} + \frac{1}{\epsilon_o} \frac{\partial \mathbf{E}}{\partial t} \quad \Leftrightarrow \quad \oint_l \mathbf{B} \cdot d\mathbf{l} = \frac{1}{\mu_o} \int_S \mathbf{J} \cdot d\mathbf{s} + \frac{1}{\epsilon_o} \frac{\partial}{\partial t} \int_S \mathbf{E} \cdot d\mathbf{S} \tag{2.9}$$

where $\mathbf{E} = \mathbf{E}(\mathbf{r}, t)$ and $\mathbf{B} = \mathbf{B}(\mathbf{r}, t)$ and $\mathbf{r} \in \mathbb{R}^3$.

Equation (2.6), known as Gauss' Law, demonstrates that the divergence of an electric field is related to the total charge density ρ_t of a given volume. Physically, this means the sources and sinks of an electric field are electric charges and the fact that ρ_t is some number means these charges can be positive or negative. The parameter ϵ_o is the free space permittivity, measuring how free space supports the separation of charge. Interestingly, ϵ_o is non-zero, meaning charges are constantly being created and destroyed in a vacuum; this fact allows electromagnetic waves to propagate through free space. Also note that the permittivity dictates the velocity of the electromagnetic wave passing through the material. The integral equation may be more revealing by describing the electric flux, the number of field lines passing through a given surface, which is directly related to the total charge enclosed.

Equation (2.7), also known as Faraday's Law, demonstrates the curl of an electric field $\mathbf{E}$ is related to a time varying magnetic field $\mathbf{B}$. The negative sign implies a $\pi/2$ phase difference between electric and magnetic fields, meaning energy is constantly transferred between the electric and magnetic field, i.e. when one has a maximu the other has a minimum. It simply describes how a shakeable flashlight or basically any turbine can generate electricity.

Equation (2.8) demonstrates the divergence of the magnetic field $\mathbf{B}$ is identically zero. The fact that the magnetic charge density is identically zero physically means there are no singular magnetic charges; there is always a positive and a negative, or north and south pole. Instead of positive and negative charges as in electric fields, magnetic fields are generated by magnetic domains, like stick magnets.

Finally, Equation (2.9), also known as Ampere's Law or Maxwell's Law, describes the curl of a magnetic field is related to the current density $\mathbf{J}$ and a time varying electric field $\mathbf{E}$. Physically this means that moving charges create a magnetic field. The first term, $\mu_o \mathbf{J}$ is related to bound charges moving and the second term is related to free charges moving. The parameter μ_o is known as the magnetic permeability of free space and describes how free space supports magnetic domain movement, or how free space magnetizes. Again, note that this value is non-zero which again allows electromagnetic fields to travel through free space. Interestingly, the speed of light is related to the dielectric permittivity and magnetic permeability by Equation (2.10):

$$c = \frac{1}{\sqrt{\mu_o \epsilon_o}} \tag{2.10}$$

Because the Earth is not free space, some parameters need to be adjusted by what are known as the constitutive equations. First, the electric field is adjusted to more accurately describe how an electric field behaves in a material. Time varying electric currents related to the separation of charge are known as displacement currents. Displacement currents $\mathbf{D}$ are related to the electric field $\mathbf{E}$ by the material's dielectric permittivity ϵ, which again describes how a material supports the separation of charge. Specifically, how a material polarizes in the presence of an electric field and how fast an EM wave can propagate through the material.

$$\mathbf{D} = \epsilon \mathbf{E} \tag{2.11}$$

Next, how electric energy behaves in a material is modified. This is done via Ohm's law, Equation 2.12, which is also a diffusion equation. Here, $\mathbf{J}$ is the current density or flux of electric charges flowing through a given volume, σ is a material property that describes how well charge flows through material, known as the conductivity, and $\mathbf{E}$ is the electric field:

$$\mathbf{J} = \sigma \mathbf{E} \tag{2.12}$$

Finally, the magnetizing field $\mathbf{H}$ is related to the magnetic field $\mathbf{B}$ by the material property μ, the magnetic permeability. As described earlier, the magnetic permeability characterizes how a material supports magnetic domains, basically how well a material magnetizes in a magnetic field.

$$\mathbf{H} = \mu \mathbf{B} \tag{2.13}$$

It is important to note that the material parameters ϵ, σ, and μ can depend on time and space and are generally represented as tensors, though this fact is usually neglected in MT with the assumption that the Earth is isotropic. With these adjustments, the generalized formulation of Maxwell's equations become:

$$\nabla \cdot \mathbf{D} = \rho_f \quad \Leftrightarrow \quad \oint_S \mathbf{D} \cdot d\mathbf{S} = \int_V \rho_f \cdot dV \tag{2.14}$$

$$\nabla \times \mathbf{E} = -\frac{\partial \mathbf{B}}{\partial t} \quad \Leftrightarrow \quad \oint_l \mathbf{E} \cdot d\mathbf{l} = -\frac{\partial}{\partial t} \int_S \mathbf{B} \cdot d\mathbf{S} \tag{2.15}$$

$$\nabla \cdot \mathbf{B} = 0 \quad \Leftrightarrow \quad \oint_S \mathbf{B} \cdot d\mathbf{S} = 0 \tag{2.16}$$

$$\nabla \times \mathbf{H} = \mathbf{J} + \frac{\partial \mathbf{D}}{\partial t} \quad \Leftrightarrow \quad \oint_l \mathbf{H} \cdot d\mathbf{l} = \int_S \mathbf{J} \cdot d\mathbf{S} + \frac{\partial}{\partial t} \int_S \mathbf{D} \cdot d\mathbf{S} \tag{2.17}$$

The important changes are to Gauss' Law eq. (2.14), which now relates the divergence of displacement currents to free charge density. Similarly, Ampere's Law eq. (2.17) now relates the curl of the magnetic field to the current density generated by bound charges and displacement currents generated by free charges. These 4 powerful equations fully characterize electromagnetic fields in materials and will be the starting point for deriving MT formalism.

A few important aspects of electric and magnetic fields arise from Maxwell's equations. First, electric fields are created by positively or negatively charged particles.

Hence, at least two dimensions are needed to characterize the interaction of a positive and negative charge because of torque. This is because the interaction of a positive and negative charge can cause rotation. Formally, the curl is non-zero. Similarly, magnetic fields always need at least two dimensions to be characterized because particles of opposite signs are always present, as there are no magnetic monopoles, at least classically. Second, because two dimensions are needed to characterize EM, polarization becomes important. Polarization is the preferred direction of a dipole moment or magnetic domain within an applied electric or magnetic field. Three types of polarization exist, two linear orthogonal polarizations and a circular polarization. Third, Maxwell's equations are described with vectors, these vectors can be in the space that spans 1, 2 or 3 dimensions for classical electrodynamics. These vectors describe fields, where a field is a function in space and time hence the name 'EM field theory'.

2.3.3 MT Derivation

The Earth has a natural magnetic field generated by electrical charges moving within the Earth's molten core (Wallace, 2003). This magnetic field gets bombarded by charge particles ejected from the sun, known as 'solar wind', generating time varying EM fields. These time varying magnetic fields induce currents into the Earth, which in turn induces secondary magnetic and electric fields; these are the fields measured to estimate the MT response. Commonly, the magnetic source fields are nominated the input signals and the secondary electric fields are the output signals. Formally, this presents a logical place to start, Faraday's Law of induction eq. (2.15). To formulate these physical processes, the curl operator needs to be applied to eq. (2.15), as it describes induction formally.

$$\nabla \times \frac{\partial \mathbf{B}}{\partial t} = \nabla \times (\nabla \times \mathbf{E})$$

The right hand side of the equation is given by:

$$\nabla \times (\nabla \times \mathbf{E}) = -\nabla^2 \mathbf{E} + \nabla(\nabla \cdot \mathbf{E}) \tag{2.18}$$

where ∇^2 is the Laplacian operator and defined in Cartesian coordinates as $\nabla^2 = \frac{\partial^2}{\partial x^2} + \frac{\partial^2}{\partial y^2} + \frac{\partial^2}{\partial z^2}$. Substituting eq. (2.15) into the left hand side of eq. (2.18) gives:

$$\nabla \times (-\frac{\partial \mathbf{B}}{\partial t}) = -\nabla^2 \mathbf{E} + \nabla(\nabla \cdot \mathbf{E})$$

The curl operates only in space so the time derivative can be pulled outside the curl operator. This leaves:

$$-\frac{\partial}{\partial t} (\nabla \times \mathbf{B}) = -\nabla^2 \mathbf{E} + \nabla(\nabla \cdot \mathbf{E})$$

The curl of the magnetic field is known from eq. (2.9) and eq. (2.17) and can be substituted in:

$$-\frac{\partial}{\partial t} (\mu \mathbf{J} + \frac{\partial \mathbf{D}}{\partial t}) = -\nabla^2 \mathbf{E} + \nabla(\nabla \cdot \mathbf{E}) \tag{2.19}$$

At this point some assumptions can be made to make the formalism simpler. First, if the Earth is assumed to act as a dielectric, then free charges are not supported, meaning displacement currents are negligible and can ignored. This is known as the quasi-static approximation and is validated when $\sigma >> \omega\epsilon_o$. For MT the ω is below

1000 Hz and ϵ_o is $4\pi \cdot 10^{-7}$, so this assumption holds provided the conductivity is larger than 10^{-2} S. Second, assume that magnetic permeability and dielectric permittivity variations are negligible and can be set to free space values, leaving:

$$\frac{\partial}{\partial t}\left(\mu_0 \mathbf{J}\right) = \nabla^2 \mathbf{E} \tag{2.20}$$

Next, assume that Ohm's Law holds and conductivity does not change with time. Move everything to one side to get:

$$\nabla^2 \mathbf{E} - \mu_0 \hat{\sigma} \frac{\partial \mathbf{E}}{\partial t} = 0 \tag{2.21}$$

This is known as the Helmholtz equation and describes a diffusive process, as there are no storage terms. Note that $\hat{\sigma}$ is left as a tensor for generality. The first term of eq. (2.21) describes a spatial acceleration that is related to the time derivative of the field by some constants known as the spatial frequency or propagation vector and will be derived next. First, assume the solution to eq. (2.21) is a decaying plane harmonic wave of the form:

$$\mathbf{E}(\mathbf{r}, t) = Ae^{i\omega t - \mathbf{k}\cdot\mathbf{r}} + Be^{i\omega t + \mathbf{k}\cdot\mathbf{r}} \tag{2.22}$$

Here -**k** is a wave propagating downwards towards the Earth, meaning, $B = 0$ because the Earth is assumed to only absorb energy and not radiate energy. Now, eq. (2.22) can be substituted into eq. (2.21):

$$\mathbf{k}^2 \mathbf{E}(\mathbf{r}, t) - i\omega\mu_0\hat{\sigma}\mathbf{E}(\mathbf{r}, t) \Leftrightarrow \mathbf{k}^2 \mathbf{E}(\mathbf{r}, \omega) - i\omega\mu_0\hat{\sigma}\mathbf{E}(\mathbf{r}, \omega) = 0 \tag{2.23}$$

Note the transformation to the frequency domain via the Fourier transform. Solving Equation 2.23 gives a definition of the spatial frequency **k**, or propagation vector:

$$\begin{aligned}
\mathbf{k}^2 &= i\omega\mu_0\hat{\sigma} \\
\mathbf{k} &= \sqrt{i}\sqrt{\omega\mu_0\hat{\sigma}} \\
\text{define: } \sqrt{i} &= \frac{1+i}{\sqrt{2}} \\
\mathbf{k} &= \sqrt{\frac{\omega\mu_0\hat{\sigma}}{2}} + i\sqrt{\frac{\omega\mu_0\hat{\sigma}}{2}} \\
\delta &:= \sqrt{\frac{2}{\omega\mu_0\hat{\sigma}}} \qquad (2.24) \\
\mathbf{k} &= \frac{1}{\delta}(1+i) \qquad (2.25)
\end{aligned}$$

From here physical interpretation of the solution and parameters, **k** and δ, can be informative. As described above, **k** is a spatial frequency with units of inverse distance. In an anisotropic media it is represented as a vector, implying variation as a function of position and preferred direction, hence the title propagation vector. Similarly, **k** is complex with a real and imaginary part. Relating this to eq. (2.22) it is apparent that the waves propagate differently in space and time, each related to the real and imaginary part of **k** eq. (2.26). The imaginary part represents a harmonic wave with spatial frequency **k** and temporal frequency ω traveling in the **k** direction as a function of time. The real part corresponds to a wave decaying as a function of distance at a rate **k**, which is inversely related to the skin depth δ. The skin depth describes the

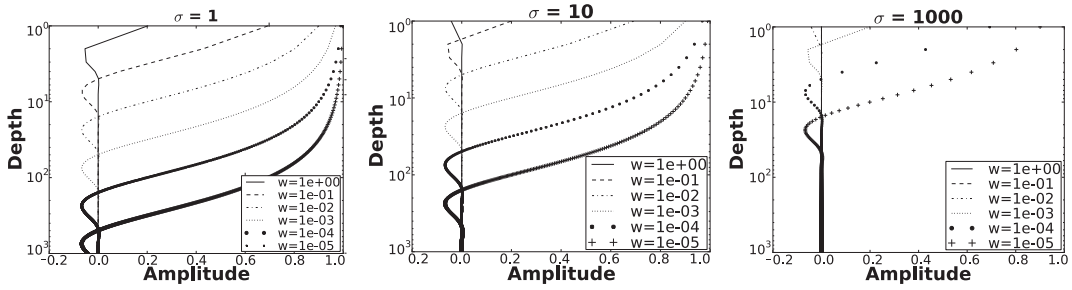

(a) (b) (c)

Figure 2.1: Plots displaying the solution to Helmholtz's equation, Equation 2.26, a decaying harmonic wave depending on temporal frequency and a constant conductivity. The skin depth is the depth a wave decays to $1/e$ visually represented after the first peak. Notice as the conductivity increases, meaning charge can flow easier through the material, the skin depth decreases. Physically, this is because the field can spread faster over a shorter distance and formally because the decay coefficient $\mathbf{k}$ increases.

depth where the wave's amplitude decays to $1/e$ and is dependent on the temporal frequency of the wave, magnetic permeability and most importantly the conductivity tensor of the material eq. (2.24). The solution is then a harmonic wave decaying with depth at a rate that depends on the temporal frequency of the wave and conductivity of the material (Figure 2.1).

$$\mathbf{E}(\mathbf{r},t) = E_0\hat{\mathbf{r}}\, e^{i\omega t}\, e^{-i\Im m\{\mathbf{k}\}\cdot\mathbf{r}}\, e^{-\Re e\{\mathbf{k}\}\cdot\mathbf{r}} \tag{2.26}$$

A general solution for the electric field has been found. From an MT point of view, a relation between the electric and magnetic field is more informative. Go back to the starting point and apply Faraday's Law eq. (2.15) to the electric field solution found in eq. (2.26). Because the inducing magnetic field is assumed to be at normal incidence, it is assumed that no vertical electric fields are present in the system. Therefore, the electric field is a function of the lateral spatial coordinates, $\mathbf{E} = \mathbf{E}(x,y,\omega)$. With this assumption the left hand side of eq. (2.15) becomes:

$$\nabla\times\mathbf{E} = \left(\frac{\partial E_y}{\partial z}\right)\hat{\mathbf{x}} + \left(\frac{\partial E_x}{\partial z}\right)\hat{\mathbf{y}} = \mathbf{k}\,\mathbf{E}(x,y,\omega) \tag{2.27}$$

For the 1D case in which the conductivity structure of the Earth varies only with depth, assume normal incidence for the magnetic field of the form $\mathbf{B}(x,y,\omega) = B_0 e^{i(\omega t - \mathbf{k}\cdot\hat{\mathbf{z}})}$. Then, the right hand side of eq. (2.15) becomes:

$$-\frac{\partial\mathbf{B}}{\partial t} = -i\omega\mathbf{B} \tag{2.28}$$

Equate eq. (2.27) and eq. (2.28) by Faraday's Law eq. (2.15) to get:

$$-k_z\,\mathbf{E}(x,y,\omega) = -i\omega\mathbf{B}(x,y,\omega)$$

Note that $\mathbf{k}$ is the same for both fields as they depend on the same properties, those of the material and the temporal frequency:

$$\frac{\mathbf{E}(x,y,\omega)}{=}\hat{\mathbf{Z}}\mathbf{B}(x,y,\omega) \tag{2.29}$$

This solution can be generalized by removing the assumption of vertical incidence within the Earth and the spatial vector $\mathbf{r}\in\mathbb{R}^3$. The impedance tensor $\hat{\mathbf{Z}}$ is a frequency

dependant linear transfer function of rank 2. It is the link between the electric and magnetic field components and contains all physical electromagnetic information about the system. The units of the impedance tensor components are length/time, implying the impedance tensor is a material property related to how charge moves through the system. To exemplify this notion, the apparent resistivity ρ can be derived by substituting the definition of $\mathbf{k}$ into eq. (2.29) and solving for $1/\sigma$. Note that the apparent resistivity is the volumetric resistivity of the hemispheroid circumscribed by δ and is therefore an average of all resistivities within this hemispheroid.

$$|\rho_{ij}(\omega)| = \frac{1}{\omega\mu_0}\left|\frac{E_{ij}(\omega)}{B_{ij}(\omega)}\right|^2 \tag{2.30}$$

where $i, j \in \{x, y\}$. The apparent resistivity defines the resistivity at a given frequency, and is the volumetric average of the hemispheroid of radius δ, hence the nomination apparent resistivity. Another important quantity is the phase between the electric and magnetic field, defined as:

$$\phi_{ij}(\omega) = \arctan\left(\frac{\Im m\{Z_{ij}\}}{\Re e\{Z_{ij}\}}\right) \tag{2.31}$$

Note that if the real and imaginary parts of the Z_{ij} are the same the phase will be $\pi/4$. This happens when there is no conductivity contrast between frequencies. It is important to note here that the phase and apparent resistivity are connected via Kramers-Kronig dispersion relationship, see eq. (2.32), which are derived from the relation between the real and imaginary parts of the impedance tensor.

A few key points need to be made. The apparent resistivity can be estimated up to the factor ρ_o, a scaling factor on the apparent resistivity. Frustratingly, ρ_o can arbitrarily shift the apparent resistivity. This is known as static shift, which is caused by near-surface inhomogeneities (Jiracek, 1990). Apparent resistivity can be estimated from the phase to within the factor of ρ_o through the dispersion relations defined in eq. (2.32). These relations depend on the dimensionality of the system (Fischer & Schnegg, 1993) and care must be taken when using the dispersion relations as they can often be violated (Berdichevsky & Dmitriev, 2008; Fischer & Schnegg, 1980; Yee & Paulson, 1988).

$$\phi_{ij}(\omega) = \frac{\pi}{4} - \frac{\omega}{\pi}\int_0^\infty \frac{1}{\nu^2 - \omega^2}\, log\left(\frac{\rho_{ij}(\nu)}{\rho_o}\right) d\nu \tag{2.32}$$

2.4 Summary

It has been demonstrated that the MT method is governed by the diffusion equation, where the source is a harmonic wave propagating at normal incidence and the solution is a damped wave that has a complex propagation vector that depends on source field temporal frequency and subsurface conductivity. Starting from Faraday's Law of induction and some intuitive assumptions, it has been shown that the relationship between the magnetic source field and induced electric field is linear in the frequency domain through the MT transfer function $\hat{\mathbf{Z}}$. Two typical parameters can be estimated from $\hat{\mathbf{Z}}$, namely the apparent resistivity and impedance phase, which are connected by the dispersion relations, and fully describe subsurface resistivity structure.

Chapter 3

Time Series Methods

Analyzing time series pre-processing can dramatically increase estimation accuracy of MT transfer functions. The advantage arises from locating coherent times to estimate $\hat{\mathbf{Z}}$ and identifying types of noise that might be present in the data, specifically periodic and coherent noise. This chapter presents some methods to analyze time series and a few methods employed for this project. In Section 3.1, time-frequency methods are reviewed. These are useful for visualizing data in a covariant representation and locating coherent times and possible source field effects, such as magnetic storms and Pc pulsations. Then, Section 3.2 reviews a few methods to remove periodic noise, such as pipeline noise from the data.

3.1 Time-Frequency Analysis

When analyzing signals it is important to have tools and methods that optimally characterizes the signal's information. Processing in the time or frequency domain proves beneficial in many areas but when dealing with a signal whose frequency content changes as a function of time it becomes necessary to use covariant methods such as time-frequency analysis (Cohen, 1989; Boashash, 2003). This allows the signal to be characterized in one domain as a function of the other. Time-frequency analysis is used in all areas of signal processing from medical imaging (Celka *et al.*, 2001; Li & Bi, 2009), to communications (Gabor, 1946; Amin, 1997), to engineering (Neild *et al.*, 2003) to space physics (Bortnik *et al.*, 2003; Ladwig & Hughes, 1989) and even MT (Chant & Hastie, 1992, 1993).

This section will briefly cover the basics of time-frequency analysis starting from the Fourier transform. Different methods will be described, namely those helpful to MT, including robust methods that suppress heavy tailed Gaussian noise. Different applications will then be introduced on how to apply time-frequency analysis in a useful way

3.1.1 Basics

Fourier Transform

Transforming a function into a different set of basis functions is a common method for signal analysis. For example a temporal Fourier transform converts a function of time into a set of orthogonal harmonic functions of frequency eq. (3.1), characterizing frequency content of the signal (Figure 3.1). The basis functions of the Fourier transform are the orthonormal set of sines and cosines, which can be written in compact form utilizing Euler's formula in complex space. The transformed function in the frequency

domain represents a sum of the weighted amplitude and phase shifted basis functions at each frequency. One key assumption of the Fourier transform is that the frequency content of the function $f(t)$ remains constant for all time. Nominally, the function is stationary.

$$F(\omega) = \frac{1}{\sqrt{2\pi}} \int f(t) e^{-i\omega t} dt \implies F[k] = \frac{1}{\sqrt{2\pi}} \sum_{n=0}^{N-1} f[n] e^{-i2\pi kn/N\Delta t} \tag{3.1}$$

When dealing with digital signals, it becomes necessary to use discrete transforms (right hand side of the arrow in eq. (3.1)) and incorporate the sampling theorem to avoid aliasing. The sampling theorem states the maximum frequency that can faithfully characterize a signal is the Nyquist frequency, $f_N = 1/2\Delta t$ where Δt is the time step between measurements. When the signal is discrete in the time domain it will be periodic in the frequency domain, which is a key property of the Fourier transform and magnifies the importance of the sampling theorem to avoid frequency folding and aliasing. Another assumption is that the function is sampled equally in time such that $f[t] = f[n\Delta t]$ where $n \in [0, 1, 2, ...N-1]$, which results in equally spaced frequencies at $1/2M\Delta t$ where M is the number of frequencies. This is important when digitizing an analog signal.

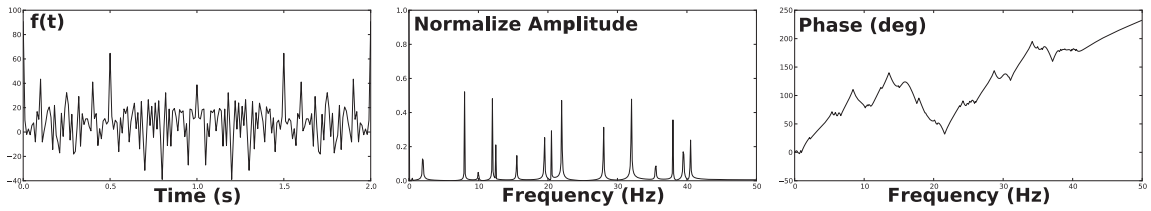

Figure 3.1: Example of time series represented in harmonic basis of sines and cosines via Fourier transform. Left: time series composed of a sum of 20 sinusoids with random integer frequencies between [0,50] Hz and random amplitudes between [0,1]. Middle: frequency representation of the time series displaying the normalized amplitude of coefficients for each frequency. Right: phase (deg) as a function of frequency.

Analytic Signal

For any real function, transformation from the time domain to the frequency domain via the Fourier transform produces positive and negative frequencies due to symmetry. The negative frequency representation is just a mirror image of the positive representation, thus doubling the information of the signal. Computationally, this can be expensive if the time series are long. Therefore, it is advantageous to fold negative frequencies onto the positive frequencies when analyzing modulated signals, which is accomplished by computing the analytic signal. The analytic signal is the complex representation of a real signal $x(t)$ and is calculated by eq. (3.2).

$$z(t) = x(t) + i\,\mathcal{H}\{x(t)\} \tag{3.2}$$

where $\mathcal{H}$ is the Hilbert transform defined as:

$$\mathcal{H}\{x(t)\} = \frac{1}{\pi t} * x(t)$$

where $*$ is a convolution. Given $X(\omega)$ is the Fourier transform of $x(t)$, the analytic signal in the frequency domain is defined as:

$$\mathcal{F}\{z(t)\} = \begin{cases} 2X(\omega) & \omega > 0 \\ X(\omega) & \omega = 0 \\ 0 & \omega < 0 \end{cases}$$

Some key characteristics of the analytic signal are important to time-frequency distributions. First, the data is reduced by half making computations faster. Second, removing symmetry reduces cross-terms in Cohen's class (quadratic, see Section 3.1.1) time-frequency distributions. Finally, it can be formulated to reduce aliasing when calculating Wigner-Ville based algorithms (O'Toole *et al.*, 2008).

Short-Time Fourier Transform

Many natural signals are non-stationary, i.e. frequency content varies as a function of time, like acoustic phenomena (Declercq *et al.*, 2004), bird chirps (Jones & Baraniuk, 1995), sonar (Gaunaurd & Strifors, 1996), music (Pielemeier *et al.*, 1996), seismic signals (Okaya *et al.*, 1992) and ionospheric currents (Lui & Najmi, 1997). This violates one key assumption of the Fourier transform: stationarity. A simple method to avoid this violation is to segment the signal into windows where the signal behaves linearly; this is called the short-time Fourier transform (STFT) and the $|STFT|^2$ is the spectrogram. The STFT represents the signal as a 2D array covariant in time and frequency eq. (3.3), where N is window length, $\tau \in [0, N]$ and $h(t)$ is a windowing function. Note it is important to apply a windowing function to the data to suppress high frequency Gibbs phenomena and possible aliasing. Moreover, resolution depends on window length, which is governed by the Heisenberg uncertainty principle, $\Delta t \Delta f \leq 1/4\pi$. Ergo, high resolution in one domain results in low resolution of the reciprocal domain. Consequently, resolution has a finite limit. This is one of the main drawbacks of the STFT and has led to the development of other methods.

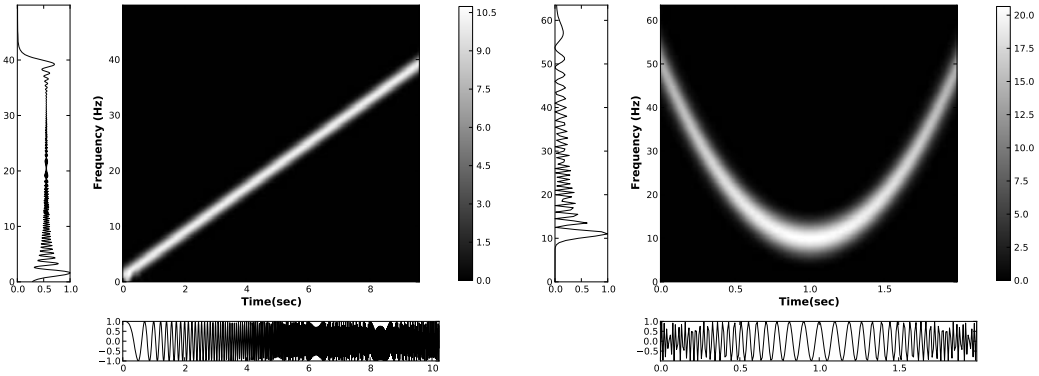

(a) Linear Chirp (b) Hyperbolic Chirp

Figure 3.2: Plots displaying the need for time dependent frequency estimation. The central plot is the time-frequency representation calculated by a STFT. Small left plot is the Fourier transform assuming a stationary signal, bottom plot is the signal in time. (a) The stationary Fourier transform displays the total frequency content of the chirp, however it is evident from the STFT that the Fourier transform cannot accurately characterize the signal as a function of time. Similarly, (b) supports time-frequency characterization of non-stationary signals.

$$\mathbf{S}(t,\omega) = \frac{1}{\sqrt{2\pi}} \int h(\tau) x(t+\tau) e^{-i\omega\tau} d\tau \implies \mathbf{S}[n,k] = \frac{1}{\sqrt{2\pi}} \sum_{m=0}^{N-1} h[m] x[n+m] e^{-i2\pi km/N\Delta t} \tag{3.3}$$

Wigner-Ville Distribution

One simple, yet elegant method to increase resolution in the time-frequency plane is to compute the short time auto-correlation. First formulated by Wigner (1932), as a correction to classical statistical mechanics at low temperatures using quantum probability functions, and later by (Ville, 1948), specifically for covariant signal representation, the auto-correlation perfectly localizes energy for a mono-component signal in the covariant space (Figure 3.3). Unfortunately, when the signal has multiple components, cross-terms appear due to the quadratic nature of the Wigner-Ville distribution (WVD) eq. (3.4) and (Figure 3.4(b)).

$$\rho_x(t,\omega) = \int x(t+\frac{\tau}{2})x^*(t-\frac{\tau}{2})e^{-i\omega\tau}d\tau \Longrightarrow \rho_x[n,k] = 2\sum_{m=-N/2}^{N/2} x[n+m]x^*[n-m]e^{-i4\pi km/N\Delta t} \tag{3.4}$$

Given a signal as the sum of two mono-component signals, $x(t) = a(t) + b(t)$. The auto-correlation function $K(t,\tau)$ defined by eq. (3.5) gives a general solution of $|a|^2+|b|^2+\Re e\{ab^*+ba^*\}$ resulting in auto-terms and cross-terms. Suppression of these cross-terms has been studied intensively the last few decades (Cohen, 1989; Boashash, 2003). The class derived from the WVD is that formulated from second order statistics nominated Cohen's class after Cohen (1989), where the general formula is given by eq. (3.6) as a double convolution in the covariant domain. The smoothing kernel $\mathbf{G}(t,\omega)$ can take an infinite number of forms but a few are of interest (Cunningham & Williams, 1994; Gonclaves & Baraniuk, 1998; Lee & Kim, 2001; Jones & Baraniuk, 1995; Boashash, 2003).

$$\mathbf{K}_x(t,\tau) = x(t+t\frac{\tau}{2})x^*(t-\frac{\tau}{2}) \tag{3.5}$$

$$\rho_x(t,\omega) = \frac{1}{4\pi^2}\int\int\int \mathbf{G}(\tau,\nu)\mathbf{K}(\eta,\tau)e^{-i\omega\tau-i\nu t+i\nu\eta}\,d\tau d\nu d\eta \tag{3.6}$$

The simplest kernel is a smoothing window in the time domain, $\mathbf{G}(t,\omega) = h(t)\delta(\omega)$, where $\delta(\omega)$ is the delta distribution and $h(t)$ is some type of window function, i.e. Hanning window or Gaussian window. This is called the pseudo-WVD, which can be taken a step further and smoothed in frequency as well with the kernel $\mathbf{G}(t,\omega) = h(t)g(\omega)$, where $g(\omega)$ is again a window function. The time frequency distribution with this kernel is nominated the smoothed-pseudo WVD (SPWVD) (Figure 3.4(c)) and has an interesting property in that the kernel is separable (the kernel can be written as a product of the individual kernels) and is not constrained by the uncertainty principle.

S-Method

Another interesting method is the S-method (Stankovic, 1994). Starting from the STFT eq. (3.3) where no cross-terms exist and iteratively moving towards the WVD eq. (3.4) in the frequency domain by widening the window function L, the S-method is cross-term free while having increased resolution. An efficient method for calculation of the S-method SM_x can be derived for discrete signals in time (n) and frequency (k) frequency eq. (3.7), see Stankovic (1994). In the limit that the window $L \to M$(number of frequencies) the WVD is calculated, conversely if $L = 0$ the STFT is calculated. The optimum width of L is large enough to not include cross-terms and is signal dependant. $P[n]$ is a windowing function that smoothes in the frequency domain similar to the

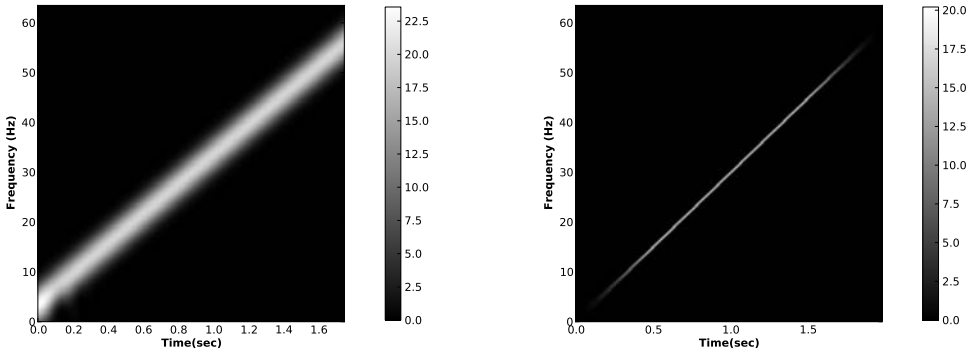

(a) STFT (b) WVD

Figure 3.3: Spectrograms of the linear chirp in Figure 3.2. (a) STFT with a window length of $N = 32$, notice the signal is spread relative to the WVD (b) which perfectly localizes the signal with a window of $N = 128$. $\Delta t = 1/128$, t has length of 256 samples.

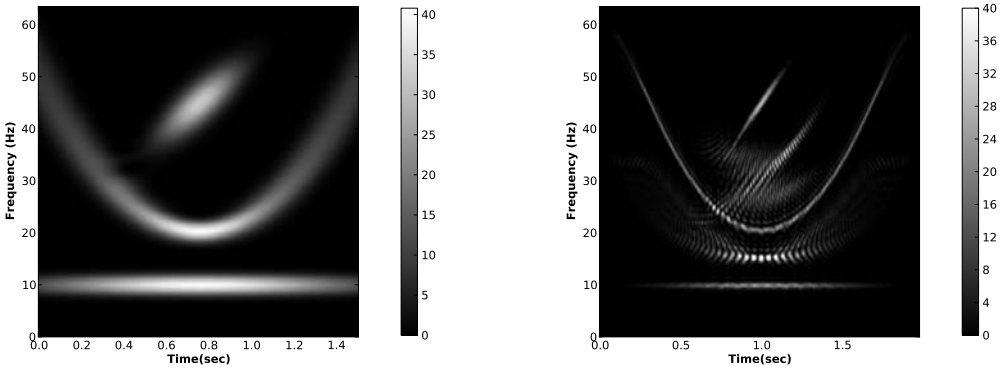

(a) STFT (b) WVD

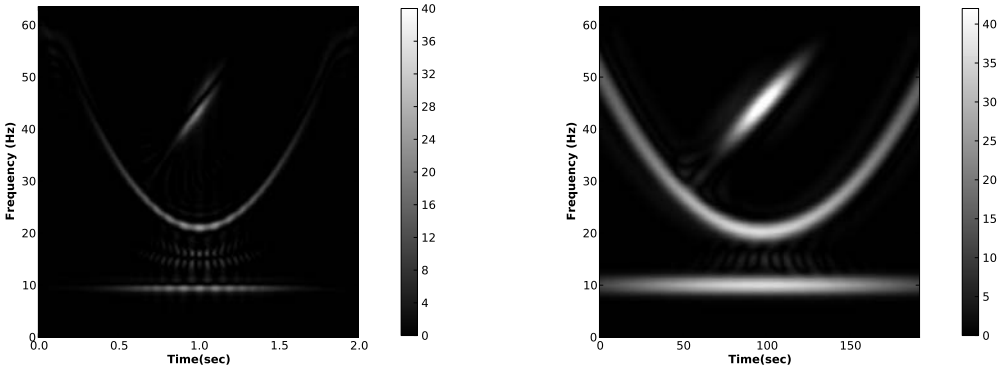

(c) SPWVD (d) S-Method

Figure 3.4: Time-frequency distributions of a multi-component signal $x(t) = \cos(110t^3 + 40\pi t) + 1.5e^{-25t^2}\cos(45\pi t^2 + 90\pi t) + e^{-t^2}\cos(20\pi t)$, where $\Delta t = 1/128$ and t has a length of 256 samples. (a) STFT computed with a window length of $N = 64$. (b) WVD computed with a window length of $N = 128$, notice the cross-terms (extraneous signal not present in (a)) making interpretation difficult. (c) Smoothed-pseudo WVD computed with a time smoothing window of length $nh = 127$ and a frequency smoothing window of length $ng = 31$. The cross terms are suppressed by using smoothing windows. (d) S-method computed with a time window of length $N = 64$ and frequency window $L = 13$. The signal is amplified and cross terms are suppressed.

pseudo-WVD to suppress cross-terms. Figure 3.4(d) displays the increase in resolution without introduction of cross-terms.

$$SM_x[n,k] = |STFT[n,k]|^2 + 2\,\Re e\{\sum_{l=-L}^{L} P[l]\,STFT[n,k+l]\,STFT^*[n,k-l]\} \quad (3.7)$$

3.1.2 Natural Signals

Natural signals can commonly be modeled as $x(t) = s(t)+n(t)$, where $s(t)$ is the signal and $n(t)$ is some sort of noise. Noise can have many different forms, for example white noise from background radiation, periodic noise from power lines, or impulse noise from transient sources such as lightning. The key assumption is that noise is additive making the system linear. Linearity allows the Fourier transform to be used as a tool to characterize the system in a different basis and also makes removing undesired signal simpler.

In MT, it is common to encounter all types of noise but can generally be characterized as heavy tailed Gaussian noise, which contains white noise added to impulse noise. Adding this to the example time series initiates insight into behavior of different time-frequency distributions. The STFT does nothing to suppress noise other than windowing the signal before the Fourier transform. Therefore, a noisy signal will have a noisy spectrogram (Figure 3.5(a)). The WVD is predisposed to cross-term presence in the non-noisy case, so when noise is added cross-terms are even more present (Figure 3.5(b)). Smoothing suppresses the noise slightly and enhances more of the signal (Figure 3.5(c)). The S-method suppresses noise the most while enhancing the signal, however resolution is still low (Figure 3.5(d)). One revealing characteristic of the aforementioned four methods is the response to impulse noise. An impulse in time is a summation of all possible frequencies, hence a linear feature in the time-frequency plane. This linear feature masks any signal beneath it and or around it, reducing interpretable information.

Robust Time-Frequency Distributions

To decrease the impact of noise, specifically heavy tailed Gaussian noise, robust time-frequency methods have been developed (Katkovnik, 1998, 1999; Djurovic *et al.*, 2001, 2003; Brotchi *et al.*, 2007; Li & Bi, 2009; Zaric *et al.*, 2010; Sejdic & Djurovic, 2010). Katkovnik (1998) describe the first robust method based on estimating non-linear amplitudes using Huber's min-max method, the M-estimate. Djurovic *et al.* (2001) expanded on this method making an elegant simplification to the iterative process by using the median as a robust estimator. Djurovic *et al.* (2003) expand further by imposing Huber's L-estimate to the robust time-frequency distribution. Zaric *et al.* (2010) expand even further by adding in complex lag terms. Brotchi *et al.* (2007) describe an iterative weighting method using the modified-B distribution. Li & Bi (2009) formulate a reassignment method for the local polynomial periodogram calculated by a short time polynomial Fourier transform.

The robust method formulated by Djurovic *et al.* (2001) is employed here because of its simplicity and commonality with existing MT processing methods based on Huber's statistics (Chave & Thomson, 2004; Egbert, 1997; Smirnov, 2003), where the goal is to minimize the error function, $\mathbf{F}(e) = |x[l] - m|$, where e is the loss function, l and m are discrete time. The solution is to calculate the median about each instance bounded by $m \in [-M/2, M/2]$.

This can be extended to the STFT using either the vector or marginal median, where the vector median assumes the real and imaginary part are mutually dependent and the marginal median $rSTFT_{MM}$ assumes they are independent eq. (3.8).

$$\begin{aligned} rSTFT_{MM}[n,k] =& \text{median}\{\Re e\{x[n+m]e^{-i2\pi km/N\Delta t}\} : m \in [-N/2, N/2]\} \\ &+ i\,\text{median}\{\Im m\{x[n+m]e^{-i2\pi km/N\Delta t}\} : m \in [-N/2, N/2]\} \end{aligned} \tag{3.8}$$

Computationally they produce similar results (Djurovic *et al.*, 2001). Since the marginal median is computationally faster, it is the preferred method. Similarly, the median can be extended to the WVD $rWVD_M$ eq. (3.9). Here the median method is negligible as the auto-correlation function will always be real.

$$rWVD_M[n,k] = \text{median}\{\Re e\{x[n+m]x^*[n-m]e^{-i4\pi km/N\Delta t}\} : m \in [-N/2, N/2]\} \tag{3.9}$$

An obvious extension is the robust S-method estimated from the robust STFT eq. (3.8). Here the robust STFT is used as a basis to estimate the S-method. Furthermore, an extension to the robust L-estimate from the robust STFT is again an obvious representation. The L-estimate is derived from the vector median, however instead of simply using the median to represent the time-frequency point, Djurovic *et al.* (2003) employ a weighted sum around the median. By doing this more information is incorporated to represent the time-frequency point. The coefficients are similar to those of an α-trimmed mean and are defined by eq. (3.10), where N is the window length to calculate the STFT and $0 < \alpha < 0.5$. It is important to note that the elements of eq. (3.11) are sorted as a non-increasing sequence separately for the real and imaginary parts. Again, the robust L-estimate can be used to calculate the robust S-method.

$$\alpha_i = \begin{cases} \dfrac{1}{N(1-2\alpha)+4\alpha} & i \in [(N-2)\alpha, \alpha(2-N)+N-1] \\ 0 & \text{elsewhere} \end{cases} \tag{3.10}$$

$$\begin{aligned} rSTFT_L[n,k] =& \sum_{m=0}^{N-1}\sum_{i=0}^{N-1} \alpha_i \Re e\{x[n+m]e^{-i2\pi km/N\Delta t}\} \\ &+ i\sum_{m=0}^{N-1}\sum_{i=0}^{N-1} \alpha_i \Im m\{x[n+m]e^{-i2\pi km/N\Delta t}\} \end{aligned} \tag{3.11}$$

Though the STFT L-estimate is robust, resolution problems can persist due to the dependance on the STFT. Reassigment methods have been introduced to move smeared energy in the spectrogram back to its origin, which is estimated in a similar way to calculating center of gravity. Djurovic & Stankovic (1999) have extended the reassignment method to the S-method by estimating the reassigned time n_r and frequency k_r points as in eq. (3.12) and eq. (3.13), where it has been extended to the robust L-estimate. Here different windowing functions are used to calculate eq. (3.7) according to the subscript, where τ_h is a time weighted window of h, usually a Gaussian window or Hanning window, and τ_D is the time derivative of window h. This is applied to magnetic data collected in Antarctica displaying a structured monochromatic Pc1 pulsations (Figure 3.6).

$$n_r[n,k] = n + \Re e\left\{\frac{SM_{\tau_h}[n,k]}{SM_h[n,k]}\right\} \tag{3.12}$$

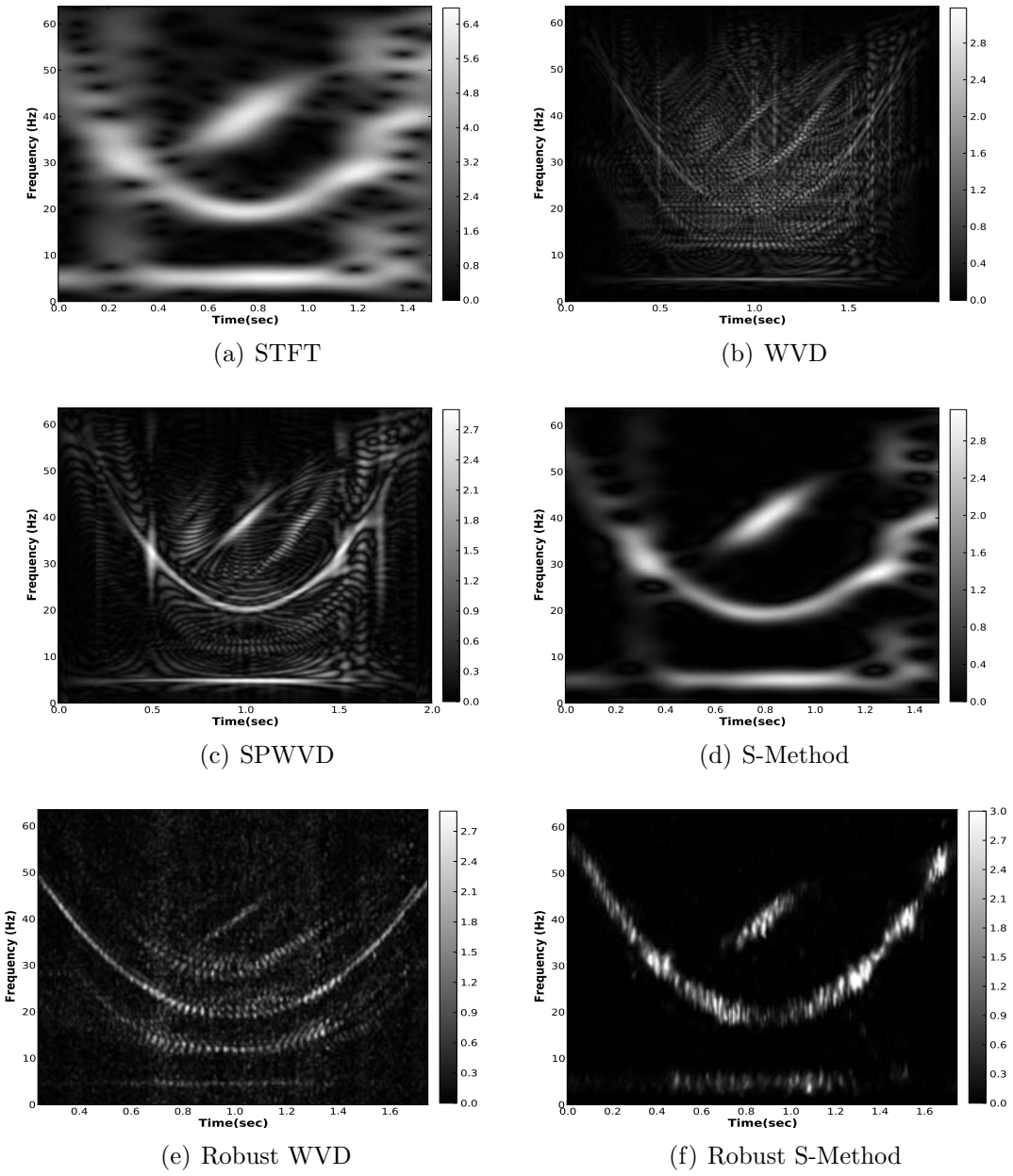

(a) STFT (b) WVD

(c) SPWVD (d) S-Method

(e) Robust WVD (f) Robust S-Method

Figure 3.5: Time-frequency distributions of a multi-component signal, same as Figure 3.4 with 15% added heavy tailed Gaussian noise. (a) STFT computed with a window length of $N = 64$. The resolution makes it difficult to interpret. (b) WVD computed with a window length of $N = 128$. Cross-terms of the signal and noise make it extremely difficult to interpret. (c) Smoothed-pseudo WVD computed with a time smoothing window of length $nh = 127$ and a frequency smoothing window of length $ng = 31$. The cross terms are suppressed by using smoothing windows, but still difficult to interpret. (d) S-method computed with a time window of length $N = 64$ and frequency window $L = 13$. Suppresses noise and enhances coherent signal. (e) Robust WVD calculated with the vector median and a window length of $nh = 127$ and $ng = 15$. Notice the noise is suppressed but cross-terms still persist. (f) Robust S-method derived from the robust STFT calculated by the vector median with a widow length of $N = 64$. Notice the noise is suppressed and cross-terms are minimal.

$$k_r[n,k] = k - \Im m\left\{\frac{SM_{D_h}[n,k]}{SM_h[n,k]}\right\} \tag{3.13}$$

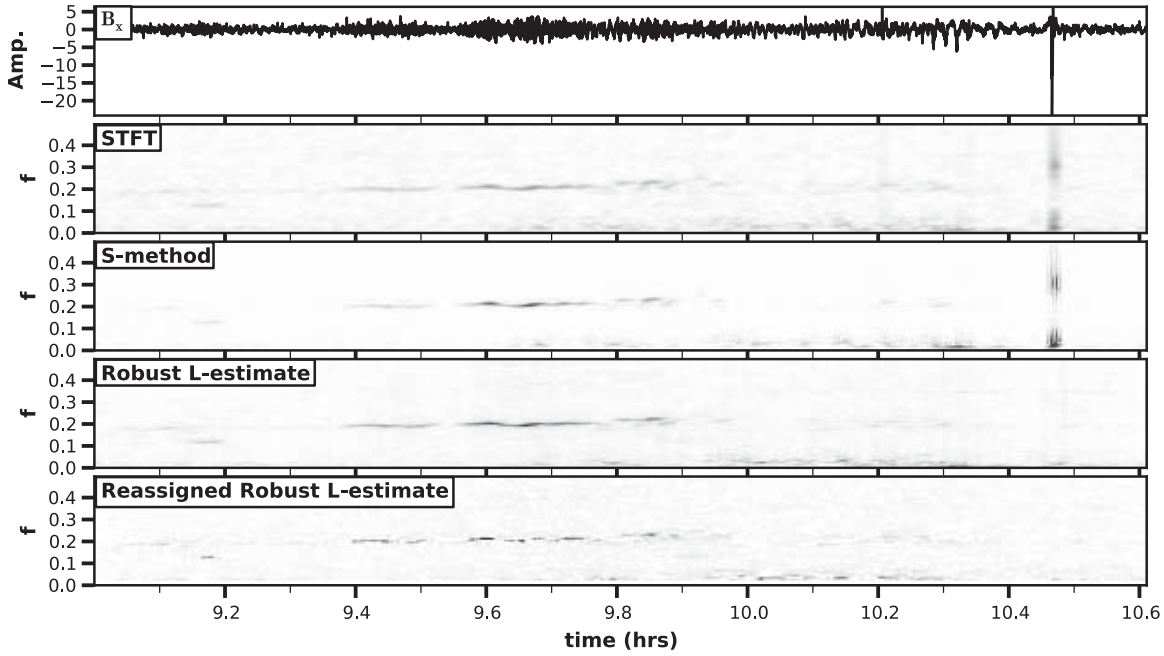

Figure 3.6: Comparison of different TFD for a magnetic time series, aligned with geomagnetic north, measured in Antarctica imaging a structured Pc1 pulsation. All spectrograms are calculated with a time step of 1 and a high pass first order Butterworth filter with cutoff frequency of .05 Hz is applied prior to TFD estimation. Notice the sharpening with each TFD and the removal of the impulse at 10.5 hrs. Bx) is magnetic time series in x1000 nT. STFT) calculated with $nh = 128$. S-method) calculated with a $nh = 128$ and $L = 11$. Robust L-estimate) calculated with $nh = 128$, $L = 11$, and $\alpha = 0.38$. Reassigned robust L-estimate) calculated with $nh = 128$, $L = 11$, $\alpha = 0.38$ and a tolerance of 0.001.

3.1.3 Applications to MT

MT is inherently formulated in the frequency domain, but measured in the time domain, instantly making it imperative to connect the two domains. Here, measured fields are represented covariant in time and frequency from which multiple interesting aspects of the source field and the MT response can be estimated and visualized. First, the source field will be characterized by visually inspecting the data for magnetic storms, Pc pulsations and other anomalous signal. Then, a statistical analysis will be discussed for characterizing the source field. Finally, locating coherent times will be discussed.

Source Field Characterization

An important first step to processing MT data is to visually inspect the data in the time-frequency domain where anomalous signal are easily detectable. Because MT data is susceptible to heavy tailed Gaussian noise, the robust L-estimate is employed to estimate the TFD. This can then be visualized as a spectrogram, where the frequency is typically on a log scale and the TFD is in decibels. Anomalous signal can take many different forms, therefore a few examples will be given.

One of the first patterns to look for in broadband data is that of Schumann resonances (Toledo-Redondo *et al.*, 2010). These are natural resonances of the cavity between the Earth's surface and the lower ionosphere (50-100 km), where a dramatic increase in ion density creates a reflector for long period EM waves. Both polarizations of EM waves can propagate within this cavity and has a resonance on the order of kHz. The Schumann resonances originate mainly from lightning strikes, where transverse magnetic modes couple with the entire cavity and resonate at harmonics of $\sim$ 7-8 Hz

(Figure 3.7).

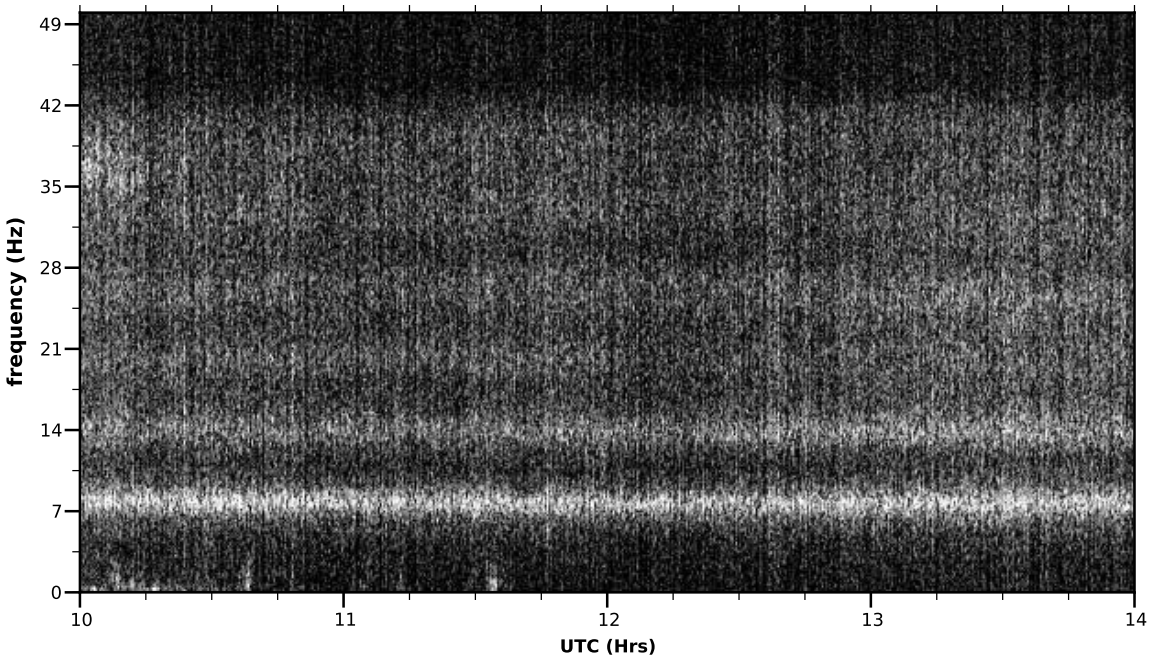

Figure 3.7: Robust spectrogram imaging the first few Schumann resonances measured from a search coil magnetometer aligned with geomagnetic north, calculated with $nh = 516$, $\delta t = 128$, $L = 11$, and $\alpha = 0.38$. Color bar represents spectral power in decibels with white being large power. Notice the variance around the central frequency caused by variations in the ionospheric cavity.

Principle component (Pc) pulsations derived from magnetospheric activity are common signals in the MT frequency band, making it important to understand the physics behind these pulsations to decide whether these are noise or signal. Nominally, five period bands of pulsations are roughly defined (Table 3.1). Pc1-2 are defined to be Pc in the period band of 0.2-10 seconds, which is also the MT dead band. Multiple sources of Pc1-2 have been suggested (Anderson *et al.*, 1992; Kim *et al.*, 2011; Menk *et al.*, 1992; Nomura *et al.*, 2011) depending on latitude, but the main source is electromagnetic ion cyclotron waves (EMIC) originating from impinging solar wind during magnetic storms or sub-storms on the equatorial plasma sheet and ring currents. These EMIC waves then propagate into the ionosphere along magnetic field lines where they are converted to compressional waves that propagate horizontally in the Alfv́en ion resonator of the ionosphere's F layer. At low latitudes Pc1 are most frequent during local night time, whereas at high latitudes, they frequently occur during local magnetic noon. Furthermore, during local winter time Pc1 are more frequent at low latitudes and during equinox months for high latitudes. Pc3-4 are the most common near surface waves, being observed in the daytime of nearly every day from auroral latitudes to equatorial latitudes (Pilipenko *et al.*, 2008). The assumed source of Pc3-4 are convected upstream waves of the magnetic bow shock that propagate into the inner magnetosphere as compressional waves. Again, sources vary with latitude, seasonal and diurnal cycles (Pilipenko *et al.*, 2008). Figure 3.8 displays different Pc pulsations characterized by robust time-frequency analysis. It is important to note that specific patterns are difficult to categorize because of the sporadic nature of source, the sun.

Periodic noise and coherent noise can be easily identified in the time-frequency domain. The pattern is typically enhanced power along a certain frequency band and harmonics. This is modulated by the single cycle Fourier transform. Figure 3.9 displays

Table 3.1: List of Pc and Pi pulsations including period band and electromagnetic source (Jacobs *et al.*, 1964).

PC	Period Band (s)	Origin
Pc1	0.2-5	EMIC and Alfvén waves
Pc2	5-10	EMIC and Alfvén waves
Pc3	10-45	Upstream Waves
Pc4	45-150	Upstream Waves
Pc5	150-600	Upstream Waves
Pi1	1-40	
Pi2	40-150	

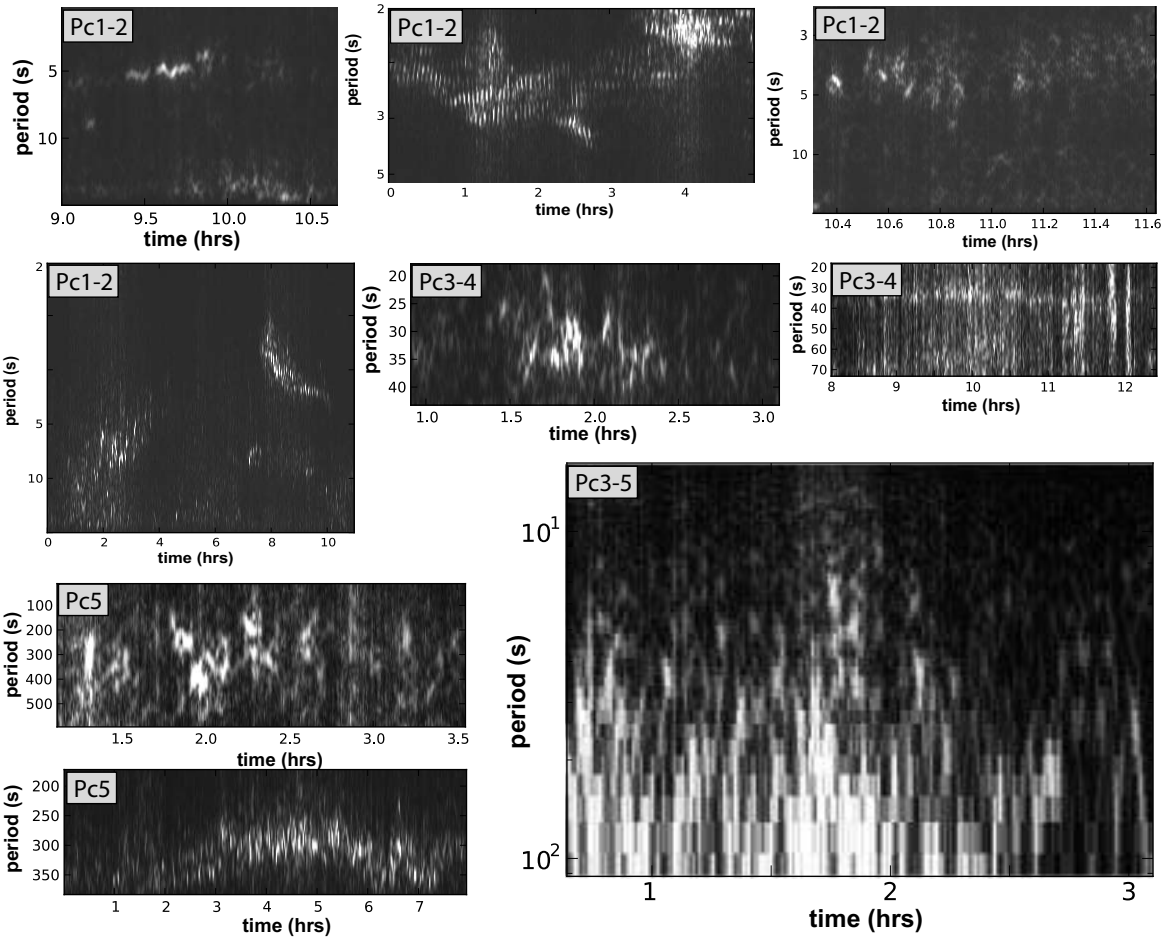

Figure 3.8: Examples of different Pc pulsations represented by the robust L-estimate TFD with $nh = 128$, $L = 5$, and $\alpha = 0.38$. Notice that Pc pulsations can occur in many different patterns and time scales. Characterization of these anomalous energies is important before estimating the MT transfer function, specifically whether the pulsation is signal or noise.

the spectrogram for a signal similar to Figure 7.6, where the bands are spaced at 12 seconds (0.085 Hz)and these are modulated by a sinc function with notches spaced at 3 seconds (0.33 Hz). An interesting result of plotting these spectrograms is that the polarization of the periodic signal changes. This is a severe case but nonetheless demonstrates the utility of covariant representation of the measured signal. The next step is to locate coherent times to estimate MT transfer functions.

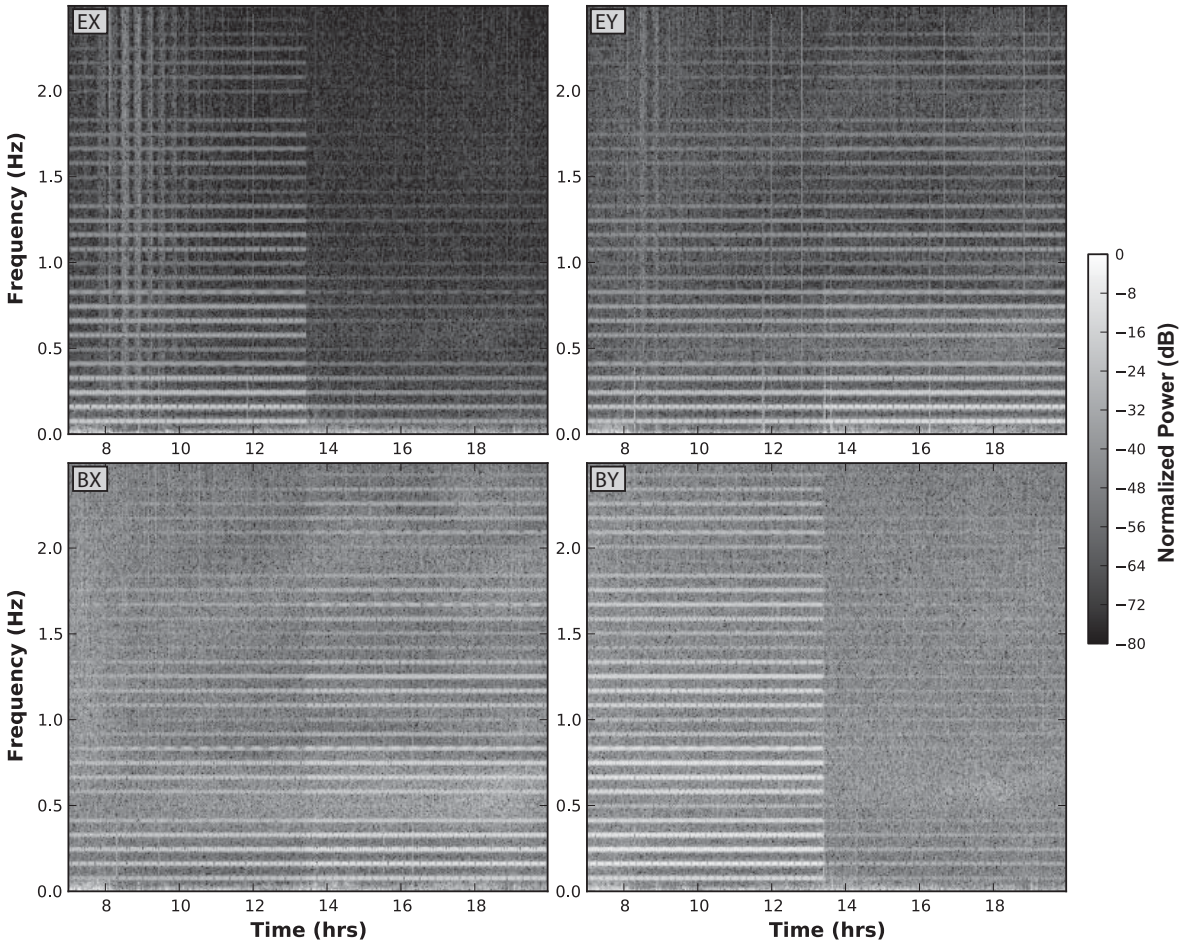

Figure 3.9: Spectrograms of periodic noise measured from a 4-component MT setup at Paralana computed via the robust L-estimate with a $nh = 516$, $\delta t = 16$, $L = 11$ and $\alpha = 0.38$. The electric field measures a periodic signal composed of a 3 second square wave every 12 seconds and the magnetic fields measure the time derivative. This signal is represented as the horizontal bars on the spectrogram that are spaced $\delta t = 12s$ (0.085 Hz) which is modulated a sinc function with central frequency of .33 Hz, the Fourier transform of the square wave. Notice that the signal changes polarization at around 13.5 hours. The vertical lines spaced about every 15 min are the initial ramp up of the square wave which apparently has periodic maximum amplitude.

Locating Coherent Times

One benefit of covariant representation is that more information is presented, making it easier to pick good times to estimate MT transfer functions. Several methods can be employed derived from covariant representation for visual inspection. First, is to visually inspect all channels for one station, checking for consistency in covariant representation. Then, check all channels that measured simultaneously for consistency looking for changes in the response as a function of distance (Figure 3.10). This can provide an indication of non-planar sources and local noise. To get a simple estimate of the MT transfer function, simply divide the electric fields by the appropriate magnetic fields and scale by the frequency. Though the magnetic source is temporally changing, the transfer function should not because it is implicitly assumed to be constant over the time of measurement. Similarly, the coherence can be estimated between channels. For a more robust estimation of planar source field times, a method similar to Egbert (1997) that is based on robust estimation of the spectral density matrix (SDM) can be used to estimate multiple parameters including number of sources, transfer functions and canonical coherence (Kappler, 2008).

$$\hat{\mathbf{S}}_r = \boldsymbol{\Sigma}^{1/2}\hat{\mathbf{S}}(\boldsymbol{\Sigma}^{-1/2})^T \tag{3.14}$$

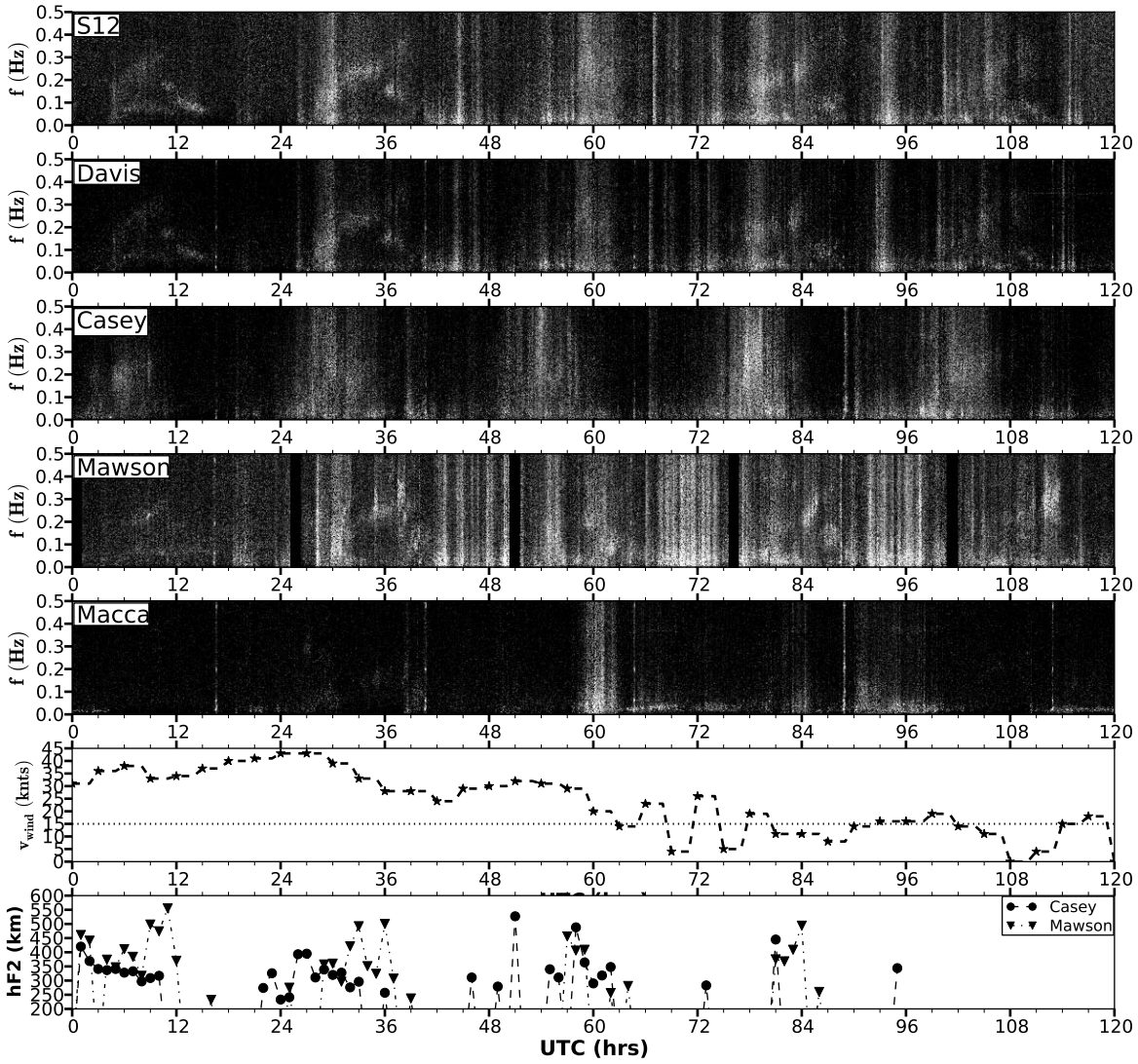

Figure 3.10: Spectrograms for selected stations collected during the Antarctic summer of 2009 illustrating changes in source field as a function of distance. Spectrograms are calculated using the robust L-estimate with $nh = 512$, $L = 11$, $\delta t = 36$, and $\alpha = 0.38$. Casey is 1800 km to the east of Davis, Mawson is 800 km to the west of Davis, S12 is 100 km away from Davis and Macca is 2500 km NE of Davis. Plotted at the bottom are surface wind speed near Davis and height of the F_2 layer to demonstrate correlation with patterns observed in the spectrograms. Notice the correlation in height of the F_2 layer and the Pc1-2 signal each day starting around 0600 UT each day. The F_2 layer is a layer in the ionosphere, usually at a height of ~300 km, where the largest density of ions reside. The height varies with thermospheric winds.

The SDM ($\hat{\mathbf{S}}$) is estimated as eq. (3.14), where $\mathbf{X}_j(f;\omega)$ is a vector of Fourier coefficients for a given time window j at frequency ω and $\mathbf{X}$ has length K stations times L channels, $M = K \times L$. Specifically, x_{ij} is a time series of Fourier coefficients estimated for the j^{th} time window at frequency ω for channel l of station k. One important logistical caveat is that the length of x_{ij} needs to be greater than one to get a statistically accurate estimation of $\hat{\mathbf{S}}$. The robust L-estimate is used to calculate the Fourier coefficients that make up $\mathbf{X}$, which already provides a robust estimation. The benefit of the method formalized by Egbert (1997) is that the end result is normalized appropriately to represent signal to noise ratio. A simple estimation of the noise

variance $\mathbf{\Sigma}$ is to fit each data channel m to all other data channels via least squares minimization, $\sigma_m^2 = \min ||\mathbf{X}_m - \sum_{p \neq m} \alpha_p \mathbf{X}_p||$. Here it is assumed that the noise is additive and defined as $\mathbf{\Sigma} = \sigma \hat{\mathbf{I}}$, where $\hat{\mathbf{I}}$ is the identity matrix of size $M \times M$. The robust SDM is then defined as eq. (3.14).

Decomposition of the robust SDM can be accomplished using SVD (see 3.2.3), where the eigenvectors describe the sources and eigenvalues describe the contribution of each source. For MT data, only two eigenvalues above the noise level should exist, where if scaled properly, should be above 0 on a log scale. Furthermore, the canonical coherence between measurements (Kappler, 2008) and transfer functions between channels can be estimated from a partitioned SDM eq. (3.15). The transfer function is estimated as $\hat{\mathbf{Z}} = \mathbf{S}_{1,2}\mathbf{S}_{2,2}^{-1}$ (Kappler, 2008), where $\mathbf{S}_{i,j}$ is a matrix of dimensions $p \times p$ (the number of sources).

$$\hat{\mathbf{S}} \approx \frac{1}{T} \left[\begin{array}{c|c} \mathbf{S}_{1,1} & \mathbf{S}_{1,2} \\ \hline \mathbf{S}_{2,1} & \mathbf{S}_{2,2} \end{array}\right] \tag{3.15}$$

A visual method to pick coherent times is plotting the aforementioned parameters as a function of time and frequency. As an example take one station and plot one mode, TE or TM, and estimate the aforementioned parameters, namely apparent resistivity, coherence, PC analysis and if possible a threshold on B_z. The things to look for here is little variation with time. For example in Figure 3.11, the colors in each subplot should not vary as a function of time. If it does then that indicates variation in the response to the source field and the source field might be non-planar. The masked out regions with the transparency have regions where the estimated value vary with time.

3.2 Filtering Periodic Noise

Every natural system contains some sort of noise, or more precisely undesired signal. Typically, the noise is random, has zero mean, and distributed across the spectrum by a Gaussian function, hence the nomination Gaussian noise. However, other noise can creep into the system that is not random, but in fact is periodic in time, such as 50 or 60 Hz signal from power lines. Multiple methods have been concocted to remove periodic noise from natural signals, mostly estimating the noise from the data itself (sources). To appropriately remove the periodic signal different methods can be employed depending on the nature of the noise. What follows is a brief description of different methods that can be utilized to remove periodic noise focusing on the MT method.

3.2.1 Time-domain Subtraction

Subtraction would appear to be the simplest method to remove periodic noise. This entails knowing the noise signal and subtracting it from the measured signal. Herein lies a problem, knowledge of the noise signal. If the noise signal can be estimated, what is the amplitude and phase? One approach is to estimate the noise signal with an analytical solution. Say the noise is from a 50 Hz power line, then one might compute a 50 Hz sinusoid with an appropriate amplitude and phase and simply subtract it from the measured signal. Unfortunately, most power lines do not always operate directly at 50 Hz but a variance of about ± 2 Hz and with drifting phase. Similarly, the power line typically has harmonics looming at $n \times 50$ Hz and sub-harmonics at $50/n$ Hz. This makes the problem much more difficult to remove what would appear to be a simple signal. One technique is to transform the time series into the frequency domain to

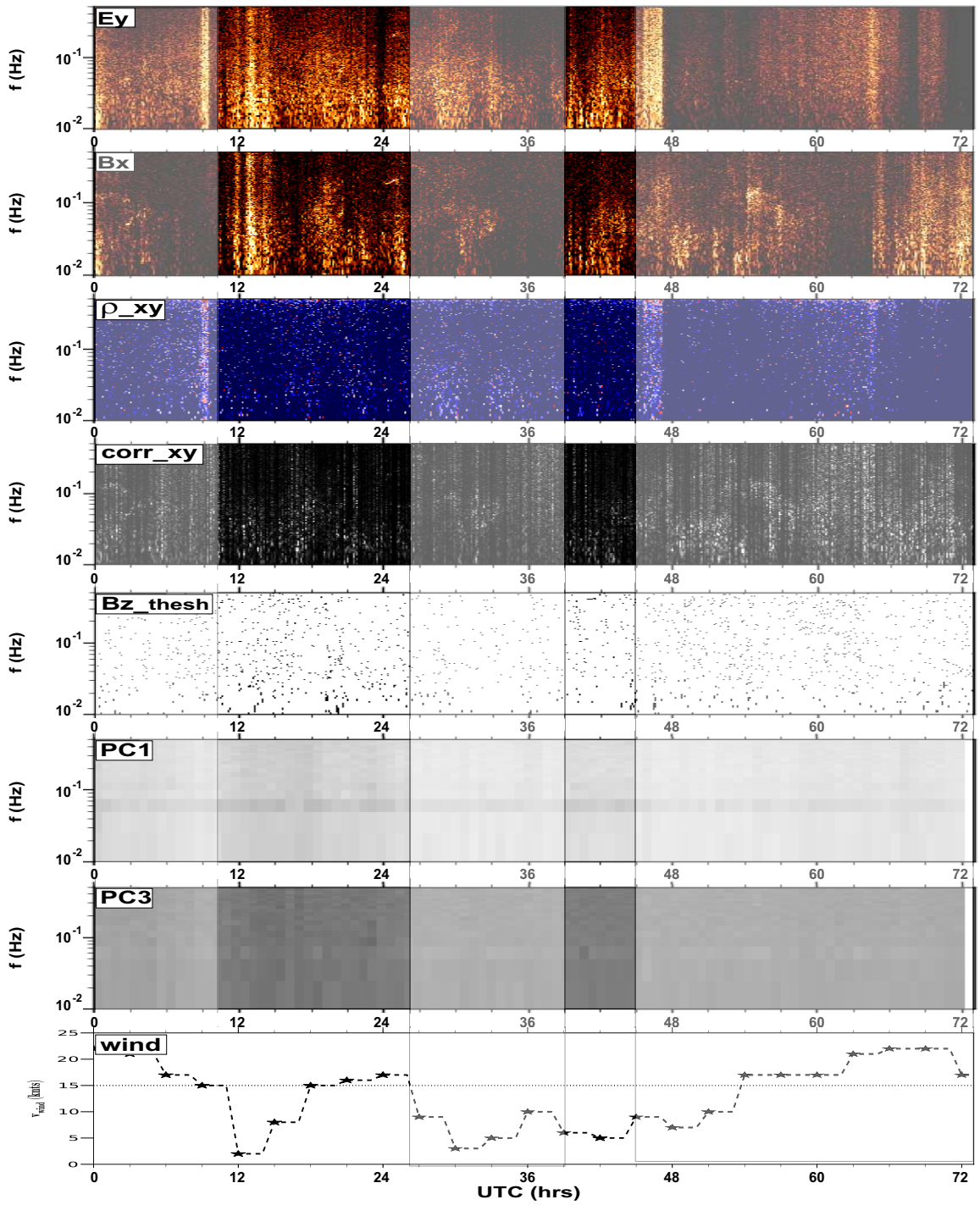

Figure 3.11: Example of locating coherent times utilizing robust time-frequency analysis. Spectrograms are plotted with time in hours on the x-axis and frequency on a log scale on the y-axis. From top to bottom is plotted the E_y component, B_x component, apparent resistivity as $0.2\,T \cdot |E_y/B_x|^2$, correlation between E_y and B_x as $(E_y \cdot B_x)/(||E_y||\,||B_x||)$, threshold of B_z with the threshold being $2 \cdot std(B_z)$, PC1 and PC3 and surface wind speeds (knts). The dark segments locate time windows where most accurate and precise transfer functions are estimated.

estimate the peak frequency and phase for the sinusoidal signal. These are then input used to generate a synthetic sinusoidal time series to subtract from the data.

An example of a periodic signal is that of pipeline corrosion remediation, where a 3 second electric square wave is sent down the pipe at a rate of 12 seconds (Figure 3.13). The periodic signal has an amplitude much larger than the natural signal, so in this case estimating the noise signal can be approximated from the signal itself with relative

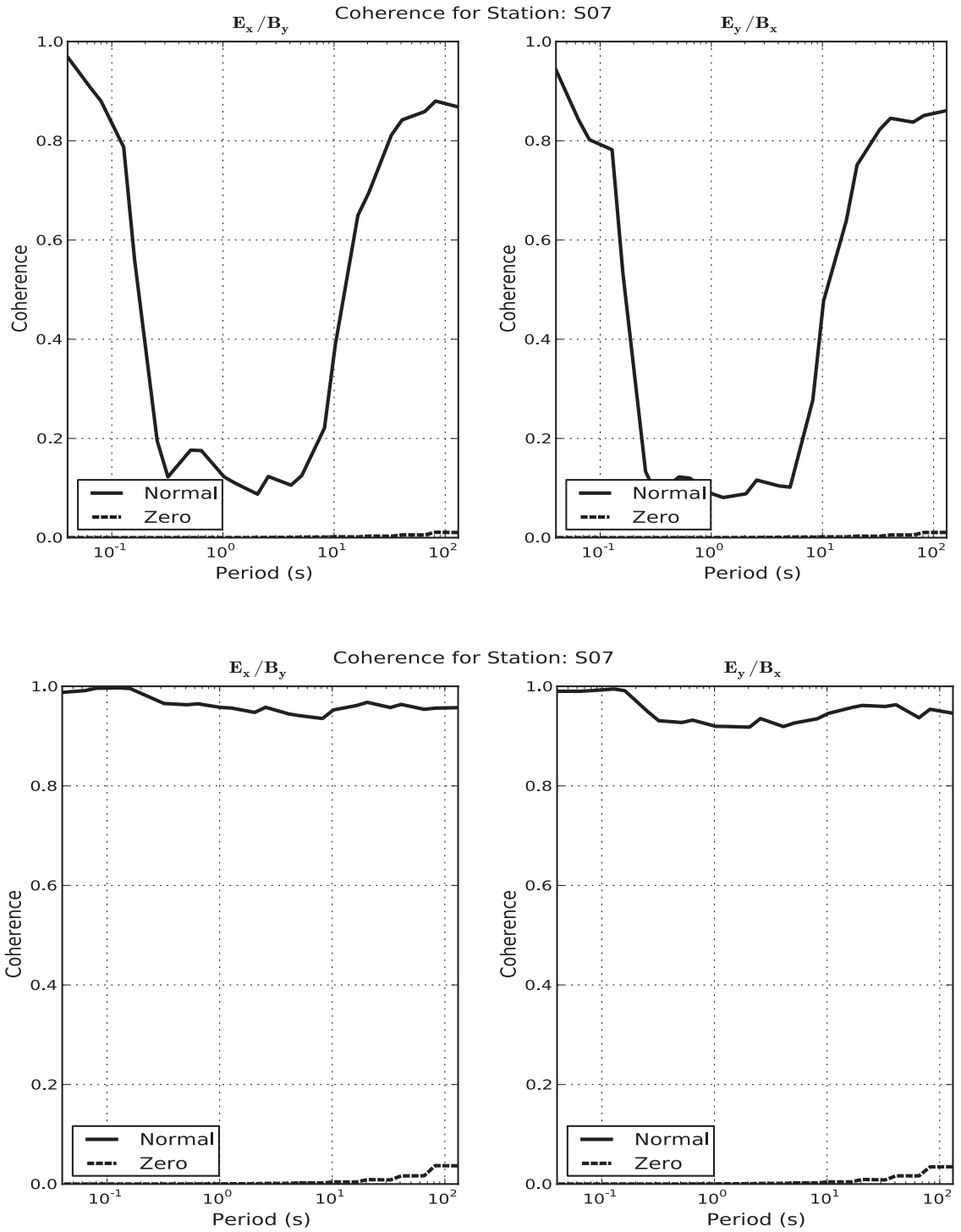

Figure 3.12: Plots of coherency between orthogonal electric and magnetic channels for a station from Antarctica used in Figure 3.11. The black line represents the coherency between the predicted electric field from the orthogonal magnetic field and and the measured electric field. The dotted line represents the coherency of noise. Top two plots are processing the entire time series, notice the coherency drops in the dead band, which is also where wind noise saturates the data (Figure 3.11). Bottom two plots show coherency processing only those times found in Figure 3.11, notice a coherency above 0.9 across all periods.

ease. Different methods can be employed to do this, but a simple yet elegant method is to window the data at non-overlapping intervals and take the average of that window length over the entire time series, providing an estimate of the periodic signal. The window length needs to have a length that incorporates a single cycle, it can have a

length of multiple cycles, but the length must be an integer of the cycle. For instance if the period is $T = 12$ seconds, the window length must be 12 seconds or octaves of 12, nT, where n is an integer. This makes the phase or placement of the windows negligible. After computing the average of all windows, a comb function is created by placing a delta function at each window instance. Finally, to estimate the noise signal the window function is convolved with the comb function of evenly spaced delta functions. Now the noise signal can be subtracted from the measured signal. One key benefit of this method is that the filter is data driven, any slight changes in the amplitude or phase of the signal will be taken into account by the windowing procedure. Similarly, the period of the window can be driven by the data by picking peaks within the Fourier transform of the input signal.

To remove the noise, a 12 second window with no overlap is passed over the data of each raw time series $f(t)$, here the file length corresponds to 10 min at a sampling rate of 500 samples/sec giving a total of 300,000 data points. Therefore, the data is split up into blocks of 6000 samples. The arithmetic mean of the windows is calculated, $w(t)$, to give an average of the signal for the 10 min block of data (note the median is a more robust estimator for removing impulse noise). This assumes that the signal is constant over the 10 minutes and any noise within the signal is Gaussian and will average out. The windowed signal $w(t)$ is then convolved with a series of delta functions, $\delta(t)$, corresponding to the start time of each window. This ensures the averaged 12 second window starts at equal intervals no matter when the signal started. The noise signal $n(t)$ is then subtracted from the raw time series $f(t)$ to give the MT signal.

$$s(t) = f(t) - n(t) \tag{3.16}$$

where:

$$n(t) = w(t) * \sum_m \delta(t + m\Delta t)$$

$$w(t) = \frac{1}{N}\sum_{n=0}^{N} f[n\Delta t : (n+1)\Delta t]$$

$$\Delta t = ldt = 6000(\text{samples})/500(\text{samples/sec}) = 12(\text{sec})$$

.

3.2.2 Frequency Domain Filtering

Time domain filtering methods can be computationally time consuming due to convolution formalism, therefore it is advantageous to exploit the convolution theorem, which states that convolution in the time domain is equal to multiplication in the Fourier domain eq. (3.17). Therefore it is computationally simpler to transform the time series into the frequency domain, multiply and transform back to the time domain than compute the convolution in the time domain, especially for long time series.

$$\mathcal{F}\{f * g\} = \iint f(\tau)g(t-\tau)\, d\tau\, e^{i\omega t} dt = \mathcal{F}\{f(t)\} \cdot \mathcal{F}\{g(t)\} = F(\omega)G(\omega) \tag{3.17}$$

In the frequency domain periodic noise has periodic pattern as well with spikes in frequency spaced at $1/T$, the inverse of period. These will be modulated by the Fourier transform of one cycle of the periodic noise. If the signal is a 3 second square wave periodic about 12 seconds than the Fourier Transform will have spikes spaced at

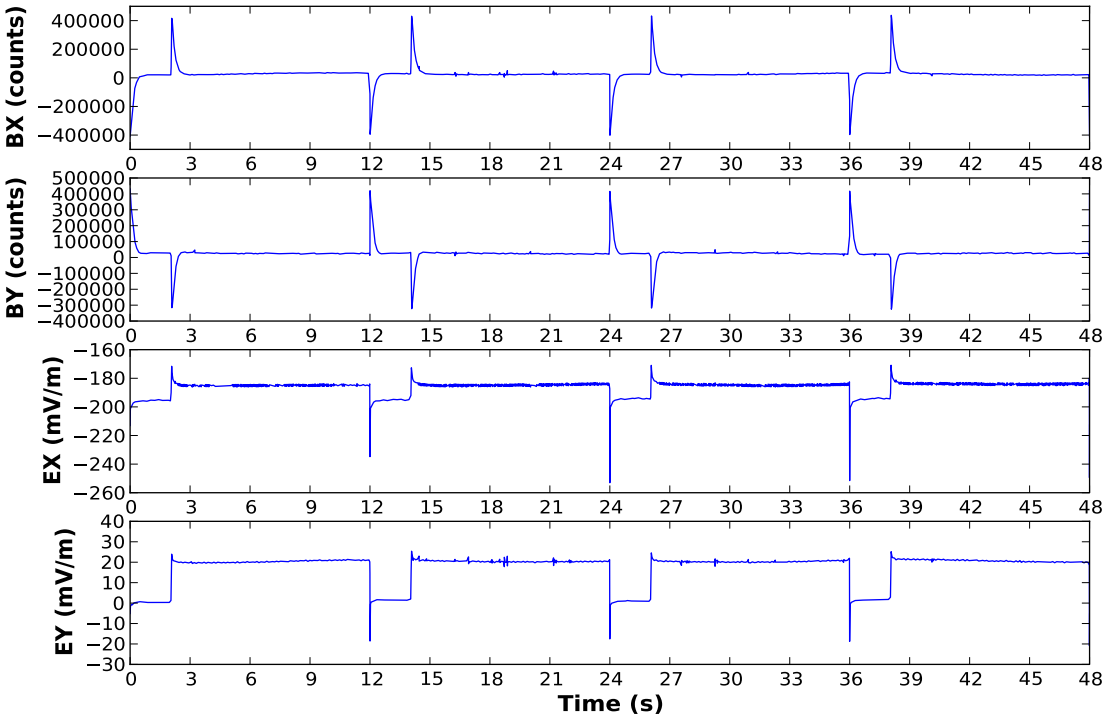

Figure 3.13: An example of periodic noise from corrosion testing on a pipeline. The signal is sent along the pipeline as a 3 second electric 'square' wave, seen in the bottom two channels, at a period of 12 seconds. The magnetic channels record the time-derivative of the square wave as opposite polarity impulses.

$1/12 = .0833$ Hz modulated by a sinc function corresponding to a three second square wave. Different frequency domain methods to remove this signal have been developed.

Comb Filter

A comb filter is a series of notches spaced at the period of the periodic signal. The goal is to remove periodic spikes in the frequency domain. A simple comb can be constructed via eq. (3.18), where a describes the depth of the notch, T is the periodic signal period, ω_o is the central frequency. Though the comb filter succeeds in suppressing periodic noise in the frequency domain, it also modulates the signal to the comb pattern suppressing or enhancing undesired signal.

$$comb(\omega) = 1 + a\, e^{-1(\omega-\omega_o)T} \tag{3.18}$$

Vector Median

Spikes in the data can be described as heavy tailed Gaussian noise. A simple method to remove such noise is by applying a median filter. The Fourier transform of a signal will be complex because it is a vector quantity with an amplitude and a phase, therefore it is appropriate to apply the median filter to both the real and imaginary parts eq. (3.19). This assumes that they are independent quantities, which is rarely valid but produces similar results to iterative median filter methods. One subtlety to consider is near DC where there is typically more signal. The median can add more signal introducing low frequency oscillations in the data.

$$vm(\omega) = \text{median}\{\Re e\{\int x(t)e^{-i\omega t}dt\}\} + i\,\text{median}\{\Im m\{\int x(t)e^{-i\omega t}dt\}\} \tag{3.19}$$

3.2.3 Component Separation

Component separation techniques attempt to split the signal into its different components assuming a linear system eq. (3.20), though algorithms do exist for non-linear problems. Given a measured response $\mathbf{X}$ composed as a superposition of multiple signals $\mathbf{s}$ measured simultaneously by different receivers with some error ϵ, separation techniques utilize correlation between the receivers to detect the different components of the signal. Component separation can be done in either the time or frequency domain using principal component analysis (PCA) and independent component analysis (ICA), or in the time-frequency plane using blind source separation (BSS).

$$\mathbf{X}(t) = \hat{\mathbf{A}}\mathbf{s} + \epsilon \tag{3.20}$$

Principal Component Analysis

The goal of PCA is to project the data into an orthonormal basis where the eigenvectors, weighted by the corresponding eigenvalue, are the principal components of the system. This can be accomplished by two formally similar methods, diagonalization of the covariant matrix and singular value decomposition (SVD) of the received signal matrix.

Given a set of zero-mean N received signals, call them n *sources*, of m number of data points:

$$\mathbf{X} = [\mathbf{x}_1, \mathbf{x}_2, ...\mathbf{x}_n]^T, \mathbf{X} \in \mathbf{R}^{(n\times m)}$$

The covariant matrix $\mathbf{S_x}$ can be computed by:

$$\mathbf{S_x} = \frac{1}{n-1}\mathbf{X}\mathbf{X}^T \tag{3.21}$$

The covariant matrix contains valuable information about a multi-channel source. Each element is defined as $\angle x_i,\ {x_j}^T\rangle$ (the inner product), describing how the parameters vary between sources characterizing dimensional correlation. The off diagonal elements, $i \neq j$, describe cross-correlation between different sources, where as the diagonal elements, $i = j$ describe auto-correlation. Logically, if the covariant matrix can be diagonalized then all cross-correlation is identically zero and only auto-correlations remain. This can be accomplished by solving the eigenvalue problem:

$$(\mathbf{S_x} - \lambda\mathbf{I})\mathbf{P} = 0$$

The eigenvalues, λ, describe the scale of each eigenvector, the trick is to pick those eigenvalues which represent the the data. For noise free data only the largest eigenvectors are assumed to be the signals. However, in noisy environments this is not always the case, where the largest eigenvalues represent noise. Recursive methods of testing the eigenvalues have been developed, see Egbert (1997). The eigenvectors, $\mathbf{P} \in [\mathbf{p}_1, \mathbf{p}_2, ...\mathbf{p}_n]$, are elements of the row space of $\mathbf{S_x}$, relating outputs of the covariance matrix. Finally, the principal components, $\mathbf{PC_x}$ are computed by:

$$\mathbf{PC_x} = \mathbf{P}^T\mathbf{X} \tag{3.22}$$

Singular Value Decomposition

Though this is a simple method, it can be computationally expensive to compute the covariance matrix. An elegant method for decomposing a matrix into orthonormal basis is singular value decomposition (SVD) (Scales *et al.*, 2001). Clever intuition suggests that $\mathbf{X}$ can be transformed into an orthonormal basis by projecting the rows and columns separately into orthonormal bases. Specifically, unitary transformation of the rows of $\mathbf{X}$ is equivalent to unitary transformation of the columns of a diagonal matrix who's elements correspond to variances of $\mathbf{X}$. Assume that for eigenvectors $\mathbf{u}$ of $\mathbf{X}^T$:

$$\mathbf{X}^T\mathbf{u}_i = \lambda_i\mathbf{u}_i$$

and the eigenvectors of $\mathbf{X}$ are $\mathbf{v}$,

$$\mathbf{X}\mathbf{v}_i = \lambda_i\mathbf{v}_i$$

These two equations state that $\mathbf{X}$ can simultaneously have orthornormal basis for the rows and columns separately. It is important to note that eigenvectors $\mathbf{v}_i$ and $\mathbf{u}_i$ have the same eigenvalue λ_i. Multiplying the first equation by $\mathbf{X}$ and the second by $\mathbf{X}^T$, presents a similar result found previously for PCA.

$$\mathbf{X}\mathbf{X}^T\mathbf{u}_i = \lambda^2{}_i\mathbf{u}_i$$

and,

$$\mathbf{X}^T\mathbf{X}\mathbf{v}_i = \lambda^2{}_i\mathbf{v}_i$$

Where $\mathbf{u}$ span the column space of $\mathbf{X}$ and $\mathbf{v}$ span the row space of $\mathbf{X}$. Notice that $\mathbf{v}^T$ is identical to $\mathbf{p}$ and is the target of PCA. It can be shown that:

$$\mathbf{X}\mathbf{V} = \mathbf{U}\mathbf{\Sigma}$$

where $\mathbf{V} \in [\mathbf{v}_1, \mathbf{v}_2, ...\mathbf{v}_n]^T$, $\mathbf{U} \in [\mathbf{u}_1, \mathbf{u}_2, ...\mathbf{u}_m]^T$, and $\mathbf{\Sigma} = \mathbf{I}\sigma$, $\sigma \in [\lambda^2{}_1, \lambda^2{}_2, ...\lambda^2{}_n]$. This powerful expression states that $\mathbf{U}$ and $\mathbf{V}$ are simultaneous eigenvectors of $\mathbf{X}$ connected by eigenvalue σ, the variance. Furthermore, the SVD of $\mathbf{X}$ is given by:

$$\mathbf{X} = \mathbf{U}\mathbf{\Sigma}\mathbf{V}^T \tag{3.23}$$

Finally, the principal components are defined as:

$$\mathbf{PC_x} = \mathbf{X}^T\mathbf{V}^T \tag{3.24}$$

Either diagonalization of the covariance matrix or SVD is appropriate for PCA. A few things that need to be considered. Both produce an orthonormal basis that is non-unique, specifically $\mathbf{V}$ can be positive or negative and is normalized. Therefore when using PCA to remove periodic signal, scale and phase of the principal components becomes important. Similarly, picking the correct component as the noise is of utmost importance.

Independent Component Analysis

Independent component analysis (ICA) is similar to PCA, however the underlying assumption is that the components are not coupled; they are statistically independent. Mathematically, signals are independent if their joint probability function is separable into the product of the individual probability density functions. One caveat is that the independent components cannot be statistically described by a Gaussian probability density function. The goal of ICA is to estimate the mixing matrix $\hat{\mathbf{A}}$ in order to find the sources, where multiple methods have been developed (Hyvärinen, 1999). Here the FastICA of Hyvärinen & Oja (2000) will be briefly described.

Because ICA only works if the the signal components are non-Gaussian, FastICA searches for directions that are maximally non-Gaussian eq. (3.25). Here, $y = \mathbf{w}^T\mathbf{X}$ is a weighted version of the measured signals with unit variance, and $\mathbf{w}$ is to be determined, $E\{G(y)\}$ is the expectation value of a non-quadratic function $G(y)$, and ν is a Gaussian variable of unit variance and zero mean. The minimization function $J(y)$ is given by:

$$J(y) \approx [E\{G_1(y)\} - E\{G_2(\nu)\}]^2 \tag{3.25}$$

where

$$G_1(u) = \frac{1}{a_1}\log\cosh(a_1 u); \;\; 1 \leq a_1 \geq 2$$
$$G_2(u) = -e^{(-u^2/2)}$$

FastICA then iteratively estimates $\mathbf{w}$ till non-linear convergence (quadratic or cubic). This is done in 4 basic steps:

1. Initialize $\mathbf{w}$ as a random weighting matrix
2. Compute $\mathbf{w}^\dagger = E\{\mathbf{X}g(\mathbf{w}^T\mathbf{X})\} - E\{g'(\mathbf{w}^T\mathbf{X})\}\mathbf{w}$, where g is either G_1 or G_2.
3. Compute $\mathbf{w}_n = \dfrac{\mathbf{w}^\dagger}{||\mathbf{w}^\dagger||}$
4. If $\mathbf{w} \cdot \mathbf{w}_n \neq 0$, iterate again starting at 2.

Once $\mathbf{w}$ is found than the sources are simply $\mathbf{s} = \mathbf{w}^T\mathbf{X}$.

Some limitations of ICA are similar to PCA, i.e. ICA can only approximate independent components up to a permutation and scaling factor. One advantage of ICA over PCA is that it is less sensitive to noise because noise is typically Gaussian, thus characterizing the signal more accurately (Figure 3.14 and Figure 3.15).

3.2.4 Blind Source Separation Based On Spatial-Time Frequency Distributions

Separation of signals can also be accomplished in the time-frequency domain, which has the advantage of characterizing non-stationary signals that can be under-determined (Abrard & Deville, 2005; Peng & Xiang, 2010). The method is nominated time-frequency blind source separation (TFBSS) and aims at locating points in the time-frequency plane that are common across all measurements to estimate source signals (Belouchrani & Amin, 1998). This is a common technique for speech recognition (Kuhne *et al.*, 2008) and can be applied to image separation (Ozgen *et al.*, 2009). Each coincident measurement is transformed into a covariant representation via Fourier

transforms of short time windows with each other coincident measurement, resulting in a spatial time frequency representations of the signal eq. (3.26). Here, $\mathbf{x}$ are the time series for one measurement, $\mathbf{x}^H$ is the conjugate Hermitian, θ is a kernel depending on the type of time-frequency representation. Then similar to PCA, the goal is to diagonalize $\hat{\mathbf{D}}$. Again, the diagonal terms are auto-correlations and the off-diagonal terms are cross-correlation terms. One difference with PCA is that the off-diagonal are important in characterizing sources.

$$\hat{\mathbf{D}}_{\mathbf{xx}}(t,\omega) = \sum_{l=-\infty}^{\infty}\sum_{k=-\infty}^{\infty} \theta(m,l)\mathbf{x}(t+m+l)\mathbf{x}^H(t+m-l)e^{-i2\omega l} \tag{3.26}$$

The first step is to whiten the data through unitary transformation of eigen-decomposition, which has the effect of decoupling the data and normalizing by the noise. Then, collect time-frequency points in the whitened $\hat{\mathbf{D}}$ that are either auto or cross terms which are above a certain statistically determined threshold (Fevotte & Doncarli, 2004). Use these points to then find a unitary matrix that diagonalizes $\hat{\mathbf{D}}$ and another unitary matrix that off-diagonalizes $\hat{\mathbf{D}}$. A common method is to use Givens rotations to simultaneously compute a unitary matrix that maximizes the difference of a diagonalized and off-diagonalized matrix (Belouchrani & Amin, 1998; Boashash, 2003). Degerine & Kane (2006) give an overview of different methods for joint diagonalization. The sources are then computed similar to eq. (3.24), which again is up to a phase and permutation of the original source signals. One advantage of TFBSS is when the signal has a distinct time-frequency pattern, such as a chirp as in Figure 3.2. However the main draw back, besides being computationally expensive, is that if the signal and noise have crossing time-frequency patterns, then TFBSS has trouble differentiating between signal and noise.

3.3 Summary

Analyzing MT time series is a crucial initial step towards understanding the data, namely signal and noise sources and coherent times. Techniques for estimating coherent times have been described utilizing robust time frequency analysis, including estimation of apparent resistivity, coherence between channels and PC analysis. Periodic noise is often an ever present noise source in MT data biasing estimations of MT transfer functions. Mulitple techniques have been described to remove such noise where the optimum technique depend on the data and noise characteristics. These steps prepare the data for estimation of the transfer function as described in Chapter 2.

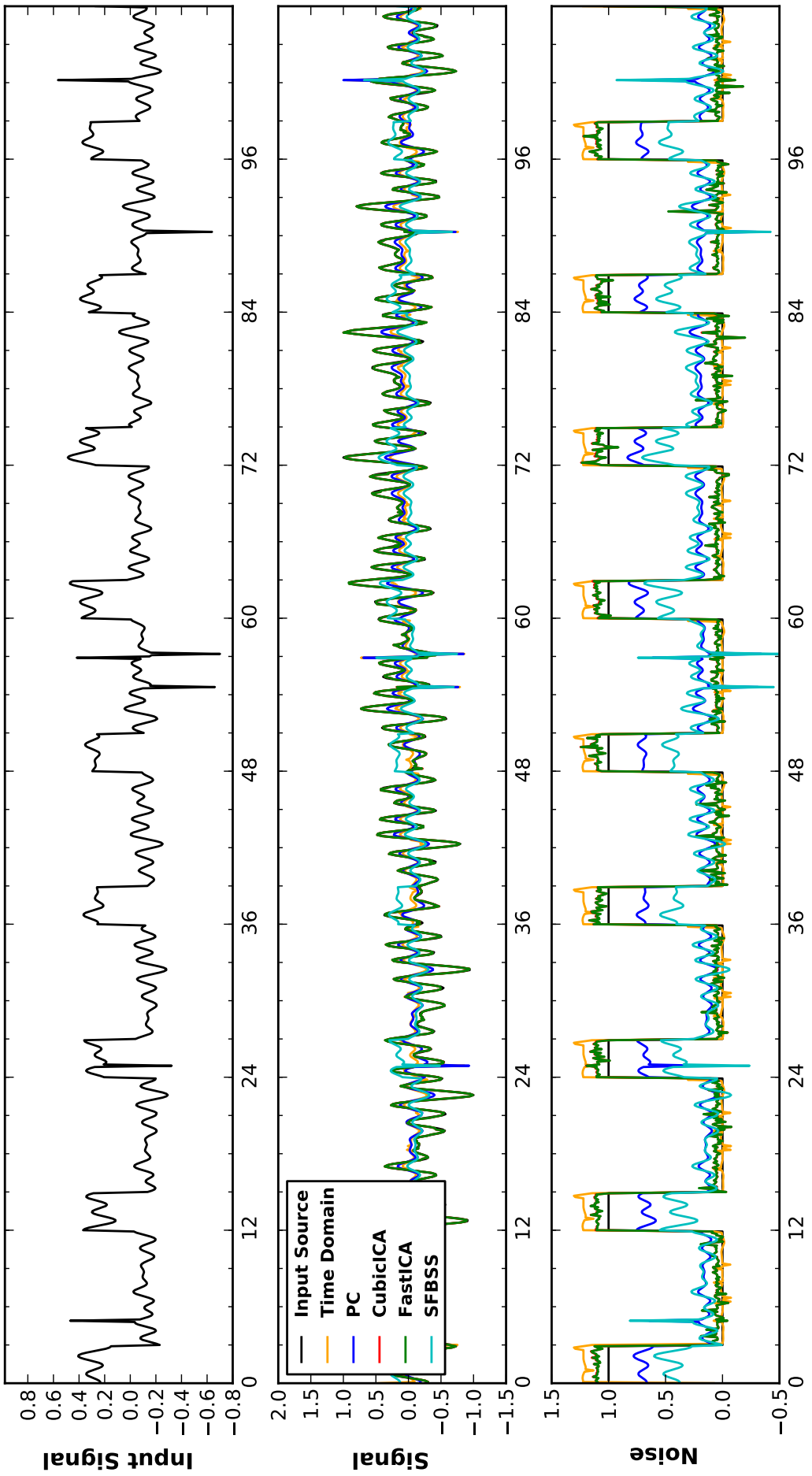

Figure 3.14: Example of periodic noise removal by different techniques. The input signal (top) is a sum of sinusoids with periods between 0.01 and 1 s with random phases plus periodic noise with an amplitude 200 percent of the input signal plus heavy tailed Gaussian impulse noise. Each method described in the text estimates the two signal, input signal (middle), periodic noise (bottom). Each plot is normalized because all methods can only estimate the signal to within a scaling constant. Notice PCA and ICA get similar results, with ICA estimating the noise more accurately and PCA still susceptible to impulse noise. BSS has troubles estimating the noise accurately because the input signal is poorly structured in the time-frequency plane whereas the periodic signal is not, also BSS is susceptible to impulse noise even when a robust TFD is used. Time domain subtraction produces similar results to ICA.

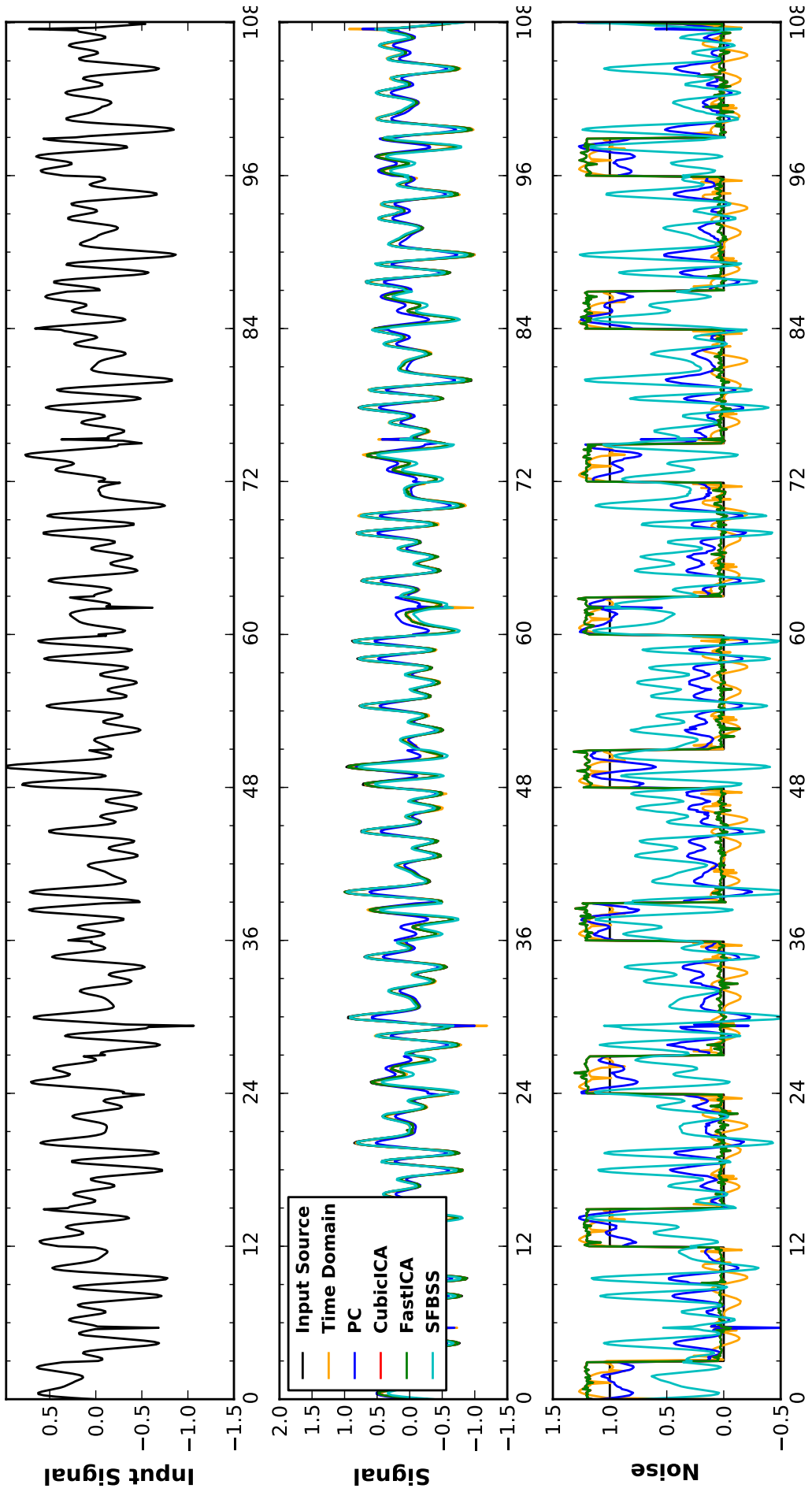

Figure 3.15: Example of periodic noise removal by different techniques. The input signal (top) is a sum of sinusoids with periods between 0.01 and 1 s with random phases plus periodic noise with an amplitude 15 percent of the input signal plus heavy tailed Gaussian impulse noise. Each method described in the text estimates the two signal, input signal (middle), periodic noise (bottom). Each plot is normalized because all methods can only estimate the signal to within a scaling constant. Again, notice ICA and PCA have similar results, with ICA more accurately characterizing the signal and noise. Time domain subtraction characterizes both signal well but adds more signal to the periodic noise resulting in larger residuals in the estimated signal. BSS characterizes the signal well but not the noise.

Chapter 4

MT Analysis

Analysis of MT responses is the next step, which turns out to be one of the most critical steps for accurate interpretation of the data. This includes observing and removing any static shift, near surface distortions, noisy periods and peculiar responses that might bias models and subsequent interpretations. Tensor representations provides dimensionality information about the MT response, inferring preferred electrical current paths within the subsurface. This chapter overviews two tensor representations of the MT response and two different methods to remove static shift and near surface distortions that are used in this experiment.

4.1 Phase Tensors

An elegant representation of $\hat{\mathbf{Z}}$ is formulated by Caldwell *et al.* (2004) and nominated the phase tensor eq. (4.2). The ratio of the imaginary and real parts of $\hat{\mathbf{Z}}$ is free of electric distortion as it is simply divided out and only the regional response remains. Assuming the distortion is real and frequency independent, then the regional impedance tensor is simply,

$$\hat{\mathbf{Z}}_R = \hat{\mathbf{D}}^{-1}\hat{\mathbf{Z}} \tag{4.1}$$

Let $\hat{\mathbf{X}}$ be the real part of $\hat{\mathbf{Z}}$ and $\hat{\mathbf{Y}}$ be the imaginary part of $\hat{\mathbf{Z}}$, then

$$\begin{aligned}
\hat{\mathbf{X}} &= \hat{\mathbf{D}}\, \Re e\{\hat{\mathbf{Z}}_R\} \\
\hat{\mathbf{Y}} &= \hat{\mathbf{D}}\, \Im m\{\hat{\mathbf{Z}}_R\} \\
\hat{\mathbf{\Phi}} &= \hat{\mathbf{X}}^{-1}\hat{\mathbf{Y}} = \begin{bmatrix} \Phi_{11} & \Phi_{12} \\ \Phi_{21} & \Phi_{22} \end{bmatrix}
\end{aligned} \tag{4.2}$$

Following Caldwell *et al.* (2004), three invariants of the phase tensor can be defined as:

$$\Phi_1 = \frac{\Phi_{11} + \Phi_{22}}{2} \tag{4.3}$$

$$\Phi_2 = \sqrt{\Phi_{11}\Phi_{22} - \Phi_{12}\Phi_{21}} \tag{4.4}$$

$$\Phi_3 = \frac{\Phi_{12} - \Phi_{21}}{2} \tag{4.5}$$

Then the phase tensor minimum, maximum and skew, which are also invariants, can be defined as:

$$\Phi_{min} = \sqrt{\Phi_1^2 + \Phi_3^2} - \sqrt{\Phi_1^2 + \Phi_3^2 - \Phi_2^2} \tag{4.6}$$

$$\Phi_{max} = \sqrt{\Phi_1^2 + \Phi_3^2} + \sqrt{\Phi_1^2 + \Phi_3^2 - \Phi_2^2} \tag{4.7}$$

$$\beta = \frac{1}{2}\tan^{-1}\left(\frac{\Phi_3}{\Phi_1}\right) \tag{4.8}$$

The angle that describes orientation of Φ_{max} is defined as eq. (4.9), which is related to geoelectric strike and is not invariant to rotation. It is important to note that a 90 degree ambiguity in orientation of the strike angle exists and only with independent information, such as Tipper information from vertical magnetic field measurements (Everett & Hyndman, 1967), can it be removed.

$$\alpha = \frac{1}{2}\tan^{-1}\left(\frac{\Phi_{12} + \Phi_{21}}{\Phi_{11} - \Phi_{22}}\right) \tag{4.9}$$

Linking invariants to physical parameters is important to fully understand phase tensor representation. eq. (4.8) defines the skew angle, which describes 3D effects of electric current flow. Specifically, if the absolute value of the skew angle is greater than 0, then subsurface conductivity structure is at least 2D heterogeneous and/or anisotropic. Φ_{min} and Φ_{max} represent gradients in subsurface conductivity structure along principle directions of current flow, where Φ_{max} is related to the maximum principle direction and Φ_{min} the minimum principle direction. Following Bibby (1986), the phase tensor can be graphically represented as an ellipse where the major and minor axis are Φ_{max} and Φ_{min}, respectively, and the orientation is defined by $\alpha - \beta$ (Figure 4.1). Another parameter that can characterize subsurface geoelectric dimensionality is the ellipticity defined as eq. (4.10) (also an invariant), where the geoelectric structure is 2D if $\eta > 0$. Plotting all these parameters for a single station provides a diagnostic tool to analyze geoelectric structure (Figure 4.2).

$$\eta = \frac{\Phi_{max} - \Phi_{min}}{\Phi_{max} + \Phi_{min}} \tag{4.10}$$

4.1.1 Phase Tensor Behavior

Behavior of phase tensor ellipses describes conductivity gradients in the subsurface, i.e. the major axis is oriented with preferred electric current direction. In a 1D case, where subsurface conductivity varies only with depth, the phase tensor ellipse will be a circle as $\Phi_{min} = \Phi_{max}$ and $\beta = 0$. In a 2D case, where subsurface conductivity structure varies with depth and one horizontal direction, the ellipse will elongate in preferred current direction as $\Phi_{max} > \Phi_{min}$ and $\beta = 0$. In a 3D case, where subsurface conductivity structure can vary in all three directions, orientation of the major axis will be skewed by complicated electric current paths as $\Phi_{max} > \Phi_{min}$ and $|\beta| > 0$. Heise *et al.* (2006) describes in detail phase tensor ellipses behavior in anisotropic media.

For the purpose of comparing collocated measurements separated in time, as in this dissertation, the residual phase tensor will be defined as eq. (6.1).

$$\Delta\Phi_{ij} = \hat{\mathbf{I}} - (\hat{\mathbf{\Phi}}_i^{-1}\hat{\mathbf{\Phi}}_j) \tag{4.11}$$

This residual representation estimates the percent change between two different measurements i and j. The advantage of using eq. (6.1) is that the resulting tensor

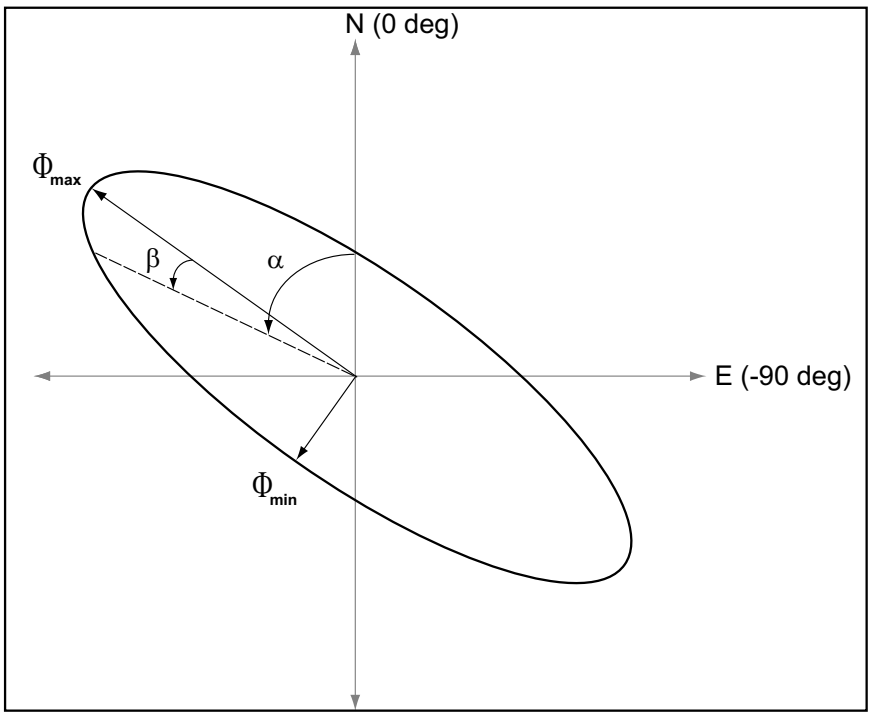

Figure 4.1: Generic plot of a phase tensor or resistivity tensor represented as an ellipse. Φ_{min} eq. (4.6) and Φ_{max} eq. (4.7) are the minor and major axis and the orientation is defined as $\alpha - \beta$ (4.9 minus 4.8) and is measured counter-clockwise.

gives the relative change between the two measurements as opposed to an absolute change, such as $\Phi_i - \Phi_j$. The residual ellipses are then oriented in the direction of maximum change. The shape is related to the percent change, where a circle represents a scalar change and an ellipses represents a heterogenous change in subsurface resistivity structure. The 3D forward modeling code of Mackie *et al.* (1993) is employed to analyze behavior of residual tensor representation by introducing a conductive body and a resistive body separately.

Conductive Body

Starting from a homogeneous half space of 100 Ω·m , a conductive cube (ρ=1.0 Ω·m) of dimensions 2 km x 2 km x 500 m was introduced at a depth of 1 km. The residuals are calculated from eq. (6.1). A few things are important to notice. First, the ellipses orient in the direction of greatest change, again there is a 90 degree ambiguity that can be removed with independent information. Second, changes occur within a period band then die out at longer periods. Also, around the boundary edges of the conductive body phase tensor ellipses are oriented parallel to the boundary and outside the body all the phase tensor point towards the body, but are much smaller. Moreover, the phase tensors directly over the body align with the longer axis because current can flow more easily. These patterns could be used to mark the lateral boundaries of the conductive body and give some indication of depth if an absolute resistivity measurement is available to constrain the depth.

Resistive Body

Here, a resistive body of the same dimensions as in Section 4.1.1 is inserted into the same half space but this time the body is resistive (ρ = 10000 Ω·m). The first phenomena to note is that change caused by a resistive body is an order of magnitude

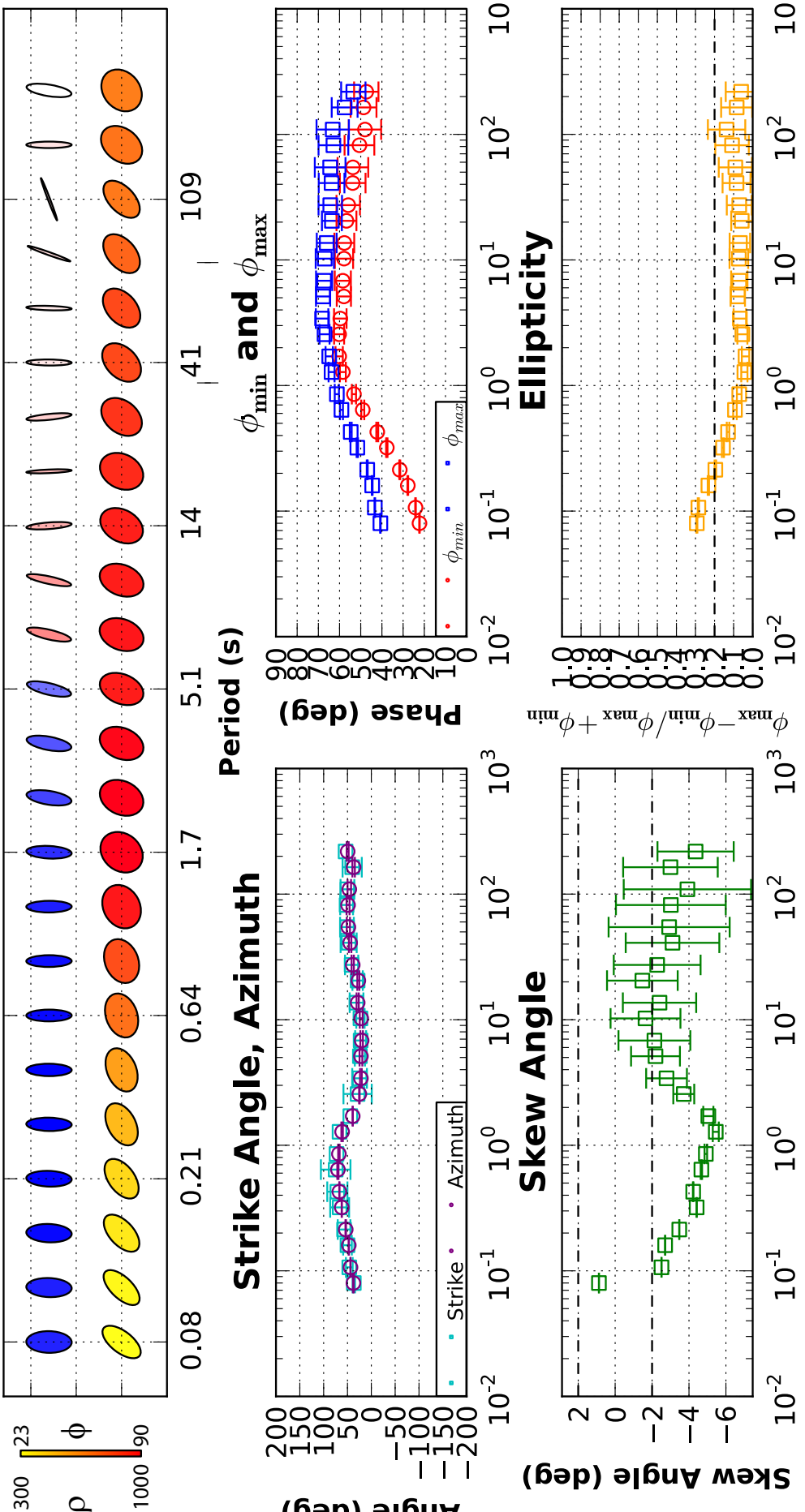

Figure 4.2: Plots of different parameters estimated from the phase tensor and resistivity tensor. Top: resistivity tensor (top) and phase tensor (bottom) versus period with N to the top of the page. Middle Left: Azimuth of the phase tensor and strike angle estimated from Weaver *et al.* (2000). Bottom Left: Skew angle with dotted lines marking approximate regions of 3D effects. Middle Right: Φ_{min} eq. (4.6) and Φ_{max} eq. (4.7) of the phase tensor. Bottom Right: Ellipticity estimating 2D effects above a threshold.

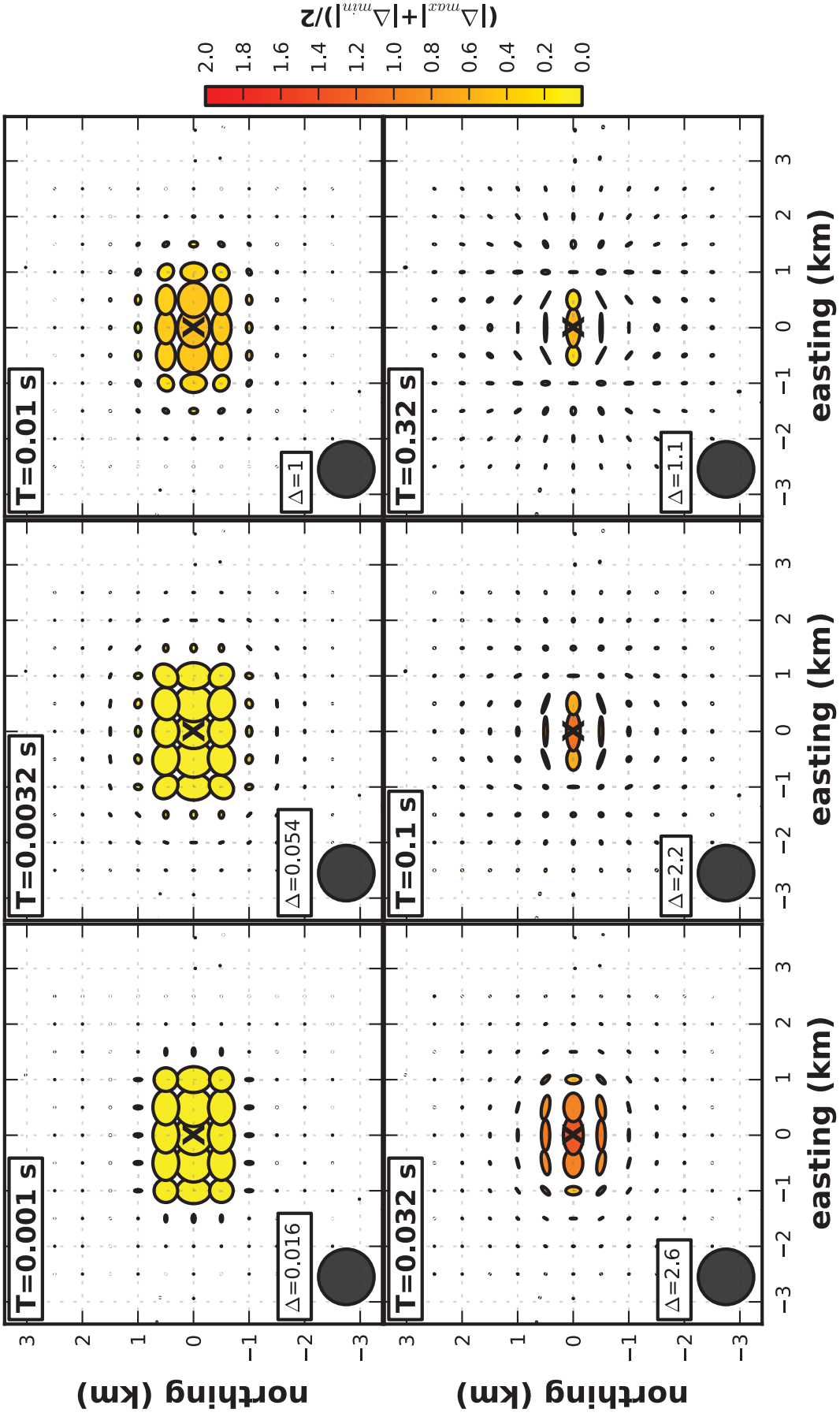

Figure 4.3: Maps of phase tensor residuals of a conductive body (2 km x 1 km x 500 m, $\rho = 1.0\ \Omega{\cdot}\text{m}$) introduced into a half space ($\rho = 100\ \Omega{\cdot}\text{m}$) at 1 km depth. Each plate maps a different period (s) labeled in the top left. Also, the ellipses are normalized to the maximum of Φ_{max} for that period for easier visualization, the scale is in the lower left. Ellipses are colored by the arithmetic mean of eq. (6.1) (deg).

smaller than that of a similar conductive body. Residual phase tensor ellipses exhibit a similar behavior to the conductive body except the tensor near the boundary tend to orient perpendicular to the boundary. Also, the volume of influence is larger, where stations farther away are more sensitive to the resistive body. Similarly, shorter periods experience larger changes, which is in contrast to the conductive case. This is because of the diffusive nature of MT, where depth of penetration is directly proportional to subsurface resistivity eq. (2.24). If the resistivity increases between measurements then the same period will penetrate deeper and therefore the volume of influence is larger. Finally, changes observed for the resistive body are about one-tenth that of the conductive body suggesting a stronger sensitivity to conductive changes.

4.2 Resistivity Tensors

Reilly (1979) formulated a real apparent resistivity tensor eq. (4.12) and real apparent permittivity tensor eq. (4.13) from the complex admittance tensor (inverse of $\hat{\mathbf{Z}}$) to help describe the MT response in anisotropic media.

$$\hat{\rho} = \mu\omega \cdot \Im m\{\hat{\gamma}\} \tag{4.12}$$

$$\hat{\epsilon} = \frac{1}{\mu\omega^2} \cdot \Re e\{\hat{\gamma}\} \tag{4.13}$$

The apparent resistivity tensor is defined by eq. (4.12), where the propagation tensor $\hat{\gamma}$ is defined by 4.14. Here, $\mathbf{Y}_{ij}$ is a component of the admittance tensor (the inverse of $\hat{\mathbf{Z}}$), μ is the magnetic permeability (N/A^2) and ω is frequency (Hz).

$$\hat{\gamma} = -\omega^2 \begin{bmatrix} Y_{22}Y_{11} - Y_{21}Y_{21} & Y_{22} \cdot (Y_{12} - Y_{21}) \\ Y_{11} \cdot (Y_{21} - Y_{12}) & Y_{22}Y_{11} - Y_{12}Y_{12} \end{bmatrix} \tag{4.14}$$

It has been suggested that the apparent resistivity tensor be nominated Reilly's tensor (RT), and will be used here. Visualization of the RT is plotted as an ellipse, following Bibby (1986), where the long axis points in the direction of greatest conductivity contrast. The face color of the ellipse represents the determinant of eq. (4.12), which is related to the apparent resistivity. The advantage of this representation is that resistivity structure directionality can be visualized. Though, one drawback is that RT can be influenced by static shift and near surface distortions, which rotates ellipse axis and changes face color. (Weckmann *et al.*, 2003) suggests that shape is not changed by distortion, however that claim has not been found to be true in analysis of RT. Frequency independent distortions can be removed by following Bibby *et al.* (2005), where the distortion matrix is derived from 1D or 2D sections of the MT response, as described in Section 4.3.1. Note that the distortion tensor is estimated up to a scaling constant and does not remove any frequency dependent distortion (Patella, 1987).

4.2.1 Behavior

Similar to PT residuals, RT residual are estimated using eq. (6.1). The same conductive and resistive anomalies are discussed.

Conductive Body

The same conductive model is used as in the Section 4.1.1. Again, the residual tensor points in the direction of greatest change. Residual resistivity tensor ellipses behave

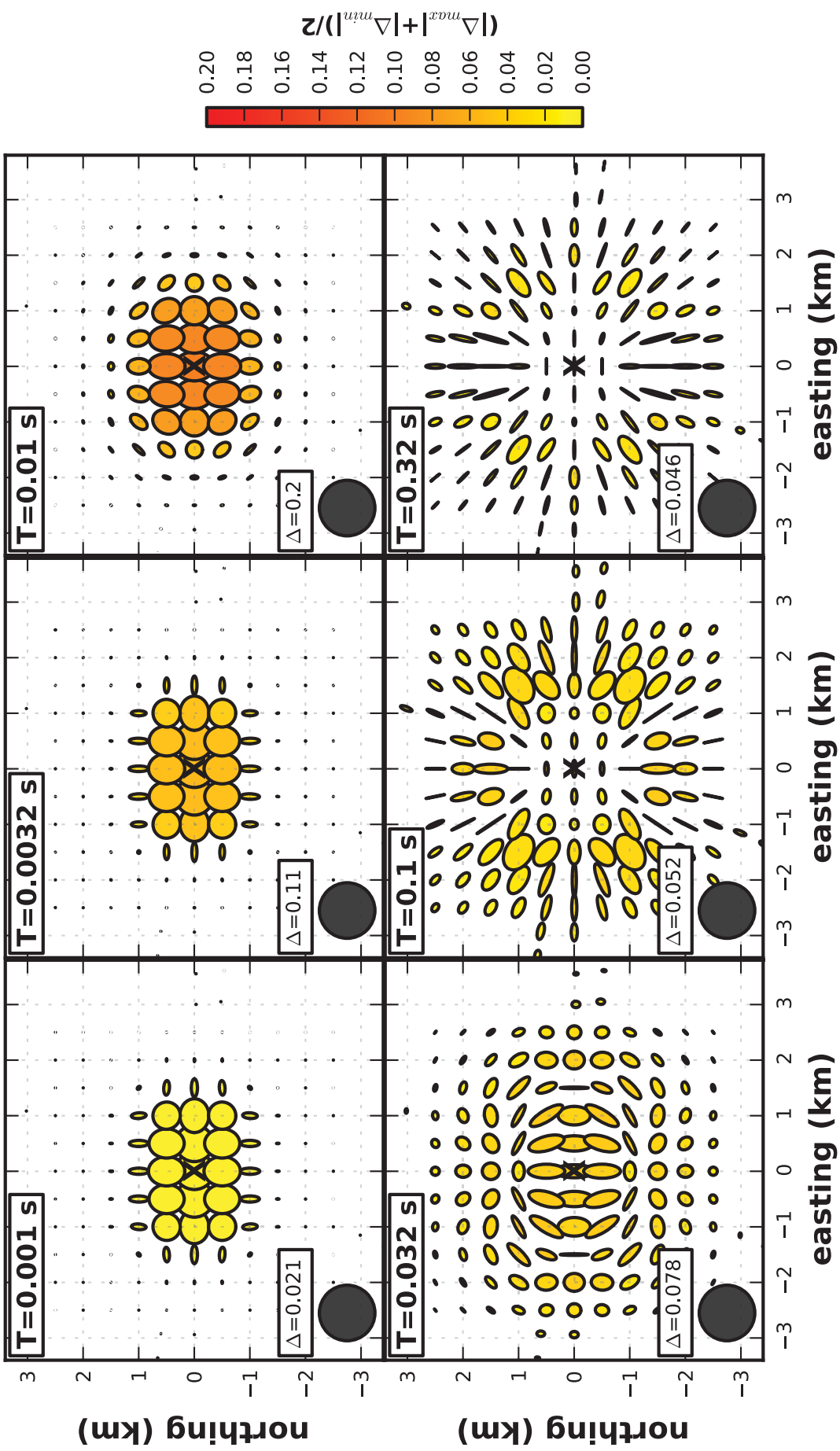

Figure 4.4: Maps of phase tensor residuals of a resistive body (2 km x 2 km x 500 m, $\rho = 10000\ \Omega{\cdot}$m) introduced into a half space ($\rho = 100\ \Omega{\cdot}$m) at 1 km depth. Each plate maps a different period (s) labeled in the top left. Also, the ellipses are normalized to the maximum of Φ_{max} for that period for easier visualization, the scale is in the lower left. Ellipses are colored by the arithmetic mean of eq. (6.1).

similar to residual phase tensor ellipses with a few differences. The largest change occurs at longer periods, which follows the dispersion relations that show the phase predicts the resistivity. Moreover, at periods with skin depths much longer than the depth of the body, the ellipses experience similar changes to periods with skin depths proportional to the depth of the body. This is cause by the volumetric nature of the resistivity, suggesting that depth to the bottom of the body cannot be estimated from the resistivity. Interestingly, near the edges of the body the ellipses align in one direction. Specifically, observe ellipses to the north of the body and to the east. To the east, ellipses align nearly parallel to the edge, whereas to the north ellipses align orthogonal to the body edge. This could be caused by the 90 degree ambiguity in orientation, but the orientation change does suggest changes in boundary edges. Another interesting result is that at the shortest period the resistivity tensor residual is resistive, which is caused by the wave nature of EM.

Resistive Body

The same body is used as in Section 4.1.1. Ellipse behavior is quite different to the phase tensor residuals where the largest changes are still observed directly over the body. Ellipse orientation is similar to the conductive case except that the change is observed over a larger area and ellipses tend to orient parallel to body edges. At a period of 0.0032 s the change is conductive, this is because of a wave guide effect between the body and the surface, commonly observed in forward modeling. Opposed from PT residuals of the same body, most of the change is observed at stations above the body not at stations outside the areal extent of the body, similar to Figure 4.5. This could help decipher the edges of the body.

4.2.2 Summary

Tensor representation of $\hat{\mathbf{Z}}$ provides valuable information about the dimensionality of subsurface geoelectric structure, furthermore the residual tensor provides information about how subsurface conductivity structure changed between measurements. The phase tensor estimates the gradient change in subsurface conductivity structure and can be graphically represented as an ellipse, where the major axis aligns with preferred electric current direction. The two examples demonstrate the behavior of residual phase tensors suggesting information about lateral and vertical boundaries can be estimated. The resistivity tensor estimates resistivity dimensionality, again represented as an ellipse, where the orientation aligns with preferred current flow. The residual resistivity tensor can be used as a supplementary tool to estimate the magnitude of change in conductivity structure between measurements. It is important to note that the phase tensor is invariant to near surface distortions, however the resistivity tensor is not. Therefore a few methods to remove distortion will be discussed.

4.3 Galvanic Distortion

MT theory assumes that no free charges are supported by the Earth, however charges can accumulate in the subsurface, for instance near structural boundaries or near surface inhomogeneities (Bahr, 1991). These charges cause galvanic distortions in the MT response. Galvanic distortions occur when the inductive response of the subsurface is much smaller than the galvanic response. Typically, this occurs at short periods, which are sensitive to the near surface. The effect of galvanic distortion is to linearly scale the

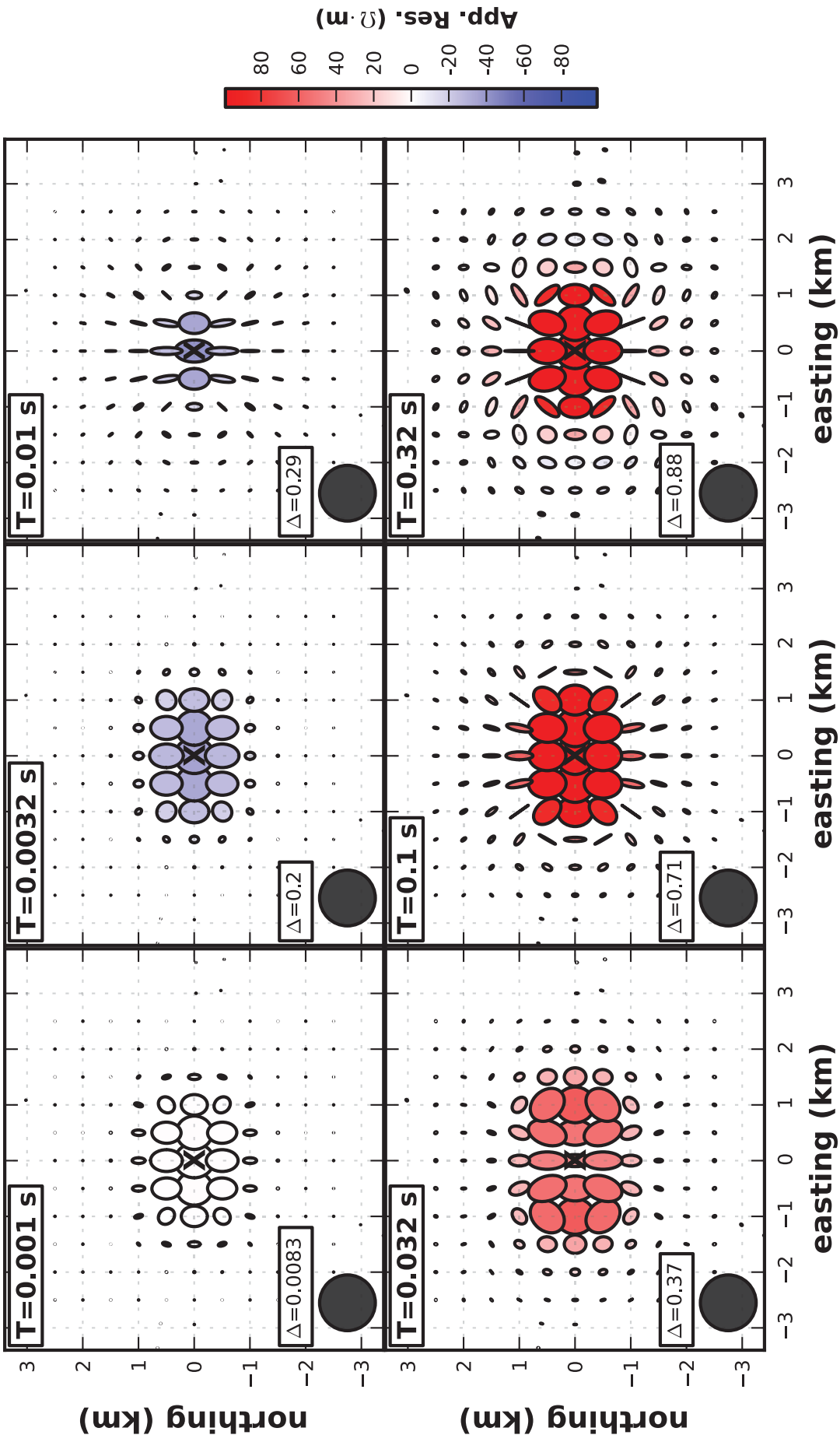

Figure 4.5: Maps of resistivity tensor residuals of a conductive body (2 km x 2 km x 500 m, $\rho = 1.0$ Ω·m) introduced into a half space ($\rho = 100$ Ω·m) at 1 km depth. Each plate maps a different period (s) labeled in the top left. Also, the ellipses are normalized to the maximum of ρ_{max} for that period for easier visualization, the scale is in the lower left. Ellipses are colored by the residual of resistivity tensor determinants, indicating a conductive or resistive change.

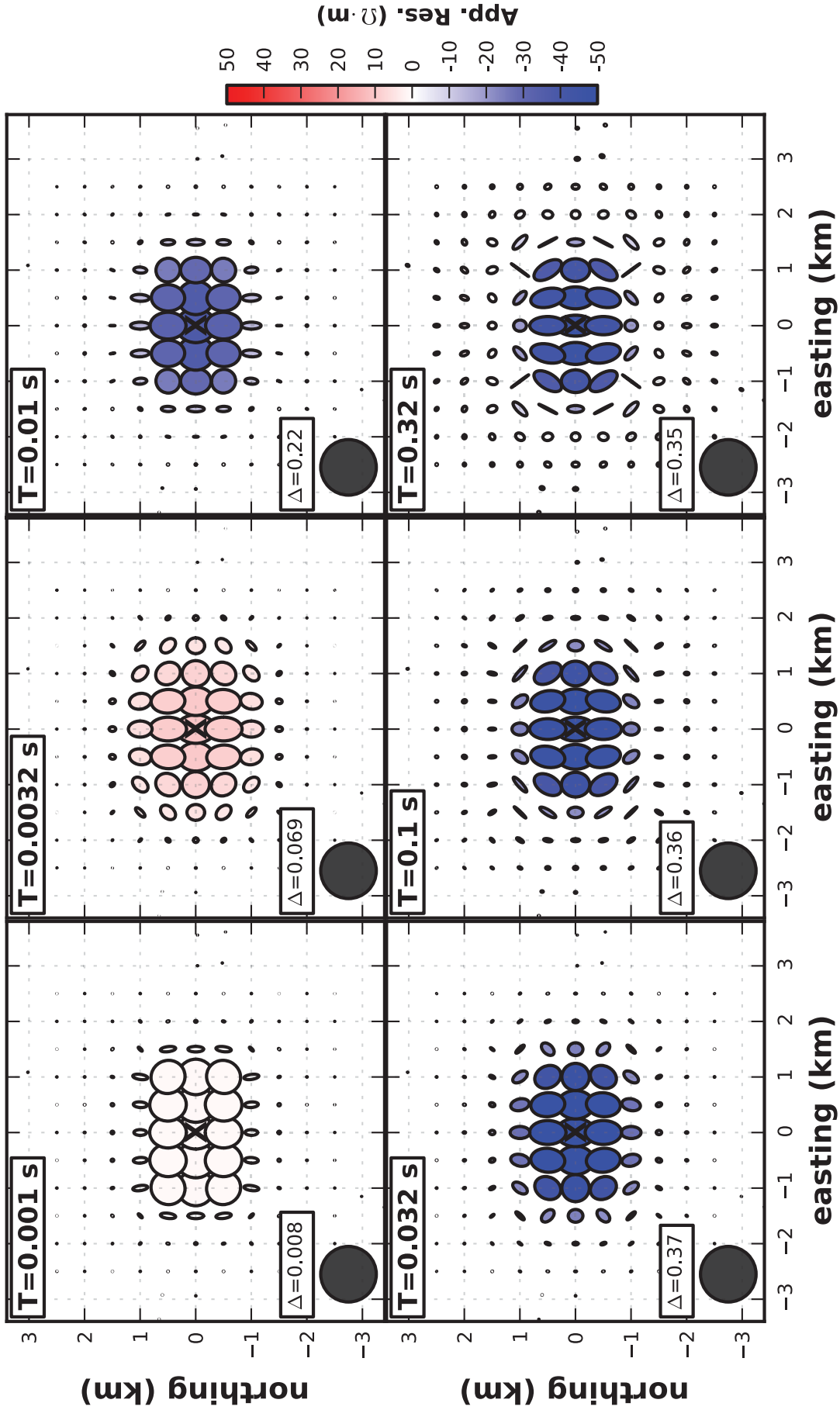

Figure 4.6: Maps of resistivity tensor residuals of a conductive body (2 km x 2 km x 500 m, ρ = 10000 Ω·m) introduced into a half space (ρ = 100 Ω·m) at 1 km depth. Each plate maps a different period (s) labeled in the top left. Also, the ellipses are normalized to the maximum of ρ_{max} for that period for easier visualization, the scale is in the lower left. Ellipses are colored by the residual of resistivity tensor determinants, indicating a conductive or resistive change.

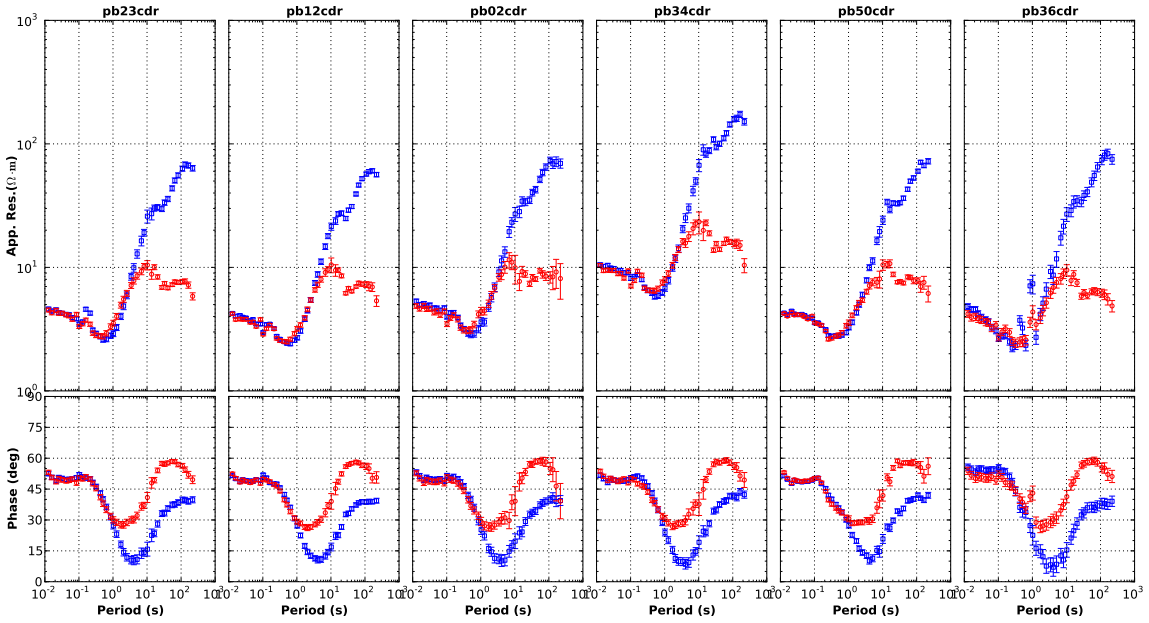

Figure 4.7: Selected stations within an 1000 m radius of station pb34. This exemplifies the utility of spatial filtering of static shifts. The correction is displayed in Figure 4.8.

apparent resistivity curves in log-log space eq. (4.15), where $\hat{\mathbf{Z}}_o$ is the true impedance tensor and the frequency independent distortion tensor $\hat{\mathbf{D}}$ is $\in \mathbb{R}^2$.

$$\hat{\mathbf{Z}} = \hat{\mathbf{D}}\hat{\mathbf{Z}}_o \tag{4.15}$$

Multiple methods have been developed to remove static shift. Jones (1988) suggests pinning an assumed homogeneous layer resistivity to adjust resistivity curves. Kaufman (1988) suggests estimating a spatial response to remove static shift, while also stating that other electric and electromagnetic information is necessary to reduce the influence of static shift. Pellerin & Hohmann (1990) suggests using transient electromagnetic techniques to get an absolute resistivity measurement of the near surface, then fitting the apparent resistivity curves estimated by MT. Berdichevsky & Dmitriev (2008) suggests a spatial filter to remove static shift. This version of this static shift removal is utilized in this project because station spacing is relatively close. Static shifts are removed by the following method. Estimates of the median of each polarization of the apparent resistivity for stations within a given radius is compared to each station within that radius for a defined period range. If the difference is larger than a given tolerance than the difference is assumed to be a static shift and is removed from the two components of $\hat{\mathbf{Z}}$ for that polarization. An example is given in Figure 4.8.

4.3.1 Removal of Galvanic Distortion

A different method to remove galvanic distortion has been suggested by Bibby *et al.* (2005), which exploits phase tensor representation of the MT response (Caldwell *et al.*, 2004). Here, two dimensionality estimations locate parts of the MT response that are 1D, 2D or 3D to estimate distortions, though one should be careful interpreting a single site because a site along a principle axis of a 3D body can appear 2D. Therefore, it is imperative to compare dimensionality of neighboring sites. One dimensionality parameter is nominated ellipticity, defined as eq. (4.10). The ellipticity describes the

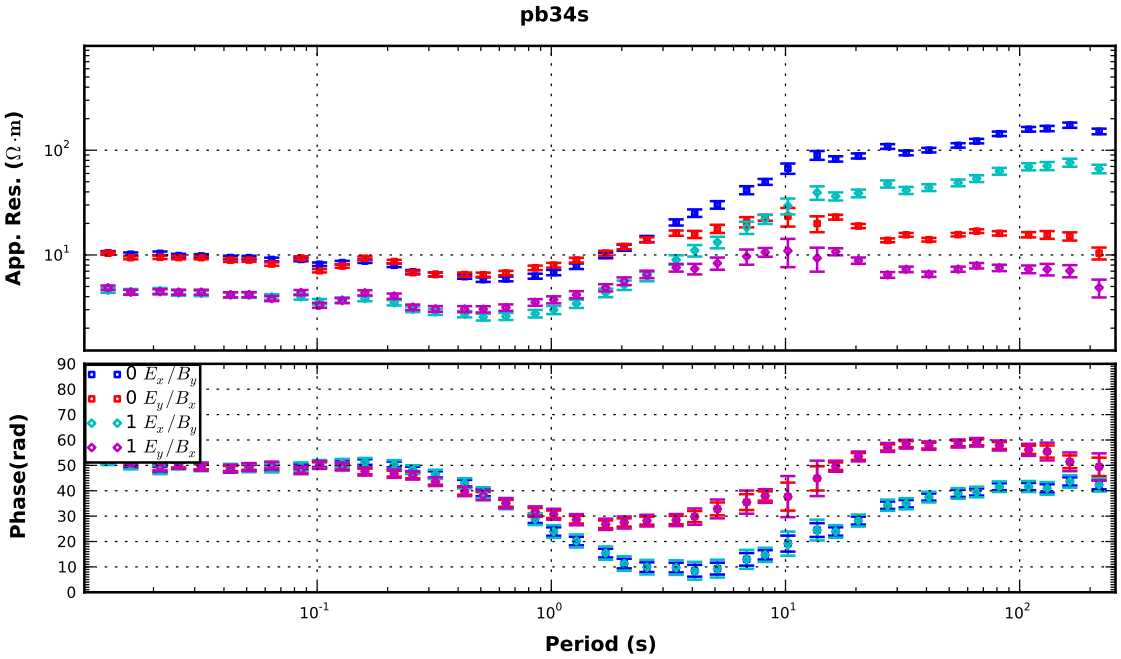

Figure 4.8: Figure showing the removal of a static shift using a spatial median filter. At first glance the apparent resistivity curves do not appear to be affected by static shift (blue and red), but comparing the curves to near by sites suggest static shift. The resulting curves are cyan and magenta. Notice that the phase is not changed.

difference between preferential current flow along principle axes. If the system is 1D than the ellipticity will be identically 0, and the phase tensor will be a circle. Another parameter is the skew angle eq. (4.5), which is an estimation of 3D conductivity structure, namely how currents are deflected due to heterogeneous geoelectric structure.

The first thing to note is that galvanic distortion is assumed to be real and frequency independent, therefore $\hat{\mathbf{Z}}$ is effected by a scaling tensor $\hat{\mathbf{D}}$ eq. (4.16) and eq. (4.17).

$$\hat{\mathbf{X}} = \hat{\mathbf{D}}\hat{\mathbf{X}}_R \tag{4.16}$$

$$\hat{\mathbf{Y}} = \hat{\mathbf{D}}\hat{\mathbf{Y}}_R \tag{4.17}$$

Solution of eq. (4.16) or eq. (4.17) depends on the dimensionality. Though Bibby *et al.* (2005) explains galvanic distortion removal for all three dimensions, only the 1-D case is used in this project and will be explained. For the 1D case $\beta = 0$ and $\eta = 0$ and eq. (4.16) can be written as eq. (4.18) or eq. (4.19), where g is the 1D regional impedance tensor and is indeterminable without other geophysical information.

$$\hat{\mathbf{X}} = g\hat{\mathbf{D}}\begin{bmatrix} 0 & 1 \\ -1 & 0 \end{bmatrix} \tag{4.18}$$

$$\hat{\mathbf{Y}} = g\hat{\mathbf{D}}\begin{bmatrix} 0 & 1 \\ -1 & 0 \end{bmatrix} \tag{4.19}$$

Equation eq. (4.18) and eq. (4.18) have determinable solutions up to the scaling factor g, which is a static shift. The solution can depend on the coordinate representation of $\hat{\mathbf{Z}}$, therefore an invariant constraint on the solution is desirable. Bibby *et al.* (2005) explains these invariant constraints in greater detail, here the constraint used is $det[\hat{\mathbf{D}}] = 1$. This constraint assumes that the determinant of $\hat{\mathbf{Z}}$ is constant under the

influence of distortion. With this constraint g can be estimated and removed from $\hat{\mathbf{X}}$ eq. (4.20) and $\hat{\mathbf{Y}}$ eq. (4.21).

$$\hat{\mathbf{X}}_s = \frac{\hat{\mathbf{X}}}{\sqrt{det[\hat{\mathbf{X}}]}} \cdot \begin{bmatrix} 0 & 1 \\ -1 & 0 \end{bmatrix} \tag{4.20}$$

$$\hat{\mathbf{Y}}_s = \frac{\hat{\mathbf{Y}}}{\sqrt{det[\hat{\mathbf{Y}}]}} \cdot \begin{bmatrix} 0 & 1 \\ -1 & 0 \end{bmatrix} \tag{4.21}$$

Finally, these can be used to estimate $\hat{\mathbf{D}}$ as eq. (4.22) for a period range $[p_i : p_f]$ where the MT response is 1-D. It should be noted that real data will have some noise, so the constraint on ellipticity will need to relaxed to a reasonable threshold, such as $|\eta| < 0.1$.

$$\hat{\mathbf{D}} = mean(\hat{\mathbf{X}}_S[p_i : p_f] + \hat{\mathbf{Y}}_S[p_i : p_f]) \tag{4.22}$$

The effect of distortion removal can be exemplified with a real example. The MT response from a survey collected in Antarctica is displayed in Figure 4.9. Here the overburden is crevassed ice thousands of years old that is between 0.5-3 km thick, needless to say the conductivity structure is complex and susceptible to static shifts and heterogeneities in the ice. The period range of 1-10 s is estimated as 1-D and used to calculate $\hat{\mathbf{D}}$. When $\hat{\mathbf{D}}$ is removed from the data, the resistivity curves pinch together at periods where they are 1-D. Notice the phase changes very little for this case, but the error bars increase. This is because information is essentially removed from the estimation of $\hat{\mathbf{Z}}$, therefore the uncertainty increases. As Bibby *et al.* (2005) states, 'Distortion removal should be used as a routine process in the analysis of MT data,' as it is a simple yet robust method to estimate the regional MT response.

4.4 Summary

Analysis of the MT response is a crucial step before making any interpretations or modeling the data. Two different tensor representations have been discussed, which provide information about dimensionality of subsurface geoelectric structure. The phase tensor is insensitive to near surface distortions, making it a powerful representation of the MT response, especially when comparing collocated temporally spaced measurements. Residuals of the phase tensor infer orientation and depth of subsurface changes while residual resistivity tensors indicate a conductive or resistive change. These two tensor representations should be used as a complimentary pair to estimate variations in subsurface resistivity structure between measurements. Two different methods have been reviewed to remove near surface distortions and static shift, which can severely bias interpretation. All MT responses estimated in this project have had the distortion removal technique applied and any static shift removed by the aforementioned spatial median filter.

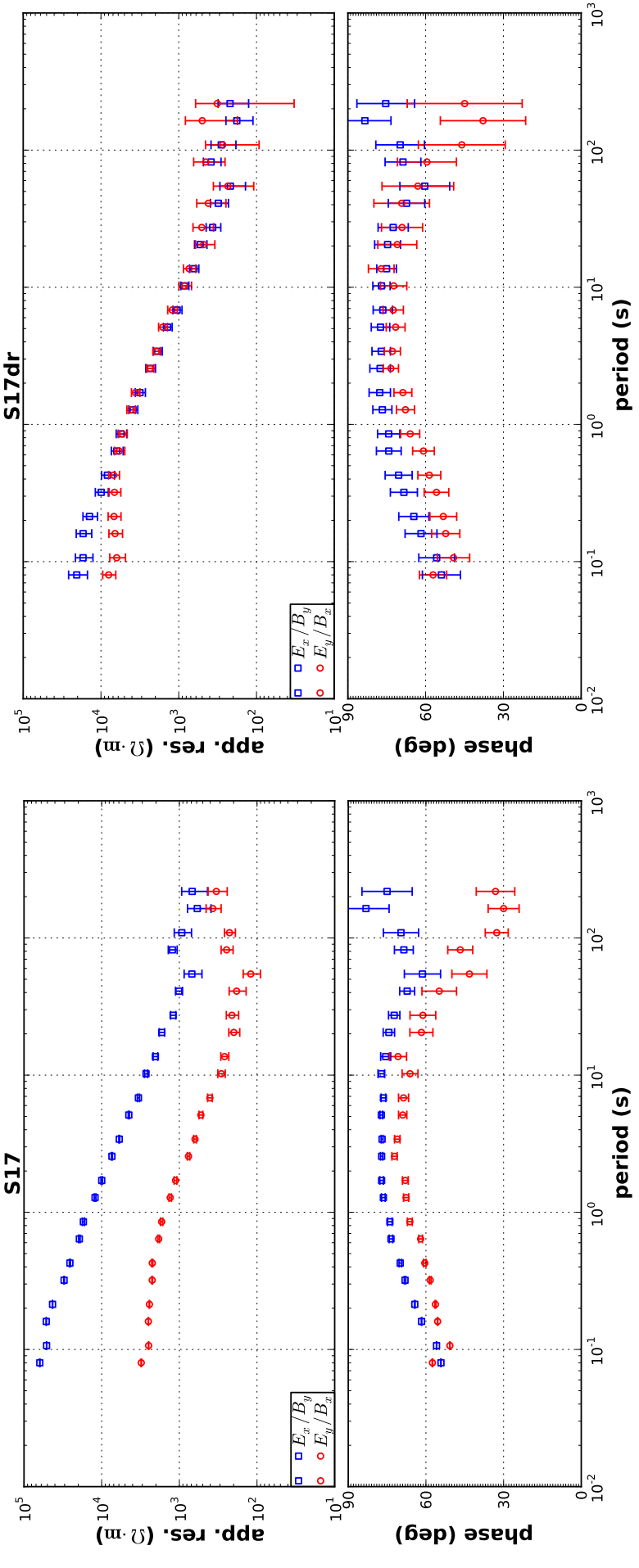

Figure 4.9: Example of removing galvanic distortion outlined in the text. The original curves are on the left, while the regional curves are on the right where distortion has been removed. Notice the two curves are pinched together, but the error bars are larger.

Part II

MT Monitoring

Chapter 5

Background Information

This chapter contains a few sections of background material that is pertinent to this experiment. First the basics of geothermal, specifically EGS, are discussed. Next, the regional geology around Paralana is reviewed. Then, the survey layout and design is described followed by a discussion on the regional resistivity structure at Paralana found from 2D and 3D inversions of pre-injection data.

5.1 Geothermal Basics

Two basic types of geothermal sources exist: magmatic and amagmatic. Each of these can be subdivided into two basic geothermal classifications: thermal reservoirs and hot dry rocks. Thermal reservoirs are typically heated by volcanic activity or zones of volcanism (Elder, 1981) and, as the label implies, fluids reside in a porous medium with permeability such that the fluids can flow. Hot dry rocks are quite the opposite. These rocks are hot, usually due to a combination of the Earth's natural heat gradient and radioactive decay from radiogenically enriched lithology in the upper crust, however no fluids are present because the hot rock has small porosity with minimal permeability. Therefore, to function as a geothermal resource fractures need to be induced to create artificial porosity and permeability through which the fluids can flow (Dash *et al.*, 1981).

This is a rather novel idea and was first thoroughly tested at Fenton Hill, New Mexico, USA, near the Los Alamos National Laboratory (Purtymun *et al.*, 1974; Dash *et al.*, 1981; Brown, 1995; Duchane & Brown, 1997; Tester *et al.*, 2006). After years of testing the site was abandoned as political patience, interest and funding ran out. Note the era in which Fenton Hill was being developed, late 1970's to early 1980's, right around the time of the first oil crisis. Peculiar how big oil and particulary automotive lobbyists have shaped the petroleum based economy in such a way that alternative energy can be pushed by the wayside with a golden carrot (McElroy, 2006). Nevertheless, the pilot project at Fenton Hill stimulated interest and investment throughout the world.

A few of the larger EGS projects have had enticing success, namely Rosemanowes in England; Hijiori and Ogachi in Japan; and more recently Landau in Germany; Soultz in Switzerland and Cooper Basin in Australia (Tester *et al.*, 2006). Nearly 100 new geothermal projects are underway as of 2008 (Biello, 2008), showing support for the potential of EGS. Optimistically, the US has pledged over $300 million (RenewableEnergyWorld.com, 2010), while the Australian government has also pledged over $111 million AUD through Federal and state grants (Goldstein *et al.*, 2008). In Australia alone, if only 2 percent of the potential heat at 5 km depth can be harnessed it could

generate power for all of Australia for the next 50,000 years. The potential for geothermal energy to reduce fossil fuel power production is there, unfortunately the political and economic force of inertia is strongly bound by the paper note.

5.1.1 Enhanced Geothermal Systems

An EGS has a basic setup of a two well system, one for injecting fluids and the other to extract fluids (Figure 5.1). The first process completed after the injection well is drilled is hydraulic stimulation of the hot rock to generate a fracture network that is porous and more importantly permeable (Carden *et al.*, 1985). Hydraulic stimulation can take a long time, sometimes the order of a month or two of constant fracturing (Yoshioka *et al.*, 2009). Once a suitable reservoir is developed an extraction well is drilled, where geophysical surveys can optimize the well location (Onacha *et al.*, 2009, 2010).

The next step in realizing an EGS is being able to flow fluids from one well to the other, which can prove to be difficult if the subsurface structure is poorly understood. The final step is to install infrastructure that will convert thermal heat from extracted fluids into useable energy. Different types of energy conversion can be employed. One idea is to use the geothermal energy to heat or cool buildings (Lund *et al.*, 2004), which is the largest sink on the power grid. The other main idea is to use the geothermal energy to run turbines which can advantageously generate base-load electricity. The idea is not new, base-load generation was realized in the 1980's using binary cycle turbines (Lacy & Jacobson, 1980), just the monetary based argument of investment versus return has slowed development. Bertani (2005) reveals geothermal development up to 2005 experienced minimal growth since 1975, while Bertani (2012) demonstrates growth in geothermal since 2003, showing optimism in the future of geothermal production.

Typical EGS are located in areas where thermally enhanced basement rock is overlain by thick blanketing sediments. A good working example of an EGS is in Soultz-sous-Forêtz near Alsace, France. The heat source is a young amphibole rich granite that intrudes an older porphyritic granite within the Rhine Graben. These crystalline rocks are overlain by 1400 m of sediments (Hooijkass *et al.*, 2006). Similarly, the initial EGS test site at Fenton Hill, situated next to the Valles Caldera, sat atop a series of tuffs and sedimentary rocks underlain by a highly jointed Precambrian complex of metamorphic and plutonic lithology located below 2700 m (Purtymun *et al.*, 1974). The site at Paralana, South Australia, lies above the hottest non-volcanic rocks in the world. The geologic setting is similar to that at Soultz, in which a graben structure is filled with over 4000 m of sediments overlaying thermally charged crystalline rock, see Section 5.2. All of these systems have similar, but unique, geology making it difficult to prescribe one recipe for EGS success.

5.1.2 Geothermal and Micro-Seismic

The main geophysical tools for characterizing and monitoring geothermal reservoirs are passive micro-seismic methods that record micro-earthquakes (MEQ) generated from hydraulically generated fractures (Tester *et al.*, 2006). Usually setup in an array including downhole instruments, micro-seismic techniques employ tomography to locate MEQ associated with fractures opening (Douglas, 1967), typically within 200 m at depths of 5 km (Lou & Rial, 1997). House (1987) showed micro-seismic can be used in crystalline rock where most EGS systems are proposed to exist. Lou & Rial

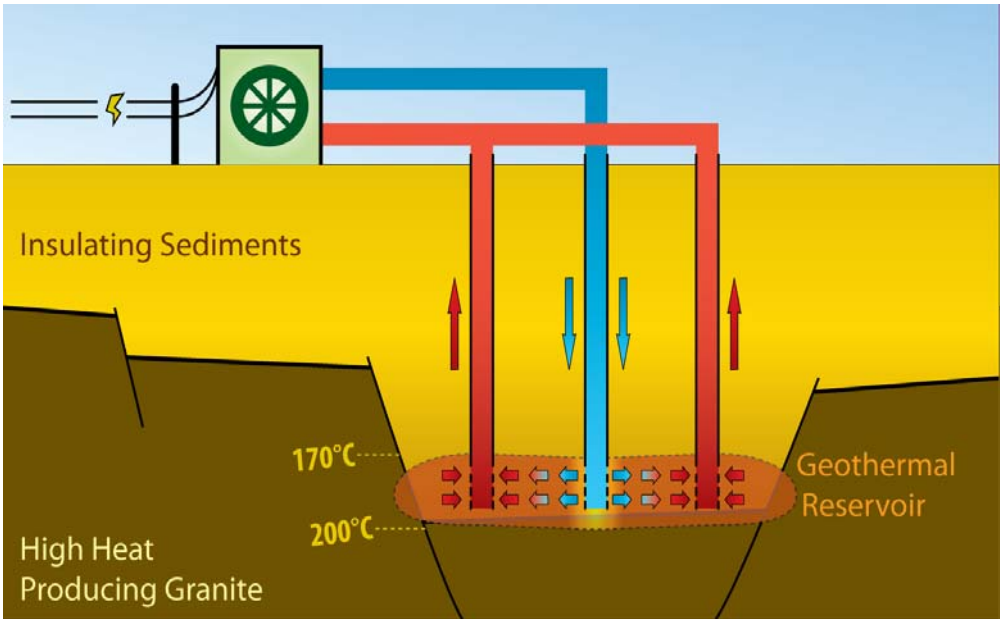

Figure 5.1: A schematic of the proposed EGS system at Paralana, South Australia. Cold water (20^o C) is injected into a hydraulically fractured reservoir where it absorbs heat generated from radiogenic granites buried beneath 4 km of sediments. The hot water is then pumped out at a temperature of $\sim$ 180^o C in the form of steam to run a binary cycle turbine for electricity generation. The water is recycled by pumping it back into the reservoir after the heat is extracted. (From http://www.petratherm.com.au/projects/paralana)

(1997) and Elkibbi & Rial (2005) demonstrate micro-seismic to be a viable method for characterizing geothermal reservoirs and Phillips *et al.* (2002) gives six examples of MEQ patterns in subsurface reservoirs. Warpinski (2009) demonstrates the utility of simultaneous interpretation of micro-seismic data, rock mechanics and well completion data. Crampin & Peacock (2005) give a detailed review on shear-wave splitting in micro-seismic data caused by fractures dilating in an anisotropic media. Shear-waves propagate with two distinct polarizations, one parallel to the major stress axis and the other perpendicular to the major stress axis. When a fracture opens in a material these two shear waves propagate at different velocities and are recorded at different times. The time difference is related to the density of fractures along the path length. The angle of rotation, as measured relative to the vertical component, characterizes the orientation of the fracture system (Rial *et al.*, 2005). Though micro-seismic tomography can infer location, size and shape of fractures opening, it does not directly measure fluid inclusion nor connectivity to other fractures. This is why other geophysical methods, such as EM techniques, need to be employed to constrain fluid location.

5.1.3 Geothermal and MT

Using MT to explore geothermal areas is not a novel idea (Gamble *et al.*, 1981; Anderson *et al.*, 1995). However, most geothermal exploration done by MT is in volcanic zones, which has characteristic signature of a conductive clay cap and resistive magma chamber (Haak *et al.*, 1989; Lagios *et al.*, 1994, 1998; Jones *et al.*, 2008; Oskooi, 2006; Garg *et al.*, 2007; Heise *et al.*, 2008; Asaue *et al.*, 2006; Aizawa *et al.*, 2005; Hill *et al.*, 2009). Because EGS is just being commercially realized, few have used MT in EGS zones. In the last decade, Wannamaker *et al.* (2004); Newman *et al.* (2005, 2007, 2008) have shown MT to be viable as an exploration and characterizing tool for volcanic systems. The advantage of MT is that it is sensitive to conductivity changes, which

is important for delineating geometry of thermally and electrically conductive fluids flowing through resistive host rocks. Spichak & Zakharova (2009) gives an overview of EM methods used for geothermal measurements.

Many MT surveys have been collected over volcanic systems. Hill *et al.* (2009) characterizes deep magmatic chambers beneath Mount St Helens in 2D, showing a deep connection with nearby volcanic systems. Jones *et al.* (2008) use 10 MT sites to do 3D inversion, using the code of Siripunvaraporn *et al.* (2005), and finding a more extensive thermal network than previously suspected at Mount Ruapehu, New Zealand. A more extensive 3D modeling of MT data in a highly 3D geologic setting is given by Heise *et al.* (2008). They use phase tensor information to interpret geologic structure. Also, Heise *et al.* (2008) estimate residual phase tensors, similar to eq. (6.1), between the model and data to characterize areas where the model fits the data poorly (large residual phase tensor). These are only a few examples to show that different methods can be used to interpret geological structure of geothermal systems using MT data. However, the combination of multiple geophysical techniques can be advantageous.

Haak *et al.* (1989) provides a detailed analysis of one dimensional MT data from the Island of Milos, circa 1986. Their goal was to map geothermal fluids and came to the conclusion that high-frequency data (above 1 Hz) characterizes near surface resistivities well, whereas low-frequencies delineate the conductive clay cap and the magma chamber boundaries well. They also provided an attempt to relate temperature, porosity and resistivity together to get spatial information about the geothermal fluids, which produces general results with large uncertainty in location.

Using rotation angles and 1D inversion, Lagios *et al.* (1994) give evidence for correlation between micro-seismic measurements and MT measurements on Kos Island, Greece. Similarly, Lagios *et al.* (1998) extend the MT processing and interpretation to 2D, showing similar results to Lagios *et al.* (1994). They demonstrate dimensionality factors like skew and eccentricity can characterize dimensionality and geoelectric structure in volcanic systems. These dimensionality estimations are important in geothermal systems as they aid in delineating geoelectric structure that fluid pathways might follow. Similarly, the correlation with micro-seismic measurements magnifies the need for complimentary geophysical techniques to characterize geothermal systems as each are sensitive to different physical properties.

Aizawa *et al.* (2005) demonstrate that MT and SP can be used to characterize volcanic geothermal areas. They find a positive SP response under the summit of Mount Fuji, Japan, that correlates well with a conductive anomaly estimate from 2D MT modeling. They conclude from the correlation of the strong SP response and the conductive anomaly that the the area is an active geothermal system. Similarly, Garg *et al.* (2007) suggests that SP, direct current (DC) and MT should be used together to characterize geothermal areas by showing none can uniquely characterize multiple electrical properties of geothermal reservoirs. Once again, the combination of different geophysical techniques aid in constraining geothermal systems.

5.1.4 Geothermal and Seismoelectric

Though the seismoelectric effect is not examined in this study, the phenomena should be studied more rigorously within the context of fracture stimulation, therefore it is briefly mentioned here. Coexisting seismic and electromagnetic responses due to fluids moving in a porous media is of great physical interest. Pride (1994) formally define acoustic and electromagnetic coupled systems, leading to Pride & Haartsen (1996) formally defining electroseismic wave propagation in an anisotropic heterogenous media. Frenkel (2005)

translates Ivanov's theory of seismoelectric processes in a moist soil and expands on electric fields induced by elastic vibrations. The basic theory is that fluidic bound charges adsorbed onto the lithologic matrix are counter balanced by a diffusive array of oppositely charged ions, forming a double layer. When a pressure gradient is applied the diffusive layer of ions will move in response creating a separation of charge and thus an electric field.

Haartsen & Pride (1997) develops numerical modeling techniques for seismoelectric measurements and finds three types of seismoelectric responses. The first is related to an acoustic wave which pushes charges resulting in an electric response with similar frequency and velocity of the inducing wave. The second is related to shear waves which generate a sheet of charges that induces a current and a small magnetic field, again with similar frequency and velocity as the inducing wave. The third type is related to seismic waves at a boundary of contrasting electrical and other material properties. The boundary can be modeled as a dipole which radiates an electric field that travels near the speed of light. Haines & Pride (2006) and Haines *et al.* (2007) extend numerical modeling and shows proof of concept with a field experiment aimed at imaging shallow sandy reservoirs. Dupuis *et al.* (2009) gives encouraging results of borehole measurements similar to a vertical seismic profile. Gharibi *et al.* (2003) gives a good overall review of seismoelectrics for monitoring oilfield reservoirs. de Ridder *et al.* (2009) describes a novel method of using Green's function interferometry to extract more information from seismoelectric measurements. The seismoelectric effect has not been studied within the context of geothermal because feasibility studies suggest the signal will be much too small to measure. However, seismoelectric has the potential suggest not only location of fractures but whether fluids are included in those fractures. The unfortunate reality is that EGS systems are typically at a depth of $\sim$5 km and the seismic response from a fracture opening at that depth is on the order of 0 on a Ricther scale. At present instruments cannot discriminate this signal from noise, but instrumentation is always getting better, perhaps someday.

5.1.5 EGS and MT

Newman *et al.* (2005, 2007, 2008) extend interpretation of the Coso geothermal field in Wannamaker *et al.* (2004) by conducting a 3D inversion of 125 MT sites in the frequency band of $250-.3$ Hz. Their main goal is to map fractures containing geothermal fluids by estimating anisotropy in the MT response; unfortunately they could not sufficiently do this due to data resolution being lower than fracture scales and non-uniqueness of the model. A general conclusion from this result is that MT surveys need to be designed in dense grids with fracture scales in mind. Also, MT is not great at delineating fractures that are smaller than the skin depth. However, they were able to delineate major fault structures controlling geothermal fluid flow. Also, their models of high conductive zones compare well with MEQ clouds estimated from micro-seismic tomography. This infers that areas of multiple seismic events are most likely fluid filled as they are found to be conductive. In performing the 3D inversion, they found that good starting 2D models of just the TM mode are necessary to steer the 3D inversion towards a global minimum. Finally, they conclude that much more work needs to be done on 3D imaging of geothermal reservoirs with MT.

Bedrosian *et al.* (2004) conducted one of the first MT surveys designed to monitor transient changes in the MT response caused by a fluid injection for an EGS. Two MT stations plus nine electric stations where set out in an L shape near the injection well for a total of eleven MT stations, where the MT response for the nine electric

stations is estimated using magnetic field data from the MT stations. They modeled the data before and after the injection to estimate any changes, but found that cultural noise levels were too high to confidently estimate changes. A forward modeling exercise preformed by Bedrosian *et al.* (2004), suggests that a conductive sphere with a diameter of 1 km at 3 km depth could be measurable from MT soundings.

5.2 Regional Geology at Paralana, South Australia

In the Northern Flinders Ranges of South Australia resides Paralana Hot Springs, the one of the only known springs in the world heated by an amagmatic source (Spriggs, 1984). Anomalous surface heat flow in parts of the Flinders Ranges can be as high as 110 mW/m^2, where typical continental heat flow is about 40 mW/m^2 depending on age (Neumann *et al.*, 2000), making it a target location for EGS (Hillis *et al.*, 2004). The Mount Painter Domain (MPD) is the underlying heat source, which is composed of Paleoproterozoic to Mesoproterozoic gneisses and granites that are innately rich in radiogenic elements (Brugger *et al.*, 2005), with an average of 30 ppm of uranium (Idnurm & Heinrich, 1993). The MPD is overlain by the Adelaide Geosyncline composed of Neoproterozoic to Mesozoic metasediments. Both where deformed during the Delamerian orogeny of the Cambro-Ordovician (Preiss, 1990). Evidence for high-grade metamorphism during the Delamerian orogeny is restricted to the MPD where amphibolite facies are observed in Adelaidean sediments near the MPD contact (Coats & Blissett, 1971; Richert, 1976; Sandiford *et al.*, 1998).

Local stress fields around Paralana are poorly characterized, however the regional stress field has been estimated to be a strike-slip regime (Hillis & Reynolds, 2000; Hillis *et al.*, 2008). From deep earthquakes Love *et al.* (2006) estimate maximum compressive stress be near horizontal trending 101 degrees east from North and plunging 16 degrees from horizontal. The intermediate compressive stress trends 18 degrees from east of North, plunging 55 degrees from horizontal (Love *et al.*, 2006). Geoelectric strike analysis using the azimuth of the phase tensor and the strike angle found from invariants of the impedance tensor show the general geoelectric strike to be parallel with geomagnetic North or 9 degrees east of North (Figure 5.6). This is perpendicular to the maximum compressive stress. Interestingly, induced fractures from hydraulic stimulation at Paralana (measured from micro-seismic tomography) tend to open perpendicular to regional maximum stress.

The Paralana fault system structurally bounds the eastern margin of the MDP (Figure 5.2), thrusting eastward over Mesozoic and Triassic sediments of the Lake Frome embayment, separating the Adelaide Geosyncline from the Curnamona Province (Coats & Blissett, 1971; Sandiford *et al.*, 1998). The Paralana fault system has been intermittently active since the Middle Proterozoic, where reverse, strike-slip, reverse-thrust, oblique-slip and normal movement have been reported (Foster *et al.*, 1994; Preiss, 1993; Teale, 1993), where current movement along the Paralana fault is reverse (Spriggs, 1984). Interestingly, Paralana Hot Springs lies within a dilated extension of the Paralana fault system (nominated the Lady Buxton Fault), however the water source has not been well studied but is assumed to be surface runoff as no deep connection has been found.

The Lake Frome embayment overlays the MDP to the East creating a thermal blanket to trap heat generated from radioactive decay. It also marks the southern edge of the Late Triassic to Late Cretaceous Great Artesian Basin (Cox & Barron, 1998), which is important for regional hydrological systems. The Mesozoic strata of the Lake Frome embayment is composed of marine sediments overlain by fluvial and lacustrine

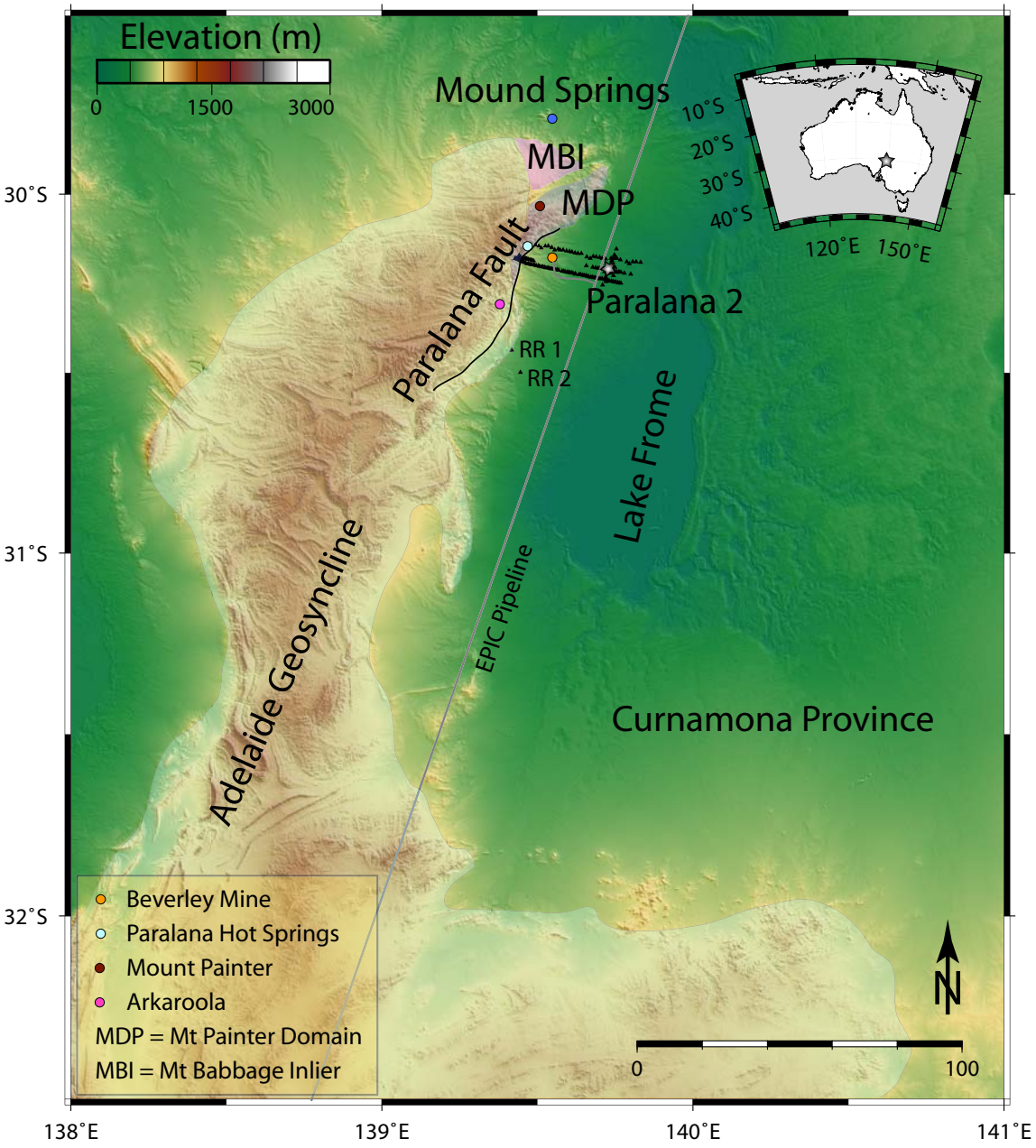

Figure 5.2: Regional map of Paralana, South Australia near the Flinders Ranges (elevated area under the Adelaide Geosyncline label). The underlying image is a digital elevation model overlain with important geologic units and structures. The inset at the top right locates Paralana relative to the whole of Australia. The MDP has heat flows of up to 110 mW/m^2, which is exposed in the north but buried towards the east under Paralana 2 borehole by 4 km of Adelaidean sediments and strata of the Lake Frome embayment. The southern edge of the Great Artesian Basin extends just south of Paralana and has surface representation at Mound Springs to the north. Paralana Hot Springs lies in a dilated portion of a portion of the Paralana Fault known as the Lady Buxton Fault due east of Paralana 2. Interestingly, no evidence has been produced to suggest a deep water source for the PHS, implying that the source is surface runoff. The station locations are marked as triangles and remote reference stations labeled as RR. The cross pattern are stations from this project, the long line to the South is the Quantec line and the line to the North was collected in May, 2012 as part of an honors project.

deposits. Tertiary strata is characterized by fluvial and lacustrine deposits, including the Bulldog Shale, Eyre Formation and Namba Formation. This is topped by deep chemical weathered layers of duricrust and silcrete. Tertiary and more recent tectonic movement is responsible for present topographic relief of the Northern Flinders Ranges

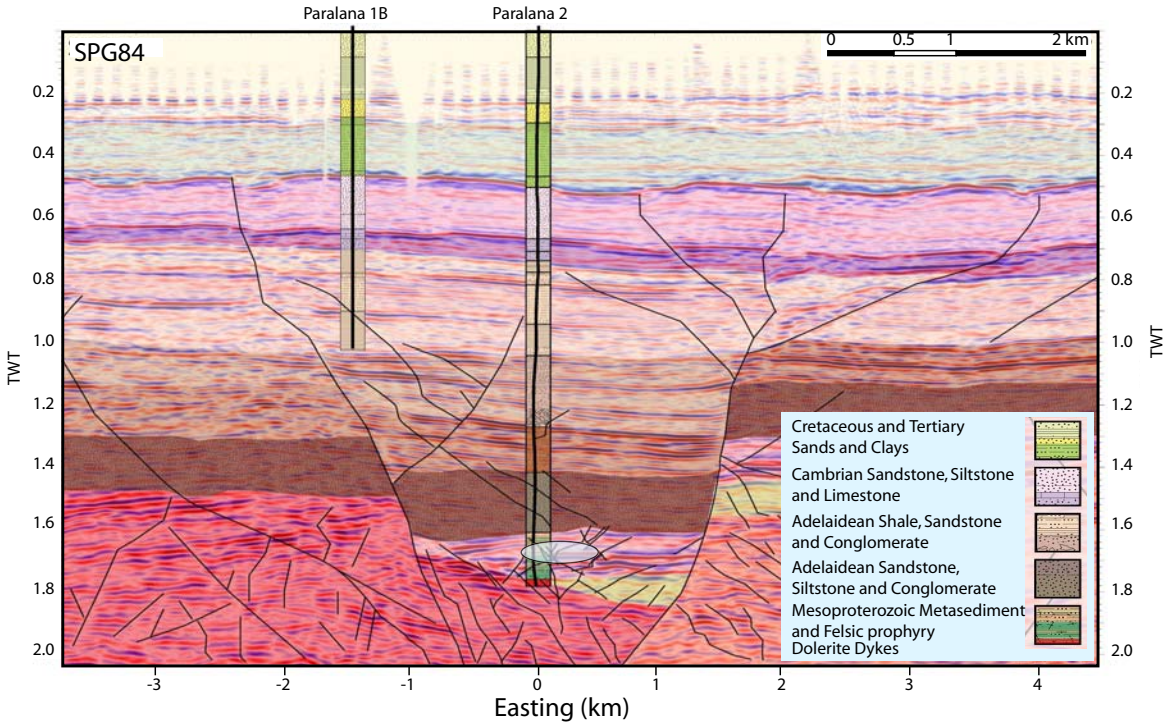

Figure 5.3: Local stratigraphic and structural elements near Paralana, interpreted from seismic and borehole data by Petratherm. Notice the graben structure into which Paralana 2 was drilled. The perforation zone and proposed reservoir is located by the blue ellipse at 1.7s (3680 m).

and neighboring Lake Frome. Uplift and resulting drainage of uranium bearing breccia is the most likely explanation for the uranium rich Tertiary Beverley sands.

At the Paralana geothermal drill site, the measured heat flow is 113 mW/m^2 (Neumann *et al.*, 2000). Here, the basement has been uplifted, while the sediments have been down faulted forming a graben type structure in which Paralana 2 has been drilled to 4012 m and cased with steel to 3725 m (Figure 5.3). Bottom hole temperature is estimated to be 190 C. Saline fluids ($\rho = 1.5$ Ω·m) were encountered at 3860 m indicating a pre-existing fluid filled fracture network, which could be linked with the Great Artesian Basin and could also be fed from lithospheric fluids. The interpreted stratigraphy from seismic and drill hole data are displayed in Figure 5.3 (from Petratherm). Similarly, the electrical resistivity structure is displayed in Figures 5.8, 5.9, and 5.10.

5.2.1 Survey Layout

The survey layout is based on existing roads from previous seismic surveys (Figure 5.4), which fortuitously aligns with regional geoelectric strike, NNE (9 degrees west of North). Two main orthogonal profile lines containing 22 sites each run NNE and WNW centered on Paralana 2 borehole. Also, two off-diagonal lines of 6 stations each, aid in constraining 3D changes in resistivity structure. Stations are set out with variable spacing that begins at 200 m near the borehole and increases to 1.5 km at the extremities; this is to get dense coverage near the borehole where larger changes are assumed to occur while getting estimates of any regional changes. Two remote reference stations are located 60 km and 80 km south of Paralana along regional roads. Surface topography is minor with a max elevation variation of 10 m and vegetation is usually sparse unless unseasonable rains fall like in 2010-2011, then knee high grasses sprout up. The EPIC gas pipeline runs parallel to the NNE line offset 2 km to the west, with a junction that runs to Beverley Mine near the southern extremity.

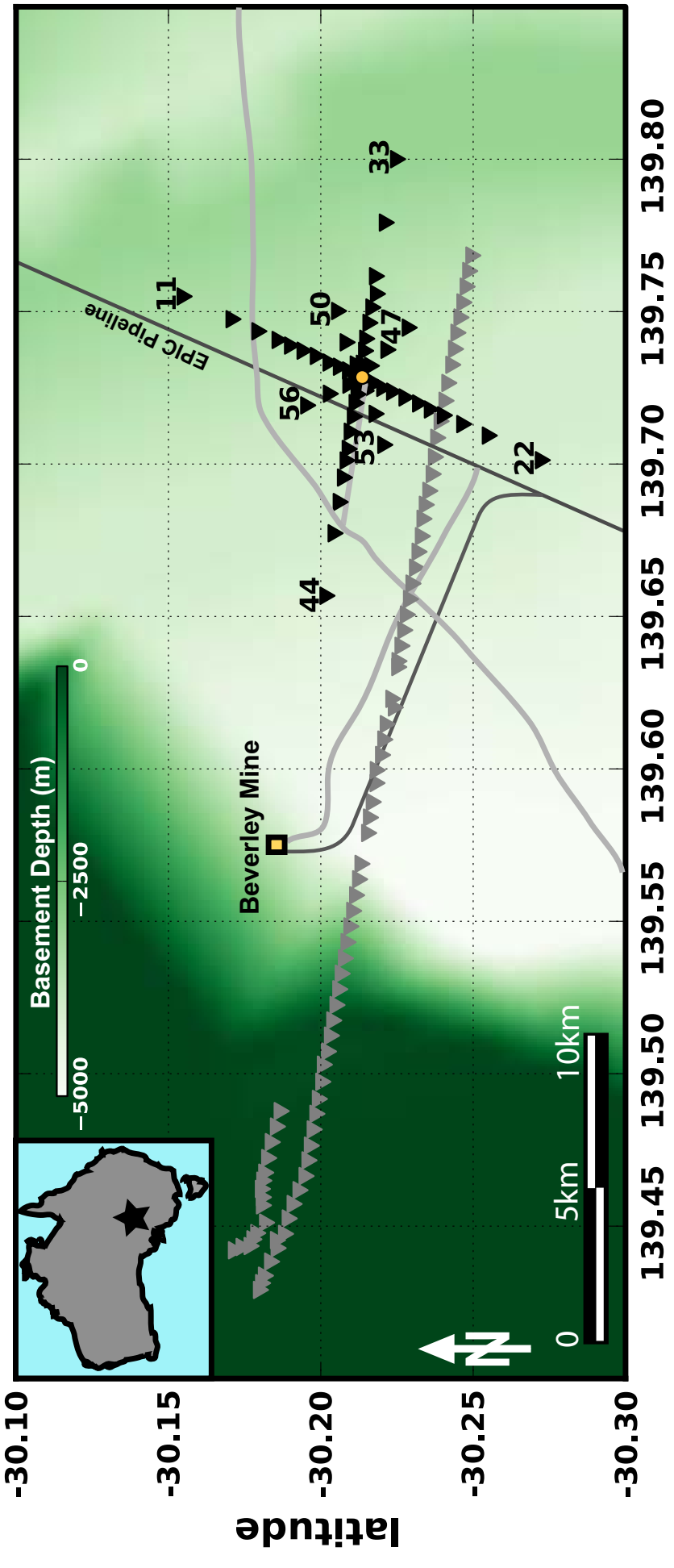

Figure 5.4: Map of survey layout. Two main MT lines are centered on Paralana 2 borehole (orange circle) contain 22 stations (black triangles) each numbered in descending order from extremity stations, and two off diagonal lines contain 6 stations each to constrain 3D resistivity structure. An MT survey collected by Quantec in 2006 for Petratherm is plotted as gray triangles. Roads are in light gray and Beverley Uranium mine is plotted as an orange box. The EPIC gas pipeline is drawn in as dark gray. The inset map of Australia locates Paralana as a black star. The base image maps basement depth (m) estimated from gravity data.

Station	Latitude	Longitude	Easting	Northing	Zone
pb01	-30.21071	139.72933	377701.57	6657183	54J
pb02	-30.20881	139.73071	377832.04	6657396.05	54J
pb03	-30.20581	139.73193	377945.78	6657728.95	54J
pb04	-30.20243	139.73331	378074.45	6658105.02	54J
pb05	-30.19824	139.73547	378277.22	6658572.02	54J
pb06	-30.19389	139.73719	378437.46	6659056.05	54J
pb07	-30.18977	139.73887	378594.14	6659514	54J
pb08	-30.18569	139.74071	378766.29	6659968.01	54J
pb09	-30.17907	139.74356	379032.59	6660705.03	54J
pb10	-30.17058	139.74752	379403.55	6661650.02	54J
pb11	-30.15392	139.75498	380101.74	6663503.99	54J
pb12	-30.21471	139.72770	377549.62	6656738.95	54J
pb13	-30.21730	139.72656	377443.11	6656450.02	54J
pb14	-30.22004	139.72499	377295.4	6656145	54J
pb15	-30.22327	139.72375	377180.06	6655786.03	54J
pb16	-30.22734	139.72185	377002.28	6655332.03	54J
pb17	-30.23180	139.71988	376818.24	6654836.06	54J
pb18	-30.23566	139.71791	376633.48	6654406.02	54J
pb19	-30.23995	139.71598	376453.13	6653928.04	54J
pb20	-30.24629	139.71310	376183.93	6653223.05	54J
pb21	-30.25468	139.70934	375832.7	6652289.01	54J
pb22	-30.27146	139.70126	375076.55	6650420.04	54J
pb23	-30.21334	139.73099	377864.59	6656893.98	54J
pb24	-30.21333	139.73289	378047.46	6656897.02	54J
pb25	-30.21409	139.73714	378457.47	6656817	54J
pb26	-30.21446	139.74111	378840.04	6656781.01	54J
pb27	-30.21552	139.74632	379342.8	6656668.95	54J
pb28	-30.21648	139.75135	379828.11	6656567	54J
pb29	-30.21798	139.75583	380261.12	6656406.04	54J
pb30	-30.21766	139.76163	380818.97	6656448.03	54J
pb32	-30.22088	139.77921	382514.83	6656109.01	54J
pb33	-30.22396	139.80001	384520.31	6655788.96	54J
pb34	-30.21202	139.72519	377304.69	6657034.03	54J
pb35	-30.21162	139.72288	377081.85	6657075.98	54J
pb36	-30.21098	139.71999	376802.87	6657144.01	54J
pb37	-30.21040	139.71557	376376.71	6657202.94	54J
pb38	-30.20937	139.71060	375897.02	6657312.02	54J
pb39	-30.20871	139.70495	375352.34	6657378.99	54J
pb40	-30.20803	139.70117	374987.62	6657449.98	54J
pb41	-30.20714	139.69557	374447.45	6657542.01	54J
pb42	-30.20576	139.68754	373672.72	6657686.96	54J
pb43	-30.20407	139.67729	372683.88	6657861.95	54J
pb44	-30.20080	139.65680	370707.17	6658202.04	54J
pb45	-30.21600	139.73222	377986.27	6656599.95	54J
pb46	-30.22141	139.73749	378500.16	6656006.03	54J
pb47	-30.22778	139.74475	379206.68	6655308.02	54J
pb48	-30.21132	139.73265	378021.89	6657118.96	54J
pb49	-30.20803	139.73993	378718.58	6657492.02	54J
pb50	-30.20461	139.75021	379703.94	6657881.95	54J
pb51	-30.21428	139.72400	377192.96	6656781.95	54J
pb52	-30.21754	139.71647	376472.25	6656412.96	54J
pb54	-30.20893	139.72604	377382.68	6657376.96	54J
pb55	-30.20251	139.72306	377087.86	6658085.02	54J
pb56	-30.19447	139.71925	376711.07	6658972.05	54J
pbrt1	-30.38133	139.41832	348028	6637898	54J
pbrt2	-30.82580	139.31666	338996	6588488	54J

Figure 5.5: Table of station locations of the repeated survey displayed in Figure 5.4. The botom 2 rows are the remote reference stations.

5.3 Geoelectric Structure at Paralana, South Australia

One of the first geoelectric parameters to understand is the electrical strike direction. This can be characterized in a few different ways. First, is decomposition of the impedance tensor (Bahr, 1988; Groom & Bailey, 1989; McNeice & Jones, 2001). Second, is by using invariants of the impedance tensor (Weaver *et al.*, 2000). Third, is by utilizing the phase tensor representation (Caldwell *et al.*, 2004). The last two methods are employed here. They find that the general strike direction is fortuitously aligned with geomagnetic North (Figure 5.6) (9 degrees west of geographic North). Interestingly, this is perpendicular to the maximum compressional stress suggesting a correlation between geoelectric strike and principle stress, a topic that needs to be examined further.

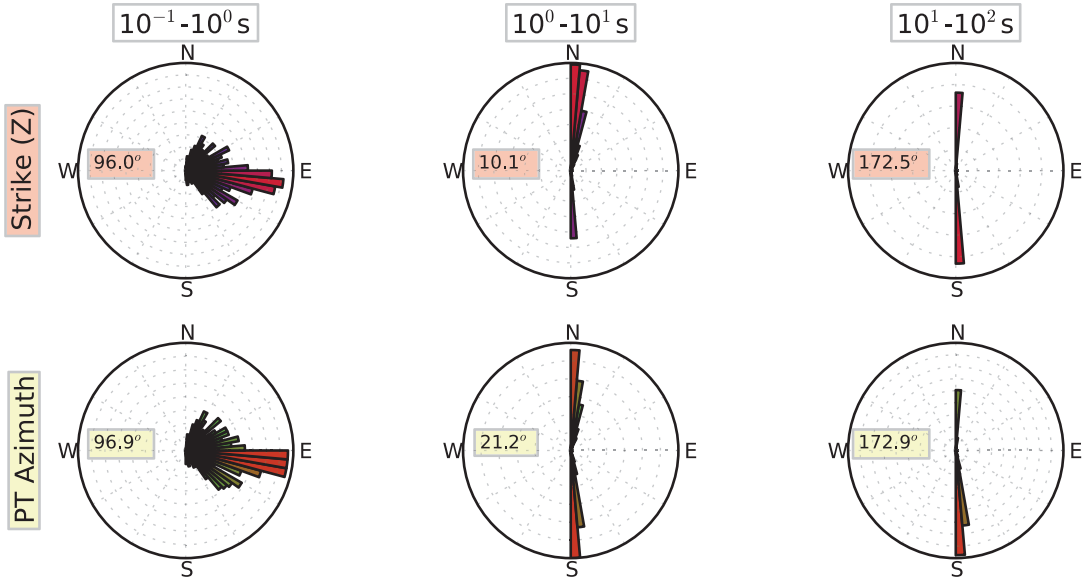

Figure 5.6: Rose plots of every station of the base survey estimating the strike direction for different period bands. The top rose plots represent the strike estimated from the impedance tensor invariants Weaver *et al.* (2000). The bottom rose plots represent the strike estimated from the azimuth of the phase tensor (Caldwell *et al.*, 2004). For short periods the strike angle is towards the East with a large spread due to 1D resistivity structure of the near surface. Below 1 s, a strike angle of 10^{o} east of North is found. Note the numbers in the rose plots represent the median angle, which does not always represent the general trend if there is a 180 degree ambiguity.

5.3.1 2D Modeling

From the multiple base surveys, an estimate of the regional resistivity structure can be inferred from 2D and 3D modeling. The inversion method of choice for 2D is the Occam method developed by Constable *et al.* (1987) and applied to MT by deGroot-Hedlin & Constable (1990). The Occam inversion tries to find the smoothest model that fits the data by minimizing the roughness of the model. The model is estimated from the forward operator of Wannamaker *et al.* (1987) and the inversion algorithm is based on Levenberg-Marquardt non-linear least squares method. This method minimizes the step direction and size between successive models, where a large step size results in a steepest decent method, while optimizing the regularization Lagrange multiplier.

The 2D Occam inversions are computed using a grid of 321 horizontal nodes of 50 m spacing within the station zone and 98 vertical layers that increased as a function of depth on a logarithmic scale with the first layer 15 m and 30 layers per decade (Table 5.1). The model extends a total 300 km in the x-direction and 1000 km in the vertical direction to ensure no boundary effects bias the model. A total of 43 frequencies were used ranging from .008 s to 300 s. An error bar of 10 percent for the apparent resistivity and 5 percent for the impedance phase where used for the first pass of the model. First the TM mode, then using that model as a starting model to invert for the TE was tested, which had similar results to inverting TE and TM simultaneously. Therefore, TE and TM were inverted simultaneously for all simulations. The inversion was let run till the lowest RMS was found (around 20 iterations); this was multiplied by 15% and set as the target RMS for the next run started from a homogeneous half space to get a smooth model; error bars were kept as aforementioned. Setting the target RMS to a value slightly higher than found from the inversion forces the inversion scheme to only add structure as needed to fit the data, resulting in a smooth model.

Table 5.1: Input parameters for 2D Occam inversion, including those for the MakeModel2DMT executable that comes with the Occam package from http://marineemlab.ucsd.edu/Projects/Occam/2DMT/index.html. This executable creates the MESH, INMODEL, and startup file for the 2D Occam inversion.

Line	E-W	N-S	Quantec
Number of Layers	92	92	83
Number of Layers Per Decade	30	30	30
1^{st} Layer Thickness (m)	15	15	5
Maximum Block Width (m)	200	200	200
Trigger	0.75	0.75	0.75
Starting Model (Ω·m)	10	10	10
Number of Frequencies	43	43	22
Frequency Range (Hz)	78-0.005	78-0.005	293-0.0005
ρ_{TE} Error (%)	10	10	10
ρ_{TM} Error (%)	10	10	10
ϕ_{TE} Error (%)	5	5	5
ϕ_{TM} Error (%)	5	5	5
Tipper Error (%)	n/a	n/a	10
Final RMS	1.45	1.60	4.45

Prior to modeling, static shift was removed from the data by using a median spatial filter used in described in Section 4.3. Also, any near surface galvanic distortion was removed following the method of Bibby *et al.* (2005), explained in Section 4.3.1. The EW line was inverted for as is. That means the data were not rotated as the data were collected along a profile perpendicular to geoelectric strike with the TE mode (Z_{xy}) to

geomagnetic North, the geoelectric strike, and TM (Z_{yx})across geoelectric strike.

The NS line is less intuitive because the data were collected along a profile parallel to strike. First, the data were inverted for as is, i.e. with no rotations and station spacing is that projected onto a line that incorporates all stations along the NS line. The reason is that down to approximately 3.5 km ($\delta \approx 500 \cdot \sqrt{T = 1(s) \times \rho = 50(\Omega \cdot m)}$) there is no preferred current direction (Figure 5.6). However, to get deeper structures the data needs to be rotated 90 degrees, but then needs to be projected onto a line such that the spacing between stations is relative to the rotation angle. This basically puts all the stations at one point. This is where 3D inversions help solve the conundrum of data rotation and line projection. The figures shown are that of the models estimated from data that was not rotated. The data and model responses are displayed in Appendix A.

Different starting half spaces were tested ranging from 0.1 Ω·m to 100,000 Ω·m to test sensitivity to conductive and resistive structures found in the inversion model. These models displayed the same model down to 20 km, changing by only 2% in resistivity values. However at 20 km the sensitivity to a conductive block is observed in the starting model of 0.1 Ω·m , but no sensitivity to a conductive structure in the model starting at 100,000 Ω·m . The EW model is sensitive to three main features: the conductive overburden, a conductor at 2 km depth to the west of the profile and a large conductor at 12 km depth. Sensitivity tests on the NS line are ambiguous as the model past 3.5 km is unreliable.

A few interesting features are observed from 2D modeling. The top 500 m is conductive ($\sim$ 5Ω·m) and thickens from West to East and from South to North. This layer corresponds to Cretaceous and Tertiary sands and clays most likely enriched with saline fluids making it conductive (Figures 5.8 and 5.9). Down to 2 km the lithology is also electrically conductive ($\sim$ 50 Ω·m) which is most likely caused by existing fluids within the local water table. In Figure 5.8 a conductive anomaly exists between stations 42 and 44. This anomaly was tested for verification by replacing it with a resistive structure, individually removing station 42, then 43 and 44, but each time the anomaly returned as the model needed it to fit the data. The conductive anomaly corresponds to a fault interpreted from seismic and a brightened set of horizons suggesting that this zone is most likely fluid filled and perhaps a conduit in the local hydrological system. Similarly, in Figure 5.9 a conductive anomaly exists between 19 and 22, again tested but each time returned. Again, the anomaly corresponds to a brightened set of horizons and interpreted faults in the seismic, suggesting that this zone is either fluid filled, contains clays or mineralized zones. Down past $\sim$ 2km the general trend is an increase in resistivity due to compaction and low porosity. An interesting phenomena is that fluids were encountered at around 3.8 km while drilling but no significant conductivity anomaly is present in the 2D inversions, at least directly under Paralana 2 borehole. This could be because the volume of fluid is not large enough for MT to be sensitive to, or the permeability is not large enough for the volume to be well connected.

A large scale broadband MT survey was collected in 2006 by Quantec and has been remodeled using the 2D Occam inversion of (deGroot-Hedlin & Constable, 1990) with parameters displayed in Table 5.1. Phase tensor analysis demonstrates that stations in the Flinders Ranges (to the far West of Figure 5.4), have strong 3D effects in the data due to complicated conductivity structures (Figure 5.11 and 5.12). These points were masked for the 2D inversion. The model mesh has 329 horizontal nodes with spacing of 85 m within the station zone and 86 vertical nodes. The starting model was 10 Ω·m , which was based on sedimentary resistivity values found from the aforementioned models.

The final model is displayed in Figure 5.10. Paralana Hot Springs is the small conductive anomaly at the surface to the West and interestingly it has no deep connection suggesting the source is meteoric fluids. The other interesting feature is the connection between the deep conductor and just below Beverley Uranium Mine, though the connection does not actually reach the surface. This connection was tested as before and is needed to model the data. This is most likely a mineralized shear zone and is probably not fluid filled. The reasoning for this conclusion is that uranium precipitates near Beverely Mine but is sourced from the Flinders Ranges. This means that there needs to be an oxidizing agent to precipitate the uranium, such as sulfides. These sulfides could have been transported through the shear zone. There also appears to be a connection with the fault structure between stations 42 and 44 (Figure 5.8), which could have the same origin as the fault beneath Beverely.

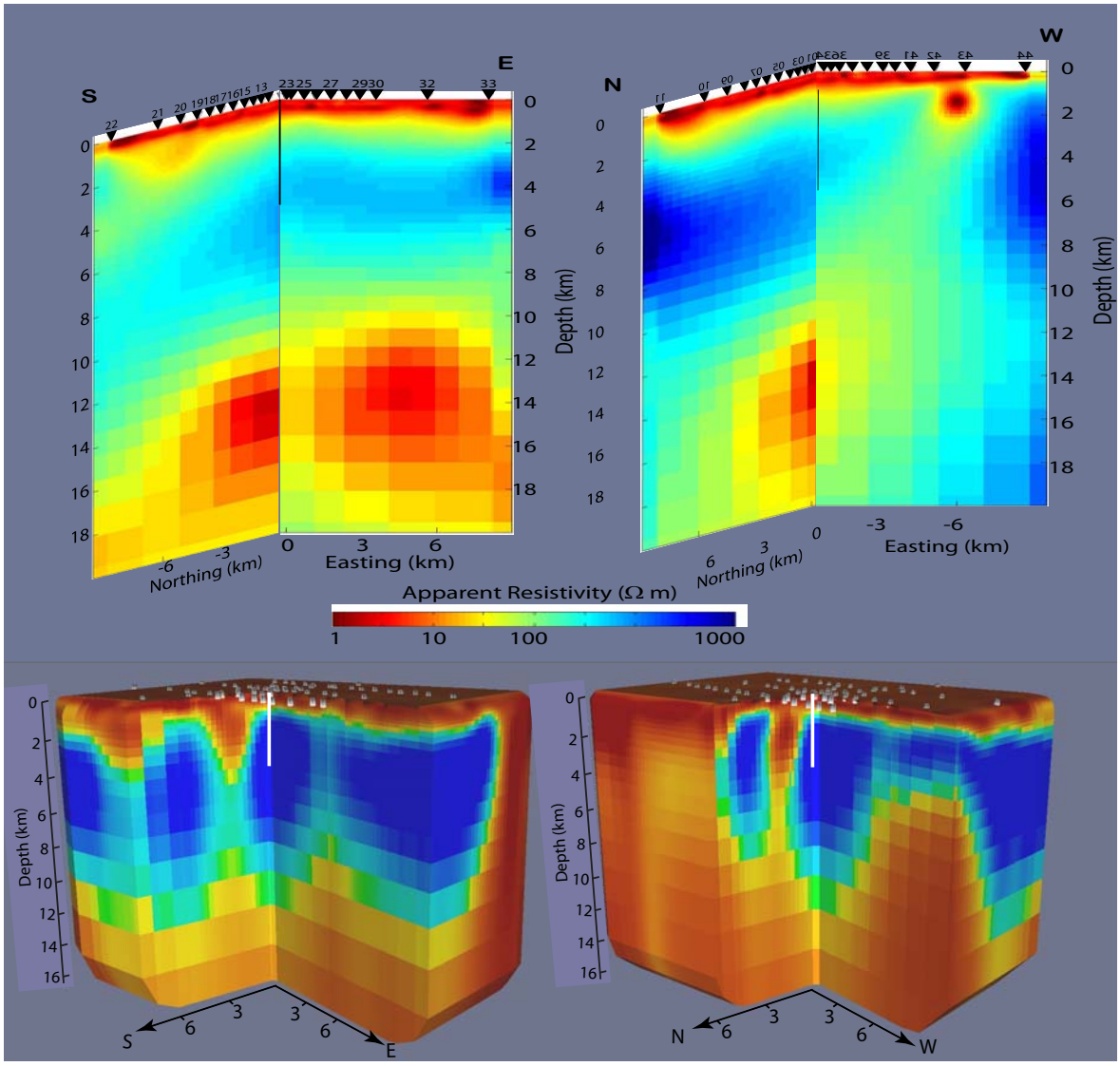

Figure 5.7: Top: Comparison of the 2D Occam models from pre-injection data. Left: South and East line comparison. Right: North and West line comparison. Notice the large conductive body at around 12 km and the possible connection with the fault system to the West. This could be a fluid filled brittle zone. Bottom: Cross sections of a 3D model computed from the inversion code of Siripunvaraporn *et al.* (2005). Left: South and East cut. Right: North and West cut. Notice some differences between the 2D models, specifically the large conductor in the North.

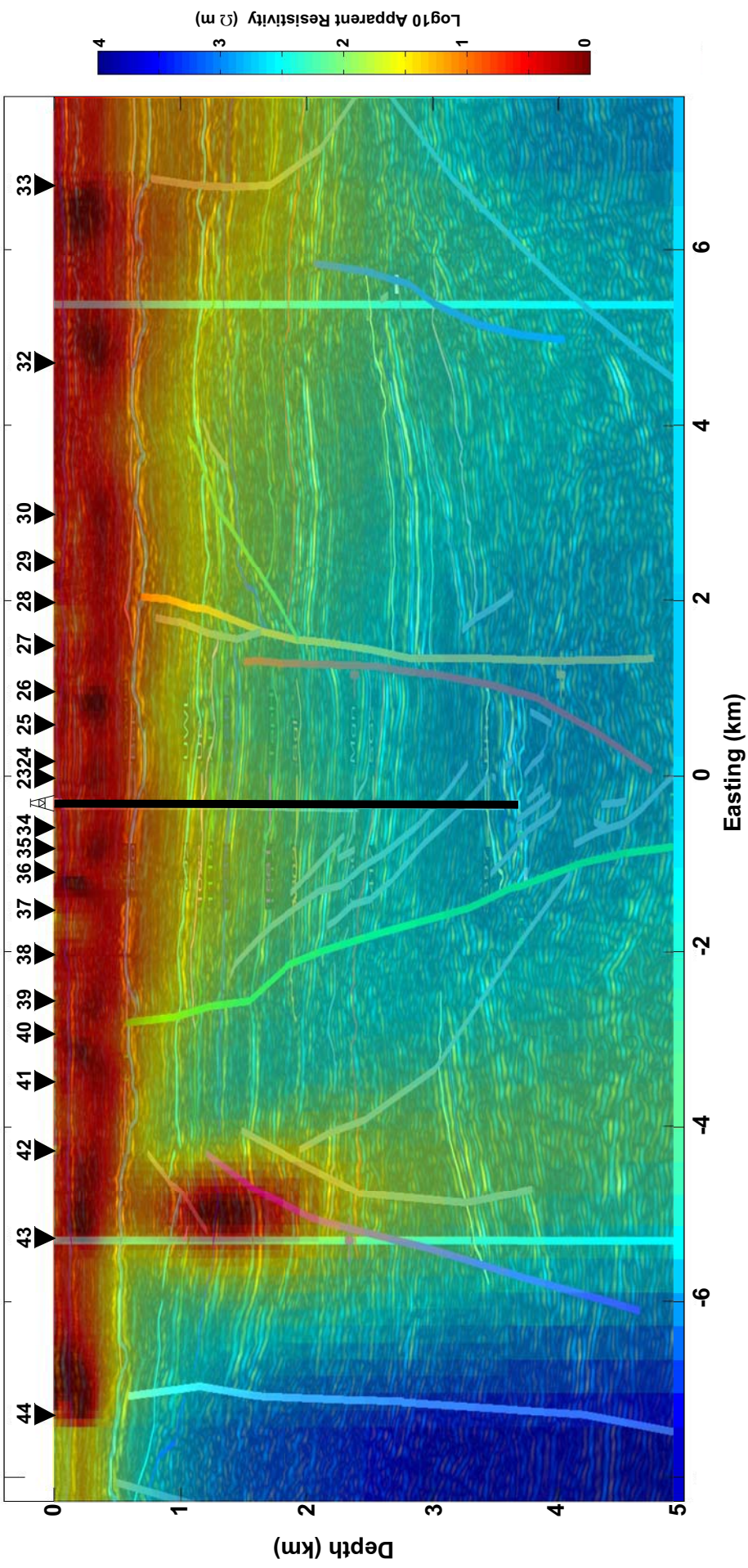

Figure 5.8: Occam inversions of EW baseline overlain with seismic data. Notice the bright horizons in the West correlate with a high conductivity zone from the MT. Also, the graben structure beneath Paralana 2 borehole is also conductive. These zones could be filled with fluids or zones of mineralization.

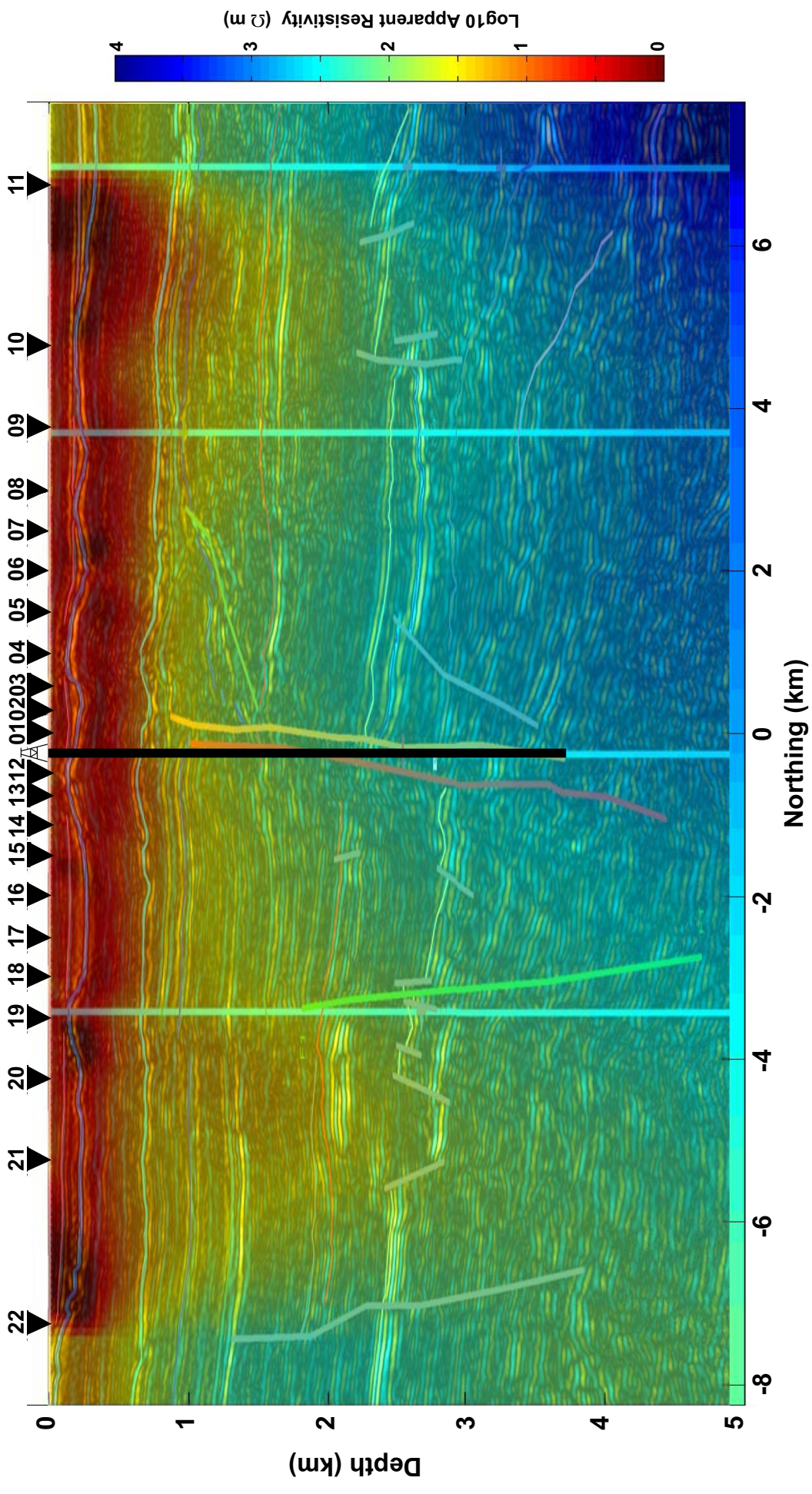

Figure 5.9: Occam inversions of NS baseline overlain with seismic data. The data is not exciting but again a bright horizon in the seismic corresponds to a conductivity high in the MT.

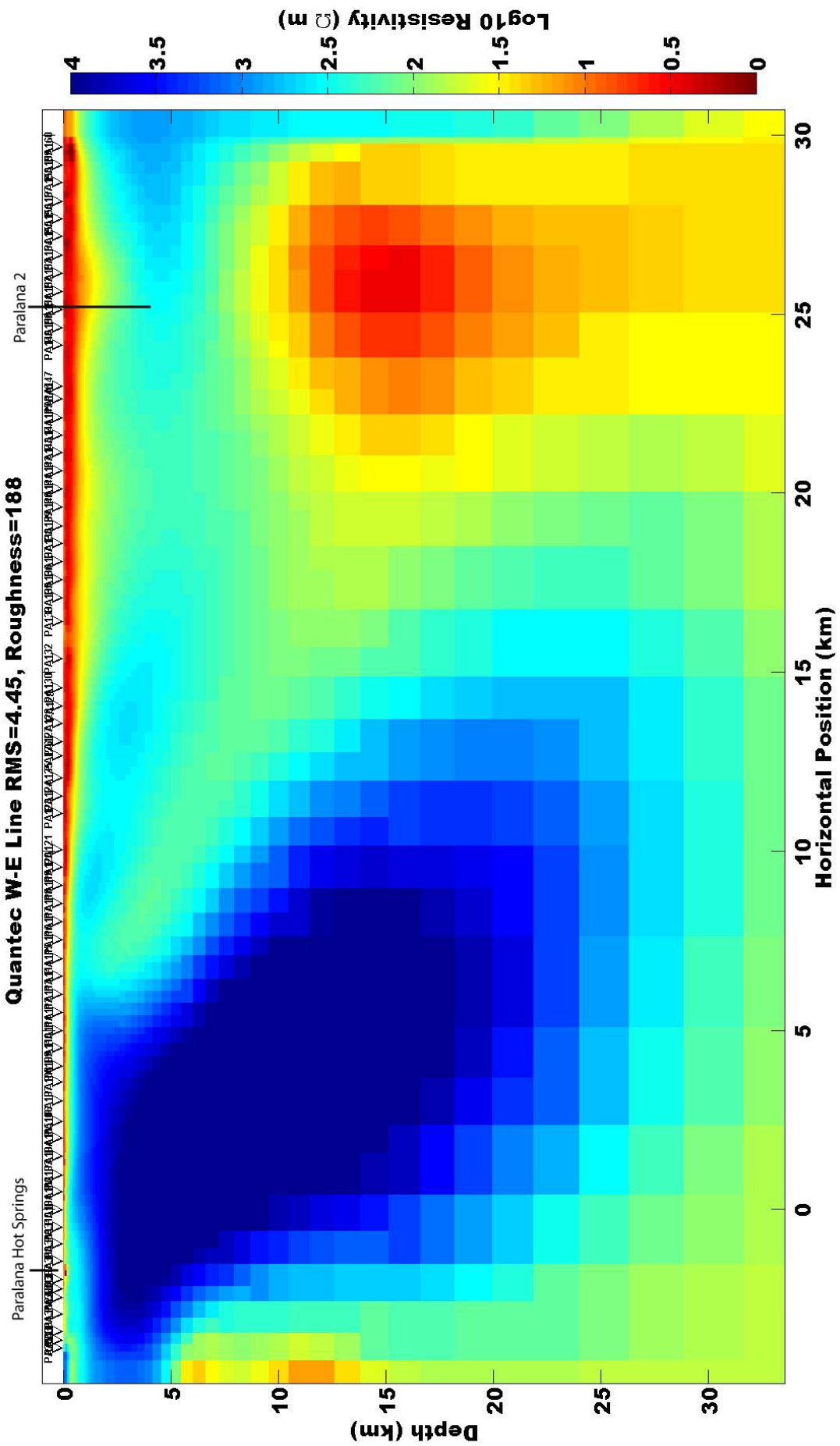

Figure 5.10: Resistivity model from a 2D Occam inversion (Constable *et al.*, 1987) of data collected by Quantec in 2006. The inversion includes Tipper. Points with 3D effect were masked around the Western edge, see Figure 5.12. The Paralana Hot Springs is the conductive anomaly near the surface in the West, notice that there is no deep connection suggesting the water source is surface runoff. The large conductor to the East is robust in the modeling as is the connection to just below Beverely Uranium Mine, though it does not reach the surface. The conductor could be a fluid filled brittle zone, while the connection is most likely a mineralized shear zone. Connection to the fault just West of Paralana 2 is also most likely a mineralized shear zone, but could be fluid filled, see Figure 5.8

.

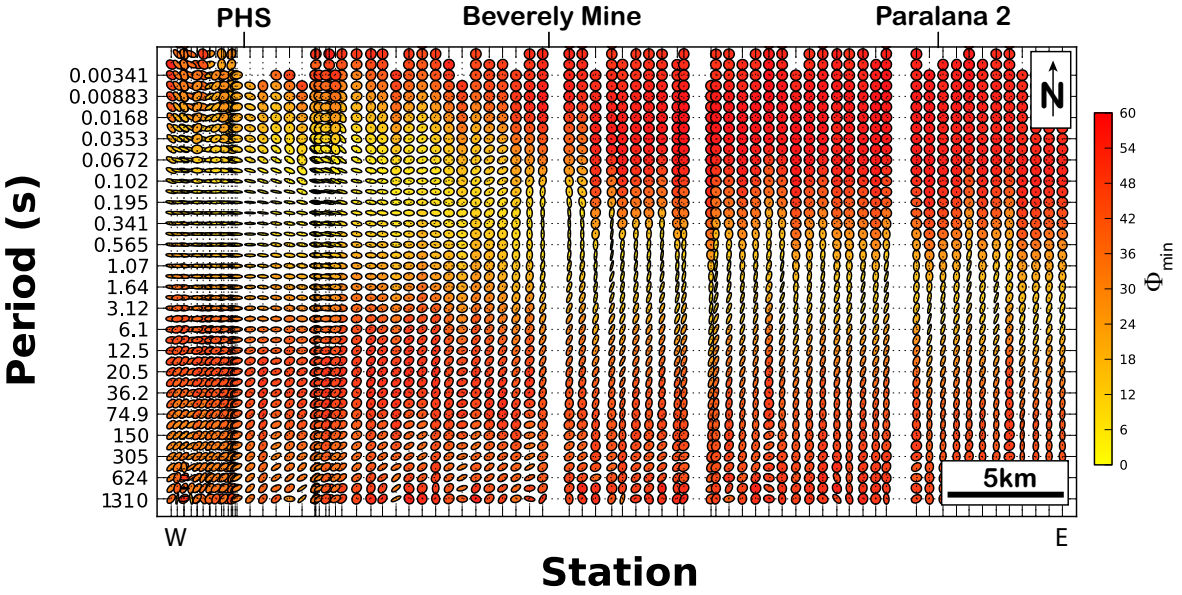

Figure 5.11: Pseudo section of phase tensor ellipses colored by the Φ_{min}. Paralana Hot Springs (PHS) is to the West. Notice the thickening of the top layer towards the East and the orientation of ellipses just below this layer. To the West they are oriented EW and to the East they are oriented NS where the change occurs just below Beverley Uranium Mine.

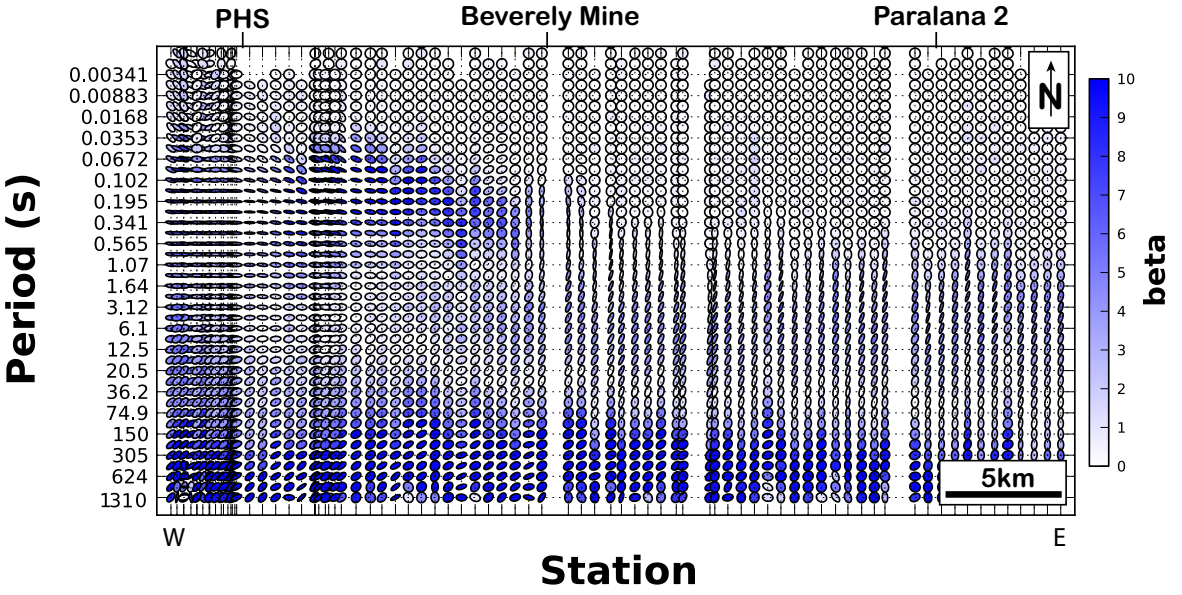

Figure 5.12: Pseudo section of phase tensor ellipses colored by the $|\beta|$, the skew angle, where the more blue the ellipse the more larger the skew angle. Paralana Hot Springs (PHS) is to the West. Notice most of the dark blue ellipses are to the West near the Flinder Ranges and at the sediment/basement boundary that deepens towards the east.

5.3.2 3D Modeling

The 3D inversion is based on an Occam type approach in the data space (Siripunvaraporn *et al.*, 2005; Siripunvaraporn & Egbert, 2009). Three different 3D inversions were preformed. Prior to modeling, static shift was removed from the data by the median spatial filter described in Section 4.3. Also, any near surface distortion was removed following the method of Bibby *et al.* (2005), explained in Section 4.3.1. For all inversions, all 8 components of the impedance tensor are inverted for. Error bars of 5 percent were placed on the off diagonal components of the impedance tensor and 50 percent for the diagonal components; this pushes the inversion to fit the main polarizations of the MT response. The model started from a homogeneous half space of 10 Ω·m and smoothing parameters of [5, 0.3, 0.3,0.3], see Siripunvaraporn *et al.* (2005). After 3 iterations the RMS reached a minimum, then the smoothing parameters were changed to [5,0.1,0.1,0.1] to let the model add structure to the smooth model.

The first run uses all stations from the base survey responses with the smallest error bars in the estimation of $\hat{\mathbf{Z}}$ except 31 and 53, because they did not have quality data, and 6 stations from the Quantec line to constrain the southern part of the grid. This used a grid of 66 (EW) x 66 (NS) x 44 (Z) cells with a spacing of 200 m within the station zone. The top layer was set to 15 m increasing on a logarithmic scale with depth down to 250 km. Similarly, the horizontal cells increase on a logarithmic scale from the station zone to a total with of 250 km in both directions. The inversion was run with 12 periods ranging from 0.013 s to 81 s, having at least two periods per decade. A total of 60 stations were used and This ran for 7 iterations to get a model with an RMS of 1.56.

The second run included 13 stations from a EW oriented line 5 km north of Paralna 2 collected during an honors project in May 2012, 14 stations from the Quantec line and 31 stations from this project. The stations were picked to have about 500 m spacing. The 3D grid is 69 (EW) x 56 (NS) x 45 (Z) where the top layer is set to 15 m. After 3 iterations the RMS reached a minimum limit, then the smoothing parameters were changed to [5,0.1,0.1,0.1] to let the model add structure to the smooth model. This ran for 3 iterations to get a model with an RMS of 1.08.

The third 3D inversion was to characterize the regional resistivity structure. This employed 25 stations from the Quantec survey, 16 stations from the north EW line and 18 stations from this project. The stations are spaced at approximately 1 km. The 3D grid is 68 (EW) x 39 (NS) x 45 (Z). After 4 iterations the RMS reached a minimum, then the smoothing parameters were changed to [5,0.1,0.1,0.1] to let the model add structure to the smooth model. This ran for 6 iterations to get a model with an RMS of 1.55.

The three models have some differences. The two denser models just around the borehole are similar in the top 2 km and just around the borehole. However, to the west the first inversion there lies a strong linear conductor that trends EW extending from a depth of 2 km that is not seen in the 2D models or the other dense 3D model. The data fits in this region have larger RMS than the second dense model suggesting the model is not fitting the data. Therefore, the second dense grid is taken as the preferred model; the responses are displayed in Appendix A. This model is similar to the 2D models except for a large conductor to the North of the Paralana 2 borehole (Figure 5.7). Interestingly, this is where the fluids are assumed to flow towards and since some data was collected post-injection conductive bias in this region could indicate the location of fluids. Taking a closer look into the model reveals a conductive zone just to the NE of the borehole that could be associated with an existing fluid filled fracture network, which was stimulated during the fluid injection (Figure 5.13). The other interesting

feature that is different between the two models is the large conductor at 12 km depth. The 2D models suggest this to be a concentrated zone of conductive material, however the 3D model does not need this in the model, instead the conductive material is distributed heterogeneously at a depth of 12 km. Unfortunately, resolution at this depth is poor due to the conductive over burden and period range measured.

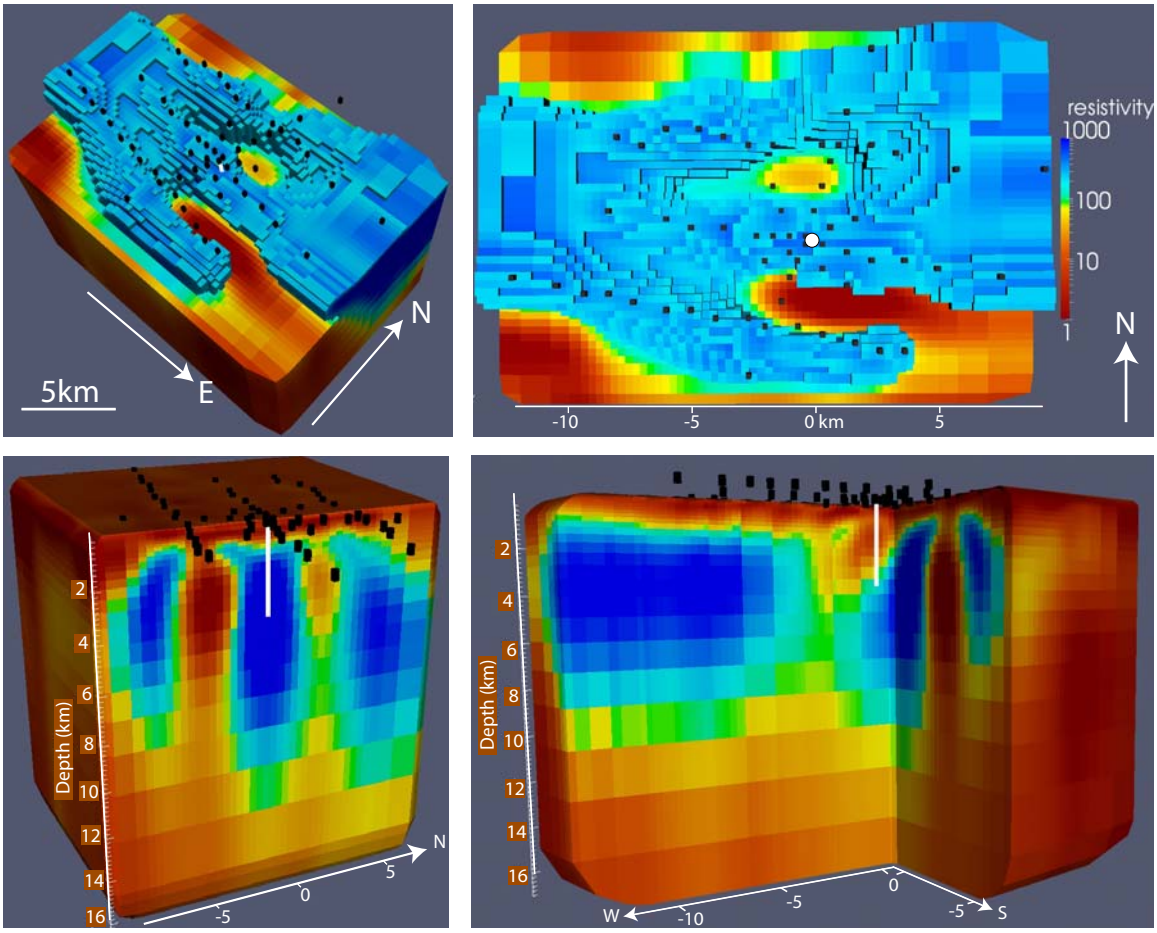

Figure 5.13: Different views of the 3D resistivity structure found from a 3D inversion of a the second dense grid, see text. Notice the conductive zone just to the NE of the borehole that could be interpreted as an existing fluid filled fracture network as this is the area in which injected fluids migrated towards. In the top right figure anything above 50 Ω·m has been stripped off the model to leave the resistive structure of the compacted sediments and basement.

5.4 Summary

The underlying goal of this chapter is to provide some background information that will help with understanding the forthcoming experiments. First, an EGS system is one where thermally enhanced lithology is engineered such that fluids can flow through connected fracture networks to synthetically create a geothermal reservoir from which energy can be extracted. This is typically done through hydraulic stimulation, meaning fluids are forced into the hot rocks at high pressures and at slow rates to push open fractures (Figure 6.3). This is done at Paralana, South Australia where anomalously high heat producing basement rocks of the MDP are covered by 4 km of sediments. Moreover, the Paralana 2 borehole was drilled into a graben structure to interact with the deepest and hottest of these basement rocks. The regional resistivity structure is modeled in both 2D (Constable *et al.*, 1987; Rodi & Mackie, 2001) and 3D (Siripun-

varaporn *et al.*, 2005) which correlate well with each other. The resistivity structure is nearly 2D (Figures 5.11 and 5.12), but with some interesting features. A large conductor 4 km to the West of Paralana 2, starting near the surface and possibly connecting down to a large conductor under Paralana 2 at 12 km depth, could be a fluid filled fault system that is important in the local hydrology cycle. Also, the deep conductor appears to have a connection just below Beverley Uranium Mine, which is most likely a mineralized shear zone. Geoelectric strike near Paralana is in a NNE direction which aligns orthogonal with the principle stress direction. All this information helps in understanding changes in the MT responses before, during and after fluids are injected.

Chapter 6

Continuous MT Monitoring

This chapter covers continuous MT measurements during the injection test for the development of a geothermal reservoir at Paralana, South Australia. Parts of this chapter were accepted by *Geophysical Research Letters* as a short paper, therefore a more detailed discussion will be provided where necessary. The structure will follow the scientific method, starting with a problem statement followed by a hypothesis, methods, experiment, data analysis, discussion and conclusions. Subsections will be added to supplement published material for longer explanations. The accepted paper is included as Appendix C.

Abstract

EGS are on the verge of becoming commercially viable for power production, where advancements in subsurface characterization are imperative to develop EGS into a competitive industry. Theory of an EGS is simple, pump fluids into thermally enhanced lithology and extract the hot fluids to produce energy. One significant complication in EGS development is estimating where injected fluids flow in the subsurface. Micro-seismic surveys can provide information about where fractures opened, but not fracture connectivity nor fluid inclusion. Electromagnetic methods are sensitive to conductivity contrasts and can be used as a supplementary tool to delineate reservoir boundaries. In July, 2011, an injection test for a 3.6 km deep EGS at Paralana, South Australia was continuously monitored by both micro-seismic and magnetotellurics (MT). Presented are the first results from continuous MT measurements suggesting transient variations in subsurface conductivity structure generated from the introduction of fluids at depth can be measured. Furthermore, phase tensor representation of the time dependent MT response suggests fluids migrated in a NE direction from the injection well. Results from this experiment supports the extension of MT to a monitoring tool for not only EGS but other hydraulic stimulations.

6.1 Problem Statement

Is it possible to measure transient variations in the MT response estimated from continuous measurements while saline fluids are injected into the subsurface at 3.6 km depth?

6.2 Hypothesis

To test the feasibility of measuring transient variations in the MT response, the 3D forward modeling code of Mackie *et al.* (1993) is employed to estimate the MT response of a NNE evolving 0.3 Ω·m conductive body at 3.6 km depth in a geoelectric setting estimated from previous MT measurements at Paralana (see Chapter 5). The resistivity at 3.6 km is 200 Ω·m . The choice of direction is based on an injection test done at Paralana in July, 2010 and concurrent micro-seismic survey that suggested the preferred fracture direction is to the NNE. The conductivity is that of sea water as the proposed fluid injection is with saline fluids. Evolution of the body was segmented into 6 steps, where step 1 was designated as the base survey. The reservoir began to grow on step 2 as a 400 m (EW-direction) x 400 m (NS-direction) x 200 m (thickness) conductive block, equivalent to 32,000 liters of saline water. The reservoir grew to approximately 1.2 km x 0.8 km x 500 m trending NNE on step 6, equivalent to 480,000 liters of saline water. The final dimensions are based on the proposed reservoir dimensions predicted by Petratherm. The evolution dimensions were dictated by the 3D grid. The grid around the injection well is 8 km x 8 km with 400 m x 400 m cells in the horizontal direction; this is dictated by the size of the model that WinGLink can handle. The model grid extended over 200 km in the horizontal direction. The vertical layers increase in size with depth starting with 5 m thickness and at 4 km the thickness is 200 m, while the model extends vertically to 1000 km. Therefore, the evolution of the conductive body is limited to cell size. Also, for the evolution, the conductivity of each cell of the conductive body is set to that of sea water. This is to test the maximum response that would be possible. Stations were placed at 400 m spacing in an 8 km x 8 km grid on the surface.

Multiple parameters can be estimated from $\mathbf{Z}$, here the apparent resistivity, impedance phase and phase tensor ellipses (Caldwell *et al.*, 2004) will be analyzed. Different visualizations have been attempted, where mapping the residuals between step one and each subsequent step for different periods as a function of time proved to be most informative.

A few key observations can be made from forward modeling. First and foremost, MT parameters vary by only a few percent, meaning accurate and precise data are needed to confidently observe perturbations produced from the introduction of a conductive body at depth. Second, variations in the two dominant orthogonal polarizations of apparent resistivity and impedance phase exhibits a larger change in the component parallel to reservoir strike, ($\mathbf{Z}_{xy}$) aligned as electric field to geomagnetic north (x) and magnetic field geomagnetic east (y). Third, the period range of changes for apparent resistivity (10-30 s) and impedance phase (1-8 s) are causal, where the phase predicts the resistivity (Berdichevsky & Dmitriev, 2008). Similarly, apparent resistivity residuals are positive and on the order of 5 Ω·m , while impedance phase residuals are negative and on the order of 1 degree. Fourth, variations in phase tensor ellipses are most informative where the major axis is oriented in the direction of largest change. The residuals are calculated following eq. (6.1), where phase tensor $\mathbf{\Phi}_o$ is the base measurement, $\mathbf{\Phi}_j$ is time step j, $\mathbf{I}$ is the identity matrix and $\mathbf{\Phi}^{-1}$ is the inverse. The face color of the ellipse represents the geometric mean of Δ, where red is a large change and yellow is a small change.

Residual phase tensors ellipses display an abundance of information. At short periods, the phase tensor ellipses begin to align with the conductive body (reservoir). As period increases, the size of the ellipse grows and the geometric mean of $\Delta\Phi$ increases. Near the edges of the body, the ellipses elongate and align to the edge orientation and

the geometric mean of $\Delta\Phi$ is near zero, while inside the reservoir the ellipses are more circular and the geometric mean of $\Delta\Phi$ increases. When the period of the inducing field penetrates below reservoir depth, the ellipses align to point towards the center of the reservoir while the size decreases and geometric mean of $\Delta\Phi$ goes to zero until the influence of the reservoir becomes insignificant. Heise *et al.* (2006) describes in more detail the phase tensor behavior in anisotropic media. For more basic understanding of the behavior of phase tensor residuals see Section 4.1.

Interestingly, the shape and orientation of residual phase tensor ellipses is sensitive to the regional resistivity structure as seen in the right hand side of the plots in Figure 6.1. Towards the West is the resistive MDP that dips from the Flinders Ranges beneath Paralana which displays a more circular patter in the ellipses, while towards the East the subsurface is more conductive causing the ellipses to be more elongated. This suggests that if conductive fluids are injected into resistive lithology the response of residual phase tensors ellipses will be more circular than if conductive fluids are injected into less resistive lithology. This is important in what the predicted changes might look like, specifically how the residual ellipses will behave. A larger change in a particular direction will occur if the background resistivity of the injection lithology is low.

Behavior of phase tensor residuals suggests that depth can be inferred however an absolute resistivity measurement needs to be known to tie the phase response to. Also, the two different polarizations of the phase tensor sample different depths if the resistivity structure is not 1D (Hamilton *et al.*, 2006). This is where an inversion is useful. An Occam 1D inversion (Constable *et al.*, 1987) can be employed to invert the component most effected by the change in resistivity structure, namely Z_{xy}, which is the TE mode and more sensitive to changes in subsurface conductivity structure. This gives a depth estimation of 3.3 km from the forward model responses. The difference is in the smooth inversion technique which smooths over the conductance of the layers above the reservoir. Here the conductance is over estimated as the anomaly depth is underestimated leading to a shallower depth. In addition, a 2D inversion scheme (deGroot-Hedlin & Constable, 1990) can be employed to estimate the depth of the anomaly and magnitude of change as a function of time, where the abscissa is time instead of distance. Here the MT responses for the same station at different times are spaced such that there is no influence from near by stations, thus giving a 1D estimate of the evolving body. Again only the Z_{xy} mode is modeled because of its sensitivity to the conductive body. This exercise also gives a depth estimate of 3.3 km for the same reasons previously state.

All these observations predict that transient changes can be measured in the MT response. However, care must be taken in data acquisition because the data needs to be both accurate and precise. Two patterns to look for in the data are causality, in that changes in the phase predicts the apparent resistivity. Moreover, that they occur together, so a change in the phase must be accompanied by a change in the apparent resistivity in the appropriate period band according to the dispersion relations. Another pattern to look for is the sign of change, where the residual phase should be negative and the apparent resistivity residual should be positive. Estimation of residual phase tensors provide directional information, orienting in the direction of largest change. Finally, estimating a depth can be accomplished by employing an inversion scheme.

6.3 Experiment

In July, 2011, for their EGS project at Paralana, South Australia, Petratherm Ltd. injected 3.1 million liters of saline water (resistivity of 0.3 Ω·m) into a sedimentary

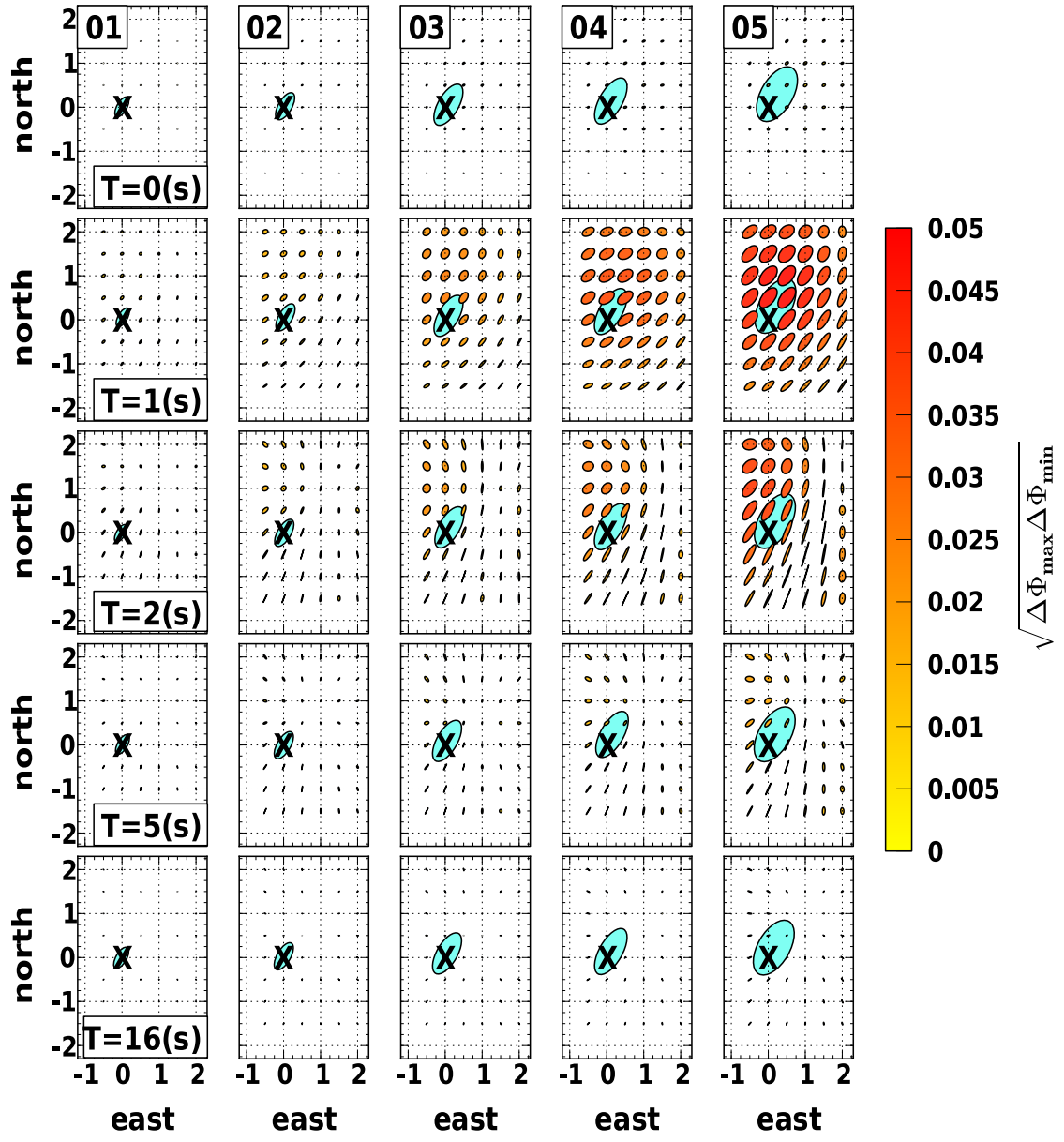

Figure 6.1: Time lapse map of phase tensor residuals calculated as pre injection minus subsequent days calculated from 3D forward modeling (Mackie *et al.*, 1993) of a growing conductive body 3.6 km depth similar to Paralana. Each column represent one day (labeled top left), each row represents one period (s)(labeled bottom right), and the blue ellipse represents the boundaries of the conductive body that changes with depth. The ellipse color is calculated as the arithmetic mean of eq. (6.1). Notice ellipse alignment and size as a function of time and period.

package at 3.6 km depth through an 8 m perforated zone of the cased Paralana 2 borehole. The injection took 4 days to complete, starting on day 193 at 0400 universal time (UT) with low flow rates (2 barrels per minute = 300 liters per minute) followed by a sequence of shutting in and increasing flow rates step wise to a maximum of 16 barrels per minute = 2500 liters per minute (Figure 6.3). Pumping concluded on day 196 at 0400 UT when the well was shut in. A micro-seismic array measured over 11,000 events suggesting the fractures opened in a NE preferred direction, with the majority located in the NE quadrant from the Paralana 2 borehole (Hasting *et al.*, 2011) (blue dots in Figure 6.2). Two days before the injection, 11 broadband 4-component AuScope MT instruments were placed around the Paralana 2 borehole; the furthest station

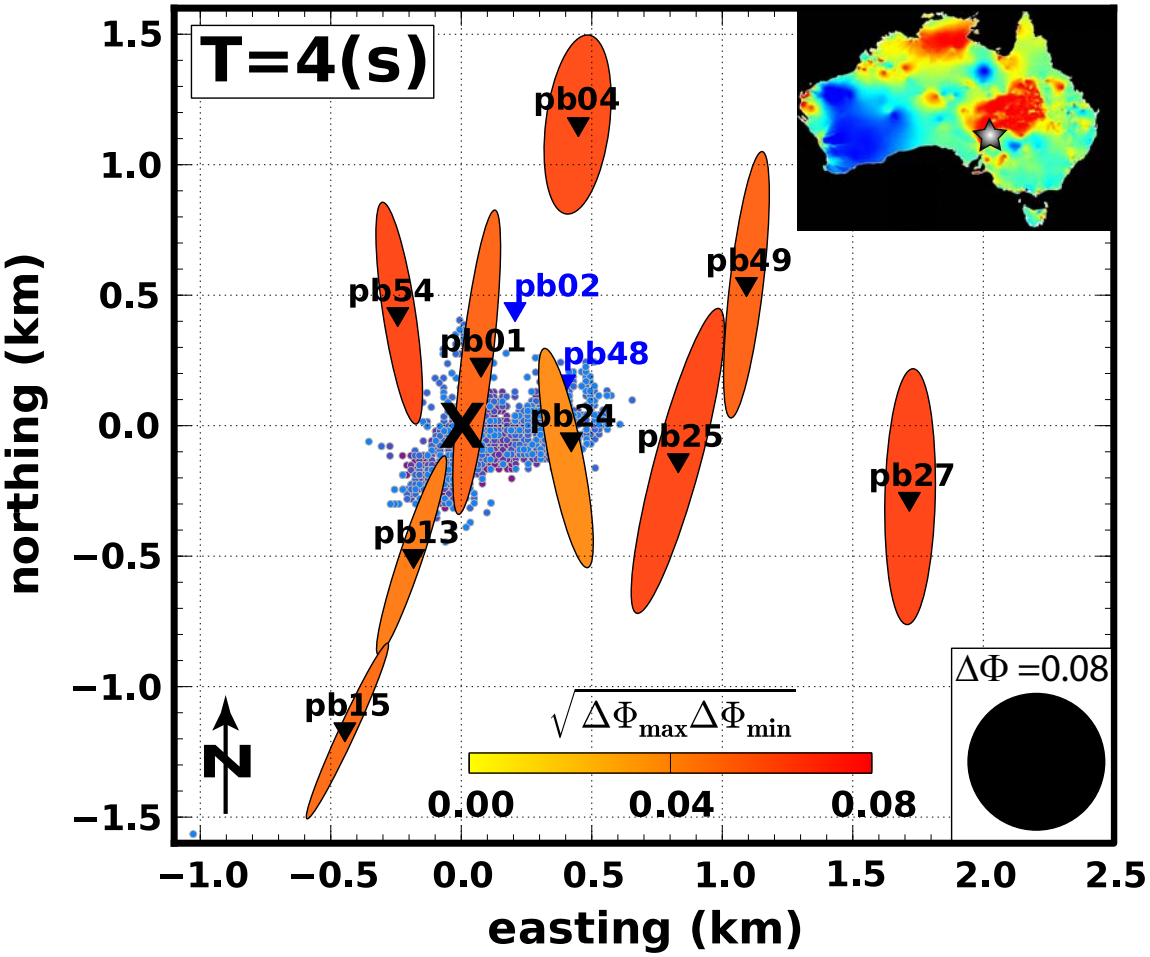

Figure 6.2: Map of Paralana, South Australia displaying MT station locations (triangles) centered on Paralana 2 injection well (X), and micro-seismic events measured during the injection experiment from Hasting *et al.* (2011) (circles colored by day–192 as red to 196 blue). Top right is a temperature map of Australia from Geoscience Australia at 5 km depth where reds represent 285 C and the gray star locates Paralana. Stations that malfunctioned are colored blue and are not used in this analysis. The ellipses represent phase tensor residuals eq. (6.1) of pre-injection and day 196 for a period of 4 s. The face color is estimated as $\sqrt{\Delta\Phi_{max}\,\Delta\Phi_{min}}$ (Heise *et al.*, 2008). Interestingly, ellipse orientation generally aligns with the seismic cloud, suggesting that fluctuations in the MT response correlate with geoelectric alteration provoked by connected fluid filled pathways developed during the injection experiment.

being about 2 km away (Figure 6.2). Survey design was based on a previous injection test that showed fracturing tendency to be NE of the borehole. MT instruments recorded for an entirety of 8 days, including 2 days pre-injection, 4 days during injection and 2 days post-injection. A solar powered AuScope instrument was set up 60 km south of Paralana as a remote reference. Instruments sampled at 500 Hz and were synchronized by GPS. Dipoles were approximately 50 m in length, employing Cu-$CuSO_4$ non-polarizing porous pots as electrodes laid out in an L-shape aligned with geomagnetic north, which is fortuitously also regional geoelectric strike. Data were retrieved from the instruments every day to ensure data quality, while instrument setup was checked for functional completeness and batteries where changed every third day.

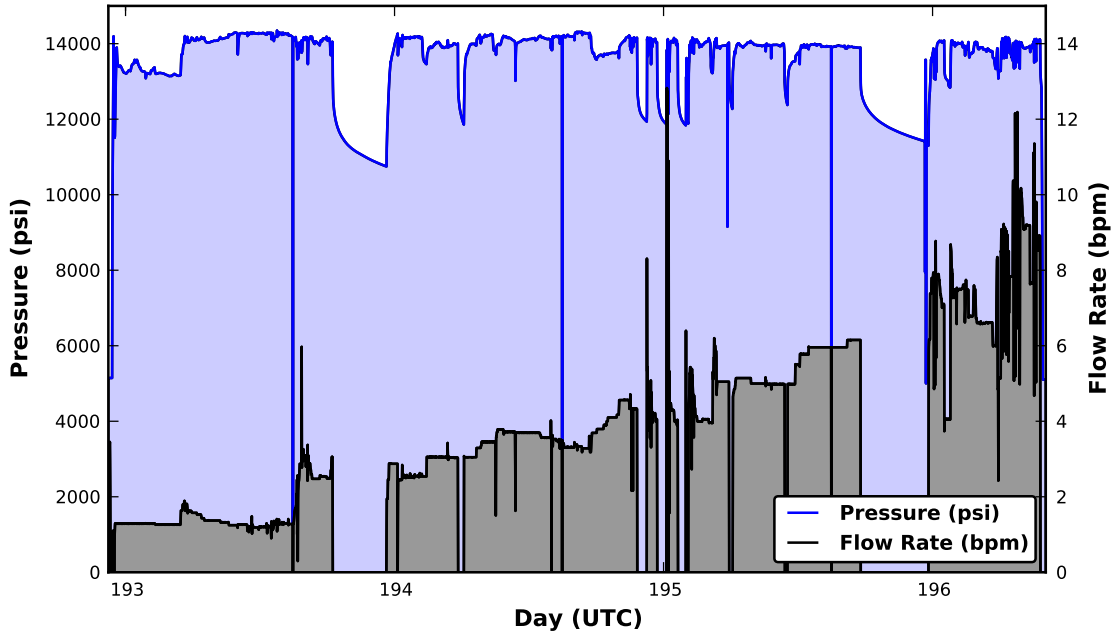

Figure 6.3: Plot of pumping pressures and flow rates during the July injection test at Paralana. Notice the erratic pumping schedule meant to punch and push the rock to fracture causing the flow rate to increase over time. Also, visible changes in the MT response begin around day 194 when the volume of fluids in the subsurface causes a large enough change to record.

6.4 Data Processing and Analysis

Time series were checked for quality and coherent noise using robust time-frequency analysis formalized by Djurovic *et al.* (2003). Magnetic source field effects were estimated using a principal component analysis similar to Egbert (1997), finding only two dominant principal components except for a window of 1400-2400 on UT day 194. MT transfer functions were estimated for 1, 4, 6, 12, and 24 hour blocks utilizing a robust bounded influence remote referencing method developed by Chave & Thomson (2004). As source field power was low in the MT dead band (1-10 s) during local night time, a magnetic coherency threshold between the station and remote reference station was applied to remove influence of non-coherent and weakly coherent signal on **Z** that might produce false anomalies (Mareschal, 1986). Coherency between measured electric fields and predicted electric fields from measured magnetic fields was maximum across all periods for **Z** calculated using 24 hour blocks. Estimated mean error for **Z** of 24 hour blocks is approximately 1.4 percent, while average repeatability of MT parameters for the period range .01-1 s is within 0.4 percent between 24 hour blocks. Therefore, the following data analysis is focused on **Z** calculated from 24 hour time windows.

One benefit of conducting electromagnetic surveys in the Australian outback is the lack of electromagnetic noise sources, nevertheless there are other logistical aspects of data collection. Out of the 11 instruments deployed, 6 functioned consistently throughout the survey. The other 5 instruments were sporadically disrupted by mice chewing electrode cables or electrodes being dug or pulled out by other animals. These time windows of poor data quality are not used to estimate **Z**. Stations pb02 and pb48 are not used in this analysis because they malfunctioned too often to estimate reliable transfer functions. Other noise sources include pumps used for the injection (operating at periods of ∼1 s and ∼6 s) and site specific noise. Fortunately, influence from these noise sources is minimal in these data. Also, it is important to note that the resid-

uals, calculated as the MT response pre-injection minus each 24 hour time window, are calculated for each station. Therefore, any time invariant systematic noise, such as instrument noise, will be subtracted out. Near surface distortion is estimated and removed following Bibby *et al.* (2005). Note the phase tensor is invariant to near surface distortions, making it an advantageous parameter to represent the MT response (Caldwell *et al.*, 2004).

Variations in MT parameters are estimated by computing residuals of pre-injection MT parameters minus subsequent 24 hour blocks, specifically for apparent resistivity, impedance phase and the phase tensor parameters. Phase tensor residuals provide information about geoelectric strike transformation during the injection and gradients in resistivity structure, suggesting reservoir boundaries. Here the phase tensor residuals are calculated as a percent change eq. (6.1), where Φ_o is the phase tensor pre-injection, Φ_j is the phase tensor of a 24 hour block, $\mathbf{I}$ is the identity matrix of rank two and $\mathbf{\Phi}^{-1}$ is the inverse. The face color can be represented as the geometric mean $\sqrt{\Delta\Phi_{max}\,\Delta\Phi_{min}}$ (Heise *et al.*, 2008). For more on phase tensor behavior in anisotropic media see Heise *et al.* (2006) and Caldwell *et al.* (2004). Finally, to ensure bulk changes are estimated robustly, a median filter is applied to the each MT parameter, calculating the single station median for three periods at three different times.

$$\Delta\Phi oj = \mathbf{I} - (\mathbf{\Phi}_o^{-1}\mathbf{\Phi}_j) \tag{6.1}$$

6.5 Discussion

First and foremost, confidence in variations of the MT response must be instilled before any in-depth interpretation can begin. The first thing to look for is a clear separation between the MT response pre-injection and MT responses estimated at later times. This provides an indication of variational magnitude and suggests a confidence level that observable temporal changes beyond measurement error exist. The second pattern to look for is causality, where variations in impedance phase should predict apparent resistivity changes according to the dispersion relation (Berdichevsky & Dmitriev, 2008). Specifically for a conductive change at 3.6 km at Paralana, the phase should increase at ∼1-10 s and the apparent resistivity should decrease beyond ∼8 s. The key is that an observed change in the phase is related to a change in the apparent resistivity at a physically plausible period band. The general trend for most stations is similar to Figure 6.4 where the apparent resistivity is reduced below periods of 8 s and the phase increases around 1-10 s for MT responses estimated during the injection. Moreover, most of these changes are near or just above the measurement error where variational magnitude is larger in the Z_{xy} than the orthogonal polarization, suggesting that change in geoelectric structure has a preferred direction towards the North. The other components do not show coherent changes above measurement error in both the resistivity and phase (Figure 6.5). Not all stations have consistent measurable changes above the noise level, therefore those that did will be discussed, namely pb01, pb04, pb24 and pb27. The others had intermittent periods where mice chewed cables or electrodes got pulled out by curious marsupials.

Another method to provide confidence in observable changes is to estimate an error floor by propagating an error estimate to each MT parameter, assuming that the error is identically isotropic. An error estimate can be calculated as the ratio of the sum of the error in estimation of $\mathbf{Z}$ and repeatability divided by $\mathbf{Z}$ as a function of period and time for each station; this gives a percent change confidence floor. Applying a median filter and taking the maximum percent change estimated as a function of

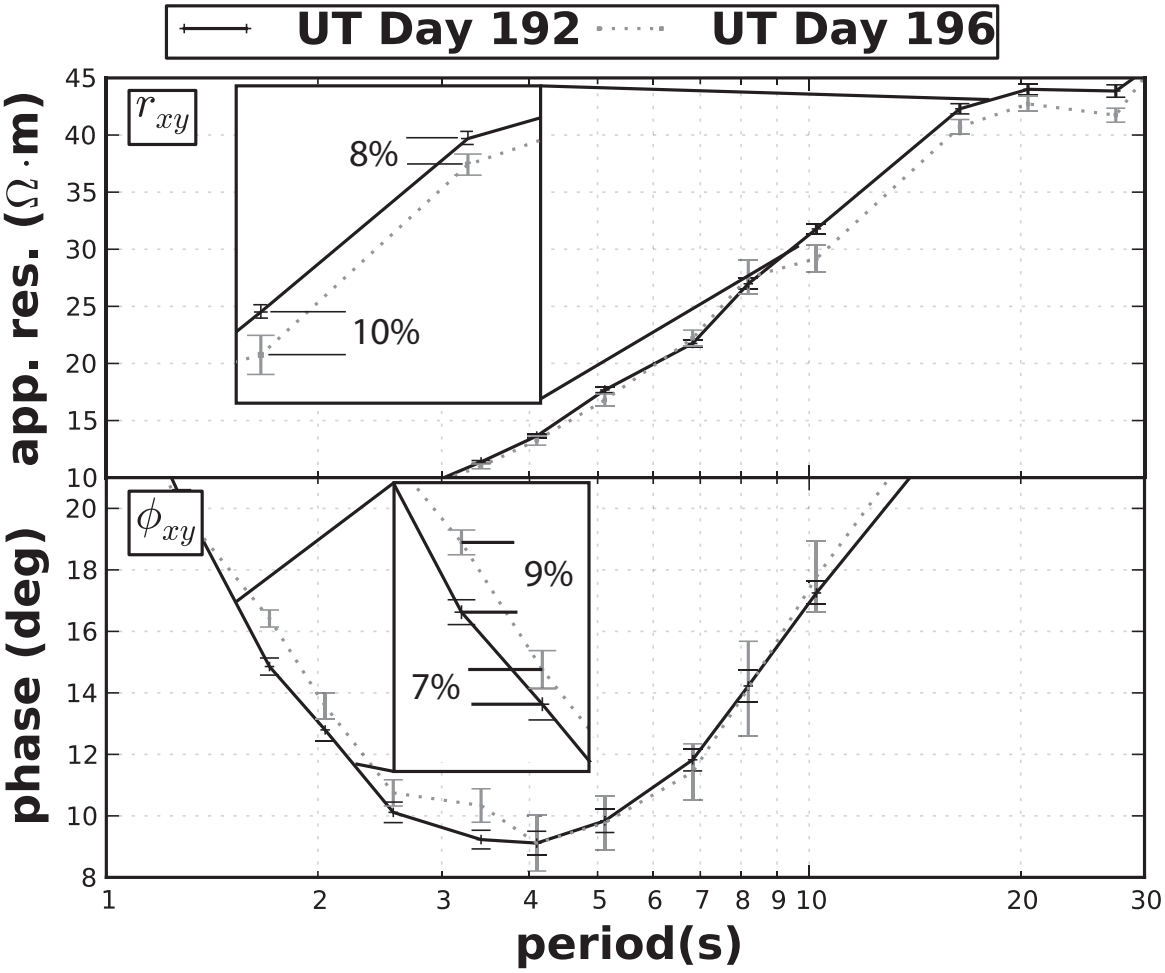

Figure 6.4: Comparison of the MT response for station pb01 on day 192 (black) and 196 (gray). Top graph represents apparent resistivity of $\mathbf{Z}_{xy}$ and bottom the phase. Notice phase change increases at 1-5 s and apparent resistivity above 10 s, displaying causality. Similarly, the magnitude of change is near or just above measurement error representing a measurable change in subsurface geoelectric structure originating from the injection of fluids at depth.

time and frequency of the aforementioned stations provides a robust baseline to which MT parameters can be compared to. Namely, if the residual in the MT parameter is above this baseline then it can confidently be analyzed as a measurable signal (Figure 6.6). Estimating parameters of the phase tensor (Caldwell *et al.*, 2004) provides dimensionality information and a representation of the MT response that is insensitive to distortions. Phase tensor representation of the time dependent $\mathbf{Z}$ suggests a general trend of increase in $\Delta\Phi_{max}$ as a function of time between 1-10 s, conversely $\Delta\Phi_{min}$ does not change above the error floor, again suggesting a directional dependence. Interestingly, for periods in the dead band (1-10 s), the error floor displays an increasing linear trend from the start date to the end date. However, magnetic source field power did not decrease from start to finish enough to cause an increase in error of estimating $\mathbf{Z}$. Moreover, electrical noise from mechanical pumps (1 s and 6 s) remained nearly constant for the pumping period. Similarly, cathodic protection from the EPIC pipeline (2 km west of injection well see Figure 5.2) was time-invariant. Electrode drift would effect all periods. A plausible explanation is that the subsurface sampled at periods between 1-10 s (skin depth of ∼3-8 km) became more conductive over the duration of pumping due to the injection of saline fluids. This would cause a decrease in electric field strength at those periods and cause a decrease in coherency between the measured

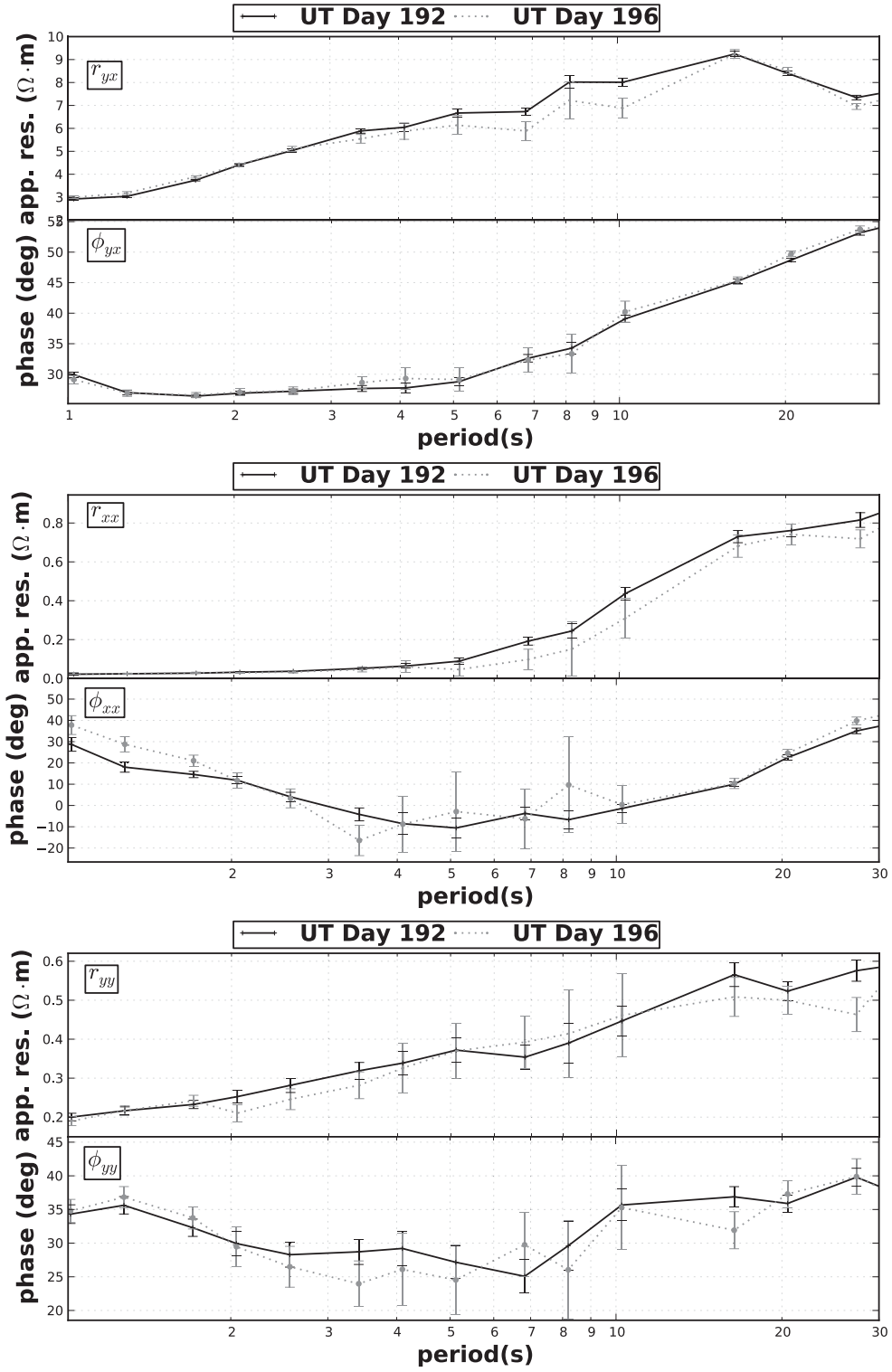

Figure 6.5: Comparison of the MT response for station pb01 on day 192 (black) and 196 (gray). Top plots are of the Z_{yx} mode (TM) showing a small coherent change in the apparent resistivity but not a corresponding change in the phase. Middle plots are the Z_{xx} component, again showing a larger change in apparent resistivity than phase. Bottom plots are the Z_{yy} components showing little coherent change above measurement error.

electric and magnetic field, propagating into an uncertainty increase in the estimation of **Z**.

After confidence is instilled in measuring observable changes, a helpful visualization is to plot a pseudo section of the apparent resistivity and impedance phase as a function of time for one station, again plotting the Z_{xy} component shows the largest change.

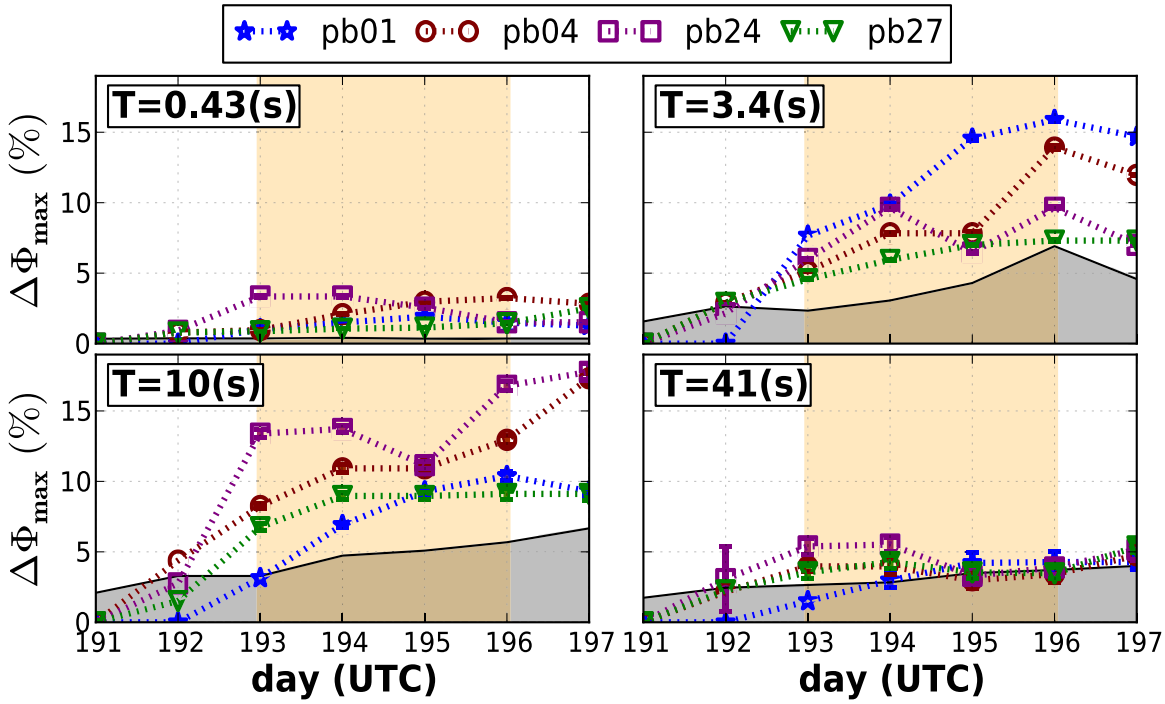

Figure 6.6: Plots of percent change in Φ_{max} (an invariant of eq. (6.1), see Caldwell *et al.* (2004)) as a function of time for selected stations and periods (T). The shaded gray region is the estimated error floor as a function of time and period, giving a baseline to which variations can be confidently estimated and interpreted. The shaded orange region designates the pumping period when fluids were injected into the subsurface. Notice that periods between 1-10 s experience a general increasing change above the error floor, while periods outside this band do not.

Figure 6.7 displays both apparent resistivity and impedance phase versus period and time. Also, plotted is the pumping start time(yellow), pumping end time (black), and time of increased flow rates (purple). It should be noted that a 2D median filter was applied to the MT response to ensure a robust estimation of changes, where the median kernel estimated the median for 3 days and 3 periods. Interestingly, the response shows a lag of when pumping started and when an observable change occurred in the MT response. Also, it is important to note that the anomalous response is present after pumping indicating that it is not caused by noise but a conductive change in the subsurface. Furthermore, as found above the conductive changes in the MT response is causal, where the phase increases at about 1-5 s and the apparent resistivity decreases at around 8-20 s. The extra anomalous phase at 27 s is of unknown origin and is assumed to be noise because this anomaly is not observed in similar plots for other stations.

Estimating depth to the conductive anomaly can ensure the change is occurring at the correct depth. An 1D Occam inversion using the code of (Key, 2009) estimates depths ranging from 2.8-3.3 km (Figure 6.8). Only the TE mode, where the electric field is aligned with maximum change, is modeled here because of its sensitivity to subsurface electrical variations. Error bars of 2% and 4% are put on the impedance phase and apparent resistivity of the TE mode to force the model to pick out small changes in the response, the responses are plotted in Figure 6.9. The RMS of the models increase with time, which is a pattern observed in Figure 6.6, where the error in the estimation of $\hat{\mathbf{Z}}$ increases. However, the Occam inversion scheme deals with noisy data points well.

The estimated depth is 3.2 km, which is off by about 400 m from the known depth, but nevertheless is close to the expected depth range. Occam's method finds the

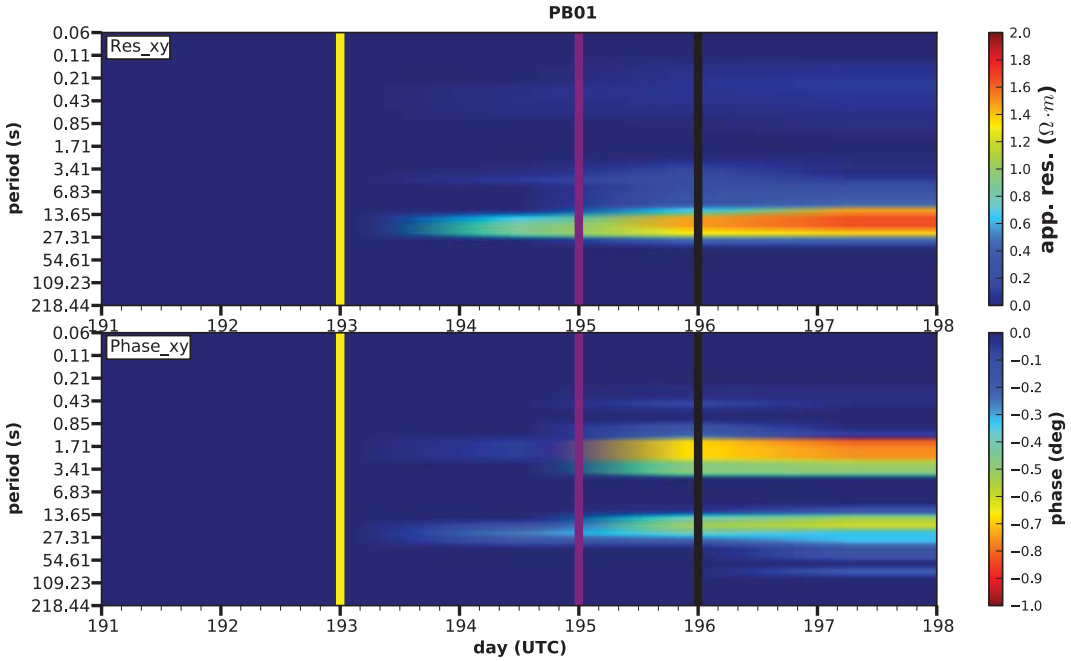

Figure 6.7: Apparent resistivity (top) and impedance phase (bottom) of the residual MT response computed as pre-injection minus subsequent 24 hour blocks for Z_{xy} from station pb01. On the y-axis is period (s) and along the x-axis is day (UTC). The yellow line is when pumping started, purple is increased flow rates and black represents when pumping seized. Notice a time lag in the MT response and when pumping started, signifying a threshold on the measurable volume of conductive material. Also, note the change in impedance phase occurs at a shorter period than the apparent resistivity supporting causality.

smoothest model possible and can smooth the resistivity structure increasing the uncertainty in the depth. Similarly, because MT is an integral method, if the conductance above the body is not properly estimated the depth will also not be accurately estimated. Accuracy can be improved with other electric and electromagnetic measurements.

The change in resistivity with depth is larger than the observed change in the MT responses, which could be because the model is fitting noise in the data, biasing the conductive change. Nevertheless, the point of the depth estimation is to get an approximate depth of the change to give confidence that observed variations in the MT response are invoked by a conductive body at approximately 3.6 km.

Mapping the apparent resistivity as a function of time and period can infer spatial variation of the MT response. Figure 6.10 displays the variation in apparent resistivity over period and time. Again a 2D median filter has been applied as above. Interestingly, the largest conductive anomaly occurs just to the North of the injection well at 16-20 s but then increases towards the East at later periods. This could be because two fault systems were penetrated at different depths, one trending NNE at a shallow depth and one trending ESE slightly deeper. Micro-seismic data suggests that deeper micro-earthquakes occurred to the East of the injection well, however this correlation is still speculative as variational magnitude in apparent resistivity is still small. Directional interpretation of the MT response can be more helpful.

Dimensional variations in the MT response can be estimated from the residual phase tensor eq. (6.1). Interestingly, phase tensor residuals are larger than forward modeling predicts by an order of magnitude, suggesting a greater contrast between host rock and the conductive body, also supporting experimentation over feasibility studies as feasibility studies are like thought experiments and cannot be tested unless experiments

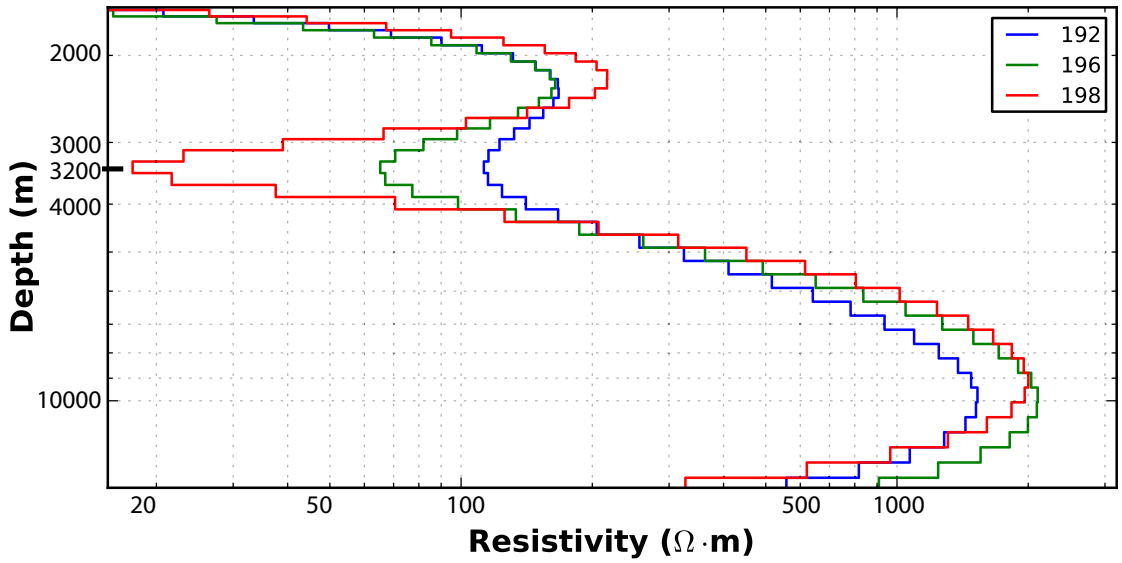

Figure 6.8: Depth estimation from 1D Occam inversions of TE mode for different days measured at station pb24, labeled in the legend. Day 192 is pre-injection, 196 is the last day of pumping and day 198 is 2 days after the injection. The conductive anomaly occurs at about 3200 m which is 400 m shallower than the injection point. This is because Occam is a smooth inversion and the depth depends on the resistivity structure of the overburden. Here the overburden resistivity is under estimated giving a shallower depth. Nonetheless, the depth is on the correct order of magnitude, supporting observed changes are caused by a conductive change in subsurface resistivity structure.

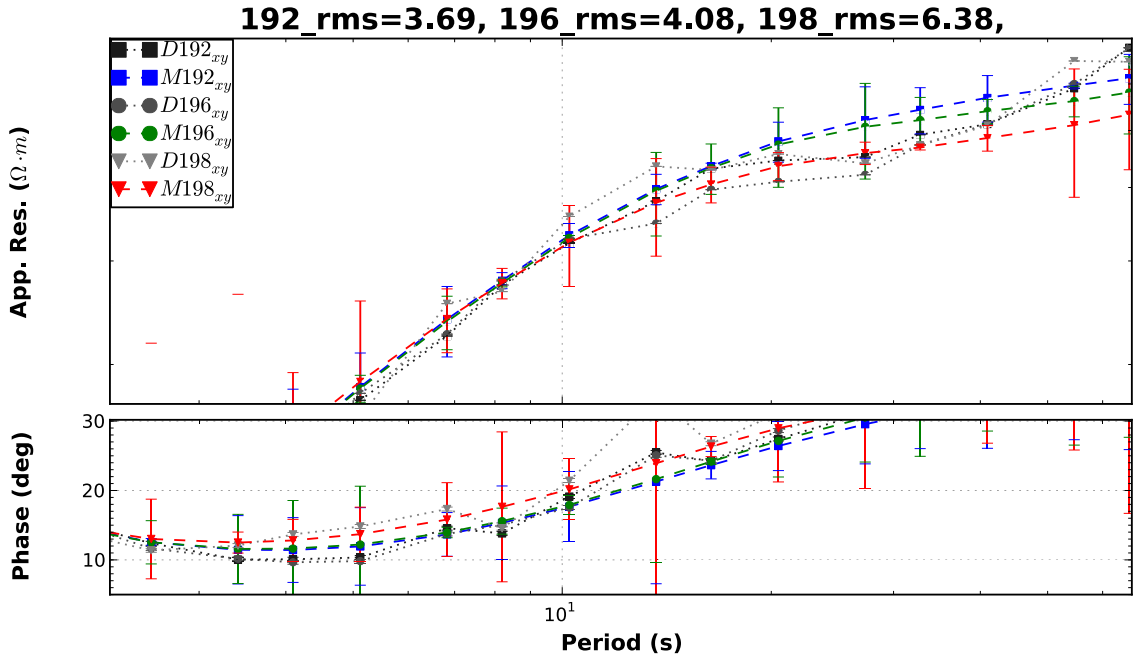

Figure 6.9: Responses from depth estimation from 1D Occam inversions of TE mode of different days measured at station pb24, labeled in the legend. Day 192 is pre-injection, 196 is the last day of pumping and day 198 is 2 days after the injection.

are conducted. Three general observations can be made from phase tensor residuals represented as an ellipse (Figure 6.11). First, average ellipse orientation aligns in a NE direction from periods between 1-10 s (Figure 6.2). This is also the regional strike direction and orthogonal to principle stress direction suggesting a correlation between electric strike and principle stress directions. Second, larger changes are observed to the NE of the borehole. Third, for periods between 1-10 s, size of phase tensor ellipses

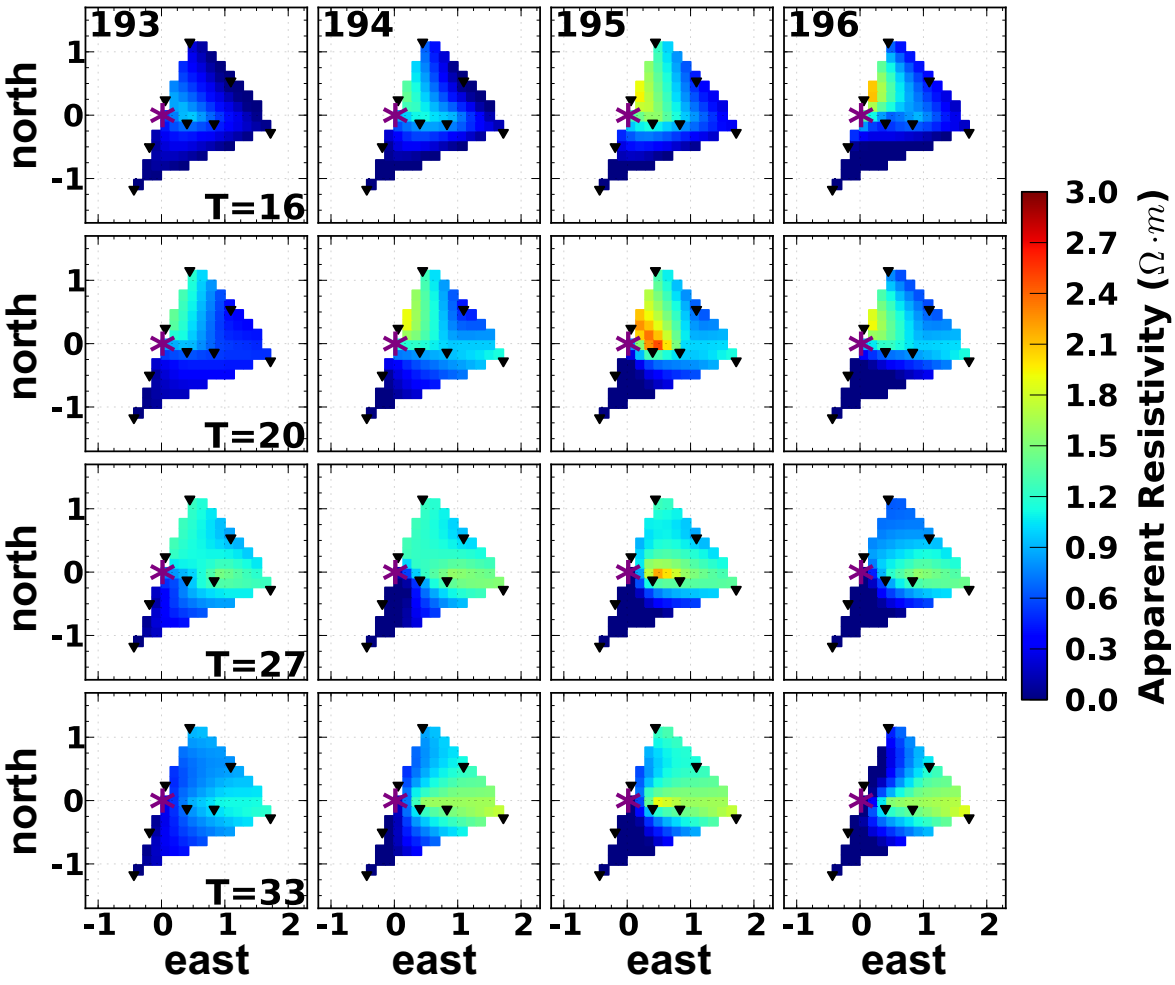

Figure 6.10: Maps of apparent resistivity residuals for $\mathbf{Z}_{xy}$ estimated as the difference between pre-injection apparent resistivity and apparent resistivity from subsequent days. A 2D median filter has been applied with a 3 x 3 window estimating the median of 3 days and 3 periods per station ensuring estimation of bulk coherent variations. The map is interpolated by a nearest neighbor algorithm that can smear anomalies. Each column represents a day labeled in UT and each row represents a different period (s). The borehole is marked by the purple asterisk and stations are marked by black triangles. Changes are observed to the NE of the borehole and are coherent between most stations. Distortion is removed following Bibby *et al.* (2005).

increases and face color becomes more red with each day, imaging changing geoelectric structure due to a growing conductive body at depth. However, phase tensor orientation can be influenced by noise but also exhibits behavior not of a simple homogeneous conductive block, but a complicated system of heterogeneous anisotropic pathways. Further work and more experimentation needs to be done to fully understand the MT response in time-variant fractured media. These three observations correlate well with micro-seismic data showing the majority of micro earthquakes occurred NE of the borehole and elongated generally in the NE direction. It is important to note that micro-seismic data can locate fractures opening, while MT estimates volumetric changes in the geoelectric structure associated with fluid filled fracture networks. Therefore, these two geophysical techniques should be used in tandem as complementary pairs.

6.6 Conclusion

In this experiment, MT has been successfully applied to monitoring a fluid injection for the first stage of an EGS, where changes in the MT response are assumed to originate

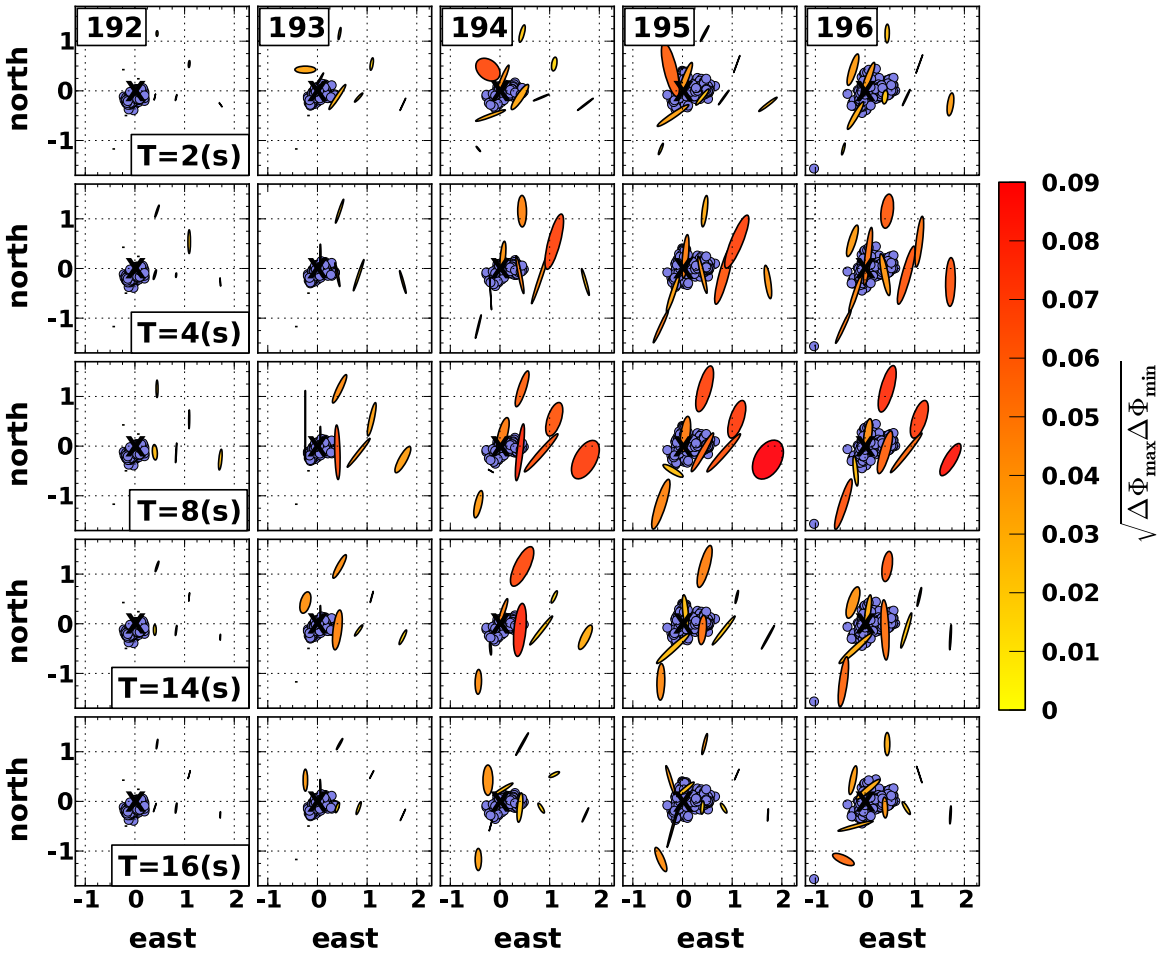

Figure 6.11: Maps of phase tensor residual ellipses calculated as eq. (6.1) and colored as the arithmetic mean of Δ. Each column represents one day and each row represents one period. Paralana 2 borehole is marked as an X. An outline of the seismic cloud for each day is represented as the gray blob with interpreted faults (gray lines) from Hasting *et al.* (2011). Generally, ellipse orientation aligns with interpreted faults while size increases from day 193 to 196.

from the injection of electrically conductive fluids connected by induced fracture networks at 3.6 km depth. Though the variations in MT parameters are on the order of a few percent, they are coherent in space and time, while being above measurement error. Furthermore, temporal and spatial variations correlate with the pumping schedule and results from a concurrent micro-seismic survey. Plotting apparent resistivity and impedance phase of pre-injection and subsequent 24 hour blocks provides visual conformation that observable changes exist above measurement error, while inverting the MT response as a function of time using a 2D algorithm is useful for estimating depth to the evolving conductive body, though absolute depth can have large errors stemming from regularization of the smooth inversion schemes and inaccurate estimation of the resistivity structure above the injected anomaly. Estimating an error floor for each MT parameter can be used as another tool to instill confidence in observable changes. Finally, mapping the phase tensor residuals prove most informative for observing temporal and spatial changes generated by a growing conductive body at depth, indicating that reservoir evolution is a complex growth to the NE of the borehole, expanding in a NE preferred orientation.

MT alone cannot provide all the information about the reservoir. The combination of MT and micro-seismic measurements should be used as a complimentary pair to characterize injected fluids in the subsurface. Micro-seismic tomography provides

locations of fractures opening up, a point in the subsurface. However, micro-seismic tomography can not discriminate whether that fracture is fluid filled or connected to other fractures. MT is sensitive to volumetric conductivity contrasts and can suggest whether the volume of seismic events are fluid fill or not.

Two methods to improve monitoring MT surveys are to utilize more than one remote reference to better understand regional variations in the magnetic source field (Kappler *et al.*, 2010) and increase the number of stations to cover a larger area for improved lateral resolution. Positive results from this experiment demonstrate the potential of expanding MT monitoring to other fluid injections, such as non-conventional natural gas where controlled source techniques can be applied (Orange *et al.*, 2009; Streich *et al.*, 2010; Wirianto *et al.*, 2010).

Chapter 7

Time-lapse magnetotelluric monitoring of an enhanced geothermal system

Peacock[1], J. R., S. Thiel[1], P. Reid[2] and G. S. Heinson[3]

[1]South Australian Centre for Geothermal Energy Research, University of Adelaide, Adelaide, South Australia, 5005

[2] Petratherm Ltd., Level 1, 129 Greenhill Road Unley SA 5061

[3]TRaX, Department of Geology and Geophyics, University of Adelaide, Adelaide, South Australia, 5005

Geophysics; 2012: Submitted

STATEMENT OF AUTHORSHIP

TIME-LAPSE MAGNETOTELLURIC MONITORING OF AN ENHANCED GEOTHERMAL SYSTEM

***Geophysics*– 2012 –Submitted**

PEACOCK, J. R (Candidate)

Planned survey, collected data, processed, analyzed and wrote results.

I hereby certify that the statement of contribution is accurate

Signed..... Date 24/08/2012

THIEL, S.

Planned survey, collected data, helped analyze data.

I hereby certify that the statement of contribution is accurate

Signed..... Date 24/08/2012

REID, P.

Helped plan survey, helped with geological interpretation, provided logistical support and funding.

I hereby certify that the statement of contribution is accurate

Signed..... Date 22/08/2012

HEINSON, G. S.

Provided valuable supervision, helped plan survey, aided in data interpretation and critical analysis.

I hereby certify that the statement of contribution is accurate

Signed..... Date 24/08/2012

Abstract

Realization of enhanced geothermal systems (EGS) prescribes the need for novel methods to monitor subsurface fracture connectivity and fluid inclusion. Magnetotellurics (MT) is a passive electromagnetic method sensitive to electrical conductivity contrasts as a function of depth, specifically hot saline fluids in a resistive porous media. In July, 2011, an EGS fluid injection at 3.6 km depth near Paralana, South Australia was monitored by comparing repeated MT surveys before and after hydraulic stimulation. An observable coherent change above measurement error in the MT response is present and causal, in that variations in phase predicts variations in apparent resistivity. Phase tensor residuals prove the most useful representation for characterizing alterations in subsurface resistivity structure, while resistivity tensor residuals aid in determining sign and amplitude of conductivity variations. These two tensor representations of the residual MT response suggest fluids migrated towards the northeast of the injection well along an existing fault system trending north-northeast. Forward modeling and concurrent micro-seismic data support these results, though micro-seismic data suggest fractures opened along two existing fracture networks trending north-northeast and northeast. This exemplifies the need to employ electromagnetic methods for monitoring fluid injections due to its sensitivity to conductivity contrasts.

7.1 Introduction

World energy production is gradually shifting from fossil fuels to renewable energy sources increasing the necessity for novel methods and technologies to be developed. A promising energy source is geothermal, specifically EGS, which not only produces base load power but can be implemented for direct use of heating and cooling buildings (Green & Nix, 2006), the largest energy drain on the grid. The exciting advantage of geothermal is that it can be exploited anywhere compliments of the Earth's natural thermal gradient, where typical target depths for electricity generation being between 3-10 km (Tester *et al.*, 2006). Additionally, geothermal energy production is environmentally friendly, producing a minimal foot print with minimal emissions of greenhouse gasses (DiPippo, 1991). First tested at Fenton Hill, NM in the 1970's, EGS is theoretically simple: introduce fluids into a zone of thermally active lithology via fracture stimulation to create a reservoir for heat transfer, then extract the hot fluids to produce energy. Unfortunately, realizing an EGS in practice proves to be difficult stemming from limited experience and technologies, and multiple unknowns of the subsurface (Brown, 1995). The first step to creating an EGS is fracture stimulation to establish porosity and more importantly permeability within the thermally enhanced lithology, however characterizing and locating connected fluid networks within the subsurface proves to be difficult. The main geophysical technique to characterize fractures opening during hydraulic stimulation is micro-seismic (Wohlenberg & Keppler, 1987; House, 1987), where size and orientation of the fractures can be estimated from shear wave splitting (Rial *et al.*, 2005). However, micro-seismic is not directly sensitive to fluids being included in fractures nor how well fractures are connected. Electromagnetic (EM) techniques are directly sensitive to electrical conductivity contrasts, specifically connected paths of conductive material, such as a brine solution in a resistive host rock.

Electric and EM methods have been successfully employed to monitor subsurface processes. Typically used for shallow targets (above $\sim$ 2 km), the self-potential (SP) method maps electrical potential differences as a function of position on the surface and

is directly sensitive to subsurface fluid movement (ex. Aizawa *et al.* (2005); Yasukawa *et al.* (2005)). However, deeper targets need different methods. Magnetotellurics (MT) is a passive EM method that measures the Earth's response to natural time varying magnetic fields, which gives it a versatile depth of investigation (Kaufman & Keller, 1981). In one of the first detailed long term monitoring MT studies, Kappler *et al.* (2010) collected continuous MT measurement along the San Andreas Fault. No precursor electromagnetic signal to seismic activity was detected, however Kappler *et al.* (2010) described vigourous and thorough analysis methods valuable to monitoring MT surveys. Bedrosian *et al.* (2004) conducted one of the first MT surveys aimed at monitoring a fluid injection. They continuously measured during the fluid injection with 11 MT stations setup in an L centered on the borehole. Then, 2D inversions were employed to compare the MT response before and after, unfortunately they found noise masked any MT response originating from fluid inclusion at depth. Aizawa *et al.* (2011) deployed two continuous MT stations aimed at monitoring volcanic processes on Sakurajima volcano, Japan and found a 20% change in the apparent resistivity coincident with subsurface uplift and degassing. These monitoring surveys support the extension of MT to a monitoring tool, while exhibiting the necessity for precise, accurate, and spatially dense measurements.

Presented are the first positive results from repeated MT surveys collected before and after a hydraulic stimulation for the first phase of an EGS at Paralana, South Australia. First, a few key points of the MT method will be provided, followed by a description of the experimental setup and hypothesis. Subsequently, data analysis of pre and post injection surveys will be followed by a detailed discussion and conclusions.

7.2 Magnetotellurics

MT is a passive method that measures the Earth's electromagnetic response to natural time varying magnetic fields, first formulated by Tikhonov (1950) and Cagniard (1953). Measured orthogonal lateral components of the electric fields ($\mathbf{E}$) and magnetic fields ($\mathbf{B}$) are assumed to be linearly related in the frequency domain by the rank 2 impedance tensor $\hat{\mathbf{Z}}$ through $\mathbf{E}(\omega) = \hat{\mathbf{Z}}\mathbf{B}(\omega)$. As with most EM methods, MT is measuring a diffusive process where energy is only lost in the system. As a consequence, the depth of penetration, or skin depth $\delta = \sqrt{2\rho T/\mu_o}$, is proportional to the period of the inducing magnetic field, where T is period in seconds and ($T = 1/\omega$), μ_o is the magnetic permeability of free space (N/Amp^2)and ρ is resistivity in Ohm meters (Ω·m). Furthermore, MT is a volumetric measurement that incorporates the hemisphere of radius δ. One unfortunate consequence of this is that resolution is also dependent on source field period and decreases with increasing depth.

Information about the electromagnetic source field is crucial to understanding variations in the MT response (Kappler *et al.*, 2010). Time-frequency distributions characterize source field power as a function of time and frequency suggesting times of maximum coherency. Moreover, principal component analysis (PCA) of the scaled spectral density matrix (SDM) can give estimates about the number of sources present in the data, where typical MT data have only two sources corresponding to orthogonal polarizations (Egbert, 1997). Here a robust time-frequency distribution formulated by Djurovic *et al.* (2003) is employed to estimate the SDM, which is scaled to represent the principal components in signal to noise power ratio, following Egbert (1997).

Two common ways to represent the data are the apparent resistivity and impedance phase. The relationship between apparent resistivity and phase is causal, where phase predicts apparent resistivity through the Kramers-Kronig dispersion relationships. It

should be noted that the dispersion relations should be used with great care as they can be quite often violated (Fischer & Schnegg, 1993; Berdichevsky & Dmitriev, 2008). The apparent resistivity is the volumetric electrical resistivity of the hemisphere circumscribed by δ and is calculated as the modulus of $\mathbf{Z}$ scaled by the period and magnetic permeability. Typically, apparent resistivity and phase are analyzed and visualized in two separate polarizations, however it can be useful to use all four components of $\mathbf{Z}$, such as estimating the determinant (Spichak & Manzella, 2009) or tensor representation for directional and dimensionality characterization (Reilly, 1979; Weckmann *et al.*, 2003; Caldwell *et al.*, 2004).

Reilly (1979) formulated a real apparent resistivity tensor (RT) and real apparent permittivity tensor from the complex admittance tensor (inverse of $\mathbf{Z}$) to describe the MT response in anisotropic media. Though, one drawback is that RT can be influenced by static shift and near surface distortions, which rotates ellipse axis but does not change the shape (Weckmann *et al.*, 2003). Formulated by (Caldwell *et al.*, 2004), the phase tensor (PT) is an alternative representation of the MT response. The PT is simply the ratio of the imaginary part of the impedance tensor to the real part, $\mathbf{\Phi}(\omega) = Im\{\mathbf{Z}(\omega)\}/Re\{\mathbf{Z}(\omega)\}$. A fortuitous result is that near surface distortions are removed and only the regional response remains. Both tensor representations can be represented as ellipses following (Bibby, 1986), where orientation is related to geoelectric strike and the shape characterizes dimensionality of subsurface resistivity structure. For an extensive study on PT behavior in anisotropic media see Heise *et al.* (2006) and Caldwell *et al.* (2004). Similarly, for a detailed description on RT behavior see Weckmann *et al.* (2003). For this study estimating the residual between pre-injection and post-injection MT responses is a key parameter of interest. This can be extended to tensor representation by calculating the residual PT or RT between collocated measurements temporally spaced as equation 7.1, where $\mathbf{\Phi}_1$ is PT or RT pre-injection, $\mathbf{\Phi}_2$ is the PT or RT post-injection, Φ^{-1} is the inverse, and $\mathbf{I}$ is the identity matrix.

$$\mathbf{\Delta\Phi}_{1,2} = \mathbf{I} - (\mathbf{\Phi}_1^{-1}\mathbf{\Phi}_2) \tag{7.1}$$

7.3 Experiment

South Australia is a prime target for EGS because it contains some of the hottest granites in the world (McLaren *et al.*, 2002). One EGS target lies in the Northern Flinders Ranges near the Paralana Hot Springs (Hillis *et al.*, 2004), the only amagmatic thermal spring in the world. The heat source is an anomalously enhanced density of radiogenic elements within the Paleoproterozoic to Mesoproterozoic gneiss, granites and metasediments of the Mount Painter Domain that underly the Flinders Ranges. Anomalous surface heat flow in parts of the Flinders Ranges can be as much as 90 mW/m^2 (Brugger *et al.*, 2005), while at the Paralana geothermal drill site the estimated heat flow anomaly is 113 mW/m^2 (Neumann *et al.*, 2000). Paralana 2 borehole has been drilled to 4012 m and cased to 3725 m, where bottom hole temperature is estimated to be 190 C. Saline fluids ($\rho = 1.5\ \Omega$·m) were encountered at 3860 m indicating a pre-existing fluid filled fracture network, which could be linked with the Great Artesian Basin.

The goal of this experiment is to measure a change in the MT response originating from the introduction of a saline reservoir at depth. To do this, the same survey layout is repeated before and after fluids are injected and then compared. The survey layout contains 56 stations with the design parallel and orthogonal to geoelectric strike (NNE), following existing seismic lines (Figure 7.1). Two main orthogonal lines, oriented close to the cardinal directions, intersect on the Paralana 2 borehole. Each line contains 22

stations with variable spacing starting at 200 m near the borehole increasing to 1.5 km at the extremities. Two off diagonal lines of 6 stations each, again centered on the borehole with variable spacing, increase spatial coverage. Two remote reference stations are located to the South of the survey along existing roads, one 60 km and the other 80 km away. AuScope broadband MT instruments are employed utilizing Cu-$CuSO_4$ non-polarizing porous pots as electrodes and LEMI induction coils as magnetometers. Dipoles are approximately 50 m, dictated by brush, topography and cable length, and deployed in an L-shape. Earth Data Loggers store the data at a sampling rate of 500 Hz. Instruments are synchronized by GPS and powered by 12 V gel cell batteries. Four base surveys were collected pre-injection with one post-injection survey.

In July, 2011, 3.1 million liters of saline water (0.3 Ω·m) was pumped into a Mesoproterozoic metasediment sequence via a 6 m perforated zone in the Paralana 2 borehole around 3680 m. Pumping lasted 4 days starting on UT day 193 with low flow rates (2 barrels per minute) slowly increasing step wise to 15 barrels per minute, periodically shutting in. Pumping ceased on UT day 196 when the well was shut in. Coincidentally, a micro-seismic array and an MT array were deployed to monitor subsurface changes originating from fluid injection. The micro-seismic array measured over 13,000 events with 98% being less than magnitude 1.0 (Hasting *et al.*, 2011),where the data suggest fractures opened in a preferred NE orientation along four existing fault systems that strike NNE, NE, and ESE (Figure 7.1). Most seismic activity occurred along the NE and NNE faults extending approximately 1 km x 200 m x 400 m. This is supported by MT data collected during the injection, suggesting most of the fluid propagated into these two fault systems (Peacock *et al.*, 2012).

7.4 Hypothesis

Forward modeling can be educational in testing MT as a viable method to monitor fluid inclusion at depth (Pellerin *et al.*, 1996; Spichak, 2001; Bedrosian *et al.*, 2004; Orange *et al.*, 2009; Streich *et al.*, 2010; Wirianto *et al.*, 2010), notwithstanding forward modeling can only predict plausible outcomes not accurately determine experimental outcomes. The 3D forward modeling code of Mackie *et al.* (1993) was employed to model a resistivity structure derived from pre-injection MT surveys, which contains a conductive (10 Ω·m) top 1 km, then a layer of 200 Ω·m. A resistive quarter space (700 Ω·m) that trends NNE with a dip of 15 degrees towards the East is placed 15 km to the West of the borehole on the surface to represent the Flinders Ranges and the Mount Painter Domain. A block of 0.3 Ω· m oriented in the NE direction with volumetric dimensions of 1.5 km x .1 km x 500 m was introduced at 3.6 km depth to represent fluids introduced into an existing fault. The residual between the MT response without and with a conductive block was calculated for the four aforementioned representations, namely apparent resistivity, impedance phase, RT, and PT where a few key observations can be made.

The most important observation is that the variational magnitude in impedance phase and apparent resistivity introduced by the conductive body is on the order of a few percent. Interestingly, the limiting factors of residual magnitude depend significantly on conductivity of the sediment overburden, size and conductivity contrast. Secondly, apparent resistivity variations occur in the period band of 10-30 s, while phase changes develop in the period band of 1-10 s. An unfortunate reality is that variations in the MT response are suggested to occur in the MT dead band (1-10 s) where signal power is naturally low, especially from 2009-2011.

Multiple methods can be employed to compare the MT response before and after

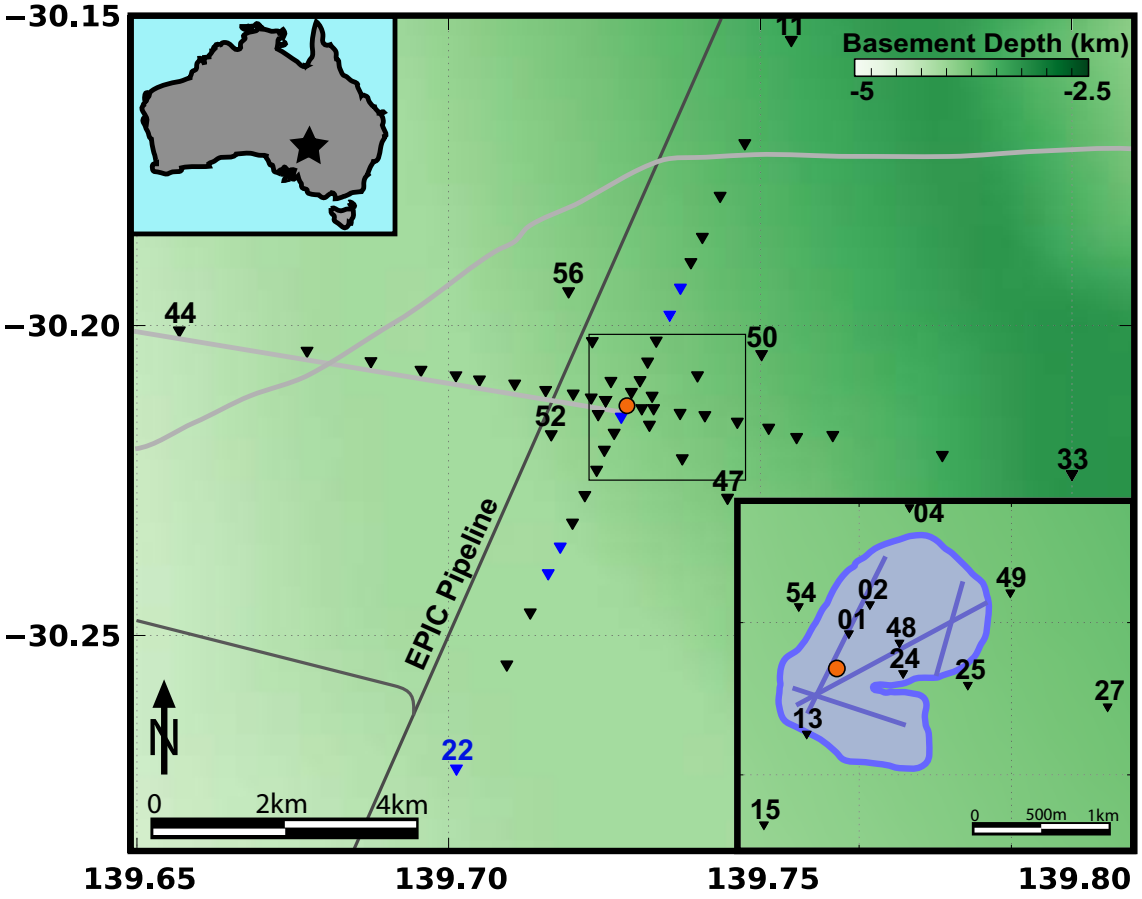

Figure 7.1: Map of MT station locations (triangles) centered on the Paralana 2 borehole (orange circle) and important infrastructure (roads–light gray, gas pipeline–dark gray). Blue triangles indicate stations that malfunctioned in at least one of the surveys and are not used for analysis. Numbers are placed on the outermost station for each line, subsequent station numbers count down towards the borehole. The background color depth to basement. The rectangle is blown up in the bottom right inset showing the approximate seismic cloud (gray blob) and interpreted faults (gray lines).

fluids are injected into the system. The approach of Bedrosian *et al.* (2004) of modeling the data and comparing before and after has a few drawbacks, such as smoothing over small changes and model sensitivity to near surface distortions. Another method would be to compare the apparent resistivity and phase. Again, comparing the apparent resistivity needs to be done with care so as to remove distortions caused by near surface inhomogeneities between measurements. Spichak & Manzella (2009) suggests estimating the determinant of the impedance tensor for monitoring purposes because the determinant incorporates all components of the impedance tensor, measuring the bulk change in electrical properties of the subsurface. However, in this experiment micro-seismic data suggest that fractures have a preferred orientation and propagation direction to the NE that should be discernable by MT, where the $\hat{\mathbf{Z}}_{xy}$ should be larger than $\hat{\mathbf{Z}}_{yx}$. Therefore, methods that represent the residual in a spatial sense are desirable, such as PT and RT residuals.

Two visualizations prove most useful for observing residual changes in MT parameters. First, mapping tensor residuals as a function of period is useful for visualizing lateral variations (Figure 7.2). Second, plotting a pseudo section of the MT parameters, where the vertical axis is period and the horizontal axis is distance, is useful for estimating variation with depth (Figure 7.14 and 7.13). Behavior of RT and PT residuals between measurements without and with a conductive body at depth will be exemplified with the aforementioned forward model.

Figures 7.2, 7.14, and 7.13 demonstrates behavior of the residual PT ellipses, where the color represents the geometric mean of the PT residual. Generally, orientation of PT residual ellipses align with the direction of largest change between collocated measurements, specifically, a circle represents a scalar change and an ellipse represents a larger change in one direction in subsurface resistivity structure. At the boundaries of the anomaly, ellipses elongate and begin to differ in shape relative to subsurface resistivity structure. More precisely, to the East ellipses align with the boundary edge and are elongated in a NNE direction, but to the West ellipses show more homogeneous variation being more circular caused by the resistive block representing the Flinders Ranges. Also, the areal extent to which PTs are influenced by the conductive anomaly is proportional to the depth of the body and varies with period. At shorter periods the areal influence is proportional to anomaly size. Moreover, the areal extent is largest at a period that has a skin depth proportional to anomaly depth. Ellipses align to point towards the center of the conductive anomaly at longer periods suggesting that PT residuals can also locate vertical boundaries. However, estimating a depth cannot be done from phase information alone unless an absolute resistivity measurement is available to scale phase responses, also care must be taken as the two dominant polarization of the PT are sensitive to different depths. Furthermore, face color indicates variational magnitude, but it does not identify whether the change is caused by a conductive or resistive variation; this can be rectified by utilizing the RT. For more on PT behavior see Heise *et al.* (2006) and Caldwell *et al.* (2004).

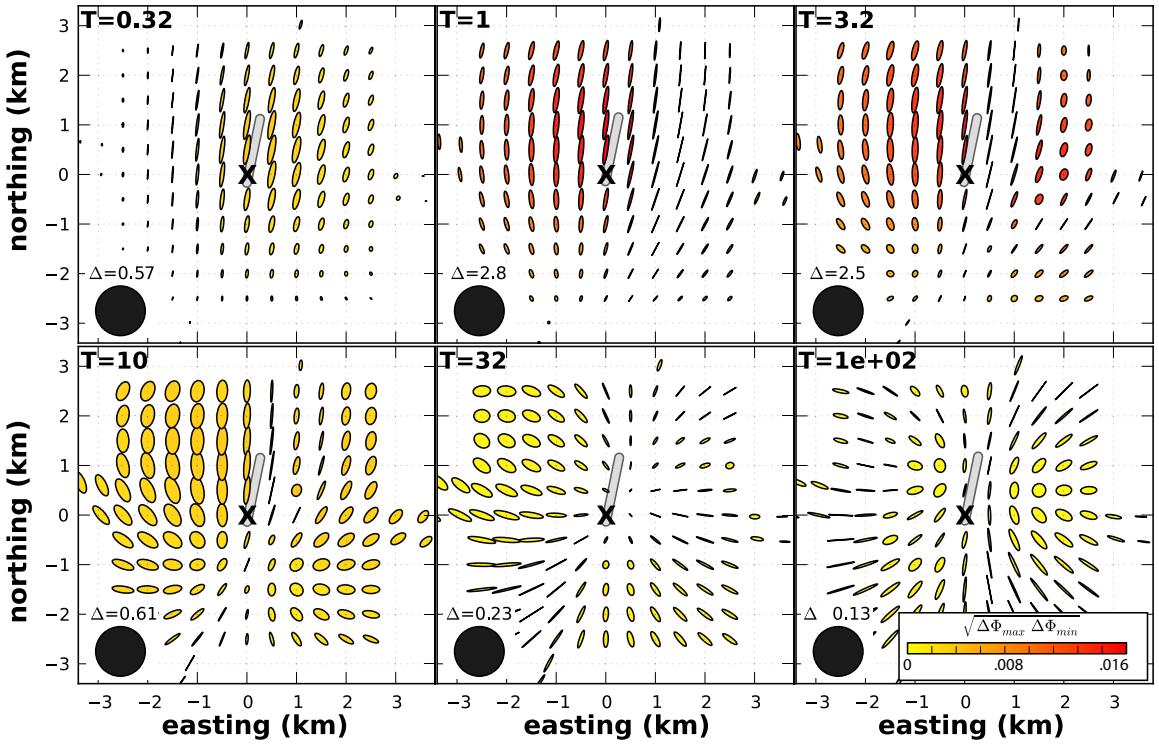

Figure 7.2: Maps of PT residuals between forward models without and with a conductive anomaly (light gray square) of 0.3 Ω·m oriented NNE elongated about 1.5 km x .1 km x 500 m. Each panel represents a different period (s) labeled in the top left. Scale of the ellipse residual ($\times\ 10^{-3}$) is represented by the black circle in the bottom right of each block. Color of the ellipses represents the arithmetic mean of the PT residual eq. (7.1). Generally, the residual ellipses orient in the direction of largest change between pre and post conductive body measurements. Notice ellipses behavior around the boundaries of the conductive anomaly.

Behavior of residual RT ellipses are similar to PT ellipses where the residual is oriented in the direction of greatest change (Figure 7.3, 7.14, and 7.13), however subtle

differences exist. Here, ellipse face color is calculated as the difference between pre and post-injection RT determinants, representing resistivity variation and indicating whether the change is resistive or conductive. As with the PT residuals, near the lateral edges of the conductive anomaly, ellipses tend to align with the anomaly's electric strike. However, at long periods (20 s), the RT residual continues to be effected by the conductive body, this is because of the volumetric nature of MT. RT cannot provide information about depth, just lateral boundaries and resistivity contrast. Utilizing both PT and RT residual analysis spatial characterization of alterations in subsurface resistivity structure can be estimated. For more on RT behavior see Weckmann *et al.* (2003).

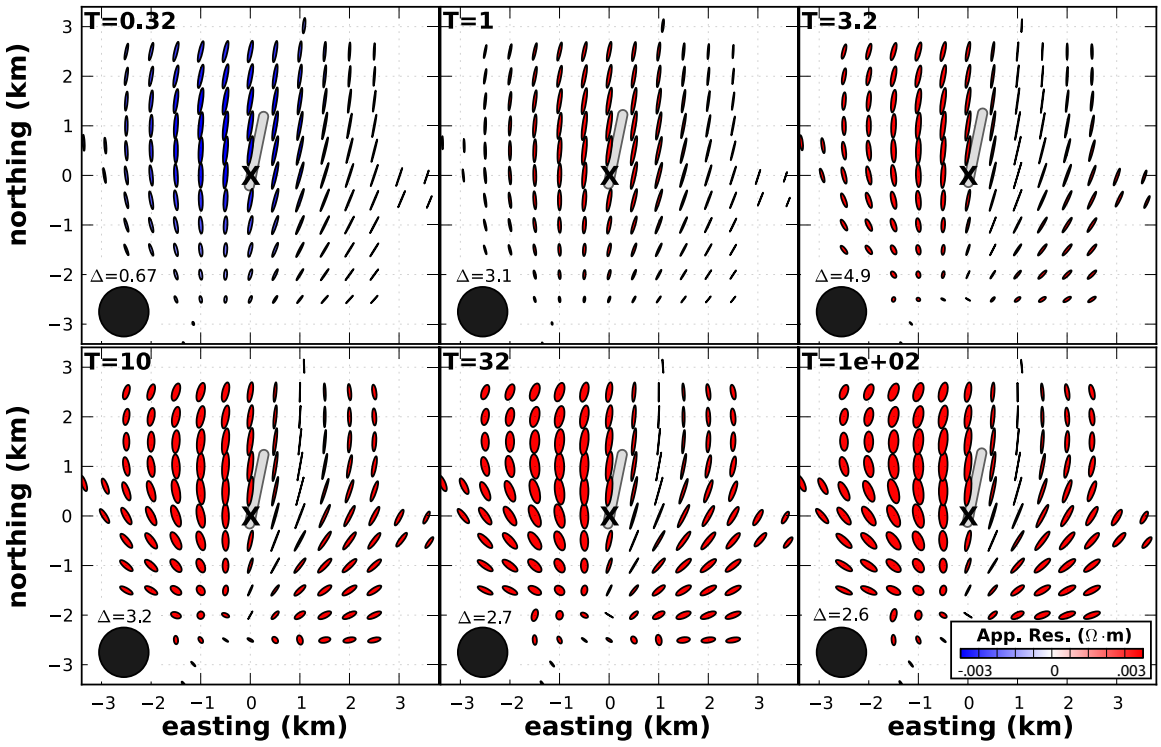

Figure 7.3: Maps of RT residuals between forward models without and with a conductive anomaly (light gray square) of 0.3 Ω·m oriented NNE elongated about 1.5 km x .1 km x 500 m. Each panel represents a different period (s) labeled in the top left. Scale of the ellipse residual ($\times$ 10^{-3}) is represented by the black circle in the bottom right of each block. Color of the ellipses represents the residual of the determinant resistivity tensors pre and post conductive body. Generally, the residual ellipses orient in the direction of largest change. Notice ellipses behavior around the boundaries of the conductive anomaly and at longer periods RT continues to be effected by the conductive anomaly.

7.5 Data

Multiple base surveys were collected to get accurate and precise data to compare with post injection data. Source field effects are estimated by the aforementioned PCA. MT transfer functions are estimated using the advanced mode of the robust bounded influence remote reference method developed by Chave & Thomson (2004), where a coherency threshold on the magnetic channels between the station and remote reference removes non-coherent magnetic noise. Each station collected at different times were processed with the same parameters that guide algorithm statistics to insure no influence from the processing code. Near surface distortions are removed following Bibby *et al.* (2005). Repeating each station exactly in the same setup is relatively easy

in the Australian outback where weathering processes are slow, unless unseasonable rains occur like in 2010-2011. Data from each survey will be discussed below.

7.5.1 Base Survey

Four different base surveys were collected due to varying data quality and for an estimation of repeatability between measurements. The first survey was collected in March 2010 during a climactically dry period. Instruments were left out for an average of 18 hours. Vertical magnetic coils were deployed at selected sites, unfortunately digging a 1.5 m hole was impossible with hand tools due to a calcrete layer at about 40 cm. The coils were buried as deep as possible, but all the vertical magnetic data collected was too noisy to use. Time-frequency analysis demonstrates power in the dead band was two orders of magnitude smaller than at long periods during local night time. Short period data were well characterized, having error bars of a few tenths of a percent. Periods above 1 s have increasing error bars especially in the MT dead band (1-10 s) and after 100 s. Characterizing the source field PCA finds 2 dominant components and a third that has a peak at 2 s and significant power at periods longer than 10 s (Figure 7.4). Two lessons were learned from this survey. First, leave the instruments out longer than 18 hours to increase the accuracy of estimating $\hat{\mathbf{Z}}$. Second, digging vertical holes requires mechanical assistance. Logistically getting a post hole digger to the outback is expensive and time consuming, therefore vertical magnetic components are not used in this study.

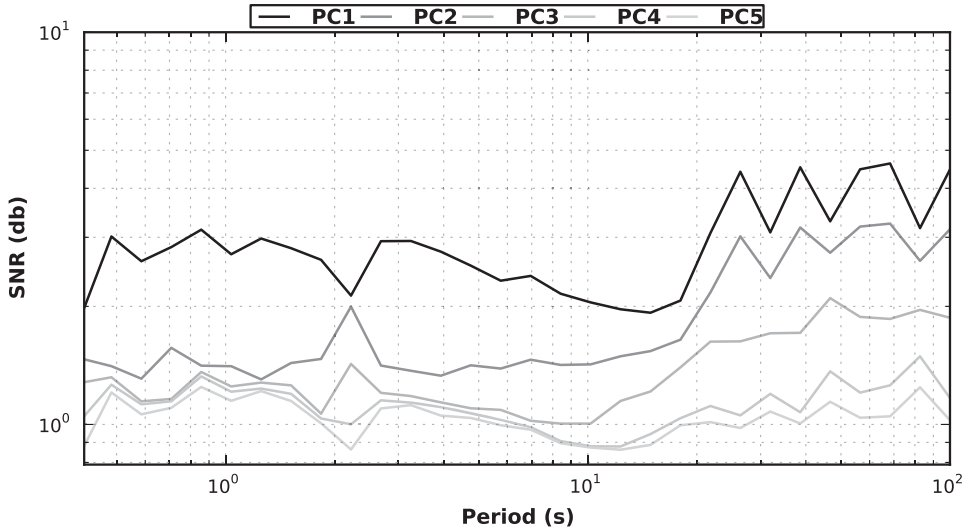

Figure 7.4: PCA as described in Section 3.1.3. Each PC is plotted in signal-to-noise ratio (SNR) in decibels against period on a log scale. The top two PC's represent the main polarizations of the magnetic source field. The others indicate affects from other sources. The peak around 2 s could be a near by set of solar panels used to power monitoring equipment for the EPIC pipeline.

Those sites that did not record quality data were repeated during a second survey in May, 2010. Learning from the first survey, instruments were deployed for an average of 30 hours. Unfortunately, the EPIC pipeline that runs parallel to the N-S line, offset 1 km to the West (Figure 7.1), was performing its annual corrosion test by sending a 3 s electric square wave every 12 s, saturating the MT data in the period range of 1-12 s and harmonics of 12 s. Also, the polarization of the square wave changed about every 12 hours. It was discovered that the remote reference stations were also contaminated with the periodic noise as the pipeline is only 20 km away and could not aid in removing said noise. To remove the periodic signal emitted by the pipeline,

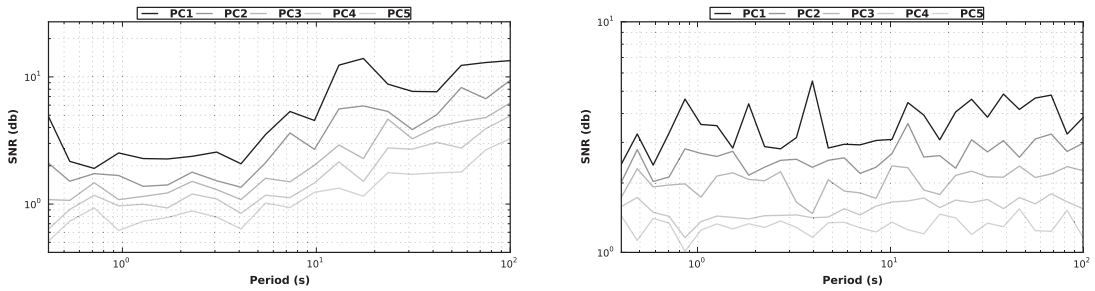

(a) Unfiltered (b) Filtered

Figure 7.5: PCA as described in Section 3.1.3. Each PC is plotted in SNR (dB) against period on a log scale. The top two PC's represent the main polarizations of the magnetic source field. The others indicate affects from other sources. The peak around 2 s could be a near by set of solar panels used to power monitoring equipment for the EPIC pipeline. The peak at 3 s and 12 s is the anti-corrosion signal emitted by the EPIC pipeline (Figure 7.6). Even with filtering these periods are still present in source field characterization but reduced in amplitude.

time domain subtraction of a data driven replication of the periodic noise was applied to each component for each station (Figure 7.6). The periodic signal was replicated by averaging multiple 12 s windows from the data and convolving that with a comb function composed of equally spaced delta functions separated by 12 s. Stations closest to the pipeline had larger error bars in estimating $\hat{\mathbf{Z}}$ for the period range of 1-12 seconds owing to larger residuals between data and the filter. Interestingly, prior to filtering PCA reveals larger amplitude around 12 s (Figure 7.5(a)). After removing the periodic noise, the first PC has spikes at 1, 3, and 12 s suggesting that not all the noise was removed (Figure 7.5(b)).

The entire survey was repeated in March, 2011, where the pipeline was again emitting a similar periodic signal, but reduced in amplitude; this was removed as before. Instruments were deployed for an average of 40 hours to increase estimation of $\hat{\mathbf{Z}}$. Again, PCA of filtered data revealed 2 components with peaks at 3 seconds and harmonics of 12 seconds as before. The farthest remote reference malfunctioned and did not record any data, so only one remote reference was used. The 10 month gap in data sets is due to unseasonable rains denying access to the site and delaying hydraulic stimulation. One natural consequence of heavy rains is lush and thriving vegetation, making it difficult to find previously dug holes at some sites. Similarly, several sites had to be repeated as the mouse population had also inflated, increasing the number of shorts caused by nibbled on cables. Just before the injection, 11 stations near the borehole were repeated to get an estimation of changes just before the injection, which were found to be minimal having a repeatability with previous surveys less than 1 percent.

7.5.2 Post Injection

One week after the injection, when all the pumping equipment was gone and the reservoir had some time to equilibrate, the full survey was repeated. The pipeline was not producing a significant signal and source power in the dead band was an order of magnitude stronger than previous surveys, consequently instruments were deployed for an average of 20 hours. Repeating the sites exactly as originally deployed was relatively easy as the disturbed top soil from previously dug coil holes and electrode holes was still visible from the surface at most sites. Sites 18, 19, 22 could not be repeated because the unseasonable rains had turned the dry creek bed into a muddy bog. Sites 05, 06,

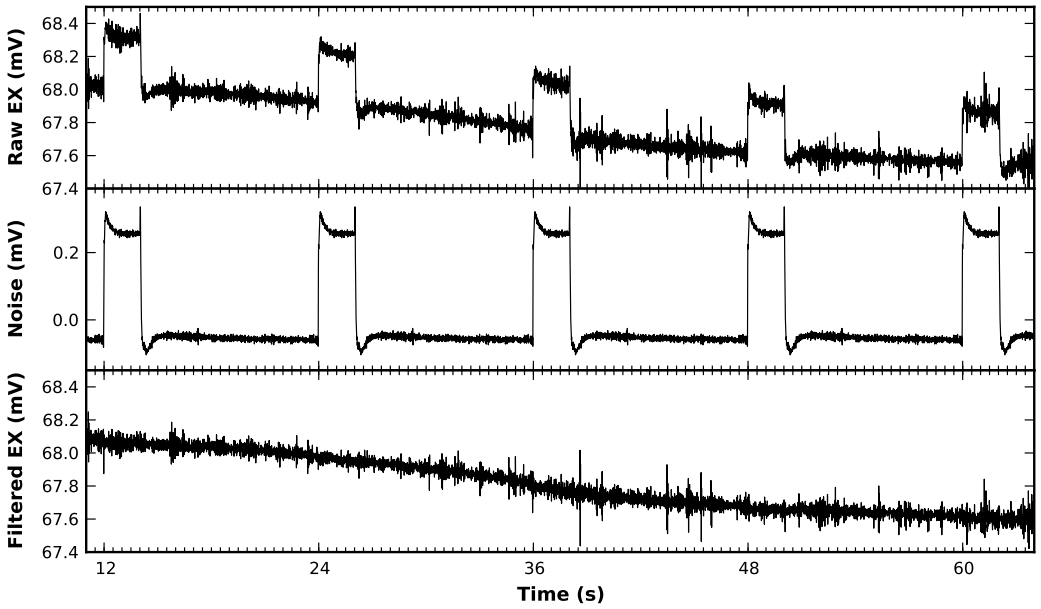

Figure 7.6: Time series from electric channel oriented with geomagnetic north displaying periodic noise emitted from a nearby gas pipeline. Top: raw time series in mV. Middle: reconstructed time series of the periodic noise from an average of data driven windows convolved with a series of delta functions spaced every 12 seconds. Bottom: residual of reconstructed noise signal and the raw time series.

and 12 did not record properly and are not used for comparing data sets. The mouse population had decreased but shorted chewed cables were still an issue, as some sites had to be repeated. A small family of mice were found nesting in the remote reference box, but did not effect the data. PCA estimates only two significant components with no peaks at 3 s or harmonics of 12 s. Average error in estimating $\mathbf{Z}$ is below 0.5% for periods smaller than 1 s and 1% for periods larger than 1 s.

7.6 Data Analysis

7.6.1 Repeatability

One important parameter to estimate when comparing data from different surveys is a measurement of repeatability, specifically what are the errors in repeating an MT site at different times. This can be calculated as a percentage difference between collocated measurements separated in time for apparent resistivity and impedance phase, though care must be taken because of bias introduced by near surface distortions not removed following Bibby *et al.* (2005). The PT is invariant to near surface distortions and is therefore a better estimation of repeatability. A graphical representation can be derived from the PT residuals eq. (7.1) between temporally spaced collocated measurements, where a circle represents a scalar change and an ellipse represents a larger change in one direction (Figure 7.9). To get a quantitative estimate of repeatability, the ratio of the PT determinant between measurements of the same site are estimated, as the determinant is invariant to rotation, near surface distortions and error in aligning the electric and magnetic fields (Bibby *et al.*, 2005).

Between the 4 base survey collected only 2 quality measurements (error in the estimation of $\hat{\mathbf{Z}}$ is less than 5% for all periods of interest 0.50-50 s) were collected for each station. These are compared using the aforementioned method (Figure 7.9). For periods up to 1 s, repeated measurements estimate the PT determinant to within 0.4

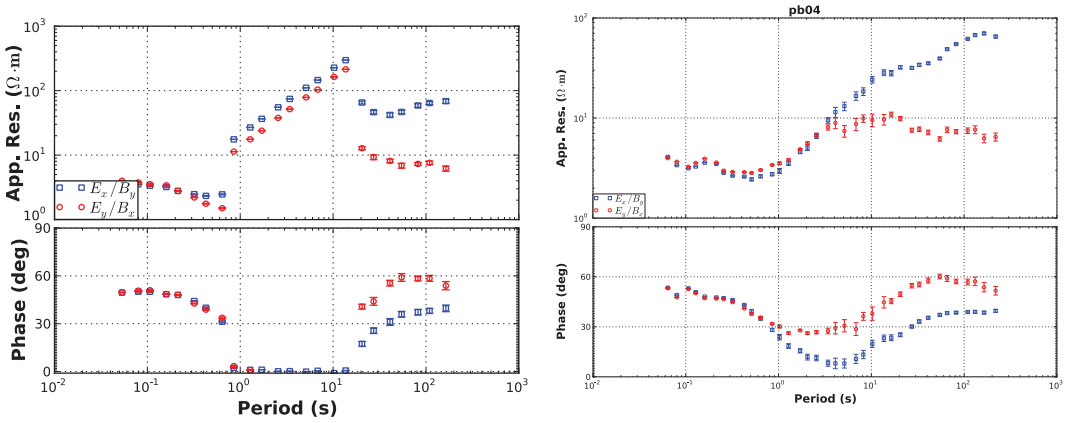

(a) Unfiltered (b) Filtered

Figure 7.7: (a) MT response computed from raw data which incorporates pipeline noise from Figure 7.6. Notice the phase goes to zero and the resistivity between 1-12 s is linear in log-log space with a slope of 45 deg. (b) MT response of data filtered using the method described in the text. The curve is much more smooth and error bars decreased.

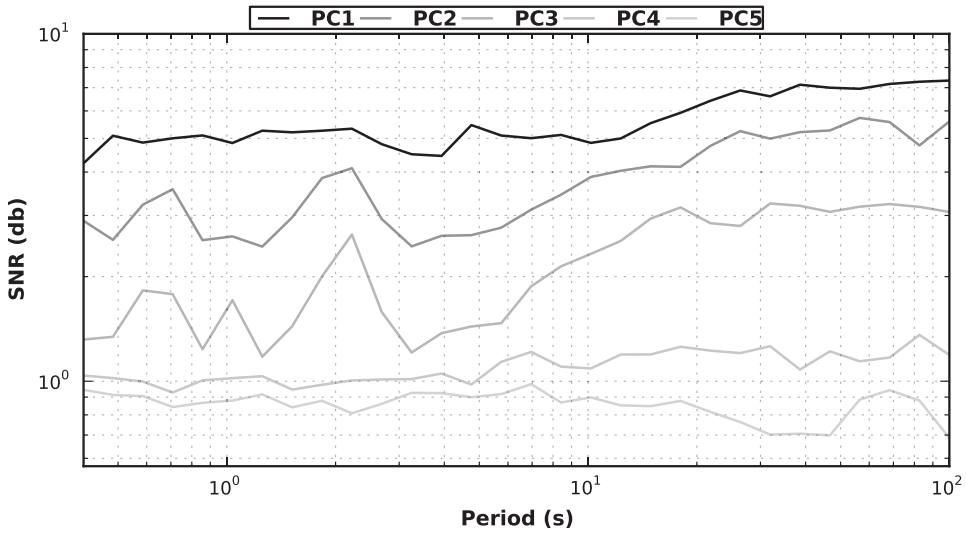

Figure 7.8: PCA as described in Section 3.1.3. Each PC is plotted in SNR (dB) against period on a log scale. The top two PC's represent the main polarizations of the magnetic source field. The others indicate affects from other sources. The peak around 2 s could be a near by set of solar panels used to power monitoring equipment for the EPIC pipeline.

percent of each other on average. However, in the MT dead band (1-10 s) and band of pipeline noise (1-12 s), PT determinants are estimated on average to within 3 percent between temporal measurements. Periods greater than 12 s are estimated within 2 percent, on average. The discrepancy in repeatability between period bands derives from low signal to noise ratio in the dead band and residual pipeline noise not removed as previously described. Seasonal variations could also lead to variations in the MT response. Unseasonable rains fell during 2010 and 2011 and got absorbed into the local hydrodynamic system flowing along faults and existing porous media. Unfortunately, the hydrodynamic system near Paralana is not well defined.

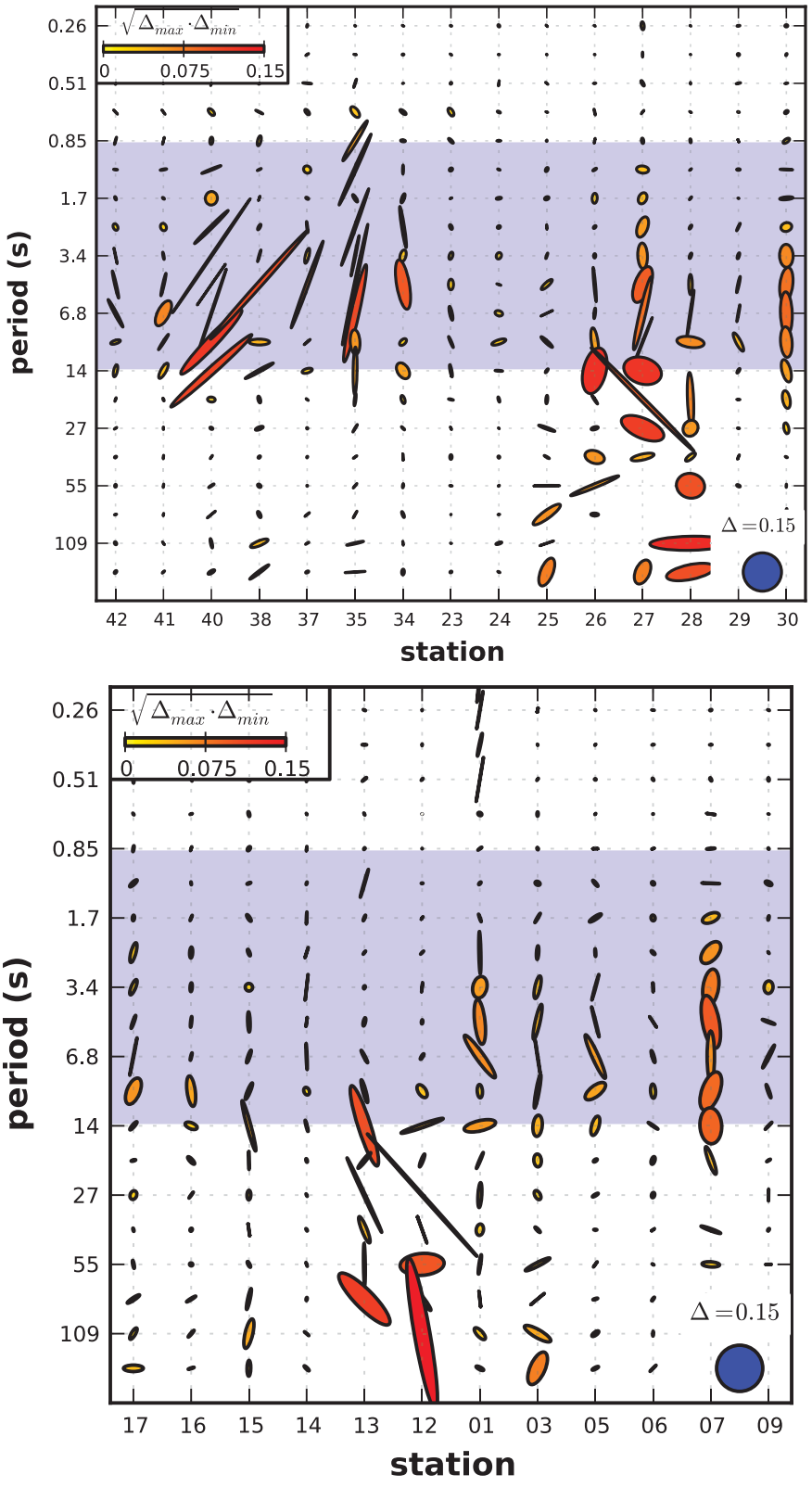

Figure 7.9: Phase tensor residuals between multiple collocated temporally space base measurements representing a measure of repeatability for the EW line. Periods down to 1 s display little discrepancy between measurements, while the MT dead band and pipeline band (1-12 s) demonstrate larger residuals introduced by inaccurate estimation of $\hat{\mathbf{Z}}$ because of low source field power. Marked in blue is the target period range. On the top is the EW line and the bottom is the NS line.

7.6.2 Before and After Comparison

For comparison purposes, data from pre-injection surveys with the smallest error in estimating **Z** are used, while all data from the post-injection survey are used. First, clear changes in the MT response pre and post-injection need to be examined to give confidence that an observable change exists above measurement error. This can be done by plotting the apparent resistivity and phase pre and post-injection to visually confirm clear separation between the responses (Figure 7.11). Two phenomena indicate measurable changes caused by subsurface variation in resistivity structure. First, impedance phase should predict the apparent resistivity (Berdichevsky & Dmitriev, 2008). Second, phase should increase and apparent resistivity should decrease. Specifically for a conductive body at 3.6 km depth, the phase should increase around 1-10 s and apparent resistivity should decrease at periods larger than ∼8 s. This pattern is observed in nearly all sites within 1 km of Paralana 2 injection well and sites further to the north and east, signifying an observable change above measurement error. Interestingly, this pattern is larger in the Z_{xy} component, while being at or below measurement error in the Z_{yx} component suggesting directional dependence.

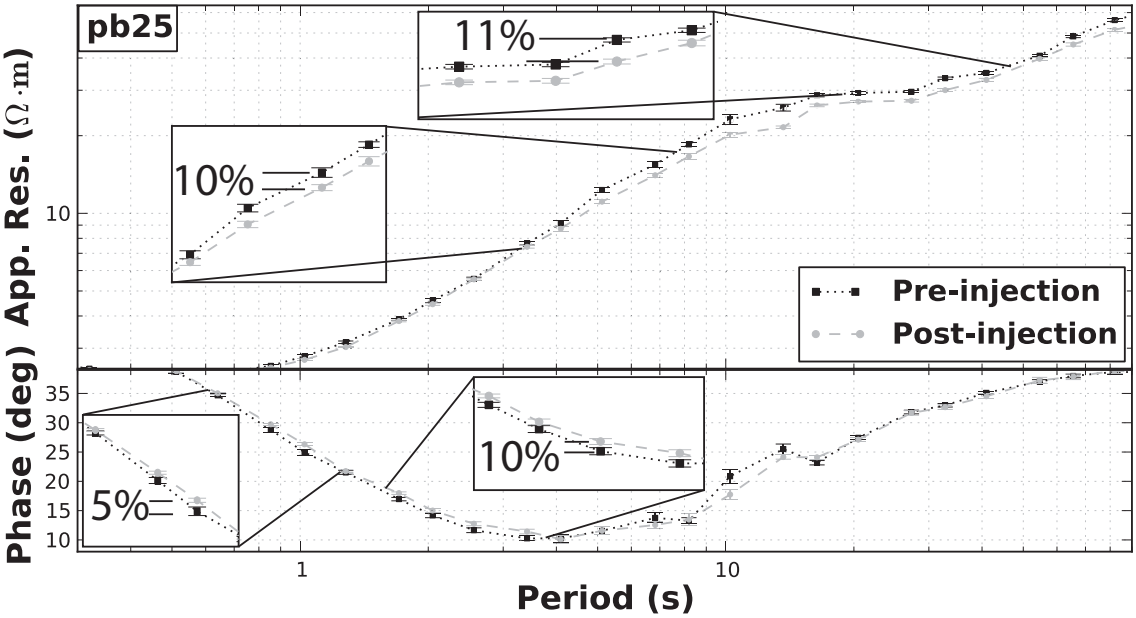

Figure 7.10: Apparent resistivity and impedance phase pre (black) and post-injection (gray) for the Z_{xy} component of station pb25. Impedance phase increases around 1-8 s while the apparent resistivity decreases around 8 seconds and beyond displaying consistency with the MT dispersion relationships. Moreover the change is just above measurement error suggesting an observable change.

PT representation is directional, invariant to near surface distortions (Caldwell *et al.*, 2004) and misalignment of the electric and magnetic fields (Bibby *et al.*, 2005), making it a useful tool for comparing temporally spaced collocated data sets. Residual PT are estimated as eq. (7.1), where graphical representation are ellipses oriented in the direction of largest change and colored as the geometric mean of the residual. Figure 7.12 maps residual PTs for 6 different periods, while Figures 7.14, and 7.13 show pseudo sections that demonstrate PT behavior as a function of period versus distance. An abundance of information is contained in PT residual ellipses, therefore a detailed description follows.

General trends can be compared to forward modeling results, being careful not to over interpret the data. In Figure 7.12, ellipse size increases to a period of 8 s, becoming hotter in face color; then size decreases and face color cools at later periods,

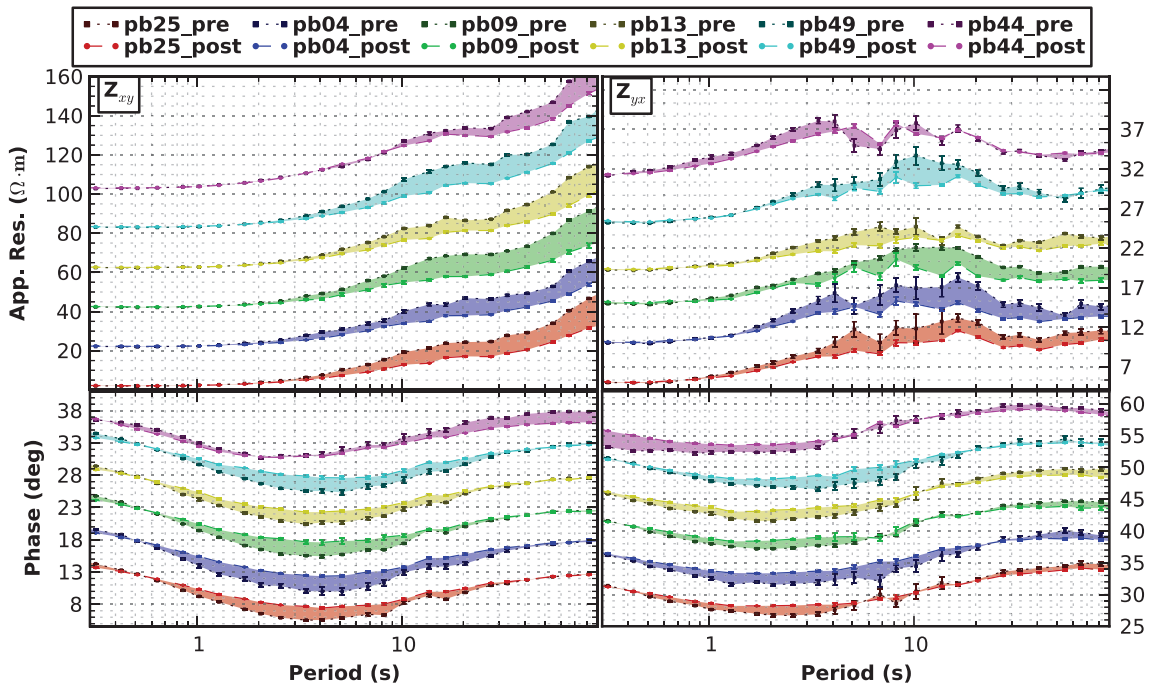

Figure 7.11: Apparent resistivity and impedance phase for different stations around the survey comparing responses pre and post injection. Impedance phase increases around 1-8 s while the apparent resistivity decreases around 8 seconds and beyond displaying consistency with the MT dispersion relationships in the Z_{xy} component. However, the change is not as coherent in the Z_{yx} component and the change in the phase occurs slightly earlier. Moreover, the change is just above measurement error suggesting an observable change.

exemplified in Figure 7.14 and Figure 7.13. Furthermore, the change occurs mostly to the northeast of the borehole and ellipse orientation generally aligns towards a conductive body to the northeast of the borehole. Stations along the north line observe the largest phase variations, with a larger change to the northeast than the orthogonal direction. Correlation between the forward model and the NS line displayed in Figure 7.13 suggests variational geoelectric structure before and after the injection is similar to the introduction of a north-northeast trending fluid filled fault system. Similarly, stations along the EW line also observe large changes with ellipse orientation pointing towards a conductive body to the north-northeast of their respective location. Just to the east of the injection well the PT ellipses are larger and color hot between 3-10 s, demonstrating a large change between measurements. For stations 25, 26 and 27 the ellipses at ∼5 s are rotated clockwise relative to near by ellipses, this is caused by noise in the data as there is a decrease in source field power at this period band on the day the base stations were collected. Note that noise influences the orientation more than the size. Extending further from the injection well ellipses reduce in size and cool off in color except to the far west. From previous MT surveys a large fault system is present between stations pb42 and pb44 which could have become fluid filled from unseasonable rains. Nevertheless, patterns in calculated PT residuals correlate well with the forward model.

RT residuals provides information about whether geoelectric variation is conductive or resistive along with direction, but are susceptible to near surface distortions thus making interpretation more difficult and less accurate than PT residuals. As previously discussed, behavior of RT ellipses is similar to the PT, except that the resistivity tensor residual continues to be influenced by the conductive body at long periods. Map view of RT residuals is uninformative and not shown here. The coloring suggests to the

east the geoelectric structure became more conductive, while the west more resistive. This is evident in the Figure 7.14, where the conductive body to the east has a dip to the east starting around 20 s. Stations 35, 36, 37 and 38 where largely influenced by pipeline noise in the base surveys especially in the period band of interest, therefore the coloring is not a good indication of subsurface variations between surveys. RT residuals estimated on the NS line slightly resemble the forward model (Figure 7.13), though more change is observed in the north than the south. Stations 01, 02, 03, and 04 resemble the forward model near the boundary of the conductive body, where there is little change in the EW direction and a large change in the NS direction. Likewise, further to the north the pattern is similar to the stations close to the borehole in the forward model.

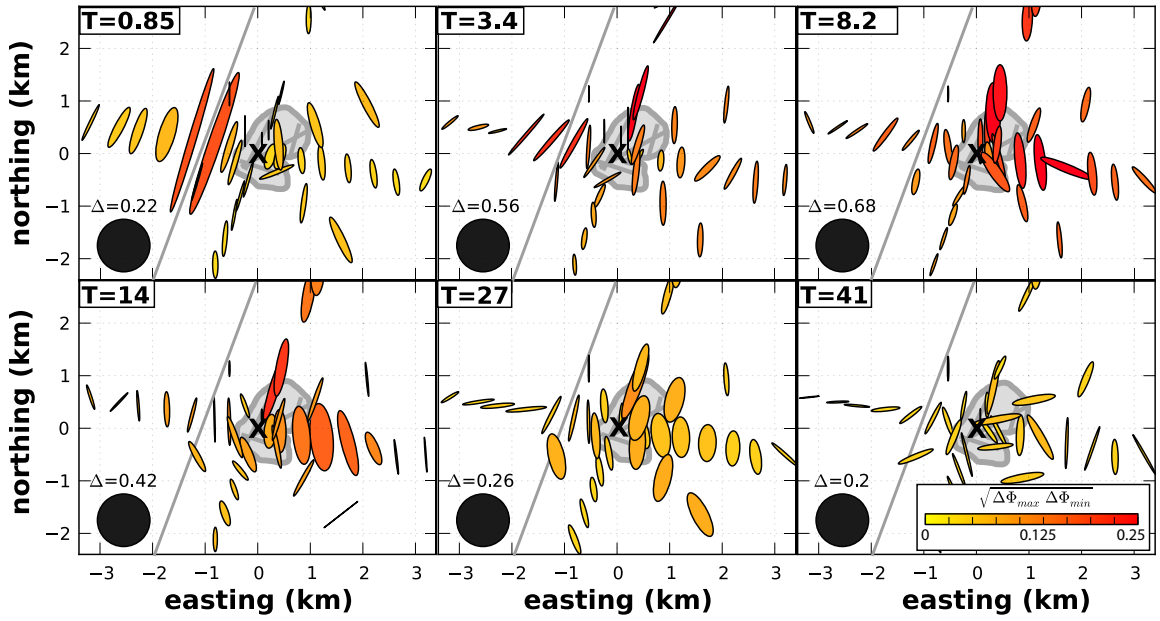

Figure 7.12: Maps of PT residuals between pre and post injection measurements calculated as equation 7.1. Each panel represent all stations at period T, where the ellipses have been normalized to 3 times the median for all PTs calculated at that period. Scale of the ellipses is represented by the black circle in the lower left. Coloring represents the geometric mean of equation 7.1. The gray blob represents the seismic cloud estimated from micro-seismic data collected during the injection, with gray lines representing interpreted faults. The EPIC pipeline is drawn as a gray line extending across the map.

7.7 Discussion

Coherent variations are estimated above measurement error between pre and post surveys that resemble the forward model, though with subtle differences. Causes of these differences can be numerous. The primary discrepancy could be the model. The single fault oriented north-northeast was chosen here because it had the smallest RMS compared to other models. One model included a conductive block oriented northeast with dimensions 1.5 km x 0.8 km x 0.5 km and a resistivity of 0.3 Ωm. Here, the pattern in PT and RT residuals is similar but covers a larger area, a pattern which is not observed in the data. Another model contained a north-northeast trending fault and a northeast trending fault with dimensions of 1 km x 0.1 km x 0.4 km and similar resistivities. They displayed a pattern similar to the aforementioned conductive block. A single fault trending northeast was also computed but the orientation of ellipses was not as similar as a north-northeast trending fault. Finally, a two fault

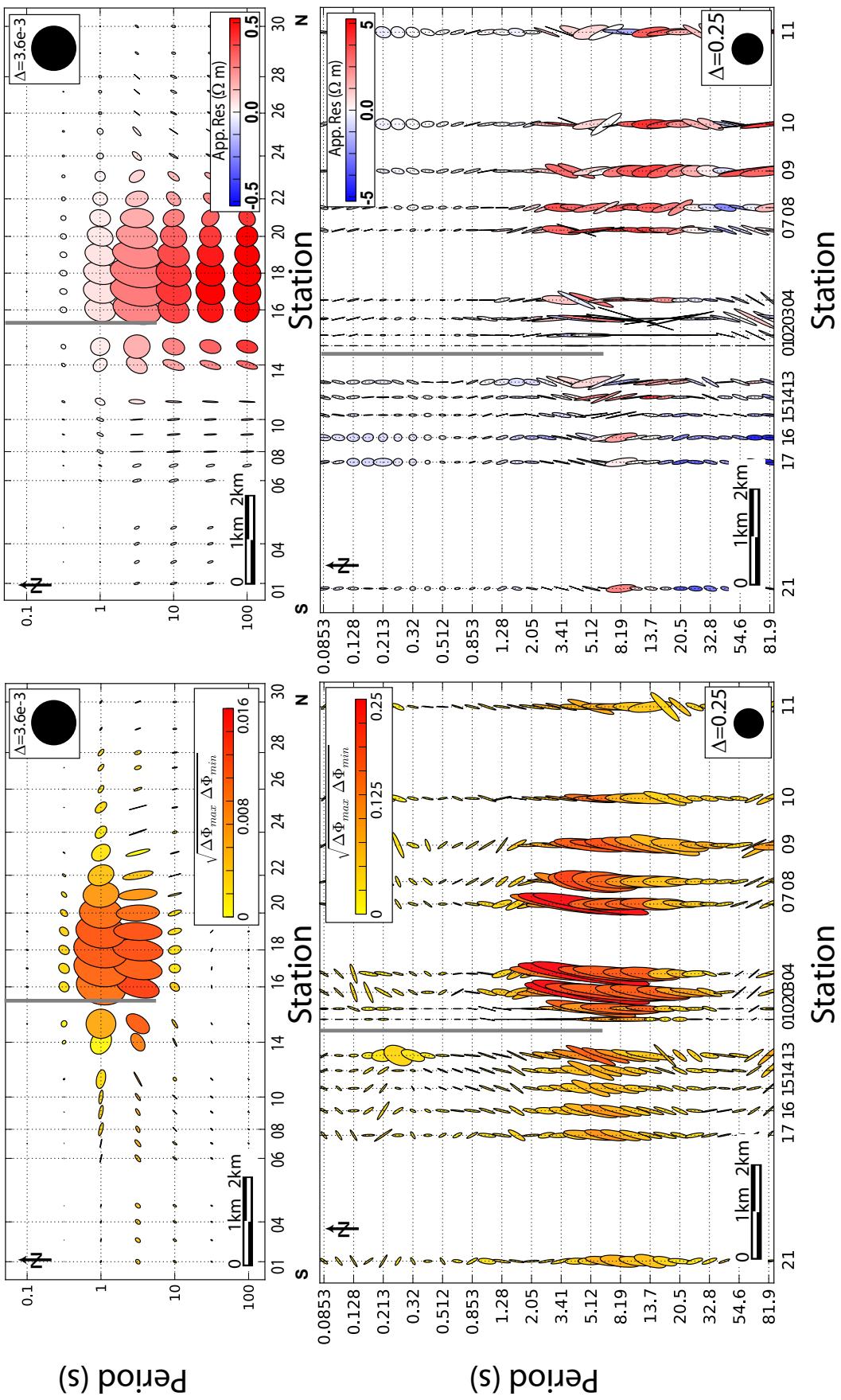

Figure 7.13: Pseudo sections of phase tensor and RT residuals for forward models and data calculated from eq. (7.1) for a N-S profile, where coloring indicates the magnitude of change as arithmetic mean of eq. (7.1) for the phase tensor and residual of RT determinant from pre and post measurements. Left panels represent the phase tensor and right panels represent RT. Each ellipse is plotted in map view with N to the top of the page and is normalized to three times the median off all stations maximum principle direction to aid visualization. Note the orientation and coloring of the ellipses near the injection well (gray line) around 1-20 s.

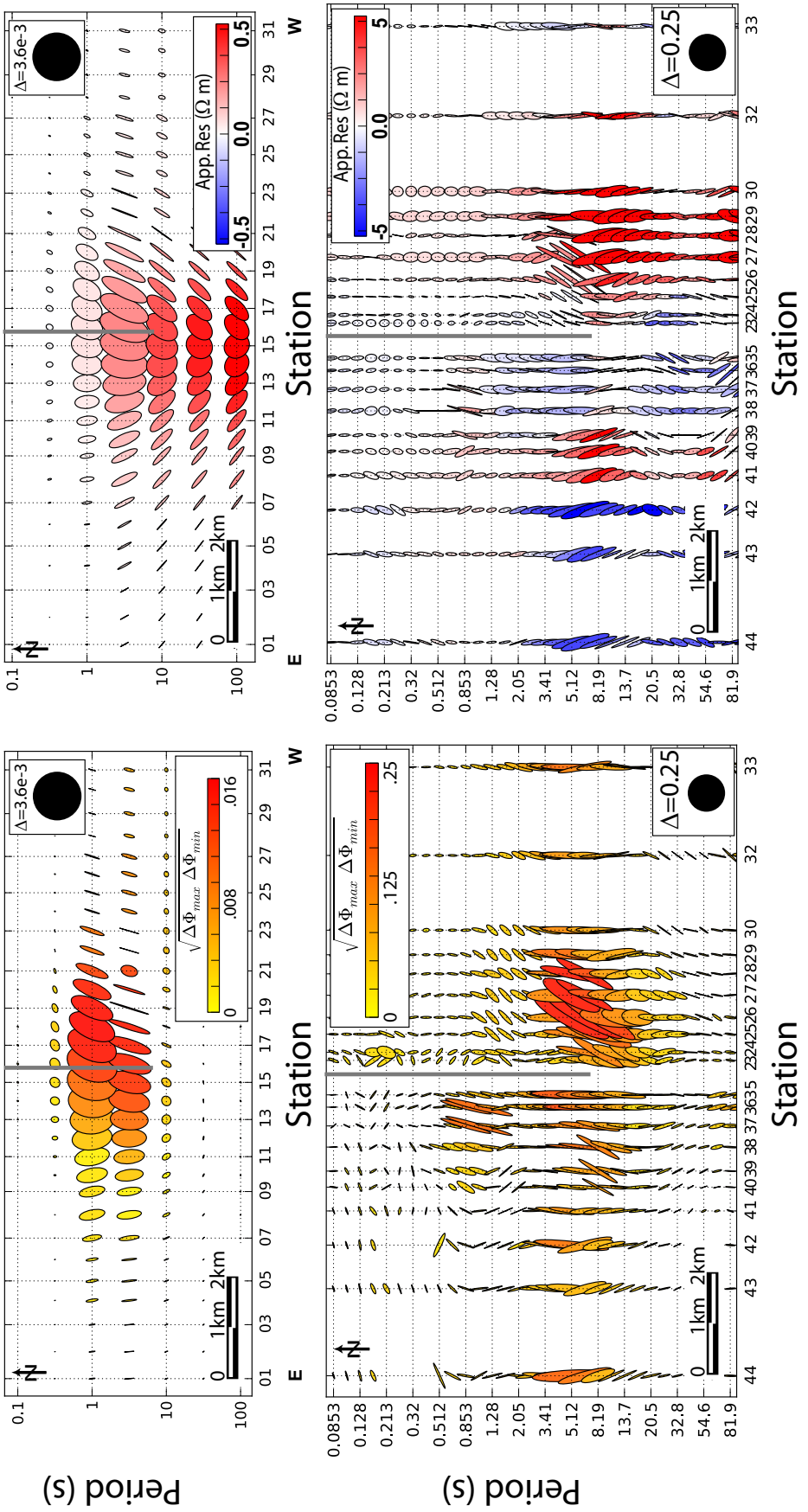

Figure 7.14: Similar to Figure 7.13 except for an E-W profile.

system with a north-northeast trending fault and a ESE trending fault demonstrated again a similar pattern to the conductive block. Though the north-northeast trending fault discussed here is the most likely model, it is still simplistic and does not fully characterize patterns observed in the data. The more likely model is an intrinsically anisotropic heterogeneous complex fracture network that trends north-northeast away from the injection well, however modeling this is currently very difficult with existing MT modeling codes.

The secondary discrepancy between the data and model is noise, which can rotate residual tensor ellipses. The most obvious source of noise is the EPIC pipeline. Fortunately, this noise signal is regular and can be accurately extracted from the data, but still some bias is left in the data especially between 1 and 12 s and at stations just over the pipeline, namely 35, 36, 37, and 38. For all stations along the NS line the bias is consistent because the pipeline runs parallel to the NS line. Similarly, poor source signal strength in the dead band can cause larger error bars in impedance estimation giving a false anomaly. Care was taken to remove this influence by using robust time-frequency distributions to find optimal times to estimate $\mathbf{Z}$ when source field strength in the dead band was maximum. Not repeating the exact same station can cause error. For example if the same instruments are not used, the electrodes are placed in a different place, the magnetic coils are oriented slightly off angle of the previous measurement, mice chewing cables, wind blowing cables around or vegetation growth. Fortunately, using the PT determinant is insensitive to most of these noise sources, whereas the RT is. The RT is susceptible to distortion and static shift. Furthermore, any inaccuracy in estimation of $\mathbf{Z}$ is squared, exaggerating errors and noise by rotating RT ellipses and coloring them inaccurately. Therefore, RT residuals are not as useful as PT residuals. Calibration of the induction coils is important to make sure there is no change due to instrument response. Seasonal changes in the subsurface can generate a change in the MT response. 2010 was an unusually wet year for south Australia, however these changes normally occur in the top kilometer and the repeatability in this period range implies little change in the subsurface due to seasonal changes with one exception. To the west of the borehole appears a conductive anomaly in the same location as a fault interpreted from seismic, suggesting fluids from excessive rain fall have migrated into this fault system. This could also be part of the natural water cycle which will be important in determining the extraction well location.

Tensor representation is useful for characterizing changes as a function of period and lateral distance, but depth cannot be estimated from an inversion scheme at present. To get an estimation of depth an inversion can be employed. A 1D Occam inversion (Key, 2009) of sites with the largest residuals of the $\mathbf{Z}_{xy}$ mode post injection estimates depth to the top of the conductor to be 3.1 km $\pm$ 300 m, which is not the injection depth. This could be caused by over estimating the near surface conductance above the anomaly. A similar approach to Bedrosian *et al.* (2004) can be employed where a line from the base survey is modeled and used as a starting model for the post-injection survey, then the difference between the models is estimated. An Occam inversion (**?**) estimates a depth of 3-4 km, where again the error emanates from the smooth inversion approach and overestimation of the conductivity of the overburden. Here, the difference between the two models suggests the conductive change is on the order of 4% which is larger than measurement error, suggesting that the observed change is indeed cause by the introduction of a conductive body at around 3.5 km. Other EM methods should be employed to get an accurate estimation of near surface conductance to help constrain depth to the anomalous conductive body.

Both lines show similar patterns as those observed in phase tensor residuals, both

suggesting fluids migrated primarily NNE into an existing fracture network. The EW line displays a conductive change near Paralana 2 injection well between 3-4 km. This anomaly is constrained more for the model where the pre-injection model is used as the starting model. Also, to the West, where the conductor associated with an existing fault has migrated West and broadened. This could suggest that fluids from uncharacteristic rains got trapped in porous zone mixing existing saline water with fresh water making the zone more resistive. To the East the subsurface becomes more conductive, could be because of fluids or sensitivity to near surface distortions. The NS line is not as well constrained because stations are missing (Figure 7.16), namely 22, 19, 18, 12, 05, and 06, therefore the model using the pre-injection model as a starting model is more constrained. The difference images for the NS line would suggest that fluids migrated further North than expected, but again the models are not well constrained due to missing data. Interestingly, the conductive anomaly is offset towards the North from the injection well, which corresponds to the phase tensor residuals in Figure 7.13. These models are crude and much more experimentation and methodology needs to be developed for modeling subsurface changes. This is unfortunately beyond the scope of this dissertation.

7.8 Conclusions

This pilot study demonstrates the utility of MT as a monitoring tool for fluid injections. Repeating measurements before and after fluids are injected is logistically favorable but introduces some noise. Estimating PT residuals proves to be the most useful diagnostic representation of the MT response for estimating variations in subsurface geoelectric structure between surveys. RT residuals can be employed as a supplementary tool to characterize subsurface resistivity structure but care must be exercised as RT is susceptible to noise and near surface distortions. In this study, results from PT residuals and RT residuals suggest that most of the injected fluids migrated along an existing fault system trending NNE to the NE of the injection well. Consequently, interpretations of micro-seismic data suggest 4 main pathways for the fluids, two to the NNE, one to the NE and one to the ESE, which further exemplifies the need for electromagnetic measurements as a complementary tool for characterizing fluid injections, because they are directly sensitive to conductivity contrasts. The MT did not specifically pick up a fracture system to the ESE however micro-seismic did. Three methods to improve this type of experiment can be suggested. First, rather than two densely spaced orthogonal lines, a dense grid of stations would maximize spatial coverage. Second, employ a multi-station processing scheme, such as that described by (Egbert, 1997), and utilize more than one remote reference to better characterize source field effects on the MT response (Kappler *et al.*, 2010). Third, in noisy environments controlled source EM methods need to be employed to increase the signal to noise ratio, especially in the dead band which corresponds to most EGS target depths (Orange *et al.*, 2009; Streich *et al.*, 2010; Wirianto *et al.*, 2010).

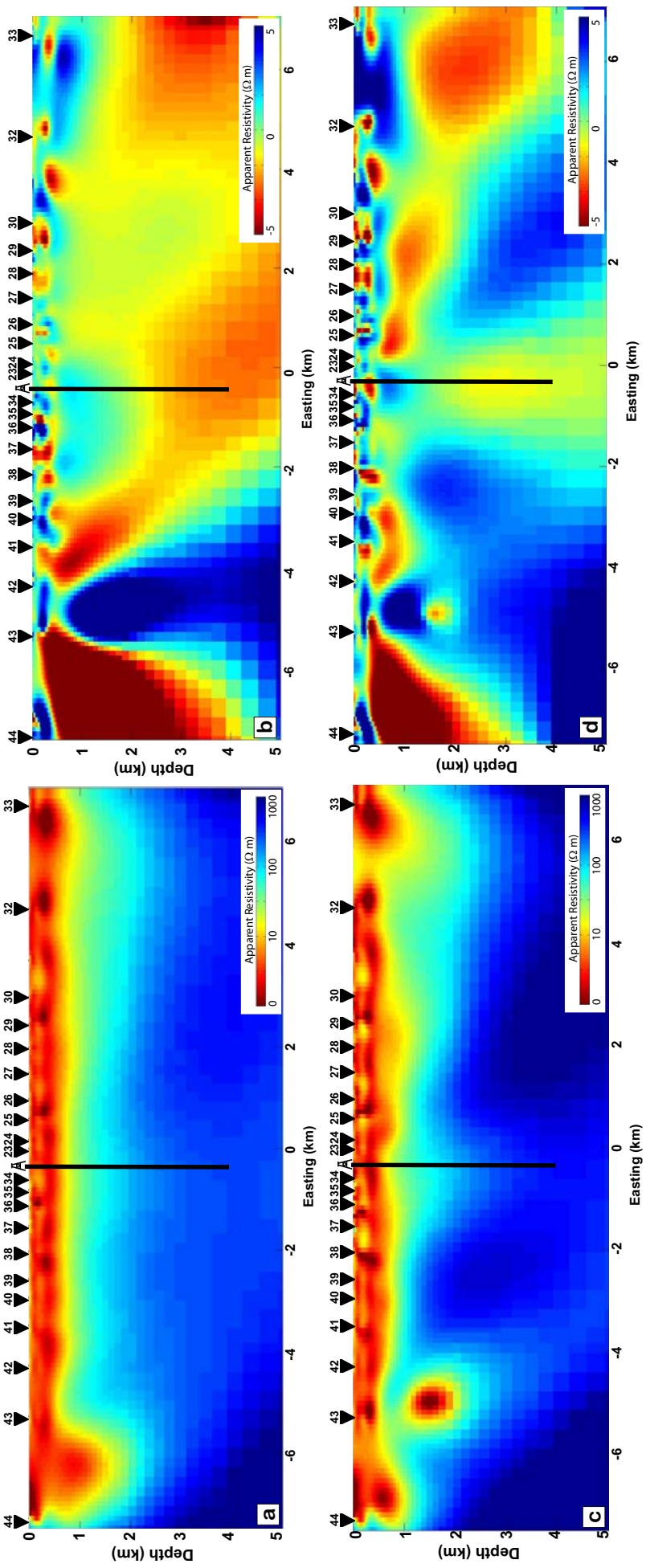

Figure 7.15: EW line Occam models. Left images are Occam inversions of post-injection survey and right are the difference images between Figure 5.8 and post-injection models. a) Occam inversion starting from a half-space of 10 Ω·m . b) Difference between Figure 5.8 and Figure a. c) Occam inversion starting from Figure 5.8. d) Difference between Figure 5.8 and Figure c.

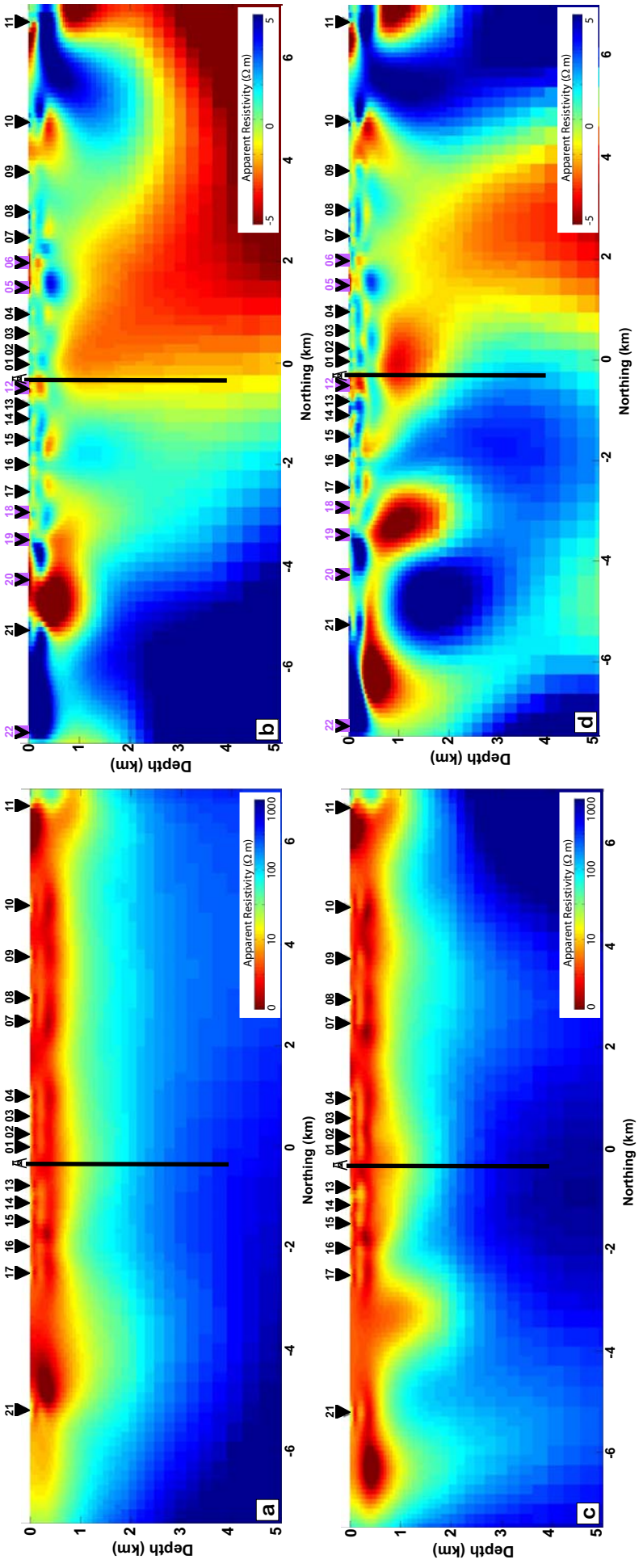

Figure 7.16: NS line Occam models. Left images are Occam inversions of post-injection survey and right are the difference images between Figure 5.9 and post-injection models. a) Occam inversion starting from a half-space of 10 Ω·m . b) Difference between Figure 5.9 and Figure a. c) Occam inversion starting from Figure 5.9. d) Difference between Figure 5.9 and Figure c.

Chapter 8

Summary

The goal of this PhD project was to develop and test the viability of using MT to monitor changes in the subsurface caused by the injection of electrically conductive fluids. This method of using MT as a monitoring tool for a fluid injection has not been rigorously developed or tested before. MT monitoring could be an economic method to characterize EGS fluid injections and other types of fluid injections, such as hydraulic stimulations for non-conventional gas extraction. These results are pioneering and with more experimentation employment of MT for monitoring fluid injection could become standard practice.

In this dissertation different aspects of the MT method were explored. Part I started with the very basics of MT in Chapter 2. Chapter 3 explored analysis of time series including removal of coherent noise and robust time-frequency analysis to characterize the magnetic source field. Chapter 4 explored different tools to represent the difference between temporally spaced collocated impedance tensors through residual phase tensor and residual resistivity tensor analysis. Chapter 5 describes background material pertinent to the project and characterized geoelectric structure at Paralana by modeling pre-injection data in 2D and 3D. Chapter 6 demonstrates that an observable coherent change in the MT response above measurement error is present in MT data collected continuously during the fluid injection; these results were accepted in *Geophysical Research Letters*. Similarly, Chapter 7 shows that repeating the same survey, before and after the fluid injection, can detect a coherent change in the MT response above measurement error; these results have been submitted to *Geophysics*. Out of this 3 year academic adventure two scientifically interesting results were found.

8.1 Continuous Monitoring

First, from continuous MT measurements during the fluid injection at Paralana, South Australia, it is shown that coherent transient changes in the MT response are observed above measurement error assumed to be cause by the introduction of conductive fluids at 3.6 km depth. Eleven instruments were set out around the injection well, with the furthest station being 2 km away, 2 days prior to the injection and left to continuously record until 2 days after the injection, for a total of 9 days. The MT response was estimated in 24 hour blocks and compared to the MT response estimated pre-injection. Two days after pumping commenced an increase in impedance phase of $\sim$ 5% at periods of 1-10 s and a decrease of $\sim$ 6% in apparent resistivity at periods larger than 8 s of the TE mode is observed. This pattern continues after pumping with the change in impedance phase having a maximum of 8% and apparent resistivity 10%. This demonstrates causality and the period range suggests that the subsurface

around 3.5 km increased in conductivity. Estimation of residual phase tensors provide directional information suggesting that the largest change in the MT response is to the NE of the injection well with a preferred NNE orientation, which is the preferred fracture direction estimated from a concurrent micro-seismic survey.

8.1.1 Improving continuous monitoring

Continuous MT measurements can provide information about transient changes in subsurface resistivity structure caused by a fluid injection at depth, though care must be taken when analyzing data because the changes can be small. Perhaps the most critical component to continuous monitoring is collecting precise and accurate data pre-injection to compare later MT responses to. This incorporates high signal to noise measurements, well calibrated equipment and a little luck with source field strength. To remove the luck factor in source field strength a controlled source should be used, especially if the depth to the target lies in the MT dead band. The other important factor for continuous monitoring is spatial coverage with an intelligently developed survey design. The optimum array would have a dense grid of stations around the area where fluids are expected to flow with the extremities of the survey at least two times the depth to the reservoir. This will not only help constrain the areal extent of the reservoir but also reduce interpretation of false anomalies as stations at the extremities should not measure a change.

When searching for anomalies in the data, the first thing to look for is any changes in the source field that might cause a false anomaly, such as low signal power, periodic noise or any coherent noise. This can be analyzed with robust time-frequency distributions from different stations. A useful practice is to employ more than one reliable remote reference, preferably at opposite ends of the survey. This can not only infer variations in the magnetic source field but variations in the MT response, because it is assumed that the remote references are not sensitive to the fluid injection. Multivariate multiple-station processing would be advantageous to characterize source field effects. The second pattern to look for is causality of the anomalous pattern, where the impedance phase should predict the apparent resistivity. Estimating phase tensor residuals provides information about direction of maximum change, which is assumed to be associated with the preferred orientation of induced fractures. Furthermore, representing phase tensor residuals as ellipses and mapping them as a function of space and period suggests lateral boundaries of the injected fluid. Finally, estimating depth to the conductive anomaly can be done with inversion though only a general depth range will be given and is only useful for ensuring the anomalous signal is logical. Full 3D anisotropic inversion would be optimal and could provide better depth estimation than current isotropic 2D modeling.

8.2 Time-Lapse Monitoring

Repeating the same survey before and after fluids are injected is logistically easier than continuous measurements because repeated surveys can cover larger areas with a denser grid. Here, a 56 station survey was used. The survey was set up with two main orthogonal lines parallel and perpendicular to geoelectric strike, which is fortuitously geomagnetic North. Each line was 15 km in length and had 22 stations spaced on a log scale starting at 200 m and extending to 1.5 km at the extremities. Two off-diagonal lines of 6 stations each aid in spatial coverage. All 4 lines intersect at the injection well. The survey was repeated 4 times pre-injection due to data quality and to get an

estimate of repeatability, the percent difference between temporally spaced collocated MT measurements. Repeatability of the MT response at periods shorter than 1 s was less than 1%, while periods between 1-12 s had a repeatability of 3%. This is caused by low source field power and periodic noise from a nearby pipeline. One post-injection survey was collected one week after the fluids were emplaced.

Comparing the MT response from pre and post-injection data shows a coherent increase of ∼10% in impedance phase in periods of 1-10 s and a decrease of ∼ 10% in the apparent resistivity in periods larger than 8 s in the TE mode. This, again, demonstrates causality and the period range suggests the subsurface at around 3.5 km to the NE of the injection well became more conductive between surveys. Residual phase tensors demonstrates the largest change is in the NNE direction to the NE of the injection well. Residual resistivity tensors are calculate but interpretation is more ambiguous as the resistivity tensor is susceptible to near surface distortions. These results agree with the continuous MT measurements and micro-seismic data collected during the injection.

8.2.1 Improving time-lapse monitoring

Time-lapse monitoring using MT can suggest linear boundaries of a hydraulically stimulated reservoir by measuring before and after the injection, but again care must be taken when analyzing the data. Accurate and precise data need to be collected and it is suggested that the MT instruments be left out for as long as logistically possible, 2 days minimum. The difference with continuous monitoring is that galvanic distortion becomes important to remove, especially if apparent resistivity is one parameter used for comparison. This makes phase tensor representation advantageous because it is invariant to near surface distortions. Phase tensor residuals provide directional information about the largest change, while suggesting lateral and vertical boundaries. Though to get a precise vertical boundary an absolute resistivity measurement needs to be collected. Vertical magnetic field data would be useful for estimating the Tipper, which can add information about lateral boundaries and geolectric strike direction. Mapping phase tensor residuals is useful if the survey design is a dense grid, otherwise pseudo sections provide the most information if the survey is designed with dense coverage. Residual resistivity tensors can provide information on directional change and magnitude of change, but orientation can be sensitive to near surface distortions. Also, there is more error in estimating apparent resistivity because of calibration to dipole length and variations in near surface resistivity structure. Source field and coherent noise effects need to be carefully analyzed, which can be characterized with intelligently designed logistics and multivariate processing. Finally, if possible a controlled source should be used.

8.3 Final Remarks

This project has demonstrated promise in utilizing MT as a monitoring tool for both continuous monitoring and repeating measurements before and after a fluid injection. The advantage of continuous monitoring is that transient variations in the MT response can be estimated. This can then be mapped to characterize evolution of lateral extent of injected fluids. However, unless you have over 30 instruments at your disposal, the spatial coverage of a continuous survey will be coarse. Also, with continuous measurements you may get unlucky with the source field or coherent noise, which is why a controlled source would be advantageous. Time-lapse surveys, where the same

survey is repeated multiple times, is advantageous because the spatial coverage can be dense and cover a larger area. Moreover, if the source field is weak or coherent noise is present or the weather turns bad, the survey can be repeated at a different time. The disadvantage of time-lapse surveys is that care must be taken in repeating the surveys in the same manner each time to make sure that any anomalies observed in the data are from changes in the subsurface only and not from survey layout. Furthermore, galvanic distortion can influence apparent resistivity values making phase tensor analysis advantageous. Finally, seasonal variations need to be taken into account for time-lapse surveys.

MT monitoring of a fluid injection is possible, but not the silver bullet save all. It is therefore suggested that MT and micro-seismic measurements be employed as complimentary monitoring tools. Micro-seismic is sensitive to fractures opening but cannot discriminate whether those fractures are fluid filled or connected. MT is sensitive to volumetric conductivity contrasts at depth but not individual fractures. Therefore, areas that contain a seismic cloud and a conductive anomaly would have high a probability of being a fluid filled fracture network. Finally, these results can be extended to other fluid injections such as non-conventional natural gas extraction, which is undeniably a tense political and social issue at present. Hope you enjoyed this project as much as I did and have a think about future MT monitoring projects.

References

Abrard, F., & Deville, Y. 2005. A time-frequency blind signal separation method applicable to underdetermined mixtures of dependent sources. *Signal Processing*, **85**, 1389–1403.

Aizawa, K., Yoshimura, R., Oshiman, N., Yamazaki, K., Uto, T., Ogawa, Y., Tank, S. B., Kanda, W., Sakanaka, S., Furukawa, Y., Hashimoto, T., Uyeshima, M., Ogawa, T., Shiozaki, I., & Hurst, A. W. 2005. Hydrothermal system beneath Mt. Fuji volcano inferred from magnetotellurics and electric self-potential. *Earth and Planetary Science Letters*, **235**, 343–355.

Aizawa, K., Kanda, W., Ogawa, Y., Iguchi, M., Yokoo, A., Yakiwara, H., & Sugano, T. 2011. Temporal changes in electrical resistivity at Sakurajima volcano from continuous magnetotelluric observations. *Journal of Volcanology and Geothermal Research*, **199**, 165–175.

Amin, M. G. 1997. Interference mitigation in spread spectrum communication systems using time-frequency distributions. *IEEE Transactions on Signal Processing*, **45**, 90–101.

Anderson, B. J., Erlandson, R. E., & Zanetti, L. J. 1992. A statistical study of Pc 1-2 magnetic pulsations in the equatorial magnetosphere 2. Wave properties. *Journal of Geophysical Research*, **97**, 3089–3101.

Anderson, E., Jacobo, R., & Ussher, G. 1995. A geothermal reservoir revealed – magnetotellurics and data management techniques in a potent combination. *In: World Geothermal Conference*.

Arango, C., Marcuello, A., Ledo, J., & Queralt, P. 2009. 3D magnetotelluric characterization of the geothermal anomaly in the Llucmajor aquifer system (Majorca, Spain). *Geothermics*, **68**, 479–488.

Asaue, H., Koike, K., Yoshinaga, T., & Takakura, S. 2006. Magnetotelluric resistivity modeling for 3D characterization of geothermal reservoirs in the Western side of Mt. Aso, SW Japan. *Journal of Applied Geophysics*, **58**, 296–312.

Avdeev, D. B. 2005. Three-dimensional electromagnetic modelling and inversion from theory to application. *Surveys in Geophysics*, **26**, 767–799.

Bahr, K. 1988. Interpretation of the magnetotelluric impedance tensor: regional induction and local telluric distortion. *Journal of Geophyiscs*, **62**, 119–127.

Bahr, K. 1991. Geological noise in magnetotelluric data: a classification of distortion types. *Physics of The Earth and Planetary Interiors*, **66**, 24–38.

Bedrosian, P. A., Weckmann, U., Ritter, O., Hammer, C. U., Hübert, J., & Jung, A. 2004. Electromagnetic monitoring of the Grob Schönebeck stimulation experiment. *In: 64 Jahrestagung der Deutschen Geophysikalischen Gesellschaft, Berlin*.

Belouchrani, A., & Amin, M. G. 1998. Blind source separation bsed on time-frequency signal representation. *IEEE Transactions on Signal Processing*, **46**, 2888–2897.

Berdichevsky, M. N., & Dmitriev, V. I. 2008. *Models and methods of magnetotellurics*. Berlin: Springer.

Bertani, R. 2005. World geothermal power generation in the period 2001-2005. *Geothermics*, **34**, 651–690.

Bertani, R. 2012. Geothermal power generation in the world 2005-2010 update report. *Geothermics*, **41**, 1–29.

Bibby, H. M. 1986. Analysis of multiple source bipole-quadrupole resistivity surveys using apparent resistivity tensor. *Geophysics*, **51**, 972–983.

Bibby, H. M., Caldwell, T. G., & Brown, C. 2005. Determinable and non-determinable parameters of galvanic distortion in magnetotellurics. *Geophysical Journal International*, **163**, 915–930.

Biello, D. 2008 (23 Oct). *Deep Geothermal: the untapped energy source*.

Boashash, B. (ed). 2003. *Time frequency signal analysis and processing: a comprehensive reference*. Elsevier Ltd.

Bortnik, J., Inan, U. S., & Bell, T. F. 2003. Frequency-time spectra of magnetospherically reflecting whistlers in the plasmasphere. *Journal of Geophysical Research*, **108**, 19 1–12.

Brotchi, J., Rankine, L., Mesbah, M., Colditz, P., & Boashash, B. 2007 (August 23-26). Robust time-frequency analysis of newborn EEG seizure corrupted by impulsive artifacts. *In: Proceedings of the* 29^{th} *Annual International Conference on the IEEE EMBS*.

Brown, D. 1995. The US hot dry rock program – 20 years of experience in reservoir testing. *Pages 2607–2611 of: Proc. World Geothermal Congress, Florence Italy*, vol. 4.

Brugger, J., Long, N., McPhail, D. C., & Plimer, I. 2005. An active amagmatic hydrothermal system: the Paralana hot springs, Northern Flinders Ranges, South Australia. *Chemical Geology*, **222**, 35–64.

Buselli, G., & Lu, K. 2001. Groundwater contamination monitoring with multichannel electrical and electromagnetic methods. *Journal of Applied Geophysics*, **48**, 11–23.

Cagniard, L. 1953. Basic theory of the magnetotelluric method of geophysical prospecting. *Geophysics*, **18**, 605–645.

Caldwell, T. G., Bibby, H. M., & Brown, C. 2004. The magnetotelluric phase tensor. *Geophysical Journal International*, **158**, 457–457.

Carden, R. S., Nicholson, R. W., Pettitt, R. A., & Rowley, J. C. 1985. Unique aspects of drilling and completing hot, dry rock geothermal wells. *Journal of Petroleum Technology*, **May**, 821–834.

Celka, P., Boashash, B., & Colditz, P. 2001. Preprocessing and time-frequency analysis of newborn EEG Seizures. *IEEE Engineering in Medicine and Biology Magazine*, **20**, 30–39.

Chant, I. J., & Hastie, L. M. 1992. Time-frequency analysis of magnetotelluric data. *Geophysical Journal International*, **111**, 399–413.

Chant, I. J., & Hastie, L. M. 1993. A comparison of the stability of stationary and non-stationary magnetotelluric analysis methods. *Geophysical Journal International*, **115**, 1143–1147.

Chave, A. D., & Thomson, D. J. 2004. Bounded influence magnetotelluric response function estimation. *Geophysical Journal International*, **157**, 988–1006.

Chave, A.D., Thomson, D.J., & Ander, M.E. 1987. On the Robust Estimation of Power Spectra, Coherences, and Transfer Functions. *Journal of Geophysical Research*, **92**, 633–648.

Coats, R. P., & Blissett, A. H. 1971. Regional and economic geology of the Mount Painter province. *Geologic Survey of South Australia Bulletin*, **43**.

Cohen, L. 1989. Time-frequency distributions–a review. *Proceedings of the IEEE*, **77**, 941–981.

Constable, S. C., Parker, R. L., & Constable, C. G. 1987. Occam's inversion: a practical algorithm for generating smooth models from electromagnetic sounding data. *Geophysics*, **52**, 289–300.

Cox, R., & Barron, A. 1998. *Great Artesian Basin: resource study.* Tech. rept. Great Artesian Basin Consultative Council, Australia.

Crampin, S., & Peacock, S. 2005. A review of shear-wave splitting in the complian crack-critical anisotropic Earth. *Wave Motion*, **41**, 59–77.

Cunningham, G. S., & Williams, W. J. 1994. Kernel decomposition of time-frequency distributions. *IEEE Transactions on Signal Processing*, **42**, 1425–1432.

Dash, Z. V., Murphy, H. D., & Cremer, G. M. 1981. *Hot Dry Rock Geothermal Reservoir Testing: 1978 to 1980.* Tech. rept. Los Alamos National Laboratory, Los Alamos, New Mexico.

de Ridder, S. A. L., Slob, E., & Wapenaar, K. 2009. Interferometric seismoelectric Green's function representations. *Geophysical Journal International*, **178**, 1289–1304.

Declercq, N. F., Degrieck, J., Briers, R., & Leroy, O. 2004. A theoretical study of special acoustic effects caused by the staircase of the El Castillo pyramid at the Maya ruins of Chichen-Itza in Mexico. *Journal of Acoustical Society of America*, **116**, 3328–3335.

Degerine, S., & Kane, E. 2006. A comparative study of approsimat joint diagonalization algorithms for blind source separation in presence of additive noise. *IEEE Transactions on Signal Processing*, **XX**, 1–9.

deGroot-Hedlin, C., & Constable, S. 1990. Occam's inversion to generate smooth, two-dimensional models from magentotelluric data. *Geophysics*, **55**, 1613–1624.

DiPippo, R. 1991. Electricity generation and environmental impact. *Energy Policy*, **19**, 798–807.

Djurovic, I., & Stankovic, L. 1999. The reassigned S-method. *In: Telecommunications in Modern Satellite, Cable and Broadcasting Services,* 4^{th} *International Conference.*

Djurovic, I., Katkovnik, V., & Stankovic, L. 2001. Median filter based realizations of the robust time-frequency distributions. *Signal Processing*, **81**, 1771–1776.

Djurovic, I, Stankovic, L., & Bohme, J. F. 2003. Robust L-estimation based forms of signal transforms and time-frequency representations. *IEEE Transactions on Signal Processing*, **51**, 1753–1761.

Dmitriev, V. I., & Berdichevsky, M. N. 1979. The fundamental model of magnetotelluric sounding. *Proceedings of the IEEE*, **67**(7), 1034–1044.

Douglas, A. 1967. Joint epicentre determination. *Nature*, **215**, 47–48.

Duchane, D., & Brown, D. 1997. *Hot dry rock geothermal energy development in the USA*. Tech. rept. Los Alamos National Laboratory.

Dupuis, J. C., Butler, K. E., Kepic, A. W., & Harris, B. D. 2009. Anatomy of a seismoelectric conversion: measurments and conceptual modeling in boreholes penetrating a sandy aquifer. *Journal of Geophysical Research*, **114**, B10306.

Egbert, G. D. 1997. Robust multiple-station magnetotelluric data processing. *Geophysical Journal International*, **130**, 475–496.

Eisel, M., & Egbert, G.D. 2001. On the stability of magnetotelluric transfer function estimates and the reliability of their variances. *Geophysical Journal International*, **144**, 65–65.

Elder, J. 1981. *Geothermal Systems*. Academic Press.

Elkibbi, M., & Rial, J. A. 2005. The Geysers geothermal field: results from shear-wave splitting analysisi in a fractured reservoir. *Geophysical Journal International*, **162**, 1024–1035.

Everett, J. E., & Hyndman, R. D. 1967. Geomagnetic variations and electrical conductivity structure in south-western Australia. *Physics of the Earth and Planetary Interiors*, **1**, 24–34.

Farquharson, C. G., & Craven, J. A. 2009. Three-dimensional inversion of magnetotelluric data for mineral exploration: an example from the McArthur River uranium deposit, Saskatchewan, Canda. *Journal of Applied Geophysics*, **68**, 450–458.

Fevotte, C., & Doncarli, C. 2004. Two contributions to blind source separation using time-frequency distributions. *IEEE Signal Processing Letters*, **11**, 386–389.

Fischer, G., & Schnegg, P. A. 1980. The dispersion relations of the magnetotelluric response and their incidence on the inversion problem. *Geophysical Journal Royal Astronomical Society*, **62**, 661–673.

Fischer, G., & Schnegg, P. A. 1993. The magnetotelluric dispersion relations over 2-D structures. *Geophysical Journal International*, **115**, 1119–1123.

Foster, D. A., Murphy, J. M., & Gleadow, J. W. 1994. Middle Tertiary hydrothermal activity and uplift of the northern Flinders Ranges SA: insights from apatite fission track thermochronology. *Australian Journal of Earth Sciences*, **41**, 11–17.

Frenkel, J. 2005. On the theory of seismic and seismoelectric phenomena in a moist soil. *Journal of Engineering Mechanics*, **131**, 879–887.

Gabor, D. 1946. Theory of Communication. *Journal of the Institution of Electrical Engineers - Part III: Radio and Communication Engineering*, **93**, 429–441.

Gamble, T. D., Gougau, W. M., Goldstein, N. E., Miracky, R., Stark, M., & Clarke, J. 1981. Magnetotelluric studies at Cerro Prieto. *Geothermics*, **10**, 169–182.

Gamble, T.D., Goubau, W.M., & Clarke, J. 1979. Magnetotellurics with a remote magnetic reference. *Geophysics*, **44**, 53–68.

Garg, S. K., Pritchett, J. W., Wannamaker, P. E., & Combs, J. 2007. Characterization of geothermal reservoirs with electrical surveys: Beowawe geothermal field. *Geothermics*, **36**, 487–517.

Gatzemeier, A., & Moorkamp, M. 2005. 3D modelling of electrical anisotropy from electromagnetic array data: hypothesis testing for different upper mantle conduction mechanisms. *Physics of the Earth and Planetary Interiors*, **149**, 225–242.

Gaunaurd, G. C., & Strifors, H. C. 1996. Signal analysis by means of time-frequency (Wigner-type) distributions–applications to sonar and radar echoes. *Proceedings of the IEEE*, **84**, 1231–1248.

Gharibi, M., Bentley, L. R., & Stewart, R. R. 2003. *Seismoelectric monitoring of producing oilfields: a review.* Tech. rept. 13. CREWES Research Report.

Goldstein, B. A., Hill, T., & Long, A. 2008. *Australian geothermal implementing agreement annual report-2008.* Tech. rept. PIRSA.

Gonclaves, P., & Baraniuk, R. G. 1998. Pseudo affine Wigner distributions: definition and kernel formulation. *IEEE Transactions on Signal Processing*, **46**, 1505–1516.

Green, B. D., & Nix, R. G. 2006 (November). *Geothermal–The energy under our feet.* Tech. rept. NREL/TP-840-40665. National Renewable Energy Laboratory.

Griffiths, D.H. 1976. Application of electrical resisitivity mearsurements for the determination of porosity and permeability in sandstones. *Geoexploration*, **14**, 207–213.

Groom, R.W., & Bailey, R.C. 1989. Decomposition of magnetotelluric impedance tensors in the presence of local three-dimensional galvanic distortion. *Journal of Geophysical Research*, **94**, 1913–1925.

Haak, V., Ritter, O., & Ritter, P. 1989. Mapping the geothermal anomaly on the island of Milos by magnetotellurics. *Geothermics*, **18**, 533–546.

Haartsen, M. W., & Pride, S. R. 1997. Electroseismic waves from point sources in layered media. *Journal of Geophysical Research*, **102**, 24,745–24,769.

Haines, S. S., & Pride, S. R. 2006. Seismoelectric numerical modeling on a grid. *Geophysics*, **71**, N57–N65.

Haines, S. S., Pride, S. R., Klemperer, S. L., & Biondi, B. 2007. Seismoelectric imaging of shallow targets. *Geophysics*, **72**, 9–20.

Hamilton, M. P., Jones, A. G., Evans, R.. L., Evans, S., Fourie, C.J.S., Garcia, X., Mountford, A., & Spratt, J. E. 2006. Electrical anisotropy of South African lithosphere compared with seismic anisotropy from shear-wave splitting analyses. *Physics of The Earth and Planetary Interiors*, **158**, 226–239.

Han, N., Nam, M. J., Kim, H. J., Song, Y., & Suh, J. H. 2009a. A comparison of accuracy and computation time of three dimensional magnetotelluric modelling algorithms. *Journal of Geophysics and Engineering*, **6**, 135–145.

Han, N., Nam, M. J., Kim, H. J., Lee, T. J., Song, Y., & Suh, J. H. 2009b. *Three-dimensional inversion of magnetotelluric data including sea effects obtained in Pohang, Korea*. In-Press.

Hasting, M. A., Albaric, J., Oye, V., Reid, P., Messeiller, M., & Llanos, E. 2011. Microseismic monitoring during stimulation at Paralana-2 South Australia. *In: presented at 2011 Fall Meeting, AGU, San Francisco, Calif., 5-9 Dec.*

Heise, W., Caldwell, T.G., Bibby, H.M., & Brown, C. 2006. Anisotropy and phase splits in magnetotellurics. *Physics of The Earth and Planetary Interiors*, **158**, 107–121.

Heise, W., Caldwell, T. G., Bibby, H. M., & Bannister, S. C. 2008. Three-dimensional modelling of magnetotelluric data from the Rotokawa geothermal field, Taupo Volcanic Zone, New Zealand. *Geophysical Journal International*, **173**, 740–750.

Hermance, J. F. 1973. Processing of magnetotelluric data. *Physics of the Earth and Planetary Interiors*, **7**, 349–364.

Hill, G. J., Caldwell, T. G., Heise, W., Chertkoff, D. G., Bibby, H. M., Burgess, M. K., Cull, J. P., & Cas, R. A. F. 2009. Distribution of melt beneath Mount St Helens and Mount Adams inferred from magnetotelluric data. *Nature Geoscience*, **2**, 785–789.

Hillis, R., & Reynolds, S. 2000. The Australian stress map. *Journal of Geologic Society of London*, **157**, 915–921.

Hillis, R. R., Hand, M., Mildren, S., Morton, J., Reid, P., & Reynolds, S. 2004. Hot dry rock geothermal exploration in Australia. *In: PESA Eastern Australasian Basins Symposium II.*

Hillis, R. R., Sandiford, M., Reynolds, S. D., & Quigley, M. C. 2008. *The Nature and Origin of Compression in Passive Margins.* Geological Society of London Special Publication 306. Chap. Presentday stresses, seismicity and Neogene-to-Recent tectonics of Australia's 'passive' margins: intraplate deformation controlled by plate boundary forces, pages 71–90.

Hooijkass, G. R., Genter, A., & Dezayes, C. 2006. Deep-seated geology of the granite intrusions at the Soultz EGS site based on data from 5 km-deep boreholes. *Geothermics*, **35**, 484–506.

House, L. S. 1987. Locating microearthquakes induced by hydraulic fracturing in crystalline rock. *Geophysical Research Letters*, **14**, 919–921.

Hyvärinen, A. 1999. Survey of independent component analysis. *Neural Computing Surveys*, **2**, 94–128.

Hyvärinen, A., & Oja, E. 2000. Independent Component Analysis: algorithms and applications. *Neural Networks*, **13**, 411–430.

Idnurm, M., & Heinrich, C. A. 1993. A palaeomagnetic study of hydrothermal activity and uranium mineralization at Mt. Painter, South Australia. *Australian Journal of Earth Sciences*, **40**, 87–101.

Jacobs, J. A., Kato, Y., Matsushita, S., & Troitskaya, V. A. 1964. Classification of Geomagnetic Micropulsations. *Journal of Geophysical Research*, **69**, 180–181.

Jiracek, G. R. 1990. Near-surface and topographic distortions in electromagnetic induction. *Surveys in Geophysics*, **11**, 163–203.

Jones, A. G., Chave, A. D., Egbert, G., Auld, D., & Bahr, K. 1989. A comparison of techniques for magnetotelluric response function estimation. *Journal of Geophysical Research*, **94**(B10), 14201–14213.

Jones, A.G. 1988. Static shift of magnetotelluric data and its removal in a sedimentary basin environment. *Geophysics*, **53**, 967–978.

Jones, D. L., & Baraniuk, R. G. 1995. An adaptive optimal-kernel time-frequency representation. *IEEE Transactions on Signal Processing*, **43**, 2361–2371.

Jones, K. A., Ingham, M. R., & Bibby, H. M. 2008. The hydrothermal vent system of Mount Ruapehu, New Zealand – a high frequency MT survey of the summit plateau. *Journal of Volcanology and Geothermal Research*, **176**, 591–600.

Kappler, K. N. 2008. *Long term electromagnetic monitoring at Parkfield, California*. Ph.D. thesis, University of California at Berkeley.

Kappler, K. N., Morrison, H. F., & Egbert, G. D. 2010. Long-term monitoring of ULF electromagnetic fields at Parkfield, California. *Journal of Geophysical Research*, **115**, B04406 1–27.

Katkovnik, V. 1998. Robust M-periodogram. *IEEE Transactions on Signal Processing*, **46**, 3104–3109.

Katkovnik, V. 1999. Robust M-estimates of the frequency and amplitude of a complex-valued harmonic. *Signal Processing*, **77**, 71–84.

Kaufman, A. A. 1988. Reduction of the geologic noise in magnetotelluric soundings. *Geoexploration*, **25**, 145–161.

Kaufman, A. A., & Keller, G. V. 1981. *The magnetotelluric sounding method*. Amsterdam: Elsevier Ltd.

Key, K. 2009. 1D inversion of multicomponent, multifrequency marine CSEM data: methodology and synthetic studies for resolving thin resistive layers. *Geophysics*, **74**, F9–F20.

Kim, H., Lessard, M. R., Engebretson, M. J., & Young, M. A. 2011. Statistical study of Pc1-2 wave propagation characteristics in the high-latitude ionospheric waveguide. *Journal of Geophysical Research*, **116**, A07227.

Kuhn, T. S. 1962. *The structure of scientific revolutions*. University of Chicago Press.

Kuhne, M., Togneri, R., & Nordholm, S. 2008. *Speech Recognition, Technologies and Applications*. Vienna, Austria: I-Tech. Chap. Time-frequency masking: linking blind source separation and robust speech recognition, pages 61–80.

Kunetz, G. 1972. Processing and interpretation of magnetotelluric soundings. *Geophysics*, **37**(6), 1005–1021.

Lacy, R. G., & Jacobson, W. O. 1980. Binary cycle geothermal demonstration power plant new developments. *In: Proceedings of the* 4^{th} *Annual Geothermal Conference and Workshop*.

Ladwig, J. M., & Hughes, A. R. W. 1989. An asymmetry in the direction of arrival of whistlers at Sanae, Antarctica. *Journal of Atmospheric and Terrestrial Physics*, **51**, 61–65.

Lagios, E., Tzanis, A., Delibasis, N., Drakopoulos, J., & Dawes, G. K. J. 1994. Geothermal exploration of Kos Island, Greece: magnetotelluric and microseismicity studies. *Geothermics*, **23**, 267–281.

Lagios, E., Galanopoulos, D., Hobbs, B. A., & Dawes, G. J. K. 1998. Two-dimensional magnetotelluric modelling of the Kos Island geothermal region (Greece). *Tectonophysics*, **287**, 157–172.

Larsen, J. C., Mackie, R. L., Manzella, A., Fiordelisi, A., & Rieven, S. 1996. Robust smooth magnetotelluric transfer functions. *Geophysical Journal International*, **124**, 801–819.

Ledo, J. 2005. 2-D versus 3-D magnetotelluric data interpretation. *Surveys in Geophysics*, **26**, 511–543.

Lee, J. H., & Kim, J. 2001. Development of enhanced Wigner-Ville distribution function. *Mechanical Systems and Signal Processing*, **15**, 367–398.

Li, X., & Bi, G. 2009. Reassignment methods for robust time-frequency representations. *In:* 7^{th} *International Conference Information, Communications and Signal Processing ICICS*.

Lilley, F. E. M. 1993. Magnetotelluric analysis using Mohr circles. *Geophysics*, **58**, 1498–1506.

Lilley, F. E. M. 1998a. Magnetotelluric tensor decomposition: Part I, theory for a basic procedure. *Geophysics*, **63**(6), 1885–1897.

Lilley, F. E. M. 1998b. Magnetotelluric tensor decomposition: Part II, Examples of a basic procedure. *Geophysics*, **63**, 1898–1907.

Lou, M., & Rial, J. A. 1997. Characterization of geothermal reservoir crack patterns using shear-wave splitting. *Geophysics*, **62**, 487–494.

Love, D., Cummins, P., & Balfour, N. 2006 (November 24-26). Earthquake patterns in the Flinders Ranges-temporarty network 2003-2006, preliminary results. *In: Presented at Earthquake Engineering in Australia*.

Lui, A. T. Y. 2002. Multiscale phenomena in the near-Earth magnetosphere. *Journal of Atmospheric and Solar-Terrestrial Physics*, **64**, 125–143.

Lui, T. Y., & Najmi, A. H. 1997. Time-frequency decomposition of signals in a current disruption event. *Geophysical Research Letters*, **24**, 3157–3160.

Lund, J., Sanner, B., Rybach, L., Curtis, R., & Hellstrom, G. 2004. Geothermal (ground-source) heat pumps a world view. *GHC Bulletin*, 1–9.

Mackie, R. L., Madden, T.R., & Wannamaker, P.E. 1993. Three-dimensional magnetotelluric modeling using difference equations—Theory and comparisons to integral equation solutions. *Geophysics*, **58**, 215–226.

Mackie, R.L., & Madden, T.R. 1993a. Conjugate direction relaxation solutions for 3-D magnetotelluric modeling. *Geophysics*, **58**, 1052–1057.

Mackie, R.L., & Madden, T.R. 1993b. Three-dimensional magnetotelluric inversion using conjugate gradients. *Geophysical Journal International*, **115**, 215–229.

Mareschal, M. 1986. Modelling of natural sources of magnetospheric origin in the interpretation of regional induction studies: a review. *Surveys in Geophysics*, **8**, 261–300.

McElroy, J. C. 2006. *For the love of oil: the fleecing of the American consumer by big oil companies, politicians and Wallstreet commodity traders*. AuthorHouse.

McLaren, S., Sandiford, M., Hand, M., Neumann, N., Wyborn, L., & Bastrakova, I. 2002. *The hot southern continent: heat flow and heat production in Australian Proterozoic terranes*. Geological Society of Australia. Chap. 12, pages 151–161.

McNeice, G. W., & Jones, A. G. 2001. Multisite, multifrequency tensor decomposition of magnetotelluric data. *Geophysics*, **66**(1), 158–173.

Menk, F. W., Fraser, B. J., Hansen, H. J., Newell, P. T., Meng, C. I., & Morris, R. J. 1992. Identification of the magnetospheric cusp and cleft using Pc1-2 ULF pulsations. *Journal of Atmospheric and Terrestrial Physics*, **54**, 1021–1042.

Neild, S. A., McFadden, P. D., & Williams, M. S. 2003. A review of time-frequency methods for structural vibration analysis. *Engineering Structures*, **25**, 713–728.

Neumann, N., Sandiford, M., & Foden, J. 2000. Regional geochemistry and continental heat flow: implications for the origin of the South Australian heat flow anomaly. *Earth and Planetary Science Letters*, **183**, 107–120.

Newman, G. A., Hoversten, M., Gasperikova, E., & Wannamaker, P. E. 2005 (Jan 31-Feb 2). 3D Magnetotelluric characterization of the Coso geothermal field. *In:* 30^{th} *Workshop on Geothermal Reservoir Engineering*. Stanford University, Stanford, California.

Newman, G. A., Gasperikova, E., & Hoversten, M. 2007. Analysis of 3D magnetotelluric measurements over the Coso geothermal field. *In: AGU Fall Meeting*.

Newman, G. A., Gasperikova, R., Hoversten, G. M., & Wannamaker, P. E. 2008. Three-dimensional magnetotelluric characterization of the Coso geothermal field. *Geothermics*, **37**, 369–399.

Niblett, E. R., & Sayn-Wittgenstein, C. 1960. Variation of electrical conductivity with depth by the magnetotelluric method. *Geophysics*, **25**, 998–1008.

Nomura, R., Shiokawa, K., Pilipenko, V., & Shevtsov, B. 2011. Frequency-dependent polarization characteristics of Pc1 geomagnetic pulsations observed by multipoint ground stations at low latitudes. *Journal of Geophysical Research*, **116**, A01204.

Okaya, D. A., Karageorgi, E., McEvilly, T. V., & Malin, P. E. 1992. Removing vibrator-induced correlation artifacts by filtering in frequency-uncorrelated time space. *Geophysics*, **57**, 916–926.

Oldenburg, D. W. 1979. One-dimensional inversion of natural source magnetotelluric observations. *Geophysics*, **44**(7), 1218–1244.

Omura, Y., Pickett, J., Grison, B., Santolik, O., Dandouras, I., Engebretson, M., Decreau, P. M. E., & Masson, A. 2010. Therory and observation of electromagnetic ion cyclotron triggered emissions in the magnetosphere. *Journal of Geophysical Research*, **115**, A07234.

Onacha, S., Shalev, E., Malin, P., Leary, P., & Bookman, L. 2010 (25-29 April). Interpreted fracture anomalies: joint imaging of geophysical signals from fluid-filled fracture zones in geothermal fields. *In: Proceedings World Geothermal Conference.*

Onacha, S. A., Shalev, E., Malin, P., & Leary, P. 2009. Joint geophysical imaging of fluid filled fracture zones in geothermal fileds in the Kenya Rift Valley. *GRC Transactions*, **33**, 523–529.

Orange, A., Key, K., & Constable, S. 2009. The feasibility of reservoir monitoring using time-lapse marine CSEM. *Geophysics*, **74**, F21–F29.

Oskooi, B. 2006. 1D interpretation of the magnetotelluric data from Travale geothermal field, Italy. *Journal of the Earth and Space Physics*, **32**, 1–16.

O'Toole, J., Mesbah, M., & Boashash, B. 2008. A new discrete analytic signal for reducing aliasing in the discrete Wigner-Ville distribution. *IEEE Transactions on Signal Processing*, **56**, 5427–5434.

Ozgen, M. T., Kuruoglu, E. E., & Herranz, D. 2009. Astrophysical image separation by blind time-frequency source separation methods. *Digital Signal Processing*, **19**, 360–369.

Parry, M., Canziani, O., Palutikof, J., van der Linden, P., & Hanson, C. (eds). 2007. *Climate Change 2007: impacts, adaptation and vulnerability.* Cambridge University Press.

Patella, D. 1987. Tutorial interpretation of magnetotelluric measurements over an electrically dispersive one-dimensional earth. *Gephysical Prospecting*, **35**, 1–11.

Patella, D. 1993. I principi metodologici della magnetotellurica su mezzi generalmente dispersivi. *Annali Di Geofisica*, **36**, 147–160.

Peacock, J. R., Thiel, S., Reid, P., & Heinson, G. 2012. Magnetotelluric Monitoring of an Enhanced Geothermal System Fluid Injection. *Geophysical Research Letters*, **In Press**, 1–6.

Pellerin, L., & Hohmann, G. W. 1990. Transient electromagnetic inversion: A remedy for magnetotelluric static shifts. *Geophysics*, **55**, 1242–1250.

Pellerin, L., Johnston, J. M., & Howhmann, G. W. 1996. A numerical evaluation of electromagnetic methods in geothermal exploration. *Geophysics*, **61**, 121–130.

Peng, D., & Xiang, Y. 2010. Underdetermined blind speparation of non-sparse sources using spatial time-frequency distributions. *Digital Signal Processing*, **20**, 581–596.

Phillips, W. S., Rutledge, J. T., House, L. S., & Fehler, M. C. 2002. Induced microearthquake patterns in hydrocarbon and geothermal reservoirs: six case studies. *Pure and Applied Geophysics*, **159**, 345–369.

Pielemeier, W. J., Wakefield, G. H., & Simoni, M. H. 1996. Time-frequency analysis of musical signals. *Proceedings of the IEEE*, **84**, 1216–1230.

Pilipenko, V. A., Chugunova, O. M., & Engebretson, M. J. 2008. Pc3-Pc4 ULF waves at polar latitudes. *Journal of Atmospheric and Solar-Terrestrial Physics*, **60**, 2262–2274.

Preiss, W. V. 1990. *The evolution of Late Precambrian-Early Paleozoic rift complex: the Adelaide Geosyncline*. Special Publication, vol. 16. Brisbane: Geological Society of Australia. Chap. A statigraphic ans tectonic overview of the Adelaide Geosyncline, South Australia, pages 1–33.

Preiss, W. V. 1993. *Bulletin 54: the geology of South Australia*. Mines and Energy Geological Survey of South Australia. Chap. Dalemarian fold belt, pages 23–24.

Pride, S. R. 1994. Governing equations for the coupled electromagnetic and acoustics of porous media. *Physical Review B*, **50**, 678–696.

Pride, S. R., & Haartsen, M. W. 1996. Electroseismic wave properties. *Journal of the Acoustical Society of America*, **100**, 1301–1315.

Purtymun, W. D., West, F. G., & Pettitt, R. A. 1974. *Geology of geothermal test hole GT-2 Fenton Hill Site, July 1974*. Tech. rept. Los Alamos National Laboratory.

Reilly, W. I. 1979 (February). *Anisotropy tensors in magnetotelluric interpretation*. Tech. rept. 136. Geophysics Division, Department of Scientific and Industrial Research, Wellington, New Zealand.

RenewableEnergyWorld.com. 2010 (Feb). *US Government expected to increase geothermal funding by 25%, http://www.renewableenergyworld.com/rea/news/article/2010/02/us-government-to-increase-geothermal-funding-by-25*.

Rial, J. A., Elkibbi, M., & Yang, M. 2005. Shear-wave splitting as a tool for the characterization of geothermal fractured reservoirs: lessons learned. *Geothermics*, **34**, 365–385.

Richert, J. P. 1976. Thrust faulting in the Northern Flinders Range, South Australia. *Journal of the Geologic Society of Australia*, **23**, 361–366.

Rodi, W., & Mackie, R. L. 2001. Nonlinear conjugate gradients algorithm for 2-D magnetotelluric inversion. *Geophysics*, **66**, 174–187.

Romo, J. M., Gomez-Trevino, E., & Antonio-Carpio, R. G. 2005 (April). New magnetotelluric response functions for geothermal applications. *In: Proceedings World Geothermal Congress*.

Sandiford, M., Paul, E., & Flöttman, T. 1998. Sedimentary thickness variations and deformation intensity during basin inversion in the Flinders Ranges, South Australia. *Journal of Structural Geology*, **20**, 1721–1731.

Sasaki, Y. 2004. Three-dimensional inversion of static-shifted magnetotelluric data. *Earth Planets Space*, **56**, 239–248.

Sasaki, Y., & Meju, M. A. 2006. Three-dimensional joint inversion for magnetotelluric resisitivity and static shift distributions in complex media. *Journal of Geophysical Research*, **111**, 05101–05112.

Scales, J. A., Smith, M. L., & Treitel, S. 2001. *Introductory Geophysical Inverse Theory*. Samizday Press.

Sejdic, E., & Djurovic, I. 2010. Robust S-transform based on L-DTF. *Electronic Letters*, **46**, 1–2.

Simpson, F., & Bahr, K. 2005. *Practical Magnetotellurics*. Cambridge University Press.

Siripunvaraporn, W., & Egbert, G. 2009. WSINV3DMT: Vertical magnetic field transfer function inversion and parallel implementation. *Physics of the Earth and Planetary Interiors*, **173**, 317–329.

Siripunvaraporn, W., Egbert, G., Lenbury, Y., & Uyeshima, M. 2005. Three-dimensional magnetotelluric inversion: data-space method. *Physics of The Earth and Planetary Interiors*, **150**, 3–14.

Smirnov, M. Yu. 2003. Magnetotelluric data processing with a robust statistical procedure having a high breakdown point. *Geophysical Journal International*, **152**, 1–7.

Spichak, V. 2001. Three-dimensional interpretation of MT data in volcanic environments (computer simulation). *Annali Di Geofisica*, **44**, 273–286.

Spichak, V. V. 2006. Estimating temperature distributions in geothermal areas using a neuronet approach. *Geothermics*, **35**, 181–197.

Spichak, V. V., & Manzella, A. 2009. Electromagnetic sounding of geothermal zones. *Journal of Applied Geophysics*, **68**, 459–478.

Spichak, V. V., & Zakharova, O. K. 2009 (9-11 February). Electromagnetic temperature extrapolation in depth in the Hengill geothermal area, Iceland. *In:* 34^{th} *Workshop on Geothermal Reservoir Engineering*.

Spichak, V. V., Zakharova, O., & Rybin, A. 2007 (January 22-24). Estimation of the sub-surface temperature by means of magnetotelluric sounding. *In: 32 Workshop on Geothermal Reservoir Engineering*.

Spriggs, R. C. 1984. *Arkaroola–Mount Painter in the Northern Flinders Ranges, SA: The last billion years*. Australia: Arkaroola Pty.

Stankovic, L. 1994. A method for time-frequency analysis. *IEEE Transactions on Signal Processing*, **42**, 225–229.

Stoyer, C. H. 1976. Consequences of induced polarization in magnetotelluric interpretation. *Pageoph*, **114**, 435–450.

Streich, R., Becken, M., & Ritter, O. 2010. Imaging CO_2 storage sites, geothermal reservoirs, and gas shales using controlled-source magnetotellurics: modeling studies. *Chemie der Erde*, **70**, 63–75.

Szarka, L., & Menvielle, M. 1997. Analysis of rotational invariants of the magnetotelluric impedance tensor. *Geophysical Journal International*, **129**, 133–142.

Teale, G. S. 1993. *Bulletin 54: The geology of South Australia*. Mines and Energy Geological Survey of South Australia. Chap. Mount Painter and Mount Babbage Inliers, pages 93–100.

Tester, J. W., Anderson, B. J., Batchelor, A. S., Blackwell, D. D., DiPippo, R., Drake, E. M., Garnish, J., Livesay, B., Moore, M. C., Nichols, K., Petty, S., Toksoz, M. N., & Jr, R. W. Veatch. 2006. *The future of geothermal energy*. Tech. rept. MIT.

Tikhonov, A. N. 1986. *On determining electrical characteristics of the deep layers of the Earth's crust*. Society of Exploration Geophysics. Reprint from 1950.

Tikhonov, A.N. 1950. The determination of the electrical properties of deep layers of the Earth's crust. *Dokl. Acad. Nauk. SSR*, **73**, 295–297.

Toledo-Redondo, S., Salinas, A., Porti, J., Morente, J. A., Fonrieles, J., Mendez, A., Galindo-Zaldivar, J., Pedrera, A., Ruiz-Constan, A., & Anahnah, F. 2010. Study of Schumann resonances based on magnetotelluric records from the western Mediterranean and Antarctica. *Journal of Geophysical Research*, **115**, D22114–24.

Viljanen, A., Nevanlinna, H., Pajunpaa, K., & Pulkkinen, A. 2001. Time derivative of the horizontal geomagnetic field as an activity indicator. *Annales Geophysicae*, **19**, 1107–1118.

Ville, J. 1948. Theorie et applications de la notion de signal analytique. *Cables et Transmission*, **2A**, 61–74.

Wallace, W. H. 2003. *Introduction to geomagnetic fields*. 2^{nd} edn. Cambridge University Press.

Wannamaker, P. E. 2005. Anisotropy versus heterogeneity in continental solid earth electromagnetic studies: fundamental response characteristics and implications for physicochemical state. *Surveys in Geophysics*, **26**, 733–765.

Wannamaker, P. E., Stodt, J. A., & Rijo, L. 1987. A stable finite element solution for two-dimensional magnetotelluric modelling. *Geophysical Journal International*, **88**, 277–296.

Wannamaker, P. E., Rose, P. E., Doerner, W. M., Berard, B. C., McCulloch, J., & Nurse, K.. 2004 (Jan 26-28). Magnetotelluric surveying and monitoring at the Coso geothermal area, California, in support of the enhanced geothermal systems concept: survey parameters and initial results. *In:* 29^{th} *Workshop on Geothermal Reservoir Engineering*. Stanford University, Stanford, California.

Warpinski, N. R. 2009. Integrating microseismic monitoring with well completions, reservoir behavior and rock mechanics. *In: SPE Tight Gas Completions*. San Antonio, TX, USA: SPE, for SPE.

Weaver, J. T., Agarwal, A. K., & Lilley, F. E. M. 2000. Characterization of the magnetotelluric tensor in terms of its invariants. *Geophysical Journal International*, **141**, 321–321.

Weaver, J.T., & Lilley, F.E.M. 2004. Using Mohr circles to identify regional dimensionality and strike angle from distorted magnetotelluric data. *Exploration Geophysics*, **35**, 251–254.

Weckmann, U., Ritter, O., & Haak, V. 2003. Images of the magnetotelluric apparent resistivity tensor. *Geophysical Journal International*, **155**, 456–456.

Wigner, E. 1932. On the quantum correction for thermodynamic equilibrium. *Physical Review*, **40**, 749–759.

Wirianto, M., Mulder, W. A., & Slob, E. C. 2010. A feasibility study of land CSEM reservoir monitoring in a complex 3-D model. *Geophysical Journal International*, **181**, 741–755.

Wohlenberg, J., & Keppler, H. 1987. Monitoring and interpretation of seismic observations in hot dry rock geothermal energy systems. *Geothermics*, **16**, 441–445.

Yasukawa, K., Ishido, T., & Suzuki, I. 2005. Geothermal reservoir monitoring by continuous self-potential measurements, Mori geothermal field, Japan. *Geothermics*, **34**, 551–567.

Yee, E., & Paulson, K. V. 1988. Concerning dispersion relations for the magnetotelluric impedance tensor. *Geophysical Journal*, **95**, 549–559.

Yoshioka, K., Pasikki, R., Suryata, I., & Riedel, K. 2009 (24-26 March). Hydraulic stimulation techniques applied to injection wells at the Salak geothermal field, Indonesia. *In: SPE Regional Meeting*.

Zaric, N., Orovic, I., & Stankovic, S. 2010. Robust time-frequency distributions with complex-lag argument. *EURASIP Journal on Advances in Signal Processing*, **1**, 1–10.

Zhang, P., Roberts, R. G., & Pedersen, L. B. 1987. Magnetotelluric strike rules. *Geophysics*, **52**(3), 267–278.

Appendix A

2D Modeling Files and Responses

This appendix displays the 2D Occam model fits. The station locations are plotted in Figure A.1 for reference. The mesh files used for inversion are displayed in Figure A.2 and Figure A.7. The pseudo section of the data and the model are displayed in Figure A.3 and Figure A.4. The data and model responses of the Z_{xy} (TE) and Z_{yx} (TM) modes are plotted in Figures A.5, A.6, A.8, and A.9. The black lines are the data with the stars representing the TE mode and the triangles representing the TM mode. The gray lines are the model responses from the best fitting model from an Occam inversion. Here best fitting is estimated as the RMS and how well structures correlate with seismic and borehole data. The plus signs represent the TE mode and the x's represent the TM mode. Note the model fits the phase well for all periods, while the apparent resistivity is fit well up to about 20 s. At this point there is a dip in data apparent resistivity which is an artifact of weak source signal at around 20 s. This dip is not predicted in the phase therefore is not fit by the model. The other feature that is not fit well is the rise in apparent resistivity past 100 s, which is due to inaccurate calibration of the induction coils past 100 s. Again, the phase does not predict this change and is not fit by the model.

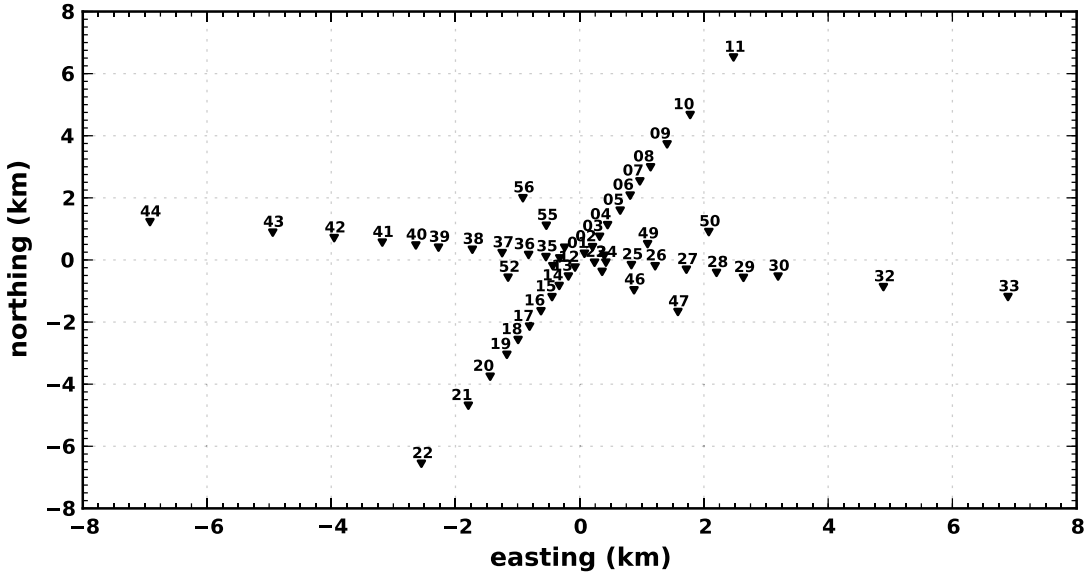

Figure A.1: Station locations relative to Paralana 2 injection well for reference.

MESH FILE FROM MAKE2DMODEL							
0	321	98	0	0	2		
104965.3	34988.4	11662.8	3887.6	1295.9	432	144	48
48	48	48	48	48	48	48	48
48	48	48	48	48	48	48	48
48	48	48	48	48	48	48	48
48	48	48	48	48	48	48	48
48	48	48	48	48	48	48	48
48	48	48	48	49.9	49.9	49.9	49.9
49.9	49.9	49.9	49.9	49.9	49.9	49.9	49.9
49.9	49.9	49.9	49.9	49.9	49.9	49.9	49.9
47.2	47.2	47.2	47.2	47.2	47.2	47.2	47.2
47.2	47.2	47.2	47.2	47.2	47.2	47.2	47.2
42.6	42.6	42.6	42.6	42.6	42.6	42.6	42.6
42.6	42.6	42.6	42.6	46.8	46.8	46.8	46.8
46.8	46.8	46.8	46.8	46.8	46.8	44.1	44.1
44.1	44.1	44.1	44.1	44.1	44.1	44.1	44.1
44.1	44.1	48.8	48.8	48.8	48.8	48.8	48.8
48.8	48.8	48.8	48.8	47.1	47.1	47.1	47.1
47.1	47.1	47.1	47.1	42.2	42.2	42.2	42.2
42.2	42.2	42.2	42.2	38.5	38.5	38.5	38.5
38.5	38.5	38.5	38.5	46.9	46.9	46.9	46.9
46.9	46.9	46.9	46.9	46.9	46.9	40.9	40.9
40.9	40.9	40.9	40.9	43.9	43.9	43.9	43.9
43.9	43.9	43.9	43.9	49.7	49.7	49.7	49.7
49.7	49.7	49.7	49.7	42.4	42.4	42.4	42.4
42.4	42.4	42.4	42.4	42.4	42.4	42.4	42.4
42.4	42.4	42.4	42.4	42.4	42.4	42.4	42.4
42.4	42.4	42.4	42.4	48.4	48.4	48.4	48.4
48.4	48.4	48.4	48.4	48.4	48.4	48.6	48.6
48.6	48.6	48.6	48.6	48.6	48.6	48.6	48.6
49	49	49	49	49	49	49	49
49	49	49	49	49	49	49	49
46.1	46.1	46.1	46.1	46.1	46.1	46.1	46.1
46.1	46.1	46.1	46.1	46.1	46.1	46.1	46.1
46.1	46.1	46.1	46.1	46.1	46.1	49.5	49.5
49.5	49.5	49.5	49.5	49.5	49.5	49.5	49.5
49.5	49.5	49.5	49.5	49.5	49.5	49.5	49.5
49.5	49.5	49.5	49.5	49.5	49.5	49.5	49.5
49.5	49.5	49.5	49.5	49.5	49.5	49.5	49.5
49.5	49.5	49.5	49.5	49.5	49.5	49.5	49.5
49.5	148.6	445.7	1337.2	4011.6	12034.8	36104.5	108313.6
15	15	15	15	30	30	30	30
30	30	30	30	30	30	30	31.1
33.6	36.3	39.2	42.3	45.7	49.3	53.2	57.5
62.1	67	72.4	78.2	84.4	91.1	98.4	106.2
114.7	123.9	133.7	144.4	155.9	168.4	181.8	196.3
212	228.9	247.1	266.8	288.1	311.1	335.9	362.7
391.7	422.9	456.7	493.1	532.4	574.9	620.8	670.3
723.8	781.5	843.9	911.2	983.9 1	062.3 1	147.1 1	238.6
1337.4	1444.1	1559.3	1683.7	1818.0 1	963.1 2	119.7 2	288.8
2471.3	2668.5	2881.4	3111.2	3359.4 3	627.4 3	916.8 4	229.3
4566.7	4931	5324.4	5749.1	6207.7 6	703.0 7	237.7 7	815.1
8438.5	9111.7	9838.6	10623.5	11471	34413	103238.9	309716.6
929149.7							

Figure A.2: The 2D Occam mesh file for NS line. The top line includes the number of horizontal nodes (321) and vertical nodes (98). The white area represents the location of horizontal nodes (m) and the gray region represents the vertical node location (m).

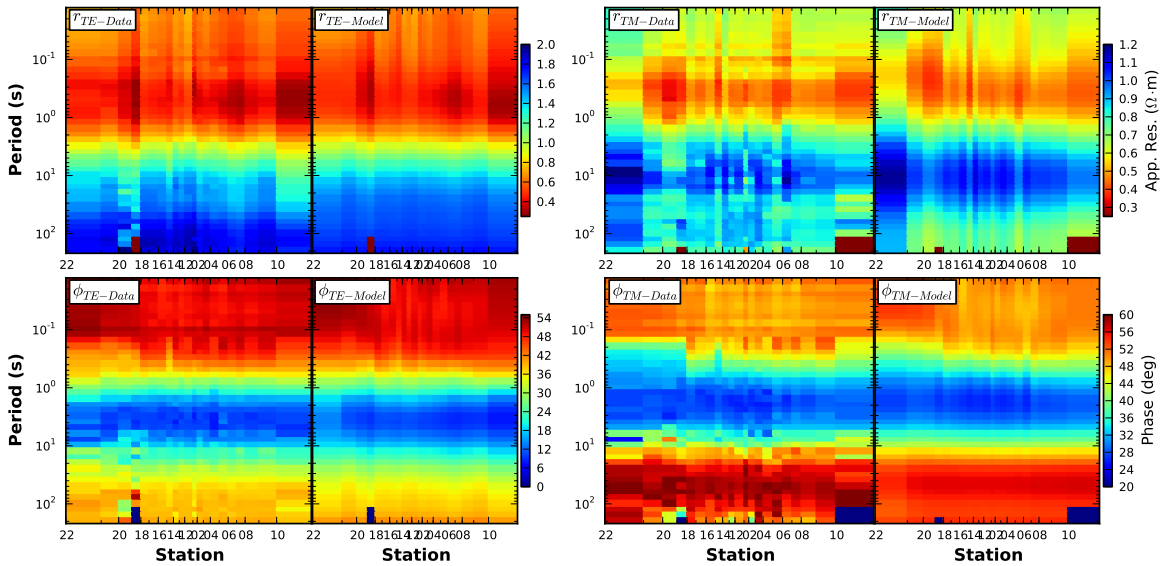

Figure A.3: Psuedo sections for the MT response of data and the model response found from a 2D Occam inversion for the NS line.

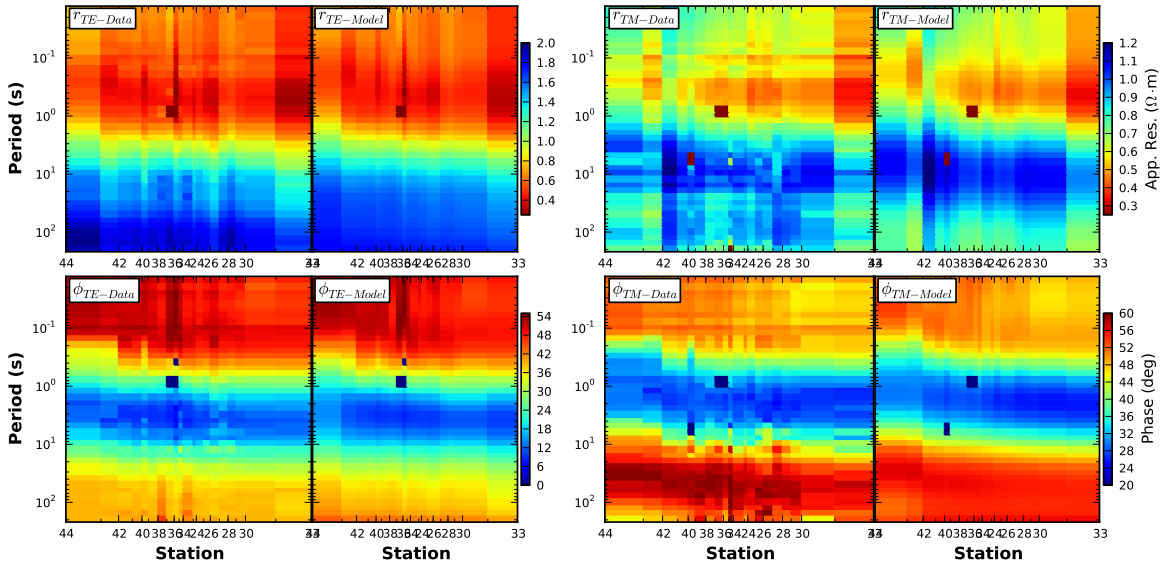

Figure A.4: Psuedo sections for the MT response of data and the model response found from a 2D Occam inversion for the EW line.

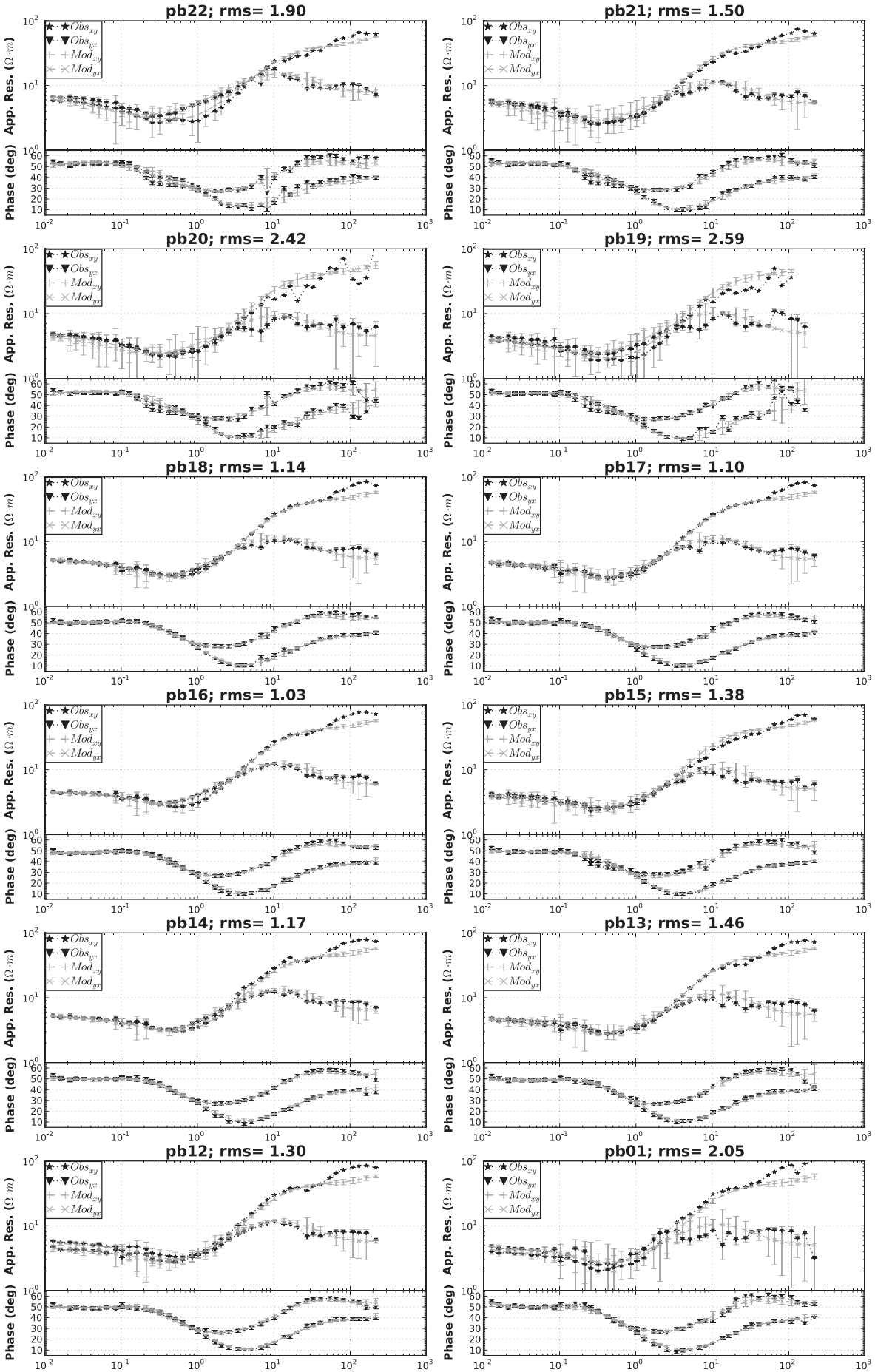

Figure A.5: Top left starts at the southern most site.

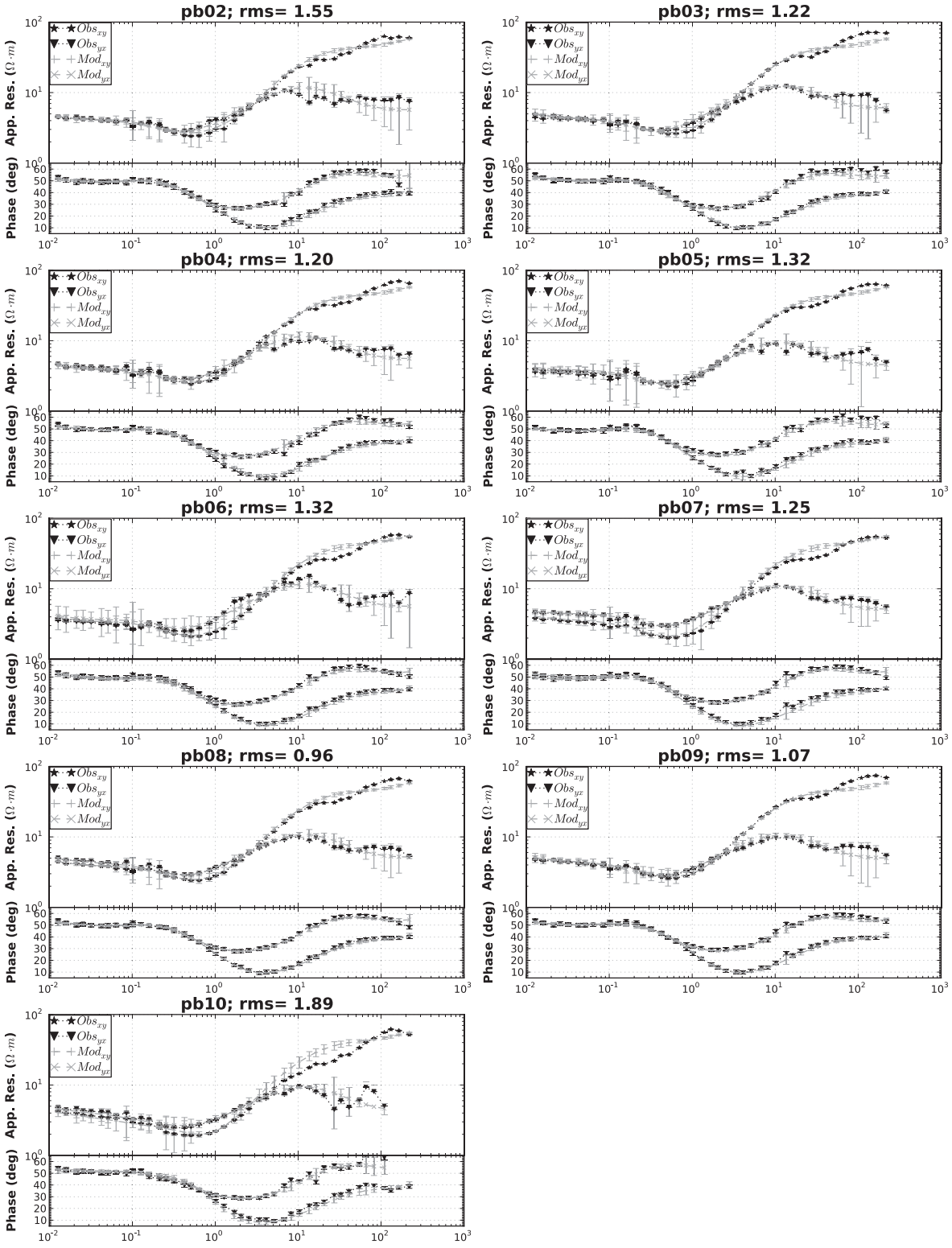

Figure A.6: Top left starts at 500 m north Paralana 2.

MESH FILE FROM MAKE2DMODEL							
0	321	98	0	0	2		
104440.5	34813.5	11604.5	3868.2	1289.4	429.8	143.3	47.8
47.8	47.8	47.8	47.8	47.8	47.8	47.8	47.8
47.8	47.8	47.8	47.8	47.8	47.8	47.8	47.8
47.8	47.8	47.8	47.8	47.8	47.8	47.8	47.8
47.8	47.8	47.8	47.8	47.8	47.8	47.8	47.8
47.8	47.8	47.8	47.8	47.8	47.8	47.8	47.8
47.8	47.8	47.8	47.8	45.6	45.6	45.6	45.6
45.6	45.6	45.6	45.6	45.6	45.6	45.6	45.6
45.6	45.6	45.6	45.6	45.6	45.6	45.6	45.6
45.6	45.6	49.3	49.3	49.3	49.3	49.3	49.3
49.3	49.3	49.3	49.3	49.3	49.3	49.3	49.3
49.3	49.3	45.7	45.7	45.7	45.7	45.7	45.7
45.7	45.7	45.7	45.7	45.7	45.7	46.4	46.4
46.4	46.4	46.4	46.4	46.4	46.4	45.7	45.7
45.7	45.7	45.7	45.7	45.7	45.7	45.7	45.7
45.7	45.7	49.1	49.1	49.1	49.1	49.1	49.1
49.1	49.1	49.1	49.1	43	43	43	43
43	43	43	43	43	43	47.8	47.8
47.8	47.8	47.8	47.8	37.8	37.8	37.8	37.8
37.8	37.8	48	48	48	48	48	48
48	48	48	48	48	48	44.9	44.9
44.9	44.9	41.8	41.8	41.8	41.8	41.8	41.8
41.8	41.8	41.8	41.8	47.9	47.9	47.9	47.9
47.9	47.9	47.9	47.9	42.9	42.9	42.9	42.9
42.9	42.9	42.9	42.9	42.9	42.9	42.9	42.9
49.6	49.6	49.6	49.6	49.6	49.6	49.6	49.6
49.6	49.6	45.5	45.5	45.5	45.5	45.5	45.5
45.5	45.5	45.5	45.5	45.2	45.2	45.2	45.2
45.2	45.2	45.2	45.2	45.2	45.2	45.2	45.2
48	48	48	48	48	48	48	48
48	48	48	48	48	48	48	48
48	48	48	48	48	48	48	48
48	48	48	48	48	48	48	48
48	48	48	48	48.3	48.3	48.3	48.3
48.3	48.3	48.3	48.3	48.3	48.3	48.3	48.3
48.3	48.3	48.3	48.3	48.3	48.3	48.3	48.3
48.3	48.3	48.3	48.3	48.3	48.3	48.3	48.3
48.3	48.3	48.3	48.3	48.3	48.3	48.3	48.3
48.3	48.3	48.3	48.3	48.3	48.3	48.3	48.3
48.3	145	435.1	1305.3	3916	11748.1	35244.2	105732.6
15	15	15	15	30	30	30	30
30	30	30	30	30	30	30	31.1
33.6	36.3	39.2	42.3	45.7	49.3	53.2	57.5
62.1	67	72.4	78.2	84.4	91.1	98.4	106.2
114.7	123.9	133.7	144.4	155.9	168.4	181.8	196.3
212	228.9	247.1	266.8	288.1	311.1	335.9	362.7
391.7	422.9	456.7	493.1	532.4	574.9	620.8	670.3
723.8	781.5	843.9	911.2	983.9	1062.3	1147.1	1238.6
1337.4	1444.1	1559.3	1683.7	1818	1963.1	2119.7	2288.8
2471.3	2668.5	2881.4	3111.2	3359.4	3627.4	3916.8	4229.3
4566.7	4931	5324.4	5749.1	6207.7	6703	7237.7	7815.1
8438.5	9111.7	9838.6	10623.5	11471	34413.0 1	3238.9	309716.6
929149.7							

Figure A.7: The 2D Occam mesh file for EW line. The top line includes the number of horizontal nodes (321) and vertical nodes (98). The white area represents the location of horizontal nodes (m) and the gray region represents the vertical node location (m).

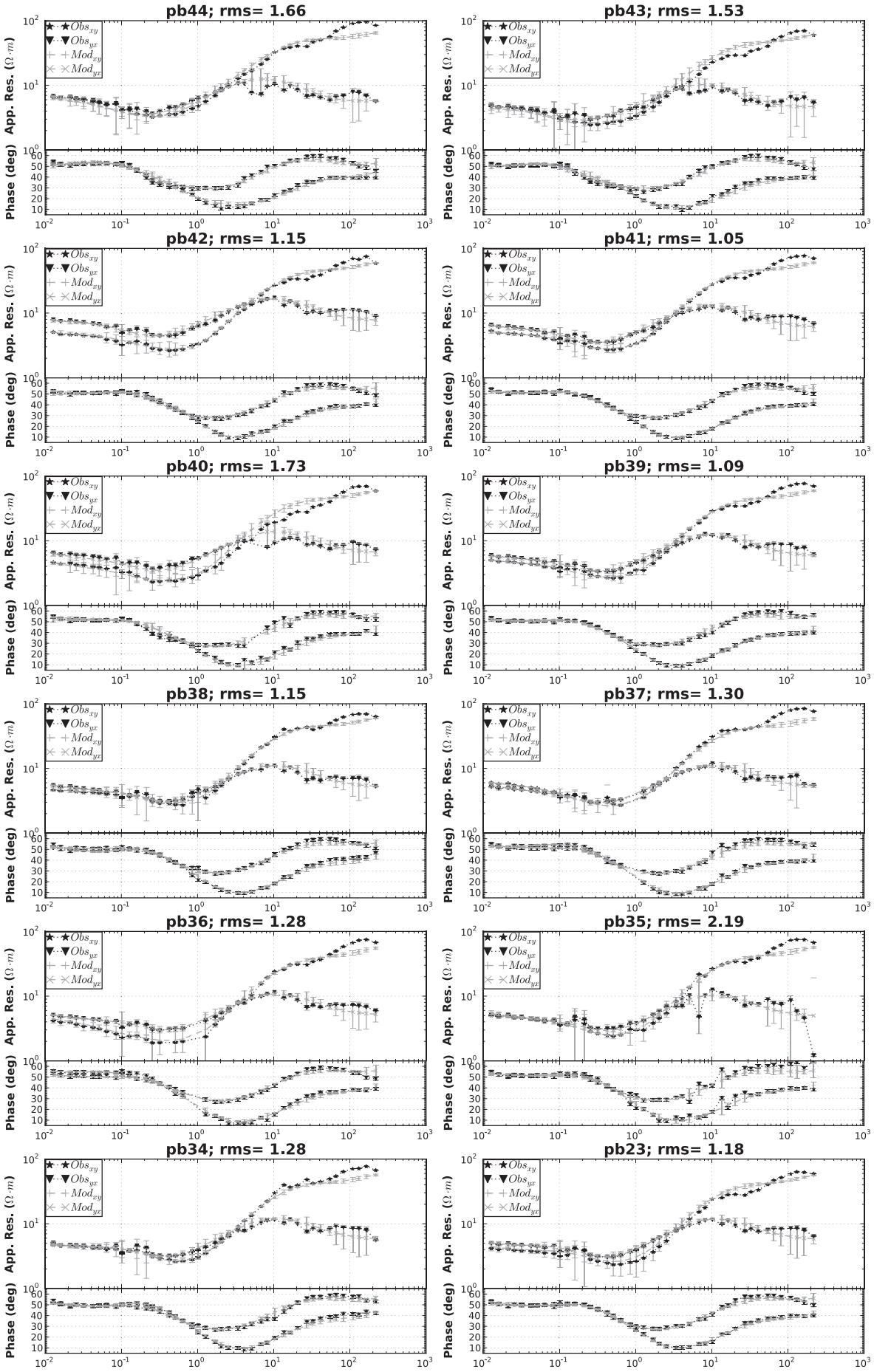

Figure A.8: Top left starts at the southern most site.

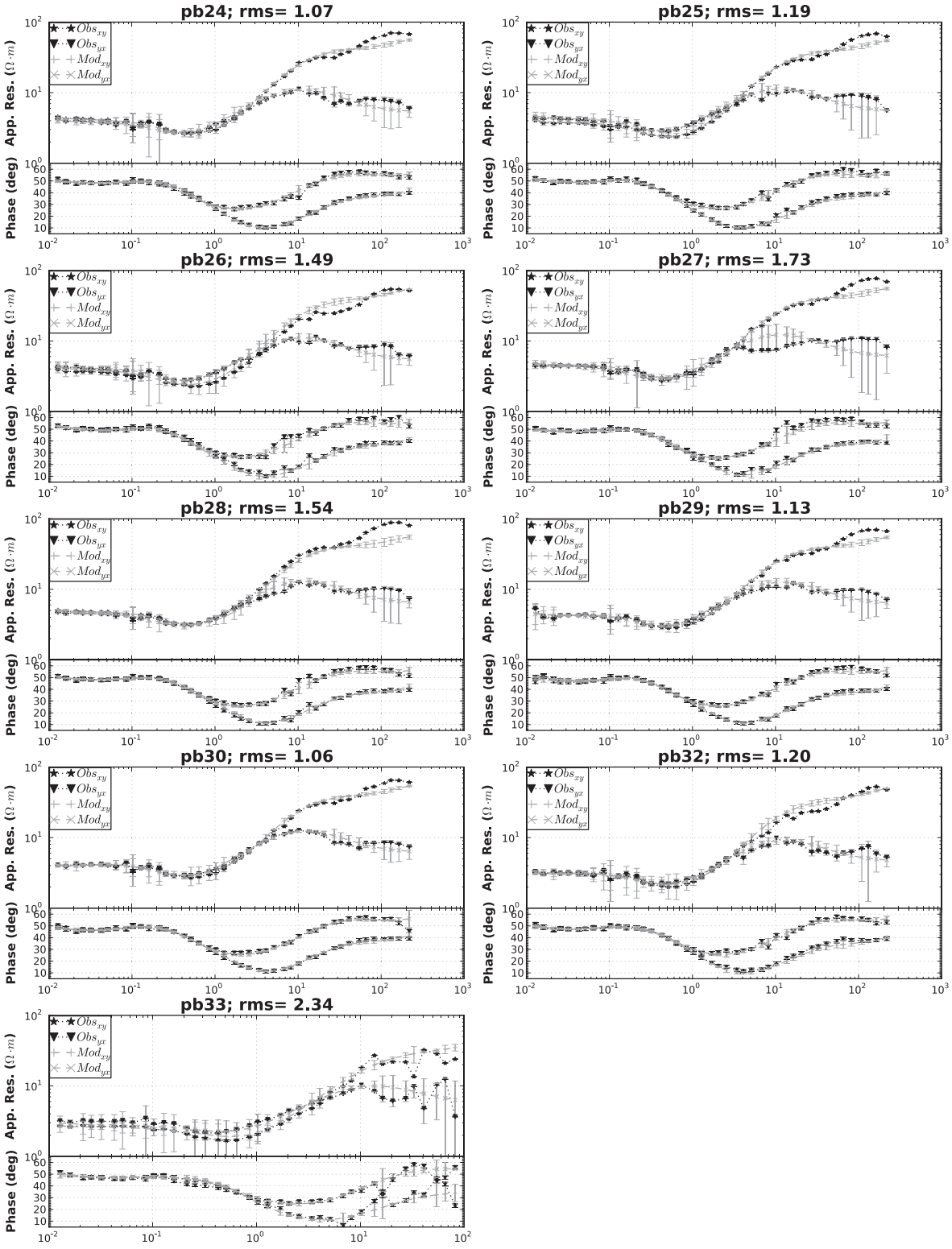

Figure A.9: Top left starts at 400 m east Paralana 2.

Appendix B

3D Modeling Files and Responses

In this section the data an model responses used to estimate subsurface resistivity structure near Paralana are displayed. The 3D inversion code of Siripunvaraporn *et al.* (2005) is employed. The mesh is 69 (EW) x 56 (NS) x 45 (vertical) with cell sized of 300 m x 300 m within the 8 km of the center of the grid (Figure B.2). The station locations are shown in Figure B.1 as a reference. All 8 components of the impedance tensor are inverted for with error bars of 5% for the off diagonal elements and 50% for the diagonal elements. The starting model is 10 Ω·m . The starting smoothing parameters were [5, 0.3, 0.3, 0.3]. These were changed after 3 iterations to [5, 0.1, 0.1, 0.1], which lets the inversion give more structure to the model. After 3 more iterations the global RMS reached a minimum of 1.08. The data and model responses are displayed later with the general layout displayed in Figure B.3.

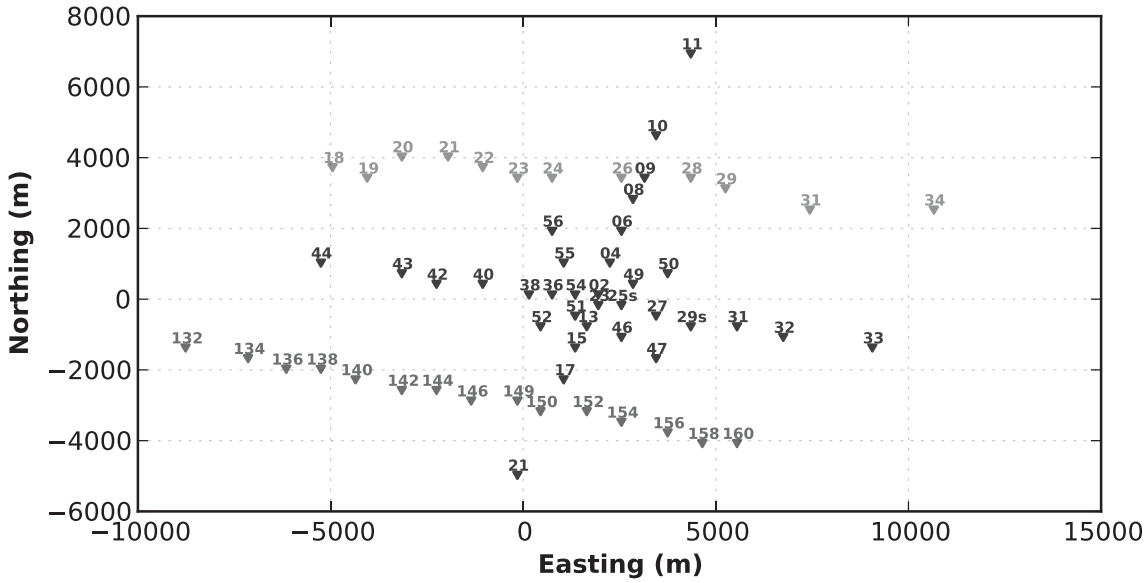

Figure B.1: Station locations relative to the center of the 3D grid used to model the subsurface conductivity structure near Paralana. Note that station locations are moved such that they are in the middle of model cells. The gray triangles labeled in the hundreds represent stations from the survey collected by Quantec in 2006, the black triangles represent data collected pre-injection for this project and the light gray triangles represent stations collected May, 2012 as part of an honors project.

#Initial	model						
56	69	45	1				
52782	32989	20618	12886	8054	5034	3146	1966
1229	768	480	300	300	300	300	300
300	300	300	300	300	300	300	300
300	300	300	300	300	300	300	300
300	300	300	300	300	300	300	300
300	300	300	300	300	480	768	1229
1966	3146	5034	8054	12886	20618	32989	52782
52782	32989	20618	12886	8054	5034	3146	1966
1229	768	480	300	300	300	300	300
300	300	300	300	300	300	300	300
300	300	300	300	300	300	300	300
300	300	300	300	300	300	300	300
300	300	300	300	300	300	300	300
300	300	300	300	300	300	300	300
300	300	480	768	1229	1966	3146	5034
8054	12886	20618	32989	52782			
15	18	22	26	31	37	45	54
64	77	93	111	134	160	193	231
277	333	399	479	575	690	828	994
1193	1431	1717	2061	2473	2967	3561	4273
5128	6153	7384	8860	10632	12759	15311	18373
22047	26457	31748	38098	45717			
10							

Figure B.2: 3D mesh file input into the 3D code of Siripunvaraporn *et al.* (2005). The top numbers indicate the number of cells in the N-S direction, E-W direction and vertical direction. The gray blocks have numbers that correspond to cell widths (m) for the N-S, E-W and vertical directions. The bottom number 10 represents the starting model in Ω·m

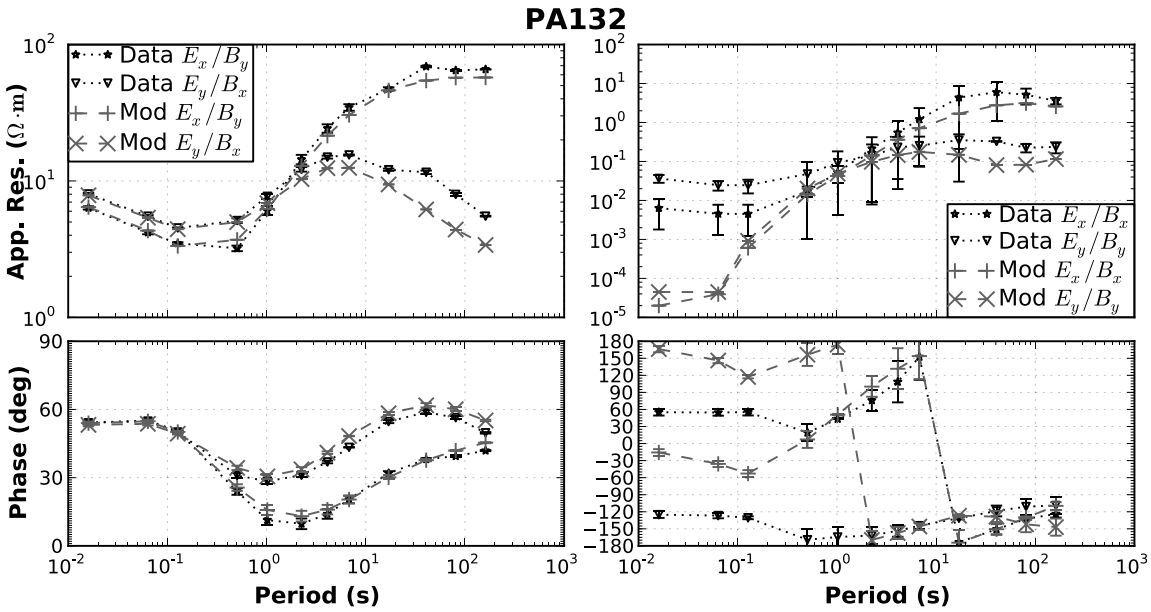

Figure B.3: Layout of displaying the 3D responses. The black lines are the data and the gray lines are the responses. The left to plots are the off-diagonal components of $\hat{\mathbf{Z}}$ represented as apparent resistivity (top) and impedance phase (bottom). The right plots the diagonal components of $\hat{\mathbf{Z}}$ represented as apparent resistivity (top) and impedance phase (bottom).

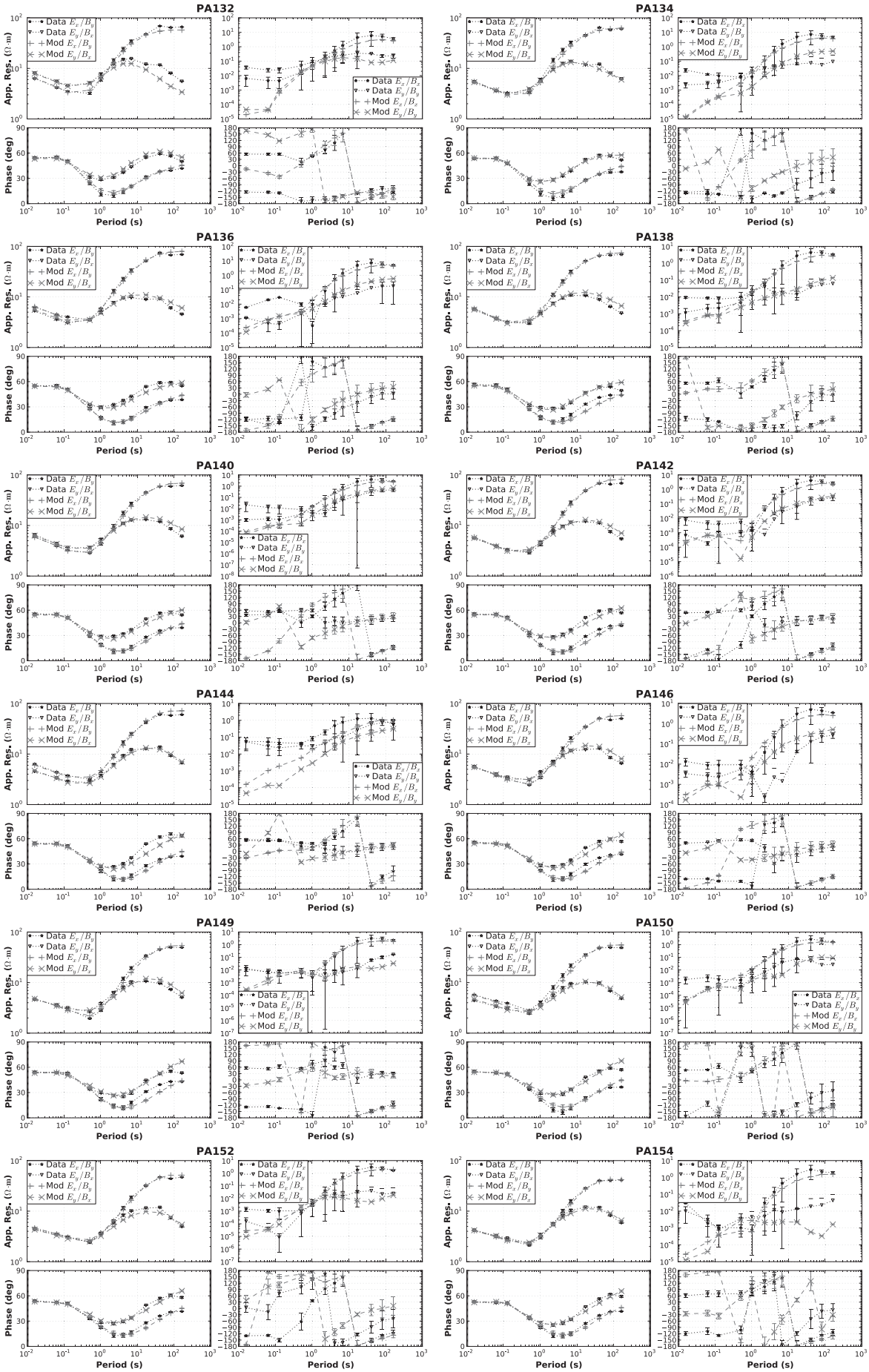

Figure B.4: Stations along the Quantec line.

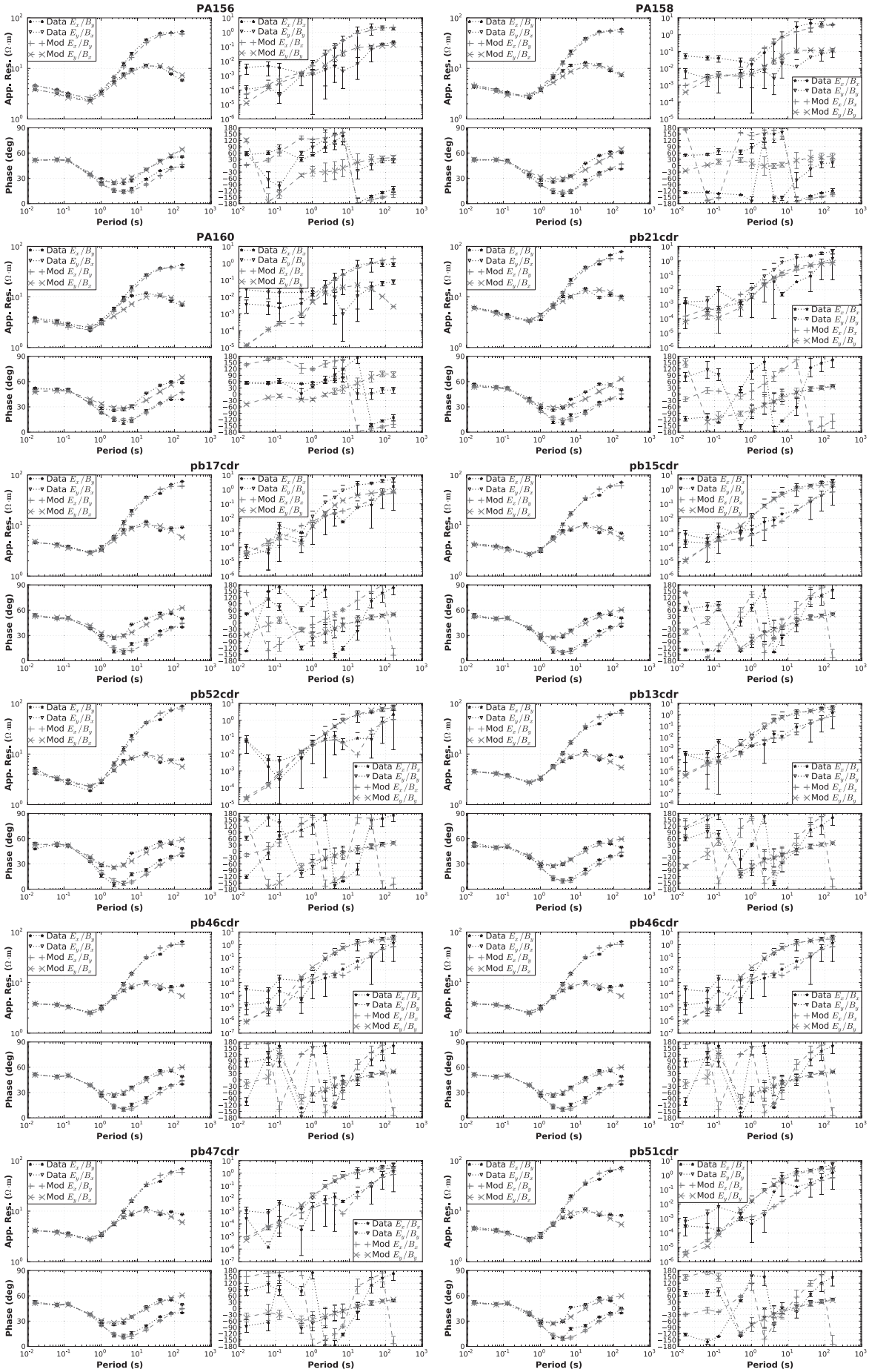

Figure B.5: Stations along the Quantec line and southern part of the survey for this project.

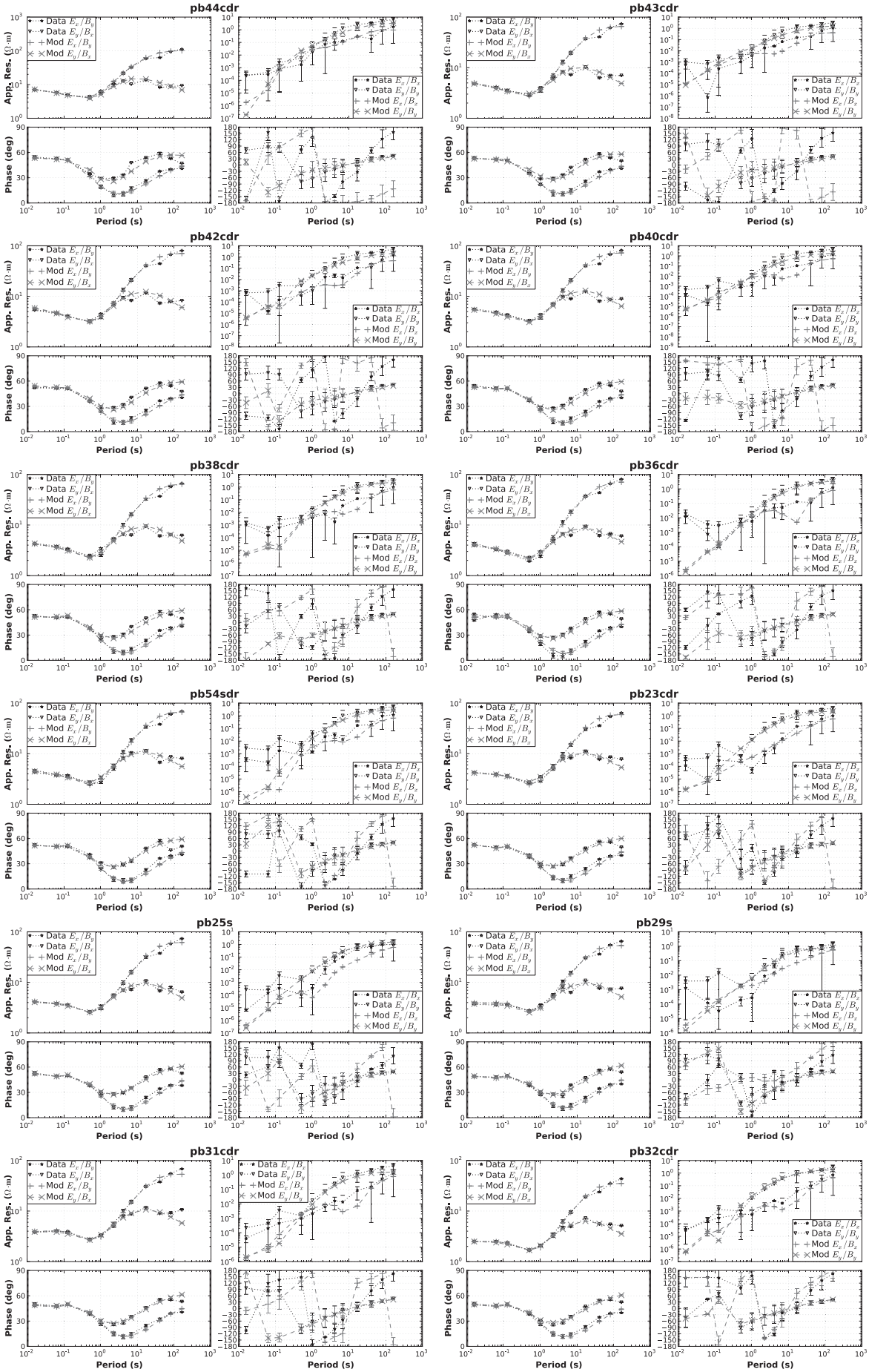

Figure B.6: EW line of data from this project.

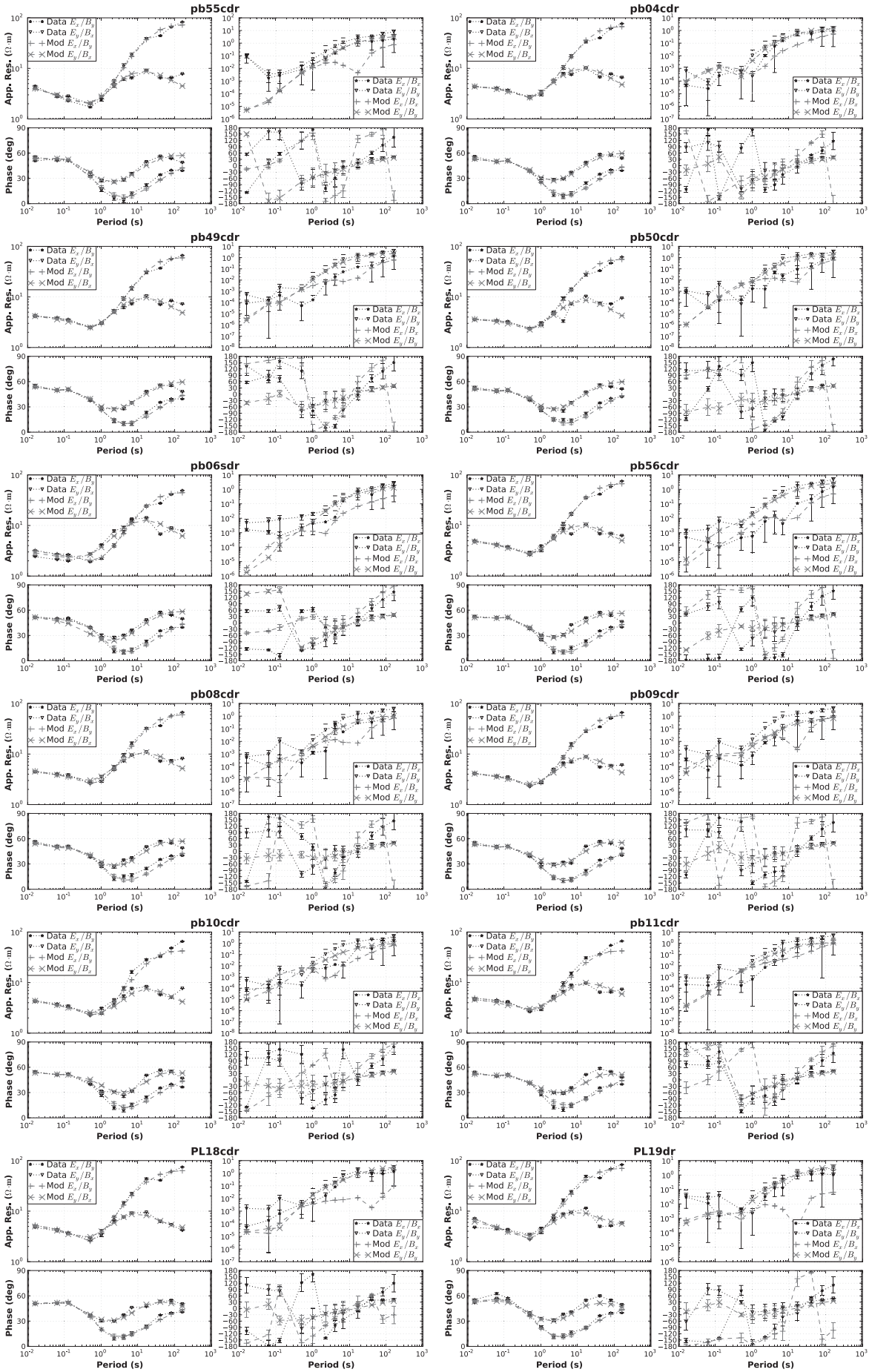

Figure B.7: Northern part of data from this project.

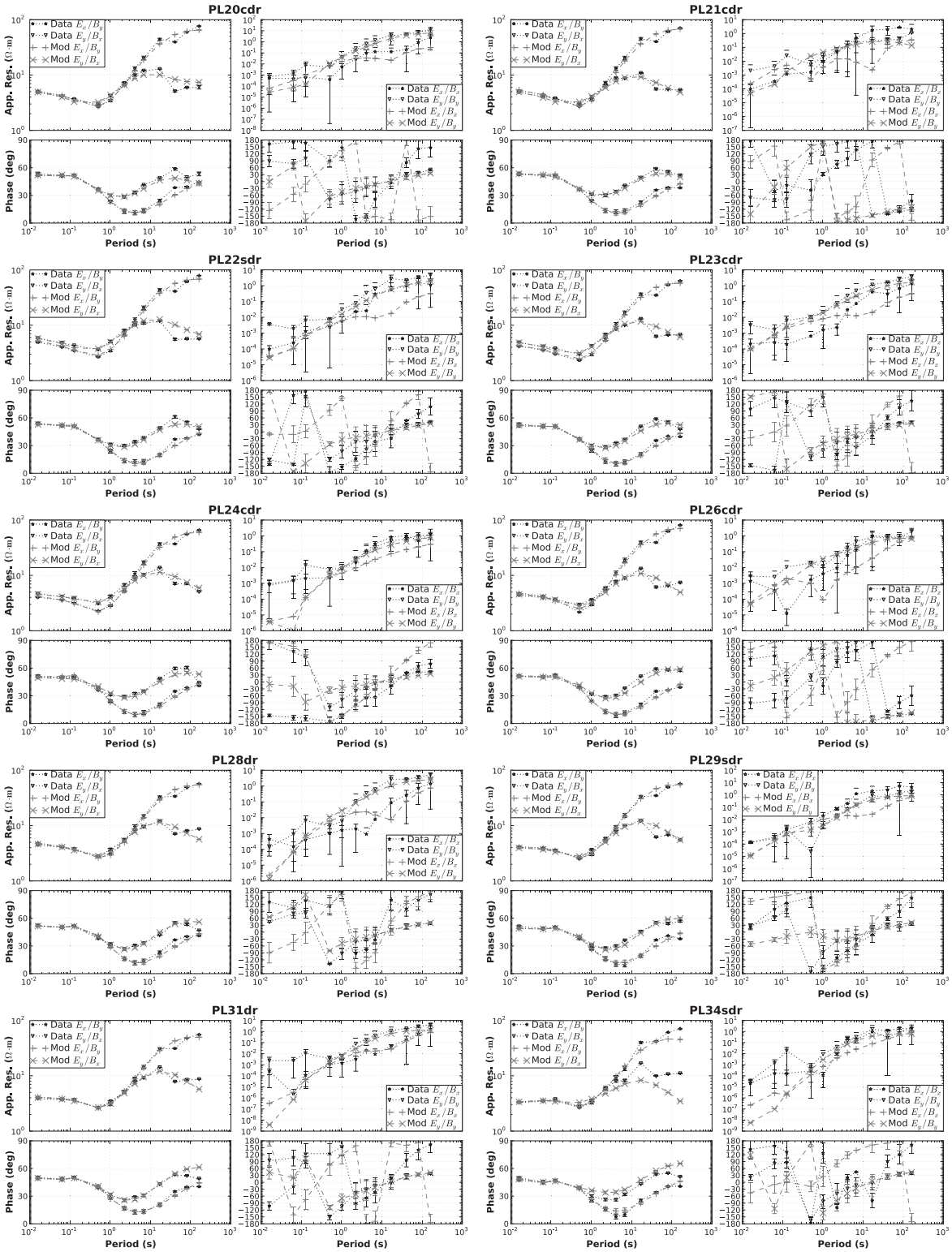

Figure B.8: Stations from the line collected in May,2012 as part of an honors project.

Appendix C

Magnetotelluric Monitoring of a Fluid Injection: Example from an Enhanced Geothermal System

Peacock[1], J. R., S. Thiel[1], P. Reid[2] and G. S. Heinson[3]

[1]South Australian Centre for Geothermal Energy Research, University of Adelaide, Adelaide, South Australia, 5005

[2] Petratherm Ltd., Level 1, 129 Greenhill Road Unley SA 5061

[3]TRaX, Department of Geology and Geophyics, University of Adelaide, Adelaide, South Australia, 5005

Geophysical Research Letters; 2012: Accepted Paper

STATEMENT OF AUTHORSHIP

Magnetotelluric Monitoring of a Fluid Injection: Example from an Enhanced Geothermal System

***Geophysical Research Letters* – 2012 – Accepted**

PEACOCK, J. R (Candidate)

Planned survey, collected data, processed, analyzed and wrote results.

I hereby certify that the statement of contribution is accurate

Signed..... Date....24/08/2012.....

THIEL, S.

Planned survey, collected data, helped analyze data.

I hereby certify that the statement of contribution is accurate

Signed..... Date....24/08/2012.....

REID, P.

Helped plan survey, helped with geological interpretation, provided logistical support and funding.

I hereby certify that the statement of contribution is accurate

Signed..... Date....22/08/2012.....

HEINSON, G. S.

Provided valuable supervision, helped plan survey, aided in data interpretation and critical analysis.

I hereby certify that the statement of contribution is accurate

Signed..... Date....24/08/2012.....

Enhanced geothermal systems (EGS) are on the verge of becoming commercially viable for power production, where advancements in subsurface characterization are imperative to develop EGS into a competitive industry. Theory of an EGS is simple, pump fluids into thermally enhanced lithology and extract the hot fluids to produce energy. One significant complication in EGS development is estimating where injected fluids flow in the subsurface. Micro-seismic surveys can provide information about where fractures opened, but not fracture connectivity nor fluid inclusion. Electromagnetic methods are sensitive to conductivity contrasts and can be used as a supplementary tool to delineate reservoir boundaries. In July, 2011, an injection test for a 3.6 km deep EGS at Paralana, South Australia was continuously monitored by both micro-seismic and magnetotellurics (MT). Presented are the first results from continuous MT measurements suggesting transient variations in subsurface conductivity structure generated from the introduction of fluids at depth can be measured. Furthermore, phase tensor representation of the time dependent MT response suggests fluids migrated in a NE direction from the injection well. Results from this experiment supports the extension of MT to a monitoring tool for not only EGS but other hydraulic stimulations.

Introduction

Novel technologies need to be developed to facilitate the switch in energy production from fossil fuels to renewable energy. One promising technology on the verge of becoming economically viable is enhanced geothermal systems (EGS) (Tester *et al.*, 2006). Initially tested at Fenton Hill, New Mexico in the 1970's, EGS is attractively simple. First, pump fluids into thermally enhanced lithology to generate a reservoir, where heat is absorbed by the fluids. Then, extract the hot fluids to produce energy. Unfortunately, realizing this simple idea proves to be complex due to numerous unknowns in the subsurface (Brown, 1995). One major unknown is tracking and characterizing location of fluids introduced into the lithology through hydraulic stimulation. The main technique for monitoring EGS reservoir development is micro-seismic (Wohlenberg & Keppler, 1987; House, 1987), where tomography locates earthquakes associated with fractures caused by hydraulic pressure and shear wave splitting can estimate size and orientation of the fractures (Rial *et al.*, 2005). However, the micro-seismic technique is not directly sensitive to fluid inclusion nor connectivity of the fractures.

Electromagnetic methods are sensitive to electrical conductivity contrasts at depth, including the presence of hot, saline, and electrically conductive fluids well connected in a resistive host rock. With typical depths of an EGS deeper than 3 km, magnetotellurics (MT) becomes an advantageous choice because of its versatile depth of investigation. MT is a passive technique that measures the Earth's electrical response to natural time varying magnetic fields, formally linked by the linear MT transfer function $\mathbf{Z}$, where depth of investigation and resolution depends directly on the period of the inducing magnetic field (Kaufman & Keller, 1981). Therefore, MT cannot directly measure individual fractures, only bulk volumetric conductivity contrasts assumed to be fluid filled fracture networks in an EGS sense. In geothermal applications, MT is typically applied as an exploration tool to characterize and locate potential geothermal targets (ex. Heise *et al.* (2008); Newman *et al.* (2008); Spichak & Manzella (2009); Arango

et al. (2009)). Utility of MT as a monitoring tool has predominantly been applied to searching for the elusive electromagnetic precursors to earthquakes (Kappler *et al.*, 2010). However, a recent study by Aizawa *et al.* (2011) demonstrates MT can monitor temporal variations in subsurface electrical conductivity associated with geothermal fluid movement. In one of the first MT surveys designed to monitor a fluid stimulation for an EGS, Bedrosian *et al.* (2004) found MT data did not measure a coherent change in subsurface conductivity caused by injected fluids because cultural noise influenced much of the data and the conductive overburden absorbed most of the electromagnetic energy. Additionally, Bedrosian *et al.* (2004) conducted a forward modeling exercise and found a conductive body on the order of 1 km^2 at 4 km depth would be detectable by MT. Notwithstanding, forward modeling and feasibility studies can only forecast plausible outcomes not exactly predict experimental results. Presented in this paper are pioneering results from continuous MT measurements that show coherent changes above measurement error generated from a fluid injection experiment designed to create the first stage of an EGS at Paralana, South Australia.

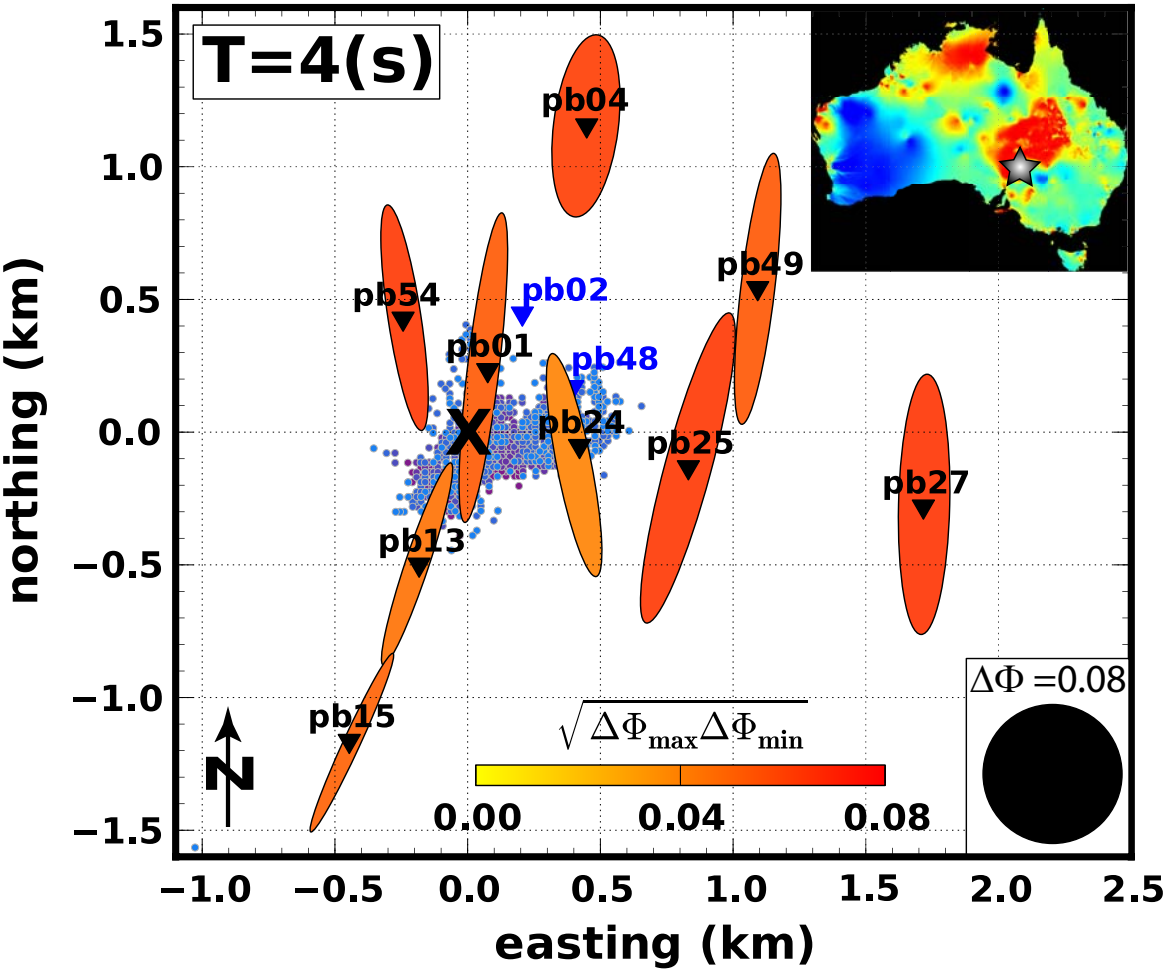

Figure C.1: Map of Paralana, South Australia displaying MT station locations (triangles) centered on Paralana 2 injection well (X), and micro-seismic events measured during the injection experiment from Hasting *et al.* (2011) (circles colored by day–192 as red to 196 blue). Top right is a temperature map of Australia from Geoscience Australia at 5 km depth where reds represent 285 C and the gray star locates Paralana. Stations that malfunctioned are colored blue and are not used in this analysis. The ellipses represent phase tensor residuals eq. (C.1) of pre-injection and day 196 for a period of 4 s. The face color is estimated as $\sqrt{\Delta\Phi_{max}\,\Delta\Phi_{min}}$ (Heise *et al.*, 2008). Interestingly, ellipse orientation generally aligns with the seismic cloud, suggesting that fluctuations in the MT response correlate with geoelectric alteration provoked by connected fluid filled pathways developed during the injection experiment.

Measurement

In July, 2011, for their EGS project at Paralana, South Australia, Petratherm Ltd. injected 3.1 million liters of saline water (resistivity of 0.3 Ω·m) into a Mesoproterozoic metasedimentary package at 3680 m depth through an 6 m perforated zone of the cased Paralana 2 borehole. The injection took 4 days to complete, starting on day 193 at 0400 universal time (UT) with low flow rates (2 barrels per minute) followed by a sequence of shutting in and increasing flow rates step wise to a maximum of 16 barrels per minute. Pumping concluded on day 196 at 0400 UT when the well was shut in. A micro-seismic array measured over 11,000 events suggesting the fractures opened in a NE preferred direction, with the majority located in the NE quadrant from the Paralana 2 borehole (Hasting *et al.*, 2011) (gray blob in Figure C.1). Two days before the injection, 11 broadband 4-component AuScope MT instruments were placed around the Paralana 2 borehole; the furthest station being about 2 km away (Figure C.1). Survey design was based on a previous injection test that showed fracturing tendency to be NE of the borehole. MT instruments recorded for an entirety of 8 days, including 2 days pre-injection, 4 days during injection and 2 days post-injection. A solar powered AuScope instrument was set up 60 km south of Paralana as a remote reference. Instruments sampled at 500 Hz and were synchronized by GPS. Dipoles were approximately 50 m in length, employing Cu-$CuSO_4$ non-polarizing porous pots as electrodes laid out in an L-shape aligned with geomagnetic north, which is fortuitously also regional geoelectric strike. Data were retrieved from the instruments every day to ensure data quality, while instrument setup was checked for functional completeness and batteries where changed every third day.

Data Processing and Analysis

Time series were checked for quality and coherent noise using robust time-frequency analysis formalized by Djurovic *et al.* (2003). Magnetic source field effects were estimated using a principal component analysis similar to Egbert (1997), finding only two dominant principal components except for a window of 1400-2400 on UT day 194. MT transfer functions were estimated for 1, 4, 6, 12, and 24 hour blocks utilizing a robust bounded influence remote referencing method developed by Chave & Thomson (2004). As source field power was low in the MT dead band (1-10 s) during local night time, a magnetic coherency threshold between the station and remote reference station was applied to remove influence of non-coherent and weakly coherent signal on **Z** that might produce false anomalies (Mareschal, 1986). Coherency between measured electric fields and predicted electric fields from measured magnetic fields was maximum across all periods for **Z** calculated using 24 hour blocks. Estimated mean error for **Z** of 24 hour blocks is approximately 1.4 percent, while average repeatability of MT parameters for the period range .01-1 s is within 0.4 percent between 24 hour blocks. Therefore, the following data analysis is focused on **Z** calculated from 24 hour time windows.

One benefit of conducting electromagnetic surveys in the Australian outback is the lack of electromagnetic noise sources, nevertheless there are other logistical aspects of data collection. Out of the 11 instruments deployed, 6 functioned consistently throughout the survey. The other 5 instruments were sporadically disrupted by mice chewing electrode cables or electrodes being dug or pulled out by other animals. These time windows of poor data quality are not used to estimate **Z**. Stations pb02 and pb48 are not used in this analysis because they malfunctioned too often to estimate reliable

transfer functions. Other noise sources include pumps used for the injection (operating at periods of ∼1 s and ∼6 s) and site specific noise. Fortunately, influence from these noise sources is minimal in these data. Also, it is important to note that the residuals, calculated as the MT response pre-injection minus each 24 hour time window, are calculated for each station. Therefore, any time invariant systematic noise, such as instrument noise, will be subtracted out. Near surface distortion is estimated and removed following Bibby *et al.* (2005). Note the phase tensor is invariant to near surface distortions, making it an advantageous parameter to represent the MT response (Caldwell *et al.*, 2004).

Variations in MT parameters are estimated by computing residuals of pre-injection MT parameters minus subsequent 24 hour blocks, specifically for apparent resistivity, impedance phase and the phase tensor parameters (see auxiliary material). Phase tensor residuals provide information about geoelectric strike transformation during the injection and gradients in resistivity structure, suggesting reservoir boundaries. Here the phase tensor residuals are calculated as a percent change eq. (C.1), where Φ_o is the phase tensor pre-injection, Φ_j is the phase tensor of a 24 hour block, $\mathbf{I}$ is the identity matrix of rank two and $\mathbf{\Phi}^{-1}$ is the inverse. The face color can be represented as the geometric mean $\sqrt{\Delta\Phi_{max}\,\Delta\Phi_{min}}$ (Heise *et al.*, 2008). For more on phase tensor behavior in anisotropic media see Heise *et al.* (2006) and Caldwell *et al.* (2004). Finally, to ensure bulk changes are estimated robustly, a median filter is applied to the each MT parameter, calculating the single station median for three periods at three different times.

$$\Delta\Phi oj = \mathbf{I} - (\mathbf{\Phi}_o^{-1}\mathbf{\Phi}_j) \tag{C.1}$$

Discussion

First and foremost, confidence in variations of the MT response must be instilled before any in depth interpretation can begin. The first thing to look for is a clear separation between the MT response pre-injection and MT responses estimated at later times. This provides an indication of variational magnitude and suggests a confidence level that observable temporal changes beyond measurement error exist. The second pattern to look for is causality, where variations in impedance phase should predict apparent resistivity changes according to the dispersion relation (Berdichevsky & Dmitriev, 2008). Specifically for a conductive change at 3.6 km at Paralana, the phase should increase at ∼1-10 s and the apparent resistivity should decrease beyond ∼8 s. The general trend for most stations is for the apparent resistivity is reduced below periods of 8 s and the phase increases around 1-10 s for MT responses estimated during the injection (see auxiliary materials). Moreover, most of these changes are near or just above the measurement error where variational magnitude is larger in the Z_{xy} than the orthogonal polarization, suggesting that change in geoelectric structure has a preferred direction towards the North. However, not all stations have consistent measurable changes above the noise level, therefore those that did will be discussed, namely pb01, pb04, pb24 and pb27. The others had intermittent periods where mice chewed cables or electrodes got pulled out by curious marsupials.

Another method to provide confidence in observable changes is to estimate an error floor by propagating an error estimate to each MT parameter, assuming that the error is identically 1D. An error estimate can be calculated as the ratio of the sum of the error in estimation of $\mathbf{Z}$ and repeatability divided by $\mathbf{Z}$ as a function of period and time for each station; this gives a percent change confidence floor. Applying a median filter

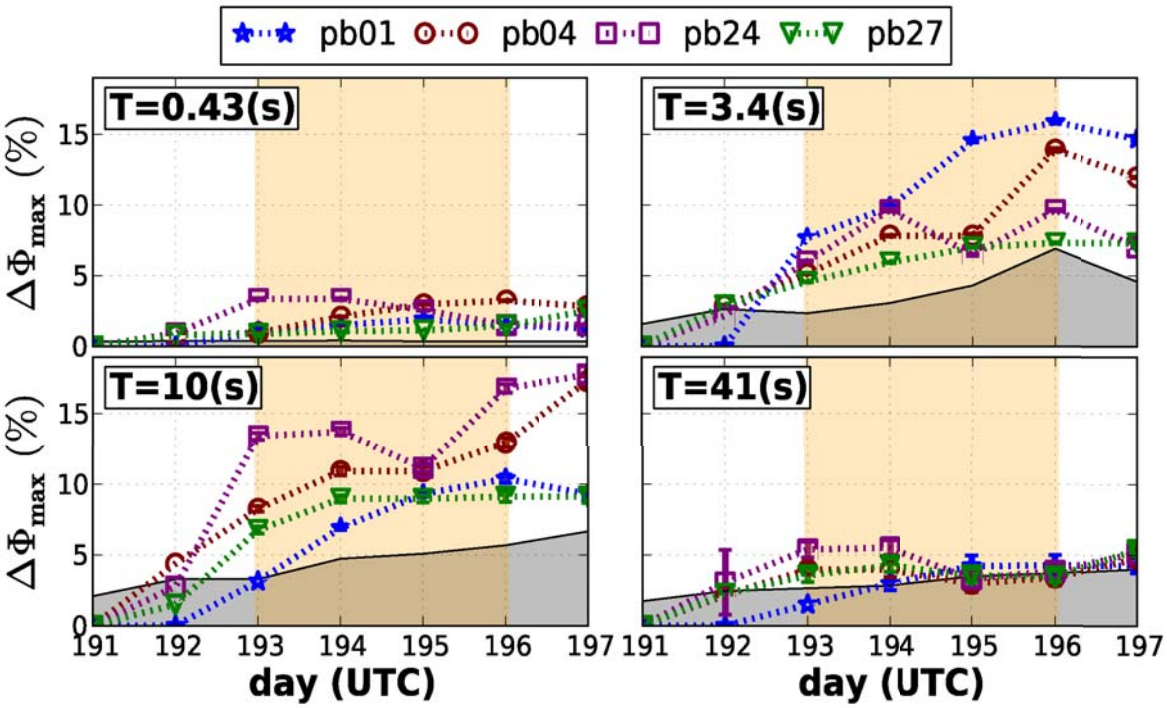

Figure C.2: Plots of percent change in Φ_{max} (an invariant of eq. (C.1), see Caldwell *et al.* (2004)) as a function of time for selected stations and periods (T). The shaded gray region is the estimated error floor as a function of time and period, giving a baseline to which variations can be confidently estimated and interpreted. The shaded orange region designates the pumping period when fluids were injected into the subsurface. Notice that periods between 1-10 s experience a general increasing change above the error floor, while periods outside this band do not.

and taking the maximum percent change estimate as a function of time and frequency of the aforementioned stations provides a robust baseline to which MT parameters can be compared to. Specifically, if the residual in the MT parameter is above this baseline then it can confidently be analyzed as a measurable signal (Figure C.2). Estimating parameters of the phase tensor (Caldwell *et al.*, 2004) provides dimensionality information and a representation of the MT response that is insensitive to distortions. Phase tensor representation of the time dependent **Z** suggests a general trend of increase in $\Delta\Phi_{max}$ as a function of time between 1-10 s, conversely $\Delta\Phi_{min}$ does not change above the error floor, again suggesting a directional dependence. Interestingly, for periods in the dead band (1-10 s), the error floor displays an increasing linear trend from the start date to the end date. However, magnetic source field power did not decrease from start to finish enough to cause an increase in error of estimating **Z**. Moreover, electrical noise from mechanical pumps (1 s and 6 s) remained nearly constant for the pumping period. Similarly, cathodic protection from the EPIC pipeline (2 km west of injection well see Figure C.1) was time-invariant. A plausible explanation is that the subsurface sampled at periods between 1-10 s (skin depth of ∼3-8 km) became more conductive over the duration of pumping due to the injection of saline fluids. This would cause a decrease in electric field strength at those periods and cause a decrease in coherency between the measured electric and magnetic field, propagating into an uncertainty increase in the estimation of **Z**.

Estimating depth to the conductive anomaly can ensure the change is occurring at the correct depth. An 1D Occam inversion (Key, 2009) of the mode where the electric field is aligned with maximum change estimates a depth of 2.8-3.3 km. Though it was found that inverting synthetic data estimated with a conductive anomaly at 3.6 km in

a similar way found a depth of 3.3 km as well. A 2D Occam inversion (Constable *et al.*, 1987) can be employed to estimate depth as a function of time for each station. Here the lateral dimension is now time instead of space and stations are spaced 20 km to remove any influence of neighboring stations at the target depth. Again, only the mode where the electric field is aligned with maximum change is modeled here because of its sensitivity to subsurface electrical variations. The estimated depth is 2.8 km, which is off by about 800 m from the known depth (see auxiliary material), but nevertheless is close to the expected depth range and similar to result found from a similar exercise using synthetic data. Occam's method finds the smoothest model possible and can smooth the resistivity structure increasing the uncertainty in the depth. Similarly, because MT is an integral method, if the conductance above the body is not properly estimated the depth will also not be accurately estimated. Accuracy can be improved with other electric and electromagnetic measurements.

Finally, dimensional variations in the MT response can be estimated from the residual phase tensor eq. (C.1). Interestingly, phase tensor residuals are larger than forward modeling predicts (see auxiliary material) by an order of magnitude, suggesting a greater contrast between host rock and the conductive body, also supporting experimentation over feasibility studies. Three general observations can be made from phase tensor residuals represented as an ellipse. First, average ellipse orientation aligns in a NE direction from periods between 1-10 s (Figure C.1 and C.3). This is also the regional strike direction and orthogonal to principle stress direction suggesting a correlation between electric strike and principle stress directions. Second, larger changes are observed to the NE of the borehole. Third, for periods between 1-10 s, size of phase tensor ellipses increases and face color becomes more red with each day, imaging changing geoelectric structure due to a growing conductive body at depth. However, phase tensor orientation exhibits behavior not of a simple homogeneous conductive block, but a complicated system of heterogeneous anisotropic pathways. Further work and more experimentation needs to be done to fully understand the MT response in time-variant fractured media. These three observations correlate well with micro-seismic data showing the majority of micro earthquakes occurred NE of the borehole and elongated generally in the NE direction. It is important to note that micro-seismic data can locate fractures opening, while MT estimates volumetric changes in the geoelectric structure associated with fluid filled fracture networks. Therefore, these two geophysical techniques should be used in tandem as complementary pairs.

Conclusion

In this experiment, MT has been successfully applied to monitoring a fluid injection for the first stage of an EGS, where changes in the MT response are assumed to originate from the injection of electrically conductive fluids connected by induced fracture networks at 3.6 km depth. Though the variations in MT parameters are on the order of a few percent, they are coherent in space and time, while being above measurement error. Furthermore, temporal and spatial variations correlate with the pumping schedule and results from a concurrent micro-seismic survey. Plotting apparent resistivity and impedance phase of pre-injection and subsequent 24 hour blocks provides visual conformation that observable changes exist above measurement error, while inverting the MT response as a function of time using a 2D algorithm is useful for estimating depth to the evolving conductive body, though absolute depth can have large errors stemming from inaccurate conductance estimation. Estimating an error floor for each MT parameter can be used as another tool to instill confidence in observable changes.

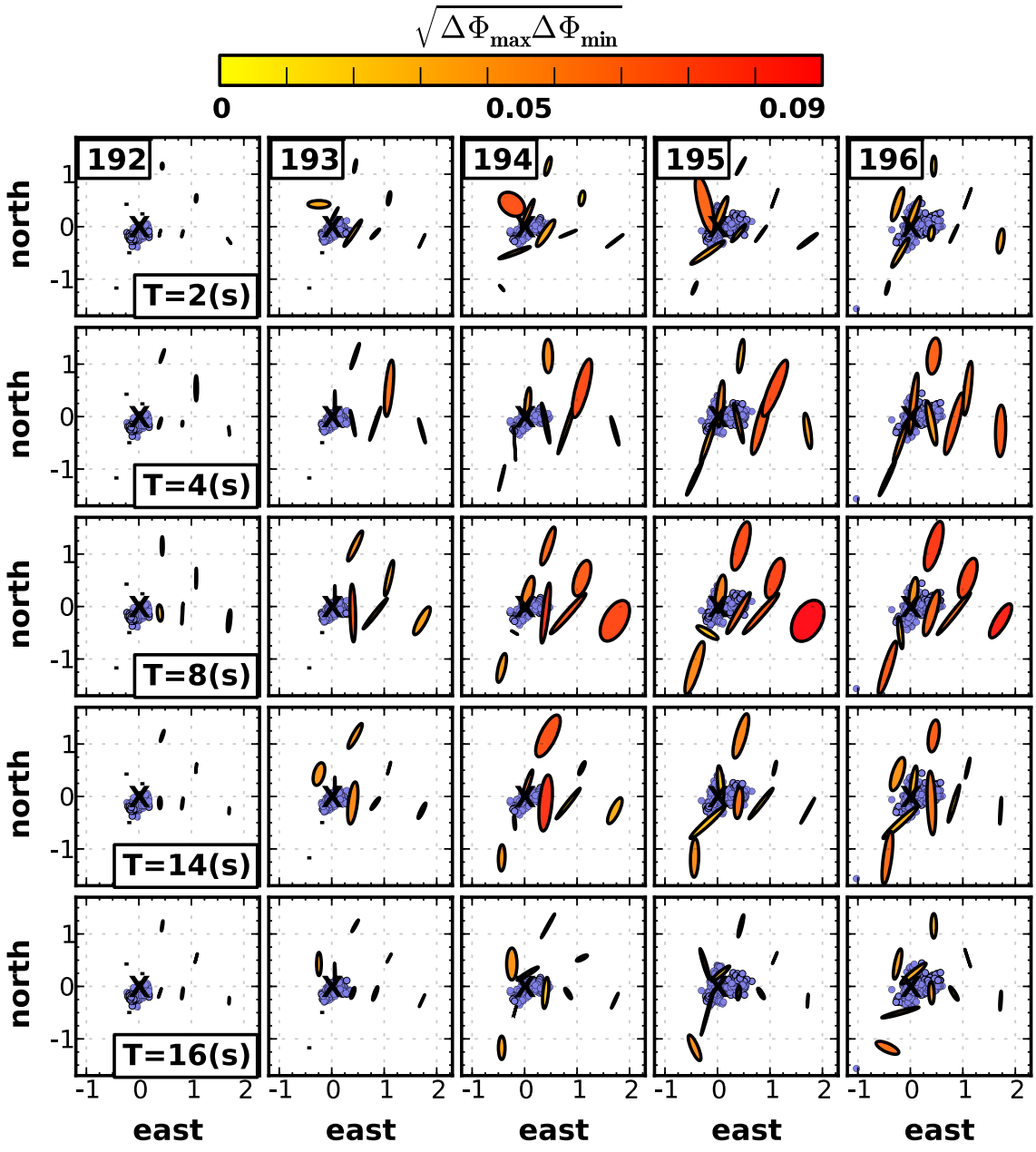

Figure C.3: Maps of phase tensor residual ellipses calculated as eq. (C.1) and colored as the geometric mean of eq. (C.1). Each column represents one day and each row represents one period. Paralana 2 borehole is marked as an X. The seismic cloud for each day is represented as by blue circles (Hasting *et al.*, 2011). Generally, ellipse orientation aligns with the direction of the seismic cloud, while size increases and color becomes warmer from day 193 to 196.

Finally, mapping the phase tensor residuals prove most informative for observing temporal and spatial changes generated by a growing conductive body at depth, indicating that reservoir evolution is a complex growth to the NE of the borehole, expanding in a NE preferred orientation. Three methods to improve monitoring MT surveys are to utilize more than one remote reference to better understand regional variations in the magnetic source field (Kappler *et al.*, 2010), measure vertical magnetic fields and increase the number of stations to cover a larger area for improved lateral resolution. Positive results from this experiment demonstrate the potential of expanding MT monitoring to other fluid injections, such as non-conventional natural gas where controlled source techniques can be applied (Orange *et al.*, 2009; Streich *et al.*, 2010; Wirianto *et al.*, 2010).

Acknowledgments

The authors would like to thank Petratherm and joint venture partners Beach Petroleum for support of this project. Mathieu Messieller, Louise McAllister, Goran Boren, Jonathan Ross, Hamish Adam, Tristan Wurst, Kiat Low, Aixa Rivera-Rios, Alison Langsford, and Kathrine Stoate for field assistance. Institute for Mineral and Energy Research, South Australian Center of Geothermal Energy Research and South Australia Department for Manufacturing, Innovation, Trade, Resources and Energy for financial support. Grant Caldwell for useful discussions on phase tensors and Mike Hatch for improving readability.